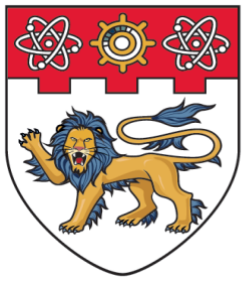

NANYANG TECHNOLOGICAL UNIVERSITY
SINGAPORE

ADVANCED STRATEGIES TO ENHANCE THE PERFORMANCES OF CRYSTALLIZATION AND PRECIPITATION OF BIOPHARMACEUTICALS

PU SIYU

SCHOOL OF CHEMICAL AND BIOMEDICAL ENGINEERING

2022

ADVANCED STRATEGIES TO ENHANCE THE PERFORMANCES OF CRYSTALLIZATION AND PRECIPITATION OF BIOPHARMACEUTICALS

PU SIYU

School of Chemical and Biomedical Engineering

A thesis submitted to the Nanyang Technological University in partial fulfilment of the requirement for the degree of

Doctor of Philosophy

2022

Statement of Originality

I hereby certify that the work embodied in this thesis is the result of original research, is free of plagiarised materials, and has not been submitted for a higher degree to any other University or Institution.

28/07/2022

. . . . . .

Date

. . . . . .

PU SIYU

Supervisor Declaration Statement

I have reviewed the content and presentation style of this thesis and declare it is free of plagiarism and of sufficient grammatical clarity to be examined. To the best of my knowledge, the research and writing are those of the candidate except as acknowledged in the Author Attribution Statement. I confirm that the investigations were conducted in accord with the ethics policies and integrity standards of Nanyang Technological University and that the research data are presented honestly and without prejudice.

28/07/2022

. . . . . .

Date

. . . . . .

A/P Kunn Hadinoto Ong

Authorship Attribution Statement

This thesis contains material from 3 paper(s) published in the following peer-reviewed journal(s) / from papers accepted at conferences in which I am listed as an author.

Chapter 2 is partly (Section 2.5) published as **Siyu Pu**, Kunn Hadinoto, Continuous crystallization as a downstream processing step of pharmaceutical proteins: A review, *Chemical Engineering Research and Design*, Volume 160, 2020, Pages 89-104.

The contributions of the co-authors are as follows:

- I have done literature review, prepared the manuscript drafts. The manuscript was revised by Assoc Prof. Kunn Hadinoto Ong.

Chapter 3 was submitted as **Pu, S.** and K. Hadinoto, Salting-out crystallization of glycopeptide antibiotics: Phase behavior study to control the crystal habit. Chemical Engineering Science, Volume 262, 2022, 118057.

The contributions of the co-authors are as follows:

- Assoc Prof. Kunn Hadinoto Ong raised funding for the project, supervised the project direction, reviewed, and edited the manuscript drafts.
- I co-designed the study with Assoc Prof. Kunn Hadinoto Ong and performed all the laboratory work at the School of School of Chemical and Biomedical Engineering.
- I have done literature review, prepared methodology, and carried out investigation, validation.
- I prepared the original manuscript drafts. The manuscript was revised by Assoc Prof. Kunn Hadinoto Ong.

Chapter 4 was submitted as **Siyu Pu,** Kunn Hadinoto, A Comparative Study of Antisolvent versus Salting-Out Precipitations of Glycopeptides: Precipitation Efficiency and Product Qualities, Powder Technology, Volume 415, 2023, 118181.

The contributions of the co-authors are as follows:

- Assoc Prof. Kunn Hadinoto Ong raised funding for the project, supervised the project direction, reviewed, and edited the manuscript drafts.
- I co-designed the study with Assoc Prof. Kunn Hadinoto Ong and performed all the laboratory work at the School of School of Chemical and Biomedical Engineering.
- I have done literature review, prepared methodology, and carried out investigation, validation.
- I prepared the original manuscript drafts. The manuscript was revised by Assoc Prof. Kunn Hadinoto Ong.

Chapter 5 is published as **Siyu Pu**, Kunn Hadinoto, Comparative evaluations of bulk seeded protein crystallization in batch versus continuous slug flow crystallizers, *Chemical Engineering Research and Design*, Volume 171, 2021, Pages 139-149. Permission has been granted by the licensed publisher "Elsevier" for utilization of the published content as a chapter in this thesis.

The contributions of the co-authors are as follows:

- Assoc Prof. Kunn Hadinoto Ong raised funding for the project, supervised the project direction, reviewed, and edited the manuscript drafts.
- I co-designed the study with Assoc Prof. Kunn Hadinoto Ong and performed all the laboratory work at the School of School of Chemical and Biomedical Engineering.
- I have done literature review, prepared methodology, and carried out investigation, validation.

- I prepared the original manuscript drafts. The manuscript was revised by Assoc Prof. Kunn Hadinoto Ong.

Chapter 6 is published as **Siyu Pu**, Kunn Hadinoto, Improving the reproducibility of size distribution of protein crystals produced in continuous slug flow crystallizer operated at short residence time, *Chemical Engineering Science*, Volume 230, 2021, 116181. Permission has been granted by the licensed publisher "Elsevier" for utilization of the published content as a chapter in this thesis.

The contributions of the co-authors are as follows:

- Assoc Prof. Kunn Hadinoto Ong raised funding for the project, supervised the project direction, reviewed, and edited the manuscript drafts.
- I co-designed the study with Assoc Prof. Kunn Hadinoto Ong and performed all the laboratory work at the School of School of Chemical and Biomedical Engineering.
- I have done literature review, prepared methodology, and carried out investigation, validation.
- I prepared the original manuscript drafts. The manuscript was revised by Assoc Prof. Kunn Hadinoto Ong.

28/07/2022

. . . . . .

Date

. . . . . .

PU SIYU

ACKNOWLEDGEMENTS

First, I would like to express my sincere gratitude to my supervisor, Assoc Prof. Kunn Hadinoto Ong, for providing me with the opportunity to pursue my Ph.D. under him. Thanks to his constant guidance, support, and encouragement, I can overcome challenges in difficult times and improve my research skills daily. Furthermore, I have significantly benefited from his patience, kindness, and insightful advice in each discussion, and completing this thesis would not be possible without him. In addition, I am deeply grateful to Assoc Prof. Judeh Zaher, Assoc Prof. Lee Jong Min, Assoc Prof. Raymond Lau Wai Man, and Asst Prof. Chen Ming-Hsu for their valuable advice during my research.

Second, I wish to acknowledge my lab mates, who have provided instrumental training for the equipment in our lab and our school and spare no effort to help me whenever I need it. I am particularly grateful for the spray-dryer training given by Ms. Lim Li Ming, the syringe pump training provided by Dr. Dong Bingxue, and the assistance from Dr. Tran The Thien and Ms. Angeline Chua during my research.

Third, I want to thank Dr. Shuddhodana for the help of the refrigerated circulator, without which I could not complete my experiments. I am also grateful to Dr. Zhong Wenbin for the assistance with the MIC test and thank Dr. Cuong for the kind help of the liquid nitrogen.

Finally, I sincerely thank my parents for their love, support, and understanding along the way. I also want to thank my friends who always show their encouragement.

TABLE OF CONTENTS

SUMMARY

Recent years have seen significant growth in the production titer of upstream of biopharmaceuticals, a level that could lead to diminishing returns upon increasing due to the downstream processing (DSP) bottleneck. The capture and polishing steps, representing the most laborious and expensive aspects of the DSP, are currently mainly dominated by pack-bed chromatography. However, due to the high cost of adsorbent and the high operation expenditure of chromatography-based theology, anything but chromatography (ABC) methodologies started to gain interest in the field as alternative method for purifying biopharmaceuticals. Precipitation and crystallization are classic unit operations that can provide promising alternatives in DSP. The aim of this dissertation is to develop advanced crystallization and precipitation strategies to improve process efficiency and product quality of biopharmaceuticals using bioactive Van glycopeptide and protein LYZ as the model biopharmaceuticals

In the first study, we investigated the phase behavior of salting-out room-temperature crystallization of glycopeptide antibiotics to determine crystallization conditions (i.e., pH, salt and peptide's concentrations, incubation time) to avoid needle-shaped crystal formation. Batch crystallizations of the prominent crystal habits identified from the phase behavior study (i.e., needle and non-needle) were subsequently performed. The batch crystallization's products were evaluated in their production yield and capacity, purity, size distribution, thermal stability, interfacial water content, dissolution profile, and antibiotic activity. The results showed that octahedral crystals were the predominant habit produced across the range of pH, salt, and peptide concentrations investigated. Needle crystal formation could be avoided by precise controls of pH and salt concentration. Octahedral crystals were produced at a significantly higher yield than needle crystals. The octahedral and needle crystals exhibited many similar properties but with distinct thermal stability and dissolution profiles.

The second study compared the antisolvent (with organic solvent) and salting-out methods in their precipitation efficiency and product qualities. The phase behavior study showed that heavy precipitates composed of nanoparticles were the

predominant products of antisolvent precipitation, in contrast to crystalline microparticles produced by salting-out. At their respective optimal conditions (e.g., pH, Van concentration), batch antisolvent Van precipitation had significantly higher yield than salting-out. Other than faster dissolution of the antisolvent precipitates attributed to their smaller size, both precipitates exhibited comparable purity, internal molecular structures, thermal stability, and antimicrobial activity.

In the third study, we evaluated for the first time the use of continuous slug flow crystallizer (CSFC) in bulk seeded protein crystallization, using lysozyme (LYZ) as the model protein. LYZ crystals preprepared in batch crystallizer were used as seeds. The crystallization was performed at supersaturation level below the metastable-zone-limit. The resultant crystal size distribution (CSD), CSD's reproducibility, LYZ's bioactivity, and crystallization efficiency as characterized by the space-time-yield (STY, mg/h·L) were determined. The results showed that the CSFC's performance was governed by the flowrate, where a trade-off existed between crystal quality and crystallization efficiency upon varying the flowrate. At low flowrates, which reduced the shear rate and prolonged the residence time, well-defined large tetragonal crystals were produced attributed to suppressed secondary nucleation and extended crystal growth, but low STY due to difficulty in transporting the seeds/products crystals. Higher flow rates led to higher STY, but increased production of small non-tetragonal crystals that formed agglomerates. Compared to batch crystallizer, the CSFC produced LYZ crystals of similar average size, morphology, and bioactivity, but with roughly 50% lower STY, as the batch's high-shear environment promoted secondary nucleation, hence higher crystallization rate. The CSD's width and reproducibility was nevertheless significantly improved in CSFC.

Lastly, in the fourth study, we developed a segmented slug flow crystallizer (SFC) of LYZ operated at short residence time (<30 min) comprising a short nucleation segment and a growth segment operated at different temperature and fluid velocity. Compared with non-segmented SFC, The segmented SFC design comprising a short nucleation segment and a longer growth segment operated at different temperatures improved the CSD's reproducibility by limiting small crystals and large-sized

agglomerates formations as evidenced by the small coefficient-of-variations between replicates (<10%). Lysozyme crystals having size of roughly 13–14 mm with well-preserved bioactivity were produced at yield and space-time yield of approximately 67% (w/w) and 93 g/L·h, respectively.

LIST OF FIGURES

LIST OF TABLES

LIST OF ABBREVIATONS

AAC
anything and chromatography.....35
ABC
anything but chromatography 35
API
active pharmaceutical ingredient 28
AS
ammonium sulfate.....47
ATPS
aqueous two-phase system.....35
BFDH
Bravais-Friedel-Donnay-Harker 78
C&GT
celluar and gene therapies.....32
CFI
coiled fow inverter 69
CHO
Chinese hamster ovary.....50
CMA
critical material attribute 55
CPFC
continuous plug flow crystallizer..133
CPP
critical process parameter 55
CQA
critical quality attribute 55
CSD
crystal size distribution 29
CSFC
continuous slug flow crystallizer.. 138
CV
coefficient of variation 58
DMSO
dimethyl sulfoxide 60
DSC
differential scanning calorimetry.... 84
DSP
Downstream processing 27
ELP
elastin-like polypeptide 50
FSF
forced solution flow..... 67
HIC
hydrophobic interaction
chromatography..... 34
HMWI
high molecular weight impurities... 50
HTO
high-temperature orthorthombic
crystals..... 53
ID
inner diameter..... 138
IEX
ion exchange chromatography..... 34
LLPS
liquid-liquid phase separation 40
LTO

CHAPTER 1 INTRODUCTION

1.1 Crystallization and precipitation of peptides for purification purposes

Biopharmaceuticals represent a rapidly growing market worth 497 billion dollars by 2021 [1, 2]. Bioactive peptides are an emerging class of biopharmaceuticals showing distinct and often superior therapeutic traits from small-molecule drugs and protein biologics [3]. They are manufactured by fermentation in the upstream, followed by the downstream processing (DSP) steps include chromatography, precipitation, ultrafiltration, or serial combinations of these methods [4]. Among these methods, affinity or ion-exchange chromatography has almost exclusively been the workhorse in DSP of bioactive peptides, similar to its prominent role in DSP of therapeutic proteins (e.g., monoclonal antibody) [5]. However, chromatography-based method bears shortcomings in its high operating costs due to costly adsorbents and limited production capacity, which fails to meet the augmented titers from the upstream production [6]. For this reason, the viability of non-chromatography purification methods to be the workhorse DSP method of bioactive proteins/peptides have been actively studied [7].

Crystallization and precipitation are the classical unit operations that are promising in replacing chromatography in the purification step of DSP of biopharmaceuticals [6]. Precipitation is a process achieved by adjusting the environmental conditions to reduce the solubility of the target proteins/peptides, resulting in a new solid phase. When the solid phase is in an ordered manner, the process is named crystallization [6]. Precipitation is usually defined as reactive crystallization that involves rapid mixing of concentrated chemical reagents and produce solids that contain the reactants [8]. Throughout this thesis, however, precipitation is the general term that characterizes the process of solid formation due to reduced solubility. In this sense, crystallization is a kind of precipitation that produces solid with orders (crystals). Compared with the workhorse (chromatography) in DSP of bioactive peptides, the main advantages of precipitation are that it is inexpensive, can be carried out with simple equipment, can be done

continuously, and importantly, it has good scalability and high throughput [9]. Moreover, from the drug product formulation's perspectives, protein/peptide crystals are known to exhibit higher purity, better physicochemical stability, and dissolution characteristics than their non-crystalline counterparts [10]. Although crystallization for purification purposes has been widely studied for small-molecule pharmaceuticals and proteins [11], crystallization of peptides, whose molecular weight (MW) typically falls between small-molecule pharmaceuticals and proteins (i.e., $1 \leq MW \leq 5$ kDa), has not been widely employed [12]. At present, ultrafiltration membrane and chromatography, which pose problems of low throughput and high operational costs, remain predominantly employed in industrial purification of bioactive peptides [13]. The few studies on peptide crystallization were mostly aimed at crystal structure determination [14-16], where method such as vapor diffusion was used to prepare large crystals for good diffraction quality [14]. On the other hand, in addition to crystal size, crystal habit (or external shape), as one of the quality attributes, can affect the active pharmaceutical ingredient (API) in the properties (e.g., filterability [17]) that can ultimately influence the downstream processing efficiency [18]. Additionally, crystal habit has been found to influence the bioavailability of the pharmaceuticals by affecting the solubility and dissolution [19, 20]. As a result, the lack of advance in bulk crystallization of bioactive peptides as a purification method limits the development of crystals engineering via controlled crystallization of bioactive peptides.

Common precipitation methods for proteins (also peptides) include isoelectric precipitation, salting out, and antisolvent precipitation using organic solvents [21]. Currently, the knowledge on precipitation of biological macromolecules was predominantly based on studies using protein as the model system [22]. Similar approaches as those used on protein precipitation have been used for peptide precipitation, despite the order-of-magnitude difference in their molecular weights, often resulting in high process uncertainties [23, 24]. It has been found that different precipitation methods (i.e., isoelectric, salting-out, and antisolvent) affect not only the precipitation efficiency (i.e., fraction of solute that precipitates), but also qualities of the precipitate proteins (e.g., solubility, bioactivity, stability, purity) [25].

Therefore, the effects of different precipitation methods, especially the effects on the peptide precipitate quality merit further investigations.

1.2 Continuous crystallization to enhance crystal size distribution of crystals

Unlike bioactive peptides, crystallization of one of the major biopharmaceuticals —— proteins for purification purpose have been widely studied for a long time. The most famous example is the crystallization of insulin. Since 1973, patent on insulin purification from animal source has been filed [26]. Current DSP of insulin production employ three times crystallization in the train, producing purest insulin with a purity higher than 98% [6]. In recent years, crystallization as a purification method for mAbs [27, 28], digestion product of full-length antibody [29, 30], and other recombinant proteins [31-34] have been reported.

For crystallization/precipitation, the crystal size and crystal size distribution (CSD) are among the most important solid-state properties to control [35]. Bulk crystallization of pharmaceutical proteins, however, faces a challenge in controlling the resultant CSD and its reproducibility [36, 37]. The CSD influences not only the efficiency of the downstream processing steps (e.g. filtration, drying), but also the dissolution and consequently bioactivity of the protein crystals [38]. Generally, uniformly distributed particles are easier to handle, filter, mix, and hence are more desirable [39]. A number of strategies have been investigated to improve the CSD in bulk protein crystallization include seeded crystallization [40, 41], sonocrystallization [42, 43], and additive crystallization [44, 45].

Conversely, another principally different strategy is moving the bulk crystallization into a continuous platform [10]. By segmentation of nucleation and growth events with precisely controlled supersaturation levels in each segment, improved CSD could be realized [46-48]. Continuous platforms can be mainly classified into mixed-suspension mixed-product removal crystallizer (MSMPRC) and tubular crystallizer (forced solution flow system, plug flow crystallizer (PFC), slug flow crystallizer (SFC), oscillatory flow baffled crystallizer (OFBC)). Theoretically, infinite number of small-volume MSMPRCs arranged in series would have similar crystallization performance as continuous PFC (CPFC) having the same

total crystallizer volume. When large, unbroken crystals are desired, tubular crystallizers are preferred due to their milder operating conditions. This is especially important for proteins crystals that are inherently more fragile than small-molecule crystals [24, 49]. Still, CPFC have disadvantages such as limited production throughput, risks of channel blockage, and the fact that the residence time is dictated by the tube length and flowrate, which both have their operating limits. Besides, while seeded crystallization has been widely employed to grow a large single protein crystal for X-ray diffraction studies, seeded protein crystallization for purification purposes so far has only been performed in the batch platform [40, 41, 44, 50, 51].

The slug flow crystallizers (SFC) is characterized by a segmented gas-liquid flow, consisting of a string of gas bubbles separated by liquid slugs of the crystallization solution, flows concurrently in a tube [52]. The presence of the gas bubbles prevents tube clogging from occurring as the flowing bubbles facilitate constant net flows of the crystals produced in the liquid slugs [53]. The constant net flow of crystals also leads to narrow residence time distribution of the crystals, which in turn improves crystal qualities in small-molecule pharmaceutical crystallization [54]. Moreover, the internal fluid circulation in the liquid slugs renders each slug operate as a well-mixed crystallizer with homogeneous supersaturation, resulting in monodispersed crystals [55]. Using lysozyme as the model protein, Neugebauer and Khinast [46] reported for the first time the application of SFC to produce protein crystals by combined salting out and cooling crystallization principles. Lysozyme crystals with an estimated average size of ≈ 26 mm were successfully produced at ≈ 68% yield after 113 min residence time. This study could have been performed at lower temperatures to increase the supersaturation levels to achieve larger yield at the same residence time, or a comparable yield could be obtained at shorter residence time. Yet, conducting crystallization at short residence time is known to have adverse effects on the crystal quality, where small crystals with inconsistent size distributions are often produced due to (i) the higher nucleation rate as a result of the high supersaturation level and (ii) uncontrolled agglomeration of the small crystals produced [56, 57]. Despite the need to control CSD in continuous crystallization conducted at supersaturation levels and short residence times, there are very few studies on this topic.

1.3 Objectives

As discussed earlier, there is a lack of knowledge regarding bulk crystallization and precipitation of bioactive peptides. Specifically, Chapter 3 and 4 of this thesis address this gap with two objectives:

In Chapter 3, an investigation into the avoidance of the problematic needle habit of a bioactive peptide (vancomycin hydrochloride) that was predominantly produced by batch crystallization was performed. The phase behaviors of vancomycin hydrochloride in bulk salting out crystallization were investigated under varying pH, salt concentrations, and peptide concentrations. Further, differences and similarities of the solid quality of the peptide crystals would be evaluated. Characterization of peptide crystals with different habits were conducted and compared in terms of the structural, appearance, physical stability, etc.

In Chapter 4, effects of different precipitation methods of vancomycin hydrochloride were explored. A comparative study on the precipitation efficiency and the product qualities between antisolvent and salting-out methods was carried out. The phase behaviors of bioactive peptide (vancomycin hydrochloride) in bulk antisolvent crystallization were investigated under varying pH, solvent volumes, and peptide concentrations for investigated for the first time. Further, the properties of peptide precipitates produced from antisolvent precipitation and crystals from salting-out were characterized and compared.

As mentioned above, continuous crystallization has been pursued as the method to control CSD in protein crystallization. However, improvement in throughput, CSD control, and operation under short residence time and high supersaturation are still lagging. Chapter 5 and 6 of this thesis address the gap with two objectives:

In Chapter 5, the hypothesis that seeding and continuous crystallization can improve CSD and CSD reproducibility were examined. To this end, the bulk seeded continuous crystallization of lysozyme were studied for the first time, with the CSD's width and CSD reproducibility compared with the batch counterpart. Key process

parameters flow rates were determined and the improvement of CSD was investigated.

In Chapter 6, a proposed strategy to limit space time of the nucleation by means of a segmented SFC design was evaluated for the improvement of CSD and CSD reproducibility of continuous protein crystallization in SFC platform. A short rapid nucleation segment and a longer segment for crystal growth at high supersaturation level and short residence time were utilized to explore the feasibility of the strategy. To further exam the effect of the process parameters such as the temperature and length of growth segment, fluid velocity, and concentration of solution entering the inlet on the CSD of product, variations of designs were also proposed and evaluated.

CHAPTER 2 LITERATURE REVIEW

2.1 Manufacturing of biopharmaceuticals

Biopharmaceuticals include monoclonal antibodies (mAbs), recombinant proteins, proteins and vaccines derived from nonengineered organisms as well as blood/plasm-derived products, and cellular and gene therapies (C&GT) [58]. In 2019, 9 out of 20 top therapeutics by sales were antibodies, making up $75 billion in earnings [59]. In April 2021, the US Food and Drug Administration (FDA) approved its one-hundredth mAb, and the mAb market is predicted to reach $300 billion by 2025 [59, 60]. Though the coronavirus disease 2019 (COVID-19) has caused severe disruptions in all the economic sectors, including the pharma industry, it has also provided opportunities especially for biopharmaceutical products such as mAbs [61, 62] and mRNA vaccines in response of the pandemic.

Compared with traditional synthetic drugs, biopharmaceuticals have advantages include higher specificity, higher potency, and less side effects associated with conventional synthetic drugs [63]. Most synthetic drugs are small molecules with simple structures, contrasting with the biopharmaceuticals that are normally 100-1000 times larger. Unlike traditional small-molecule drugs that are synthesized in chemical processes, biopharmaceuticals are produced in living cells, which is complex involving several unit operations and processes. Due to its structural complexity, the properties of biopharmaceuticals depend not only on their primary structure (e.g., the amino acid sequence), but also on the manufacturing processes. These unit operations are generally separated into two parts: upstream processing (USP) and downstream processing (DSP).

2.1.1 Upstream processing (USP)

Figure 2.1 demonstrates a series of typical upstream processing (USP) steps. USP is defined as the microbial growth required to produce biopharmaceuticals [64]. It started with the thaw of the cells, then expanded to inoculum preparation, and further moved to the production of the biopharmaceuticals in bioreactors before cell harvesting. The development direction of USP has been optimizing stable and high-

producing cell line, increasing culture scale and titer since 1990. Innovations in high density cell banking, expansion optimization, and enhanced culture productivity has also been investigated [65, 66].

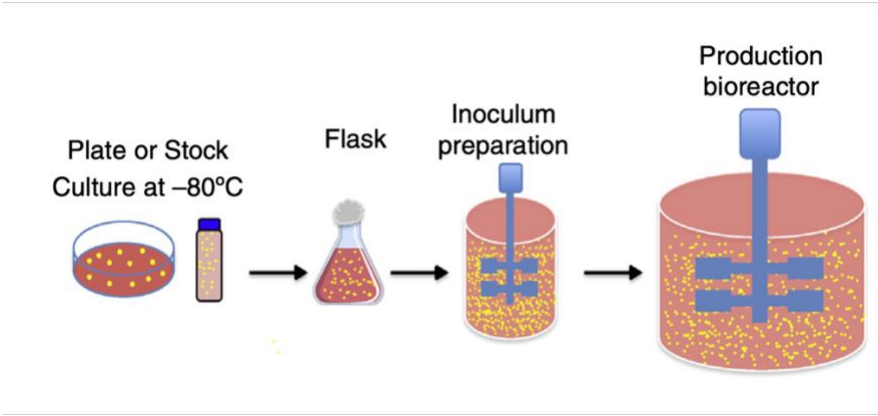

Figure 2.1 The upstream processing (USP). Revised from permission of [64]

2.1.2 Downstream processing (DSP)

DSP is engaged in the separation and refinement of the mixtures of components. The simplest definition of DSP is it refers to a collection of separation techniques designed to achieve mass transfer phenomena by converting mixtures of substances into fractions or subsets [67]. The unit operations of a standard DSP include cell harvesting [68] (also known as recovery and isolation [69] or cell recycle/product clarification [70] that is usually included in the DSP [71]), capture, and polishing (also known as final purification [67]) [72]. The initial cell harvesting separates the protein from nonprotein parts of the mixture, while the capture and polishing steps separate the desired protein from all other proteins while retaining its activity and chemical integrity. Owing to the strict quality criteria includes defined purity, efficacy, potency, stability, toxicity and immunogenicity, it is estimated that DSP makes up 50-80% of the protein manufacturing costs [73]. Common bioseparation methods include low-resolution methods such as precipitation, and high-resolution methods such as phase partitioning and chromatography [73]. The capture and polishing steps, representing the most laborious and expensive aspects of the DSP, are currently mainly dominated by pack-bed chromatography [5, 73] (**Figure 2.2**)

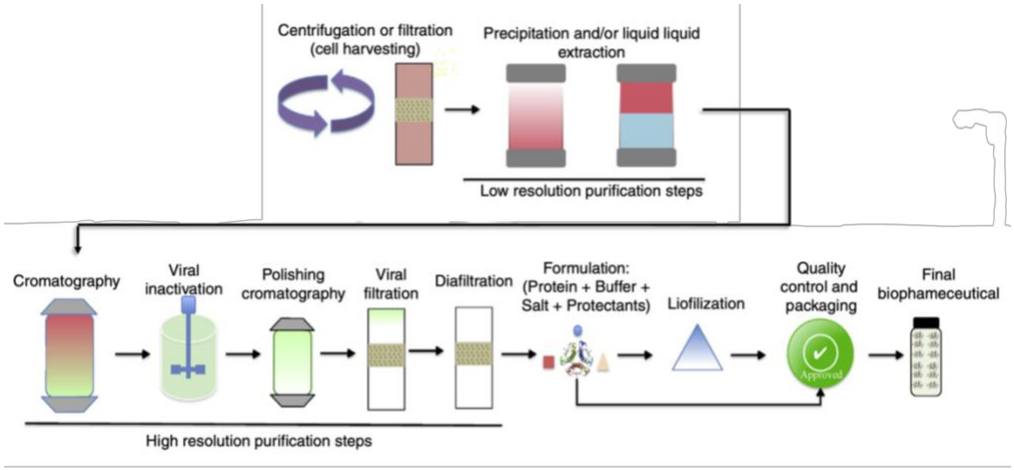

Figure 2.2 The downstream processing (DSP). Revised from permission of [64]

The advantages of chromatography in providing high resolution and selectivity, thus processing products with high purity and yield make it the most suitable technique for purification of high-value biopharmaceuticals. Due to the inconsistent nature of the process and the complexity of the impurities, it is impossible to purify a protein using single-step chromatography [66]. Typically for DSP of mAbs, protein A affinity chromatography is used in the capture step, followed by viral inactivation (VI). It has been estimated that up to 60% of the DSP come from chromatography, with protein A resin being a substantial cost contributor [74]. In the polishing period, one or two anion and/or cation exchange chromatography steps will be utilized. Then the process moves to virus filtration, and tangential flow ultrafiltration (TFUF) to produce high-pure drug substance [72]. The dynamic binding capacity of the protein A chromatography ranges from 15-100 g mAb/L resin depending on antibody, flow rate, and adsorbent. And the purity of the proteins purified can be consistently higher than 95% [75].

Despite its prevalence and advantages, protein A chromatography is far from perfect. The problems associated with it include the leachability of protein A that leads to non-specific binding of impurities, which will need other chromatography method to remove [75]. Besides, the high resin and operation cost also pose doubts. For example, protein A resins cost $5000-15000 per L, and the water consumption per kg mAb produced assuming an initial mAb titers of 2-5 g L^{-1} is about 1500-3500

L [4, 7]. Also, the cycling needed for economical use of affinity resin potentially favoring the use of a smaller column and multiple cycles instead of using a larger column and a single cycle per batch, which limiting the throughput [74]. To address the problems stated above, advances in the optimization of protein A sequence to improve the ligand stability, and improvement of resin chemistry and ligand density to increase the binding capacity has been reported [72]. Meanwhile, advances in custom affinity media and hydrophobic interaction chromatography (HIC), improved use of traditional ion exchange chromatography (IEX) and improved use of multimodal chromatography (MMC) provide alternatives to protein A chromatography as well [67].

Despite these innovations, however, the significant improvements in the upstream titers (from an average of 0.2 g/L in 1985 to 3-8 g/L at a production scale of 10 kL or larger today) rendered the chromatography-based DSP a bottleneck of manufacturing [76]. It is estimated that improving the titer from 1 to 5 g L^{-1} increases the cost of DSP from 61% to 91% of the overall manufacturing cost [77]. Consequently, alternative DSP methods are being pursued to circumvent the use of chromatography. Anything but chromatography (ABC) methodologies, despite being argued to be changed to "Anything and Chromatography" (AAC) [78], has been widely investigated in the DSP of biopharmaceuticals [7, 69]. Currently, membrane-based technology [77, 79-81], aqueous two-phase system (ATPS) [69, 82-86], magnetic separation [12, 87-90], precipitation [6, 87, 91-94], and crystallization [6, 26, 38, 84, 95-98] provide promising alternatives. Besides, to enhance the processing flexibility, better respond to fluctuating market demands, continuous manufacturing strategies have been sought as an effort to achieve process intensification in biologics manufacturing [11, 70, 99-102]. Concomitantly, single-use technologies (SUT) has also become increasingly popular in both USP (e.g., single-use bioreactor) and DSP (e.g., single-use centrifugation) of the biopharmaceutical industry [103]. Lastly, modeling of a single unit operation in DSP, and the optimization of the plant utilization have also demonstrated vast potential in bridging the gap between the empirical observation and the rational designs [67]. In this dissertation, we aimed to investigate advanced crystallization and precipitation for purification of

biopharmaceuticals include bioactive peptides and proteins, and the basic theory and development of these two methods would be reviewed below.

2.2 Phase behaviors of protein molecules during precipitation

2.2.1 Protein and peptide structure

Proteins are complex, biological macromolecules that are built up by amino acids (residues) linked by peptide bonds to form a polypeptide chain. There are 20 naturally occurring amino acids that are chemically different. The amino acid sequence of a protein's polypeptide chain is called its primary structure. Different regions of the sequence can form local regular sub-structure, which is the secondary structure, including alpha (α)-helix and beta (β)-sheet or beta (β)-strand. The tertiary structure of a protein is a three-dimensional structure formed by packing secondary structure of one polypeptide chain into one or several compact globular units called domains. The quaternary is the three-dimensional structure that contain several arranged polypeptide chains (subunits). By forming the tertiary and quaternary structures, the residues far apart can be brought close, creating a functional region, i.e., an active site. Naturally, the biological function of a proteins is determined by its folded structure, which is intrinsically determined by the amino acid sequence. From a chemical point of view, according to the widely accepted nomenclature rules, "oligopeptides" contain fewer than 15 amino acids, "polypeptides" are comprised of approximately 15-50 amino acid residues, and "protein" indicates polypeptides that have more than 50 amino acids [104]. Unlike proteins, most peptides lack well defined secondary and tertiary structures [105]. Consequently, they might have problem protecting reactive side chains in the interior of their globular structure from their environment, and they tend to leave most side chains exposed to a surrounding solvent [106]. Due to the structure similarity, the techniques required for peptide crystallography mirror the techniques developed for protein crystallography [107]. In terms of crystallization and precipitation as a purification method, the fundamental theories summarized from protein systems are generally applicable to that of peptides.

2.2.2 Protein-protein interactions

Salt-, solvent-, nonionic polymer-, and thermally-induced precipitation and crystallization are essentially self-association-based protein purification methods [108]. Since protein molecules typically have a size around several nanometers [109], proteins has been considered as colloids (sizing around nm-μm [110]) for a long time, and colloidal interactions provide a valuable framework in analysis of protein-protein interactions [111]. There are several forces involved in protein and colloidal interactions, including excluded volume effects, dispersion forces, electrostatic forces, ion binding, hydration effects, salt bridging, hydrogen bonding, and hydrodynamic forces [112-114]. Generally, protein–protein interactions involve a subtle balance of both specific (hydrogen bonds and salt bridges) and nonspecific (van der Waals and hydrophobic) interactions [49].

2.2.2.1 van der Waals force (vdW)

Generally, van der waals force is the sum of the attractive and repulsive non-bond forces between atoms or molecules other than the electrostatic forces [115]. Dispersion forces (also called London dispersion or London-van der Waals (vdW)), Keesom orientation, and the Debye polarization interactions constitute the total van der Waals interactions between two atoms or molecules [116]. Different from the first two interactions that are absent between nonpolar molecules, dispersion forces are always present, and is the dominant vdW forces in protein-protein interactions. They are attractive between similar materials and only under very particular circumstances become repulsive in certain heterogeneous systems [117]. Due to the short-range nature, the complementarity of shape and mutual orientation of the interacting molecules will determine the total energy of the dispersion interaction [114]. Resultingly, the surface effects (related to the surface area) are extremely critical in the dispersion forces [110].

2.2.2.2 Electrostatic interactions

The repulsive forces stabilizing the proteins are often imparted via surface charges of the ionizable amino acids via electrostatic interactions [118]. Specifically, the electrostatic interactions can modulate the pKa shift of the proteins, affect the protein folding stability, and impact the protein binding and condensation, etc. [118].

The electrostatic interactions of proteins are determined by charge–solvent interactions ΔG^{solv} and solvent screening of charge–charge interactions ΔG^{int} [118] (**Eq. (2.1)**). And the electrostatic energy can be also expressed into the sum of electrostatic energy in the absence of salt ions, denoted as ΔG^{el0} and the contribution of added salt ions, the Debye-Hükel term, ΔG^{DH} (**Eq. (2.2)**).

$$\Delta G^{el} = \Delta G^{solv} + \Delta G^{int} \tag{2.1}$$

$$\Delta G^{el} = \Delta G^{el0} + \Delta G^{DH} \tag{2.2}$$

2.2.2.3 Other interactions

Small ions, when attaching to the protein surfaces, affect both the global charge of the protein and the apparent surface topography. Also, the ion binding can affect the crystallization behavior of proteins and induce changes in the space group [119]. The effect of ions on proteins is traditionally described using Hofmeister series (or lyotropic series), which order the effects of ions based on their ability to stabilize or salt-out proteins [120]. Specifically, ions can be termed as kosmotropes that have a stabilizing and salting-out effects on macromolecules. While at the other end are the chaotropes that destabilize the folded proteins and cause salting-in behavior. One other interaction is the hydrophobic interactions, which is a major driving force in protein complex formation that forms the basis for a variety of events such as protein folding and phase separation [113]. Furthermore, hydrogen bonds and salt bridges are commonly observed in protein crystal contacts, but it is unclear whether these interactions stabilize or destabilize the protein [112]. Lastly, there are also hydrodynamic forces exist in protein solution when the particles move through a fluid [112].

2.2.3 Solubility

Protein solubility is a thermodynamic parameter defined as the amount of protein in a saturated solution that has equilibrium with a solid phase, either crystalline or amorphous [121]. Conducting crystallization research requires a comprehensive understanding of a protein's solubility, since only then is it possible to control the

crystallization process rationally. Therefore, the solubility of protein has been the subject of measurement for more than a century [122]. Classical method to measure the solubility is through dissolution and crystallization [123-125]. The most important factors effecting the solubility of a protein are its physical characteristics: structure and size, protein charge, and the solvent. Therefore, any perturbation of the environment of the proteins might bring the protein out of the solution and lead to precipitation. These perturbations include the pH, ionic strength, the temperature, and the properties of the solvent. Common precipitation includes salting out, isoelectric precipitation, organic solvent-driven precipitation, affinity precipitation, and addition of nonionic polymers [9, 21, 73, 126].

2.2.4 Salting in and salting out

Salt exerts two opposing energy effects: (1) the tendency of ions at surface of proteins to interact with counterions for electrostatic stabilization; (2) the tendency of mobile ions for hydration in the bulk solvent. Salts can modulate the phase transition of a protein (e.g., solid and solution) due to the difference in the surface exposure to the solvent. These two effects were characterized by (1) Debye-Hükel term (ΔG^{DH}) that represents the electrostatic stabilization of ions at the surface of protein, and (2) Kirkwood term (W^K) that represents the work to charge up the ions surrounding the proteins, which measures the dehydration cost of all ions (**Figure 2.3a**). The combination of these two terms determine the biphasic solubility of the solute molecules given by [118]

$$-k_B T \ln(\frac{S}{S_0}) = \Delta G^{DH} + W^K \tag{2.3}$$

where S and S_0 are the solubilities of protein in the presence and absence of salts. As shown in **Figure 2.3b**, as I increase from 0, S initially increase but turns over. The initial increase in S is due to the favorable ΔG^{DH}. When the I further increase, W^K becomes dominant so S decrease to less than S_0. **Figure 2.3c** shows ionic dependence of solubilities of hemoglobin after adding different salts. Most salts at lower concentrations ($I < \sim 1\ M$ M) can exert salting-in effect on hemoglobin.

However, not all proteins shows salting-in effect at low ionic strength, for example, lysozyme only shows salting out phenomenon [124].

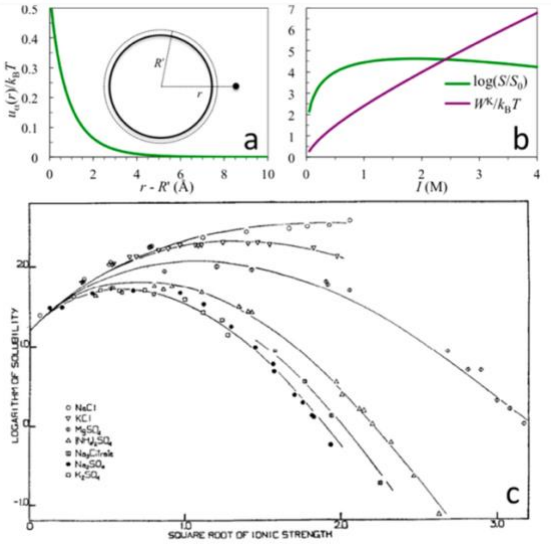

Figure 2.3 (a) Dehydration cost for bringing a single ion (diameter=r) to the surface of a spherical protein in the presence of 1 M 1:1 salt; (b) Ionic strength dependence of dehydration cost W^K and solubility calculated based on Eq. 2.3; (c) Ionic dependence of solubilities of hemoglobin under different salts. Reprinted with permission of [119]

2.2.5 Liquid-liquid phase separation (LLPS), aggregation and phase separated gelation

Liquid–liquid phase separation (LLPS) is defined as the emergence of oil-like droplets in solutions upon cooling or addition of anti-solvent [127]. LLPS has been of great interest when conducting protein crystallization, since this phenomenon indicate the attractive interactions between protein molecules, which is a necessary (though not sufficient) condition for crystallization [128]. In the pharmaceutical industry, LLPS is widely studied since it creates a different local environment for nucleation and growth. Resultingly, the quality attributes of the crystal product such as impurity profile, particle morphology, particle size, etc. might be affected [127]. Recently, the first LLPS of peptides has been reported, and it was found that LLPS is a universal phenomenon that can be observed under diverse solution conditions for various peptides [129].

Protein aggregation is defined as the self-association of protein molecules to form higher order conglomerates of low solubility that eventually precipitate [130]. Aggregates can be formed from nonnative aggregation where the polypeptide chains do not contain the native conformation and might lack the corresponding protein functions. The formation of native precipitates, however, is typically considered a positive sign yielding crystals, and is often used to optimize the concentration of a precipitant. Phase separated gelation, different from the system-spanning gelation where the entire solution behaves like a gel, is one of phase behavior of proteins [131]. The aggregates and gels are commonly observed during protein crystallization, and can be regarded as two manifestation of the same phenomenon, which is a frustrated LLPS that can be theoretically explained by mode coupling theory (MCT) prediction [122].

2.2.6 Phase diagram

Phase diagram of protein crystallization/precipitation is a map that represents the state of the protein solution as a function of different parameters such as solute concentration, precipitant concentration, and temperature. For protein crystallization studies, limited control over the temperature is available for preservation of protein activity, and the experiments are generally conducted at room temperature (around 22 °C) or at 4 °C. Accordingly, a typical empirical phase diagram is constructed by varying the protein and precipitant concentrations, as shown in **Figure 2.4A** [132]. A protein solution can display four states: undersaturated, metastable, unstable (labile), and precipitation. The location of the solubility curve is considered the most direct connection between the phase diagram and protein crystallization [128]. In **Figure 2.4A**, the blue line represents the solubility curve, under which the crystals dissolve while above which nuclei grow in the metastable region. Precipitation occurs beyond the unstable region, where spontaneous nucleation happens. From a theoretical perspective, however, protein solution responds to low temperature the same way it responds to high precipitant concentration, both driving the solution into a condensed state. Therefore, **Figure 2.4B** was modified from phase diagram with temperature as

the x-axis. It might be possible that the empirical phase diagram is a subsection of the phase diagram in **Figure 2.4B**, highlighted by the dashed square.

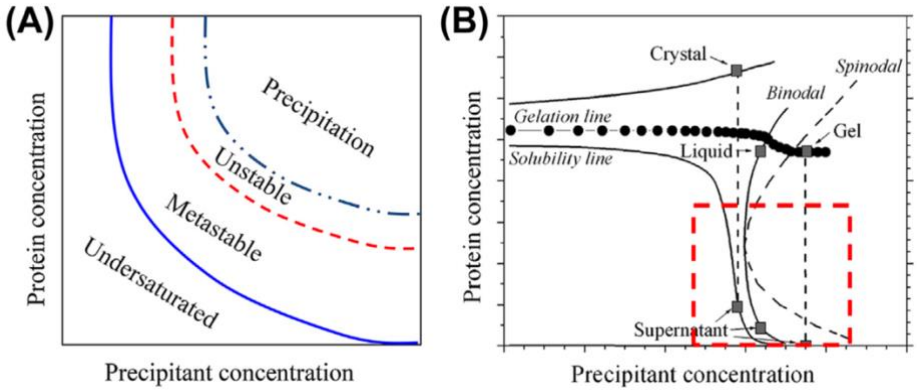

Figure 2.4 (A) Typical empirical phase diagram used in crystallization work. (B) Theoretical phase diagram highlighting the analogy between higher temperature and lower precipitant concentration as determinants of the phase behavior in protein solutions. Reprinted with permission from [132]

Despite efforts from field of physics, chemistry, and life sciences to understand mechanism of protein crystallization, it is usually difficult to design a protein crystallization rationally. Phase diagram is the key for every successful crystallization, in that it forms the basis for design of nucleation and growth. Obtaining a phase diagram is commonly achieved by screening experiments by dispensing (manually or automatically) trials varying protein and precipitant concentrations [133].

2.3 Precipitation/crystallization as DSP method of therapeutic peptides and proteins

2.3.1 Driving force for precipitation and crystallization

Since precipitation and crystallization are essentially the same process with different results, the fundamentals of these two processes are identical and will be introduced as one. Thermodynamically, when a system is in a state that is not equilibrium, the difference between this state and the equilibrium will drive the system towards the equilibrium. For precipitation/crystallization that is characterized by the liquid-solid phase transition of a solution, the supersaturation σ is defined as

the dimensionless difference in the chemical potential between a molecule in the equilibrium (saturated) state μ_{eq} and a molecule in its supersaturated state μ_{ss} [8].

$$\sigma = \frac{\mu_{ss} - \mu_{eq}}{k_B T} \tag{2.4}$$

Eq. (2.4) can be written into the equation below when changing the chemical potentials with molar potentials and thus the Boltzmann constant k_B by the universal gas constant R, where a represents activity:

$$\sigma = \frac{\mu - \mu_{eq}}{\mathrm{RT}} = \ln \frac{a}{a_{eq}} \tag{2.5}$$

$\Delta\mu = \mu - \mu_{eq} = 0$ defines equilibrium. For $\Delta\mu > 0$, spontaneous precipitation/crystallization may occur, whereas $\Delta\mu < 0$ indicates the solute molecules will spontaneously stay dissolved in the solution. $\Delta\mu/RT$ represents the thermodynamic driving force for precipitation/crystallization process, it also determines the rate of nucleation and crystal growth.

Since the chemical potential of the solute is directly related to its activity, the supersaturation can be expressed in a simpler form where the S_a represents the activity-based supersaturation and S represents the concentration-based supersaturation:

$$\sigma = \ln\left(\frac{a}{a_{eq}}\right) \approx \frac{a - a_{eq}}{a_{eq}} = S_a - 1 \approx S - 1 = \frac{x - x_{eq}}{x_{eq}} \tag{2.6}$$

In terms of chemical engineering application where the concentration is often expressed into molar concentration c, the supersaturation formula can be written as:

$$S_a = \frac{a_c}{a_{c,eq}} \approx \mathrm{S} = \frac{\mathrm{c}}{c_{eq}} \tag{2.7}$$

where the $S_a \approx$ S is the supersaturation ratio, which is also known as relative supersaturation or saturation ratio. Usually, the supersaturation is also expressed as a concentration difference:

$$\Delta c = c - c_{eq} \tag{2.8}$$

A solution is in supersaturation when the S_a >1, S >1, $\Delta c > 0$, or $\sigma > 0$.

2.3.2 Nucleation and growth in precipitation

The result of the progressive supersaturation buildup in a solid-free solution is the formation of new phase, i.e., nucleation. As shown in **Figure 2.5**, nucleation can occur via two mechanisms: primary nucleation that occur in the absence of the crystallizing material and secondary nucleation that is brought about from parent crystals. Further, the primary nucleation can be termed homogeneous/spontaneous or heterogeneous depending on whether the nucleation occurred without any presence of solid phases [8, 134].

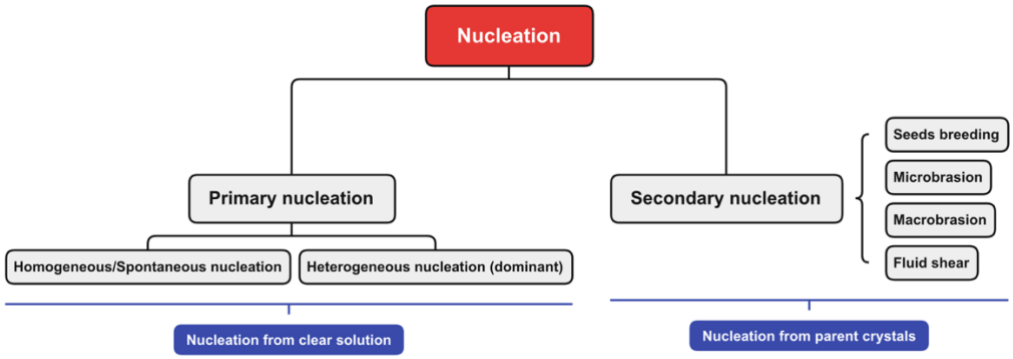

Figure 2.5 Nucleation mechanisms

After their formation, nuclei are considered to follow two processes that occur sequentially in solution: (1) the mass transport of growth unit from the bulk solution to the crystal-solution interface; (2) the incorporation of growth units into crystal lattice through surface integration process (also referred to as surface reaction process). The whole growth process can be classified as growth controlled by mass transport, surface integration or combined mechanisms. The mass transport process is determined primarily by the concentration difference of the solute between the bulk solution and the surface of growth unit. Surface integration is the process that the growth units are incorporated into crystal lattice after transported to the crystal-solution interfaces. There are two mechanisms controlling the surface integration:

Two-dimensional (2D) nucleation mechanism and screw dislocation mechanism. They explain why crystal grow in a layer-by-layer mode [34, 132].

2.3.3 Ostwald ripening

Ostwald ripening is often important after crystallization that is rapid and crystal sizes are small, which is especially true in precipitation process [34]. A solid-liquid system is not thermodynamically stable until the free energy has reached a minimum; this is resulted from the free energy contributed from the large interfacial area. Therefore, Ostwald ripening describes a spontaneous process that leads to a decrease in the surface area of the solid phase or dissolution of the small particles. It is defined as "the growth of larger crystals from those of smaller size which have a higher solubility than the larger ones." [34, 134]. The driving force for Ostwald ripening is the difference in solubility between the small and large particles of the solid phase. Crystal size distribution (CSD), growth and dissolution kinetics, and the transport properties of the solution phase determine the rate the Ostwald ripening. Generally, the Ostwald ripening reduces the number of crystals while increasing the size of individual precipitate.

2.3.4 Precipitation methods

Precipitation is known as a practical way of separating proteins in large quantities (e.g., blood, egg white and various toxins) since old times [135]. For example, the precipitation of milk by a series of dilute acids can fractionate casein effectively [136, 137]. It is mainly used for the concentration and separation of a protein mix from other products or for separation of different proteins (fractional precipitation) [138]. Pioneered by Edwin Joseph Cohn during World War II, the numerous steps of blood precipitation to obtain albumin with ethanol at low temperatures is probably the most famous example [139]. Since then, multiple proteins and peptides have been purified with precipitation method. For example, a corticotropin-releasing hormone-like peptide from human placenta was isolated using acetone precipitation [140]. Antibiotic glycopeptide vancomycin hydrochloride can be purified through antisolvent precipitation [141]. Sunflower protein has been purified using isoelectric

precipitation in a continuous tubular precipitator [142, 143]. Egg proteins including ovalbumin, ovotransferrin, and lysozyme could be precipitated by adding ammonium sulfate, acetone or ethanol [144], and protein concentrates and isolates from *Chlorella protothecoides* could be obtained using isoelectric precipitation, addition of ammonium sulfate [145]. In recent years, precipitation is mainly used for the recovery of low mass peptides to improve their detection in mass spectroscopy (MS) for peptidomics, which requires systematic peptide extraction to achieve successful analysis [22, 146]. For example, acidified (0.25 M HCl) 75% isopropanol, ethanol, and acetone were used to deplete proteins by precipitation, leaving peptides <25 kDa in soluble fractions [147]. In another example, salts such as $ZnSO_4$ combined with high level of organic solvents such as acetone and acetonitrile were used to precipitate peptides generated by pepsin digestion [23].

Methods to precipitate proteins/peptides are based on a knowledge of the solubility of proteins/peptides. From simplistic terms of thermodynamic view, the solubility of a solute in each solvent is determined by the net result of solvent-solvent, solute-solute, and solute-solvent interactions. If the free energy change of the solute-solvent interactions is sufficiently negative (attraction between solute and solvent is large enough) that it more than offsets the free energy change of either or both other two interactions, the solute will remain soluble. The most important factors effecting the solubility of a protein/peptide are its physical characteristics: structure and size, protein charge, and the solvent [8]. Therefore, any perturbation of the environment of the proteins might bring the protein out of the solution and lead to precipitation. These perturbations include the pH, ionic strength, the temperature, and the properties of the solvent. Common precipitation method includes salting out, isoelectric precipitation, organic solvent-driven precipitation, etc. [20, 127]. The precipitation methods are summarized below in **Table 2.1**.

Table 2.1 Summary of precipitation method

Precipitation method	Main mechanism	Advantages	Disadvantages	Ref

Salting-out	Electrostatic and solvation of ions	Low cost, easy, no denaturation	Low selectivity	[148]
Isoelectric precipitation	Charge Neutralization	Simple	Risk of denaturation	[142, 143, 149, 150]
Miscible organic solvents	Solubility	Simple	Risk of denaturation	[141, 151, 152]
Metal-ion	Co-precipitate	Specificity that is different from salts	Complex mechanism	[153]
Non-ionic polymer	Excluded volume effect	Biocompatible	Viscosity problem	[93, 154]
Polyelectrolyte precipitation	Electrostatic and H-bond	High selectivity, low material requirements	Expensive, risk of denaturation	[155]
Affinity precipitation	Affinity	High specificity and selectivity	Expensive	[156]
Combined method	-	High efficiency	Complex process and mechanism	[23, 92, 94, 95]

2.3.4.1 Salting out

Salting out involves the precipitation of a protein or group of proteins by addition of high concentrations of neutral salts under appropriate conditions of pH, total protein concentration, and temperature [115]. The protein precipitated is usually not denatured with the activity recovered upon dissolving the pellet, also, the salts might stabilize the proteins against denaturation, proteolysis, or bacterial contamination [157]. The effect of salting-out is on one hand determined by the structure of the protein, specifically, the number and distribution of charges, the hydrophobic residues, and non-ionic polar groups. On the other hand, it is determined by the salts used. As mentioned in section **2.2.2.3**, salts affect the stability, solubility, and the salting-in and salting-out possibilities of protein based on the Hofmeister series (or lyotropic series). The most used salt for precipitation of protein is ammonium sulfate (AS) because its excellent stabilizing effect on proteins, its high solubility in water,

and it is relatively inexpensive [158]. Also, NH_4^+ and SO_4^{2-} are at the ends of the respective Hofmeister series for cations and anions, which highly stabilize the protein structure [159]. One disadvantage of salting out precipitation is the pellet precipitated usually contained ammonium sulfate, desalting with dialysis is often needed before the protein can be tested on assays for yield and purity determination [157, 159].

2.3.4.2 Isoelectric precipitation

Proteins are less soluble at their isoelectric point (PI) where they have zero net charge and most easily approach each other with minimal electrostatic repulsion [158]. At pH above the pI, the surface of a protein is negatively charged, accordingly, pH below the pI will render the protein predominantly positively charged. In isoelectric precipitation, pH of the solution is adjusted to close or equal to the PI of the protein, which brings the self-association of proteins [157]. Usually, the isoelectric precipitation is conducted at low ionic strength condition, so the ion effects will be minimum [115]. It should be mentioned that isoelectric precipitation is often used to precipitate unwanted proteins instead of proteins of interest, this is because denaturation and inactivation can occur for protein around PI due to the nonnative aggregation [157]. Concomitantly, if the goal of precipitation is to prepare crystalline material, isoelectric precipitation is not often desired since the aggregation of protein around PI can lead to formation of amorphous proteins [160].

2.3.4.3 Organic solvent precipitation

Water-miscible organic solvents such as ethanol and acetone have been used as precipitants for well over a hundred years. However, it is probably best known for its use in fractionating human serum in the classic work of Cohen and Edsall [139, 158]. This is accomplished by the ability of organic solvents to reduce the dielectric constant, which increase the attractive electrostatic forces between isoelectric protein molecules and result in decreased protein solubility [152]. Also, the organic solvents displace the ordered water molecules around the hydrophobic regions on the protein surfaces, which minimize the hydrophobic interactions and lead to protein aggregation caused dominantly by electrostatic interactions [153]. However, since precipitation with organic solvents tends to denature the protein, the precipitation is usually carried out at low temperatures (preferably at or below 0 °C) [157]. Acetone

and ethanol are the most used solvents, other solvents like methanol, propan-1-ol, and propan-2-ol have been used as well. The requirements for the solvents are nontoxic and have relatively high flashpoint (above 20 °C). Besides, longer chain alcohols such as butanol can cause higher degree of denaturation than ethanol. In most cases, acetone is preferable since it can precipitate protein at low concentrations, and therefore less denaturation occurs. For example, it was found one volume of acetone can precipitate protein that can only be precipitated by four-volume of ethanol [157]. The precipitate pellet will normally redissolve in one or two times its own volume, if not, the precipitate might be denatured [157].

2.3.4.4 Other precipitation methods

Metal-ion precipitation has been reported to cause reversible protein precipitation since 1905 [115]. Divalent and trivalent metal cations can interact with proteins and form two kinds of complexes: (1) a simple ion-ion complex; (2) a coordination complex. The binding of positively charged metal ions to proteins can reduce protein solubility by changing the protein pI as well as changing solution pH. For example, zinc sulfate was considered one of the best precipitants to precipitate human, dog, rat, and mouse plasma with yield more than 95% from a stock of 10% w/v precipitant to plasma ratios ranging from 1:1 to 4:1 [153].

Non-ionic polymer precipitation involves the use of water-soluble uncharged polymers of varying molecular weights. Common precipitants include dextrans, polypropylene glycol, and polyethylene glycol (PEG), with PEG being the most extensively used [115]. PEG is thought to achieve the precipitation of proteins via "excluded volume effect" and increase the chemical potential of proteins. It will compete for space in solvent with protein molecules, and upon addition of PEG to 10-20% w/v (higher concentration will lead to increase of viscosity), proteins concentrate together and then precipitate out once the solubility limit is exceeded [161]. PEG won't denature the proteins under normal conditions, but since PEG interacts with proteins via hydrophobic interactions, there is the potential for long term protein damage in aqueous and solid state with PEG [161].

Polyelectrolytes are polymers with ionizable groups that can dissociate into charged polymer chains and counter ions in solution. The charged polymer chains

and the ions can then interact with proteins via a bridging action that result in insoluble complexes. Precipitation with polyelectrolytes provides the advantages of good selectivity with low material requirements compared with salts and non-ionic polymer such as PEG. However, polyelectrolytes can be expensive, also, they can run the risk of denaturing the proteins. Besides, there is no direct linearity between the concentration of polyelectrolytes in solution and the fraction of protein precipitated, which is different from salting-out and PEG precipitation [161].

In general, the precipitation methods above lack specificity, which led to the development of affinity precipitation since late 1970s [162]. Affinity precipitation offers attractive alternative in that it involves the solid-liquid separations, which are well-understood and can be easily achieved with filtration and centrifugation. The most classic affinity precipitation is that of antibody-antigen precipitates. For example, lectins has been used to selectively precipitate glycoproteins and the precipitation of glycopeptides with concanavalin A has been reported [115]. Recently, a proof-of-concept study using fusions of affinity peptides and elastin-like polypeptide (ELP) has been reported, which showed its ability to achieve a single-step purification of model, tag-free proteins [156].

Lastly, there is a trend to combine several precipitation methods in one process to achieve high productivity and economy with the requested selectivity simultaneously [94]. For example, PEG-metal precipitation is the most common combination that can achieve more than 90% yield [163]. The high yield and high selectivity were achieved by the solubility reduction by PEG and the specificity of Ca^{2+} towards proteins so the high molecular weight impurities (HMWI) can be separated [94]. Besides, ethanol-Ca^{2+} precipitation for separation of IgG from CHO cell culture supernatant [92], caprylic acid-PEG-$CaCl_2$-cold ethanol precipitation for separation recombinant antibodies [95], and the recovery of peptide with salt and organic solvent [23] were reported with satisfactory results.

2.3.5 Crystallization methods

Crystallization has been used for almost all small-molecule pharmaceuticals in the conventional chemical industries [7]. Protein crystallization was developed in the latter half of the 19th century primarily as a means for purification of proteins from an impure source when few other means existed. Since the 1930s, structure determination of macromolecules and their complexes using X-ray crystallography has become the major application of crystallization [24]. In the latter case, the goal of crystallization is to obtain a small number of crystals with good size (0.2-0.9 mm) and internal quality [164], which is essential for yielding atomic level structural images of biological macromolecules such as proteins. With the development of the biopharmaceutical industry, specifically the increase of the upstream titers, larger scale crystallization of proteins in a production process started to show its appeal. The advantages of crystallization are the low cost associated, the ability to cope with high volumes, and the high concentrations of the target molecule [6]. Furthermore, the crystalline form is more densely packed than the amorphous form produced by precipitation, thus it possesses smaller surface areas exposed to the surrounding (e.g., moisture, solvents), resulting in its superior physicochemical stability [9, 165]. In addition, the crystalline form enables a sustained release of biopharmaceuticals without the need for encapsulation, hence it can potentially reduce the dosing frequency [166]. Hence, crystallization of protein has the potential to integrate purification, stabilization, concentration, and formulation in a sing step, serving as a powerful unit operation in DSP.

Common crystallization methods include batch crystallization, vapor diffusion crystallization, dialysis crystallization, and free interface diffusion. In batch crystallization, supersaturation is reached upon the mixing of the protein/peptide and crystallizing agents. In vapor diffusion, dialysis, and free interface diffusion, the solution is started from undersaturation states, and gradually reach supersaturation during equilibrium [133]. Generally, the crystallization of proteins (especially those that have not been crystallized before) involve a systematic search, changing individual parameters that can influence the crystallization process [6]. Once the set or multiple sets of parameters yielding the best precipitate/crystals were found, optimization needed to be performed to obtain the best product quality and process

efficiency. Knowledges on protein interactions are prerequisites before designing a crystallization [37]. The related fundamentals on this topic have been reviewed in section **2.2** and **2.3**. In the sections below, specific parameters including physical, chemical, and biological factors (**Table 2.2**) that can affect the crystallization would be reviewed.

Table 2.2 Crystallization parameters affecting the protein crystallization process [49]

Physical factors	Chemical factors	Biochemical factors
Temperature	pH	Sample purity
Gravity	Buffer type	Sample homogeneity
Pressure	Precipitant type	Proteolysis/hydrolysis
Magnetic fields	Precipitant concentration	Sample isoelectric point (pI)
Electric fields	Detergents/surfactants/amphophiles	Ligands, cofactors, inhibitors
Viscosity of the medium	Heavy metals	Aggregation state of the macromolecule
Dielectric properties	Chaotropes	Chemical modifications
Vibrations and sound	Metal ions	Posttranslational modifications
Time	Ionic strength	Sequence modifications
Equilibration rate	Degree of supersaturation	Sample source
Nucleants	Cross-linkers	Sample symmetry
Surface of crystallization device	Polyions	Sample history
Sample handling	Reagent source	Purification method
Methodology	Reagent formulation	Unstructured regions
Mother liquor volume	Reductive/oxidative environment	α-Helix content
Geometry of chamber or capillary	Small molecular impurities	Thermal stability
		Allowable pH range

pH and temperature of the environment are almost exclusively the most important factors for any living system [167]. The effect of pH on protein interactions and crystallization is the modulation of protonation state of charged amino acids and N- and C-terminal groups at the surface of the proteins. By changing charge-charge distribution, pH modifies both the strength and the geometry of electrostatic interactions that are key to protein interactions at low salt concentrations. When the electrostatic interactions are screened at higher ionic strength, the effects of pH are more subtle. There are three effects pH has on the protein interactions and crystal formation at higher salt concentrations: (1) adjusting the possibilities of forming salt bridges and hydrogen bonds crucial to the formation of particular crystal contacts; (2) modification of the binding properties of small molecules and ions that can mediate protein interactions; (3) change of protein hydration due to the difference between hydration states of charged amino acids in protonated and deprotonated forms [168]. To formulate a strategy for selecting pH of enhanced protein crystallization, Chen-

Yan Zhang *et al.* therefore investigated these effects based on the crystallization results of six commercial proteins (lysozyme, concanavalin A, α-chymotrypsinogen A, catalase, glucose isomerase, and myoglobin) [169]. From the point of view of structural biologist, they concluded that (i) pI should be avoided. Although it has long been believed that the optimal pH for protein crystallization was at pI where the solubility was at the minimum. However, it was later found that there is no clear correlation between pI and pH for protein crystallization. In fact, proteins tend to aggregate rapidly at their pI, which will lead to amorphous precipitates [160]. (ii) pH should be within stable range of proteins. (iii) pH should be as low, as high, or as divergent from the pI as possible for basic, acidic, or neutral proteins, respectively. However, for most of the cases, systematical search needs to be performed on pH range or values for best outcomes in crystallization.

Temperature is another important factor that should be considered in protein crystallization. First, biological macromolecules are sensitive to temperature. Most early studies on temperature-protein interactions were associated with the temperature effects on enzymatic activities and thermal stability of proteins [170]. In the context of protein crystallization, temperature is important in several ways: first, solubility of some proteins have a dependence on temperature, which will affect the crystallization via the supersaturation level, this is more often seen in small molecule crystallizations [167]. Most proteins in high salt solutions are more soluble at cold temperature, while protein–PEG combinations and low ionic strength solutions of protein are generally more soluble at warm temperatures [167]. Second, heat-induced protein interactions and phase transition might occur when varying temperatures during crystallization. For example, a rise in temperature favors the formation of hydrophobic interactions at the same time as it weakens dipolar interactions while decrease in temperature leads to the opposite effects [6]. Ovalbumin will form irreversible gels at elevated temperature, the opposite effects is observed with gelatin, which gels upon cooling but will not return to the liquid state. Third, when involve the use of organic solvents, high temperature should be avoided since there is risk of denaturing the protein. Fourth, temperate can be the factor to modulate the crystal modification formation. For example, lysozyme can crystallize into tetragonal crystals from sodium acetate buffer in temperature ranging from -4 to 25 °C. Its

orthorhombic crystals (HTO) can be formed from acid buffer between 25, 40, and 60 °C. And another orthorhombic crystals (LTO) can only be obtained from basic solution at temperature lower than 35 °C [171]. Fifth, temperature can affect crystallization via determining the nucleation rate and growth rate of crystals [172].

Precipitants of crystallization (**Table 2.3**), with the majority of them overlap that of precipitation discussed in section **2.3.4**, can contribute to the crystallization through multiple mechanisms: salts can change the water activity, organic solvents can alter the dielectric constant of the medium, and PEG can induce molecular crowding. All of the precipitants enhance the molecule's attraction toward each other, resulting in precipitation and crystallization [49]. There is no defined theory as to which precipitant is the best for certain proteins, therefore, comparative study is always needed before optimization. For example, effect of precipitants such as lithium sulfate, sodium chloride, and PEG on the crystallization of jack bean urease has been investigated and compared [173].

For many years, the field of protein crystallization has been known to be more of a 'black art' than a science [174]. Apart from the above considerations, multiple other variables could determine the crystallization results as well. One reason that a universal method for crystallization is difficult to find is because the protein itself is a variable. Every protein is essentially unique, thus the structure diversity combining with the stereo-heterogenicity makes it difficult to generalize the trend that can be applied for all proteins. Also, some proteins may crystallize even from very heterogeneous mixtures (egg albumin, lysozyme, canavalin, α-amylase), but generally, crystallization of proteins require high purity in advance, which impose challenges on investment [167].

Table 2.3 Common precipitants used in protein crystallization [49]

Salts	Organic compounds	Polymers
Ammonium sulfate	2-Methyl-2,4-pentanediol	Polyethylene glycol 1000
Ammonium acetate	Isopropanol	Polyethylene glycol 1500
Ammonium citrate	Acetone	Polyethylene glycol 2000
Sodium citrate	Acetonitrile	Polyethylene glycol 3350
Ammonium phosphate	Ethanol	Polyethylene glycol 4000
Potassium phosphate	Succinic acid	Polyethylene glycol 6000
Ammonium nitrate	Acetonitrile	Polyethylene glycol 8000
Sodium/potassium tartrate	Dioxane	Polyethylene glycol 10000
Magnesium sulfate	Dimethyl sulfoxide	Polyethylene glycol 20000
Sodium acetate	Polyethylene glycol 200	Polyethylene glycol 35000
Lithium sulfate	Imidazole	Polyethylene glycol monomethyl 2000
Sodium chloride	1,3-Butyrolactone	Polyethylene glycol monomethyl 5000
Ammonium formate	Methanol	Polyvinylpyrrolidone K 15
Sodium formate	Ethylene glycol	Polyacrylate
Sodium phosphate	Malic acid	Polypropylene glycol 400
Sodium/potassium phosphate	Glycerol	Pentaerythritolpropoxylate
Potassium thiocyanate	Malonic acid	Modified polycarboxylates
Ammonium tartrate	2-Methyl-2,4-pentanediol (MPD)	Jeffamine T
Sodium nitrate	2,5-Hexanediol	Jeffamine M
Magnesium acetate	1,3-Propanediol	Polyethylene glycol monostearate
Sodium sulfate	*n*-Butanol	Polyeneamine
Lithium chloride	tert-Butanol	
Calcium chloride	Polyethylene glycol 400	
Sodium tartrate	Jeffamine 400	
Cadmium sulfate		
Sodium succinate		
Sodium malonate		
Magnesium sulfate		
Magnesium chloride		

2.4 Precipitate/crystals quality attributes

The concept of pharmaceutical quality by design (QbD), which is a systematic approach to development that starts with predefined objectives and emphasizes products and process understanding and control based on sound science and quality risk management, has been developed since 1992 [175]. Concomitantly, based on ICH Q8 (R2), a critical quality attribute (CQA), being defined as "a physical, chemical, biological, or microbiological property or characteristic that should be within an appropriate limit, range, or distribution to ensure the desired product quality" [176] is a crucial quality characteristic that should be achieved by controlling the input material attributes (critical material attributes, CMAs) and the process (critical process parameters, CPPs) to ensure the desired quality [175]. Common CQAs include particle size, particle size distribution, moisture content, particle shape, particle shape factor (e.g., aspect ratio), API crystalline morphology, API polymorphic form, brittleness, and dissolution, etc [175]. For biopharmaceuticals

such as mAbs, the potential critical quality attributes (pCQAs) are initially studied and their criticality would be assessed with respect to their impact on the bioactivity, pharmacokinetics (PK)/pharmacodynamics (PD), immunogenicity, and safety [177].

2.4.1 Crystalline biopharmaceuticals

DSP is a significant part in defining the quality of the biopharmaceuticals, since it controls most of the CQAs such as the impurities, the particle shape and size, and the formulation. For protein and peptide drugs, due to their susceptibility to chemical degradation in solution, they are often formulated in solid state to provide stabilization during storage [178]. However, even in the solid state, chemical and physical degradation during processing and storage can occur [179]. To improve the stability of protein drugs in the solid form, crystalline proteins are usually preferred than amorphous because protein crystals are densely packed, they have smaller surface area, reducing the interactions with solvents and moisture in the surrounding environments [161, 180], and the protein crystals can achieve sustained release [181]. As a resurrecting alternative to standard formulations, crystalline formulation has higher purity, longer shelf-life, and the controlled release profile [182]. On the contrary, the amorphous or less crystalline pharmaceuticals have no long-range order of molecular packing or well-defined molecular conformation when the molecules are conformationally flexible. Consequently, they have higher solubility and dissolution rate, less chemical and physical stability. And if a more stable crystalline state exists, an amorphous pharmaceutical can crystallize during storage, especially on exposure to heat and humidity [183]. However, crystalline proteins cannot be universally obtained due to the difficulty of crystallization of macromolecules, which is where the amorphous/less crystalline particulates provide alternatives [9]. And sometimes the amorphous form might possess higher stability as observed in insulin [184].

2.4.1.1 Importance of crystal size and CSD

In particulate processes, when a solid material is produced, the particles are characterized by both a size and a representative shape [185]. For crystallization/precipitation, the crystal size and CSD are among the most important

solid-state properties to control [34]. Generally, large particles (> 250 μm) tend to be free flowing, while the fine powder with high surface-area-to-mass ratios tend to stick. When particles are less than 10 μm, especially, this cohesiveness between particles become more evident because the vdW attraction become more dominant and the gravitational forces are less significant [34]. Since the chance of two particles having exactly the same size is pretty small, the particle size is usually characterized by the distribution of sizes, namely, the particle size distribution (PSD). When the particles are crystals, it is called CSD [185].

The CSD is a determining factor in the end-use properties of a solid material. **Table 2.4** lists some of these properties and the crystallizer interactions with CSD. In fact, some of the more important problems such as crystal habit and purity, crystallizer stability, and capacity and scale-up in the operation of industrial crystallizer can interact with CSD and can even be considered as subheadings under the CSD problem [185]. Crystallization is a surface-dependent mass-transfer operation, which can be moderated depending on the surface that is determined by the CSD. Therefore, as shown in **Figure 2.6**, all the kinetic factors in crystallization can ultimately influence CSD, with feedback interactions connect them all [185].

Table 2.4 End-use properties of particulate material that can be determined by CSD and crystallizer interactions with CSD [185]

End use (PSD or CSD)	Crystallizer interactions (CSD)
Filtration rate	Vessel fouling rate
Entrainment of liquid after dewatering	Changes in crystal habit
Dissolution rate	Changes in crystal morphology
Caking properties in storage	Mother-liquor inclusions
Fluidization properties	CSD instability
Pneumatic handling properties	
Bulk density	
Esthetic appearance	

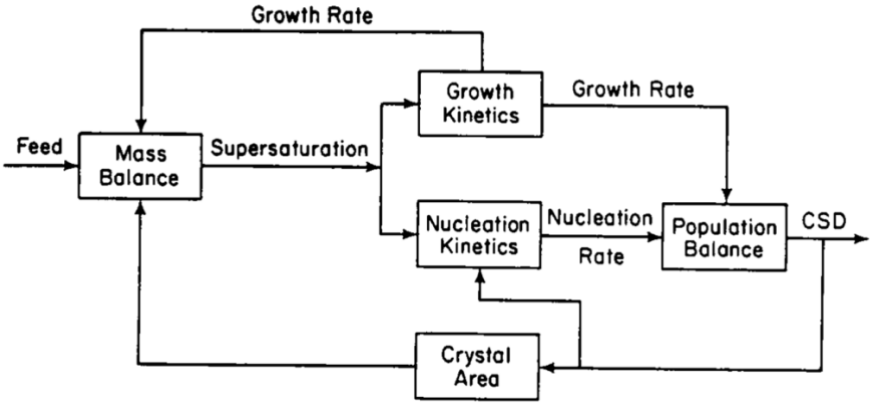

Figure 2.6 Feedback interaction of crystallization factors [185]

Generally, uniformly distributed particles are easier to handle, filter, mix, and hence are more desirable. The two most important that best describe the CSD is the mean size and the coefficient of variation (CV) that is defined as the size variation relative to the mean size [38]. Another value that is usually used for characterization of CSD is span. Span is the parameter that measure the breadth/width of a distribution and is defined as

$$Span = \frac{d_{90} - d_{10}}{d_{50}} \tag{2.9}$$

where the d_{90}, d_{50}, and d_{10} are the quantiles representing a particle size that divided the distribution such that there is a given proportion below the quantile value. For instance, d_{90} is the size for which 90% of the particles are smaller, d_{50} is the median, and d_{10} represents the size for which 10% of particles are smaller [186].

2.4.1.2 Importance of crystal habit

For crystalline active pharmaceutical ingredients (APIs), polymorphism is a prevalent phenomenon that can affect the physical properties significantly. Defined by McCrone, polymorphism is the ability of a chemical to crystalize into more than one crystal structures while the chemical composition stays the same [187]. The differences in crystal structures between polymorphs are internal disparities that leads to different properties between distinct forms. Crystal habits (or modifications), on the other hand, refers to the external appearance of the crystals, which are determined

by the geometric lengths and widths of the crystal faces [188]. The difference between the concepts of morphology and habit can be found in **Figure 2.7**.

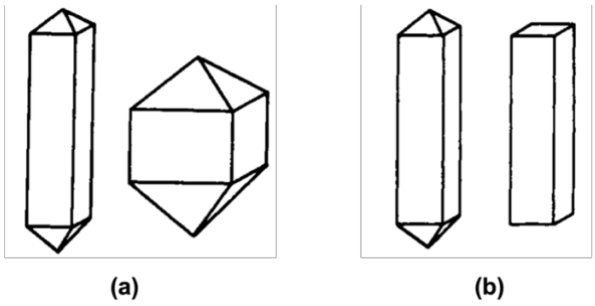

Figure 2.7 Schematics of crystals with different habits and morphologies. (a) same morphology but different habits; (b) same habit but different morphologies.

The different habit modifications were determined by the internal structure as well as the environment of crystallization, which resulted in distinctive relative growth rate for their crystal faces [189]. And the final shape and size of the crystals are determined by a combination of kinetic and thermodynamic driving forces [190], which are influenced by the growth environment. Crystal habit have a significant impact on the downstream processing in pharmaceutical industry. It will affect the filtration or centrifugation efficiency, the density of the solid, and the flow properties of the solid [191, 192]. For instance, thin needles tend to align with the flow of mother liquor and block the filtration pores, and it might also pose problem on pumping due to the high viscosity caused by dispersion of needles [193].

2.4.2 Effect of process on the quality of precipitates

Due to the complexity of biological materials, the different process parameters and precipitation methods can impact directly and distinctively on the quality of products and the economics of production [4, 24]. Hence, they should be carefully examined while developing a precipitation technique [25]. For example, pH close to pI can increase the possibility of amorphous precipitation and aggregation [160], which may result in significant change such as protein denaturation [169]. Unlike unanimously adopted pH at around 5.0, it was found that precipitation at pH 6.0 can

achieve enhanced thermal stability and functionalities of hempseed protein [194]. The pH in extraction and isoelectric precipitation were also found to be responsible for the four quality attributes of protein isolates (protein content, whiteness index, enthalpy of transition, denaturation temperature) from Amaranth (*Amaranthus cruentus*) seeds [149]. Organic solvents are good for large scale precipitation since they can be recycled efficiently, yet it is well-known that the organic solvents generally denature protein/peptides [115, 151, 195, 196]. When used in high concentration or high temperature, the Dimethyl Sulfoxide (DMSO) might lead to the denaturation of lysozyme via disrupting the tertiary structure of the molecules that leads to unfolding [197]. Besides, different organic solvents were found to affect the particle size, zeta potential, secondary structure, thermodynamic properties (T_m values), and the biological activity of lysozyme differently [198]. In isoelectric precipitation, the pH can affect the process yield as well as the structure and functional properties of proteins.

Most importantly, different precipitation methods can affect the precipitation efficiency and have large impact on the precipitate quality as well. Due to the complexity of biological materials, the different process parameters and precipitation methods can impact directly and distinctively on the quality of products and the economics of production [4, 199]. For example, based on the protein removal effectiveness and the ionization effect, precipitation with organic solvent, acid, salt, and metal ions were compared for plasma protein precipitation from different sources. It was found that at 2:1 volumes of precipitant to plasma, zinc sulphate showed the highest precipitation ability (96%), followed by acetonitrile (92%) and trichloroacetic acid (TCA) (91%) [153]. In terms of the impact on precipitate quality, in the case of salt precipitations, irreversible denaturation is not present, while for the organic solvent precipitation, the precipitate might lose enzymatic activity due to the irreversible conformation change [151]. In a precipitation study of concentrate of peanut protein, it was found that isoelectric precipitation can produce precipitates with the best solubility, foaming capacity, and stability. Whereas alcohol precipitation products had better water holding/oil binding capacity [150]. Since PEG interacts with proteins via hydrophobic interactions, which have a risk of destabilizing protein structure, there is the potential for long term protein damage in

aqueous and solid state with PEG [161]. Other factors that can impact the precipitate quality include buffer ions and ionic agents, etc. For example, the buffer ions exist in the solid state of protein and peptides might have a catalytic effect on the degradation reactions, apart from their effect on pH. And the addition of ionic agents such as NaCl was found to affect the chemical stability of the freeze-dried human growth hormone (hGH) [178].

2.4.3 Perspectives

In summary, precipitation and crystallization are promising alternatives to conventional chromatography in DSP of biopharmaceuticals. Knowledges on the structure of proteins/peptides, protein-protein interactions, solubility, and the phase behaviors are crucial for developing a successful precipitation process. However, due to the complex structure of proteins and peptides, the precipitation knowledges are notoriously limited for model protein such as lysozyme. The precipitation and crystallization on bioactive peptides, although can be pursued with similar approaches as used in protein systems, deserve to be investigated individually. Thus, obtaining the basic knowledges of the peptide such as solubility and phase behaviors merits a promising start.

Crystal size, CSD, and crystal habit are critical quality attributes (CQAs) of the APIs that affect various solid properties and end-use efficacy. For small molecules, topics of controlling these CQAs have been studied for more than one hundred years and have seen a steady growth so far [192, 200-202]. For proteins, however, similar advances in crystal engineering have only been reported recently through modelling [203, 204] and experimental techniques [171, 205]. Therefore, the lack of studies on the crystal engineering of peptides, needs to be addressed when optimizing the crystallization process.

The performance of precipitation process of macromolecules can be modulated via multiple methods and process parameters. Thus, comparing different process routes and key parameters to maximize the production efficiency and the product quality is of great significance in moving towards QbD.

2.5 Continuous crystallization

Part of this section has been published as **Siyu Pu,** Kunn Hadinoto, Continuous crystallization as a downstream processing step of pharmaceutical proteins: A review, *Chemical Engineering Research and Design*, Volume 160, 2020, Pages 89-104. Permission has been granted by the licensed publisher "Elsevier" for utilization of the published content as a chapter in this thesis [10].

While the standard manufacturing practice of high-value biopharmaceuticals is built on batch processes, transforming specific processing steps to a continuous platform has been actively explored as part of the PI, like what has been done in the manufacturing of small-molecule pharmaceuticals. In comparison to the batch process, continuous process offers (i) compelling reductions in the capital equipment cost, (ii) higher productivity with less downtime, (iii) greater flexibility, and (iv) improved product quality attributed to reduced residence time distribution [206]. The continuous platform is therefore favorable not only economically, but also from the product-quality point of view. Indeed, U.S FDA has endorsed since 2011 the advantages of the biopharmaceutical industry to gradually shift towards the continuous manufacturing platform, including for the DSP steps [207]. Research efforts to transform the key DSP steps to the continuous platform has been reviewed in Jungbauer [102] and in Zydney [70] which they emphasized on the continuous transformation of well-established processes, such as continuous centrifugation, continuous filtration, and continuous chromatography.

With regards to the ABC processes for the capturing and polishing steps of biopharmaceuticals, continuous precipitation and crystallization has emerged as one of the most promising processes owed to its simple underlying principle and well-demonstrated effectiveness [21]. The use of continuous precipitation in the purification of IgG and monoclonal antibodies (mAbs) were shown to produce comparable purity and yield as those obtained from using protein A chromatography [92, 154]. Furthermore, Hammerschmidt et al. [208] performed an economic analysis

for the recombinant antibody production at various production scales, and showed that continuous precipitation offered cost reductions across all scales compared to the standard industry processes based on chromatography.

While the need for biopharmaceutical crystals is well-established, the role of continuous crystallization in DSP of biopharmaceuticals has only been explored recently, thus it severely lags behind the continuous precipitation. Very recently, Wenqian *et al.* [209] reviewed continuous protein crystallization and illustrated its development process. Current developments in this field were covered with operation windows and results of different examples laid out. A large majority of crystallization studies for large-scale biopharmaceutical production purposes (not crystal structure determination) were performed using the batch platform [37]. One example was the study by Smejkal et al. [26] which reported the purification of recombinant mAbs by preparative batch crystallization aimed at reducing the number of chromatography steps.

Herein a review on recent advances and design challenges in continuous crystallization of pharmaceutical proteins were conducted below. The discussion is organized based on the setup used for the continuous crystallization, instead of the protein used due to the lack of variation in the model proteins used as we pointed out later. For each setup, examples are laid out and compared in terms of their crystal quality, production efficiency, and translational value to the industry. These studies predominantly employed pharmaceutical proteins as the model biopharmaceuticals as we summarized in **Table 2.5**.

Two major types of continuous crystallizers, i.e., mixed-suspension mixed-product removal crystallizer (MSMPRC) and tubular crystallizer, are used for continuous crystallization of proteins. The schematics of these two setups is illustrated in **Figure 2.8**. Theoretically, infinite number of small-volume MSMPRCs in series is equivalent, in terms of residence time, to tubular crystallizer having the same total volume. Tubular crystallizer is usually preferred for high crystallization yield with short residence time, whereas MSMPRC is preferred for slow crystallization process with long residence time [203]. Besides MSMPRC and tubular crystallizer, innovative setups, such as hybrid continuous membrane crystallization [210, 211] and microfluidic crystallization [212-215], have also been proposed.

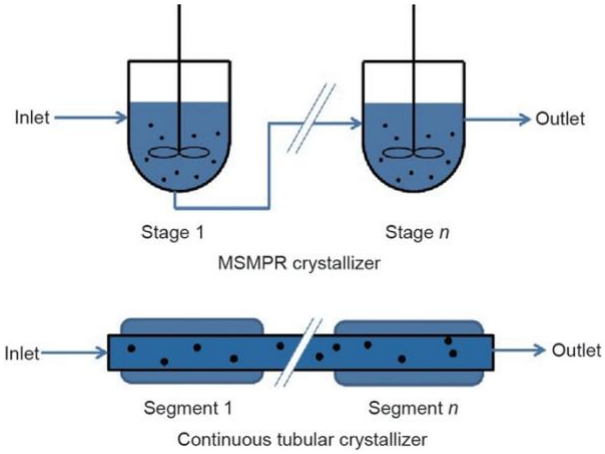

Figure 2.8 Two types of continuous crystallizers: the mixed-suspension-mixed-product-removal crystallizer (MSMPRC) and tubular crystallizer. Reprinted with permission from [216] Copyright (2017) Elsevier

In protein crystallization, tubular crystallizers are typically operated under mild conditions in the laminar flow regime at low fluid velocity to minimize particle attrition and protein denaturation [217]. Despite the slow net flow, the production capacity of tubular crystallizers can be readily increased by having multiple tubes running in parallel [100]. Operating tubular crystallizers at low fluid velocity, however, requires long residence time to achieve a reasonably high crystallization yield. Moreover, the low-velocity operation is often not practical due to the high likelihood of tube clogging caused by crystal aggregate formation and high operating costs due to excessive tube length [100].

For this reason, different strategies (e.g. slug flow, oscillatory flow crystallizers) have been developed to improve the performance of tubular crystallizers with the objective of achieving high yield at reasonable residence time, while maintaining the mild operating condition [209]. In this regard, good mixing of the crystallization solution is needed to enhance the mass and heat transfer rates, hence higher crystallization yield. Enhanced mixing also leads to homogenous supersaturation level in the radial direction, resulting in the production of crystals exhibiting uniform shape and size [218].

MSMPRC, whose operating principle is based on continuous stirred tank reactor, is better equipped for operation at long residence time owned to its similarity to the batch platform. MSMPRC is also easier to construct and operate than slug flow and oscillatory flow tubular crystallizers [219]. Owing to its similarity with the batch platform, transferring the crystallization process from the batch platform to MSMPRC is more straightforward compared to transferring from the batch platform to tubular crystallizer [216]. Achieving homogeneous mixing and good process control in MSMPRC, however, remains a challenge, particularly as the production scale is increased [220]. Furthermore, particle attrition is inevitable in MSMPRC due to the mechanical agitation. Tubular crystallizer should be preferred over MSMPRC if large crystals or crystals with specific morphology are desired. MSMPRC is also to be avoided when the crystallization involves mechanically labile proteins (e.g. insulin) [221].

MSMPRC, nevertheless, is preferred when vigorous mixing is required for crystallization, for example, in the crystallization of monoclonal antibodies in which the protein solution often separates into the aqueous phase and precipitant phase [222]. Moreover, the stirred tanks used in MSMPRC possess smaller surface area-to-volume ratios than the tubes used in tubular crystallizer, resulting in the latter's superior heat transfer in cooling crystallization [200]. As a result, tubular crystallizers produce better crystal quality and higher efficiency at shorter residence time than MSMPRC for cooling crystallization.

2.5.1 MSMPRC

The first study that used MSMPRC for continuous protein crystallization is the attempt on crystallization of a full-length therapeutic monoclonal antibody in the continuous mode by Hekmat *et al*. [45] In this study, the MSMPRC was equipped with cooled tubular bypass as shown in **Figure 2.9a** to enhance the supersaturation level by cooling and in turn increased the crystallization yield. The MSMPRC was run in quasi-continuous mode in which crystal sediments were withdrawn periodically from the base of the tank. Monoclonal IgG1-type antibody mAb01 and lysozyme were used as the model proteins. A combination of cooling crystallization

and salting out was used for the lysozyme, whereas the mAb01 was crystallized by a combination of cooling and isoelectric crystallizations. A summary of the process and product characteristics of the lysozyme and mAb01 crystallizations is presented in **Figure 2.9b**.

(a)

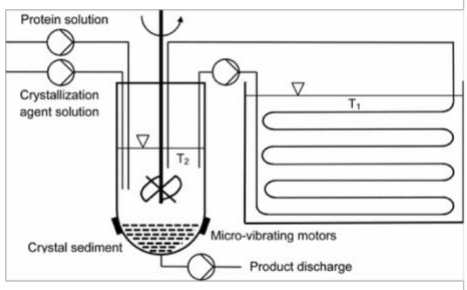

(b)

	purified lysozyme	mAb01 from pretreated harvest	recrystallization of mAb01
Flow velocity in tubular reactor (cm/s)	17	8.5	8.5
Mean residence time in tubular reactor (min)	1	2	2
Feed flow rate (mL h^{-1})	6	77–85	121
Mean residence time in stirred tank (h)	30	2.12–2.35	1.50
Recirculation ratio	320	11.3–12.5	7.9
Temperature of tubular reactor T_1 (°C)	10	0	5
Temperature of stirred tank T_2 (°C)	13	10	15
Protein feed concentration (g L^{-1})	96	14.5	19
Stationary protein concentration (g L^{-1})	7	~1	~1
Stationary crystallization rate (g h^{-1})	0.58	1.04–1.16	2.18
Stationary yield (%)	93	~93	~95
Space–time yield (g L^{-1} h^{-1})	3.2	5.7–6.4	12
Mean crystal size (μm)	13	39	30

Figure 2.9 (a) Schematic diagram of MSMPRC with cooled tubular bypass; (b) Process parameters and product characteristics of the lysozyme and mAb01 crystallizations. Adapted with permission from [45] Copyright (2017) American Chemical Society

The continuous crystallization of lysozyme was started from a batch process by mixing 96 mg/mL^{-1} lysozyme solution with 80 mg/mL NaCl solution at 1:1 v/v ratio under stirring at 200 min. The total operation volume was 180 mL, including protein and salt solutions both buffered in 50 mM acetate buffer (pH 4.6). When a drastic change in the turbidity of the solution was observed, the crystallization was switch to a continuous mode with the lysozyme concentration raised to 192 mg/mL. The NaCl solution concentration was kept the same and the stirring rate was decreased to 50 min^{-1}. The cooled tubular bypass (10-m long, 2-mm ID) was maintained at 10 °C. High crystallization yield of roughly 93% was obtained, albeit long residence time of 30 h was required. Tetragonal lysozyme crystals with mean size of about 13 μm were produced. Nevertheless, despite the long residence time of the lysozyme crystal in the MSMPRC, the production capacity (0.58 g/h) was not significantly higher than what was previously achieved without the cooled tubular bypass. For mAb01, the

harvest from CHO cell cultivation was pretreated via ultrafiltration to concentrate the protein and diafiltration to decrease the ionic strength. The continuous crystallization of mAb01 from the pretreated harvest was started from a batch process at 10 °C, during which 180 mL pretreated harvest (16 mg/mL protein, pH 6.8) was stirred at 200 min^{-1}. After 2 h, the process was switched to continuous mode by feeding 16 mg/mL protein solution in 10 mM histidine buffer and 80 mM TRIS base solution at a ratio of 10:1 (v/v) under stirring at 50 min^{-1}. The cooled tubular bypass temperature was set at 0 °C. The mean crystal size was 39 μm with negligible amount of crystals under 10 μm. Significantly, this work represents the first attempt on crystallization of a full-length therapeutic monoclonal antibody in the continuous mode. The MSMPRC achieved about 93% yield which was comparable to the yield achieved in the batch platform.

Another recent continuous crystallization using MSMPRC was reported by Mathew Thomas *et al.*[48] By conducting crystallization of lysozyme in both batch and MSMPRC under the same condition (30 g/L lysozyme and 35 or 45 g/L NaCl in pH 4.6, 0.2 M buffer at 18 °C), the authors found that the metastable needlelike form of lysozyme can be obtained from the MSMPRC while only tetragonal from can be produced in batch. The same transition of lysozyme crystals from tetragonal to the needlelike form was seen in a 3D-printed airlift crystallizer that closely mimicked the MSMPRC. The reason for the formation of needlelike lysozyme in MSMPRC was attributed to the long residence time and high precipitant concentration, although it could also be a result from a kinetic advantage of the needles in the MSMPRC.

2.5.2 Tubular crystallizer

Three types of tubular crystallizers with well-established large-scale production capability are (1) plug flow crystallizer (PFC), (2) slug/segmented flow crystallizer (SFC), and (3) oscillatory flow baffled crystallizer (OFBC). The schematics of PFC, SFC, and OFBC are presented in **Figure 2.10** with the PFC representing the simplest design among the three. Tubular crystallizers typically have internal diamater (I.D.) < 10 cm and tube length > 10 m. Another type of tubular crystallizer is a forced solution flow (FSF) system, which is traditionally used to produce fine protein crystals for X-ray diffraction and structure determination. For structural

determination of proteins via X-ray diffraction, the crystals must be large enough for the crystals' atomic and molecular structures to be elucidated. For large complex protein structures, such as viral proteins, the crystals are required to be larger than 100 μm for x-ray diffraction, which the FSF system can deliver [223].

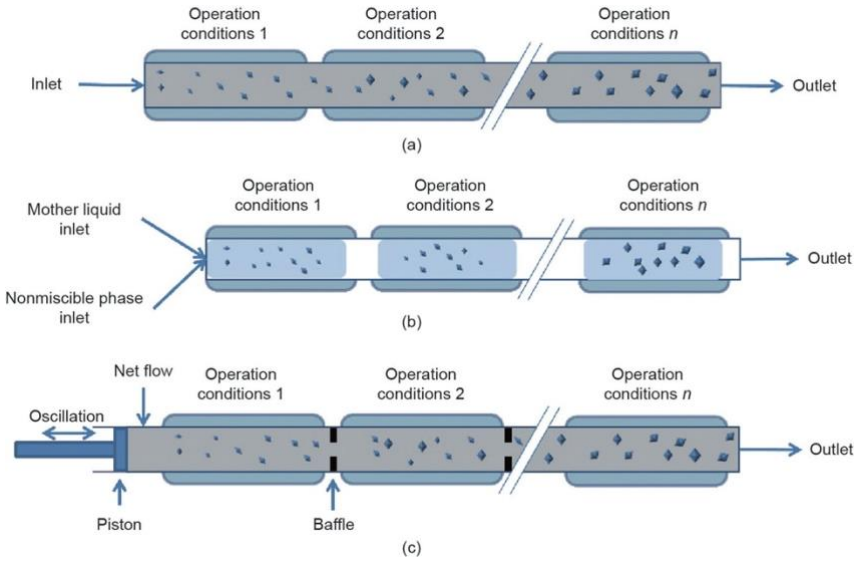

Figure 2.10 Continuous tubular crystallizers: (a) PFC; (b) SFC; (c) OFBC. Reprinted with permission from [216] Copyright (2017) Elsevier

2.5.2.1 Plug flow crystallizer (PFC)

While PFC has been successfully used for continuous crystallization of small-molecule pharmaceuticals in numerous studies [224-229], to the best of our knowledge, the use of PFC for continuous crystallization of pharmaceutical proteins has not been reported before. One of the reasons for the lack of PFC application in protein crystallization is because the handling of solid particles of macromolecules in narrow channels at low fluid velocity of the PFC is challenging due to the possibility of sedimentation and localized accumulation of the crystals, eventually leading to channel blockage. Such observation was indeed reported by Neugebauer and Khinast [46], who used PFC as the control run to demonstrate the superiority of their SFC system. Consequently, fast net flow of the crystallization solution is thus needed to prevent blockage in PFC. However, this means excessive tube length is needed to obtain sufficient residence time to achieve a reasonably high yield.

Another possible reason is because the general belief that the lack of mixing intervention in the PFC would result in its inferior performance compared to tubular crystallizers with advanced mixing strategies (e.g., OFBC), due to the longer induction time for nucleation in PFC [209]. Nevertheless, recent innovations in the design of PFC to improve its mixing efficiency have been proposed, albeit for small-molecule crystallization. One example is the coiled flow inverter (CFI) design that consists of helical coils of the tubular reactor bent at equidistant right angles [230]. The CFI design relies on the vortices generated by its helical structure to improve its mixing performance by non-invasive means. Compared to the basic PFC design, the superior performance of PFC with CFI configuration has been successfully demonstrated for crystallization of L-alanine amino acid [231].

Nonetheless, it is worth mentioning that the use of tubular plug flow reactor for continuous precipitation of proteins has been widely demonstrated. One such study is Raphael *et al.* [143] who reported continuous precipitation of sunflower protein in a 10-m long, 6-mm internal diameter glass tube equipped with four 20×11 mm kinetic static mixers. Effect of the Reynolds number, protein concentration, volumetric feed ratio on then particle size was investigated. In a subsequent study, the same group of authors investigated precipitation of canola and sunflower proteins under different operating modes (i.e., batch, MSMPR, and tubular plug flow reactor) while investigating the effects of precipitants (i.e., HCl, carboxymethylcellulose, sodium hexametaphosphate, and ammonium sulphate) [232]. Obtaining large precipitates with good distribution in plug flow reactor was reported to be difficult, particularly when high precipitation yield was also desired. Besides, enhance of the PFC crystallization of lysozyme has been reported by Fei Yu *et al.* [233] in that ultrasound was used to increase the yield via promoting of nucleation.

2.5.2.2 Slug flow crystallizer (SFC)

The SFC is characterized by a segmented flow in which a string of gas bubbles separated by liquid slugs containing the crystallization solution flow concurrently inside the tube [234]. The SFC represents an improved tubular crystallizer design from the PFC since the bubble trains ensure unimpeded movement of the crystals, even at low fluid velocity [200]. In addition, each liquid slug imitates a miniature

batch crystallizer that ensures a narrow residence time distribution of the crystallization solution, resulting in consistent crystal quality. An immiscible liquid phase can also be used in place of the gas bubbles, though it is less common due to the requirement of separating the liquid phase downstream of the SFC [53].

The SFC has been extensively utilized for continuous crystallization of small-molecule pharmaceuticals in recent years [53, 235]. In contrast, to the best of our knowledge, Neugebauer and Khinast [46] represents the first and only study that used SFC for continuous crystallization of proteins. In their study, lysozyme was used as the model protein and the slug flow was obtained by periodical injection of air flow. Using syringe pumps, 100 mg/mL lysozyme in a 0.1 mM buffered solution (pH 4.6) was mixed with 64 mg/mL NaCl solution at equal volumetric ratio prior to entering the SFC (**Figure 2.11a**). To better control the nucleation and crystal growth rates, the SFC (13 m long, I.D = 2 mm) was divided into three sections of different lengths, where each section was maintained at different temperatures enabling precise control of the local supersaturation level (**Figure 2.11b**).

Tetragonal lysozyme crystals in the size range of 15-40 μm were produced at capacity of 0.72 g/h with crystallization yield of approximately 68% after 113 min residence time. The production capacity of the SFC was comparable to that obtained from the MSMPRC with cooled tubular bypass (i.e. 0.58 g/h) presented in Hekmat *et al.* [45] The yield of the MSMPRC, however, was significantly higher at 93% due to its much longer residence time (i.e., 30 h). The work of Neugebauer and Khinast [46] successfully demonstrated the feasibility of employing SFC for protein crystallization with good residence time distribution, CSD, and production capacity. Nevertheless, a higher yield is desirable for the SFC platform to be attractive for industrial-scale production. PI strategies for the SFC, such as rapid temperature cycling [200], crash cooling nucleation [55], seeding crystallization [236], cycles of growth and dissolution [237], which have been proven effective in crystallization of small-molecule compounds, could be adopted to improve the SFC yield in protein crystallization.

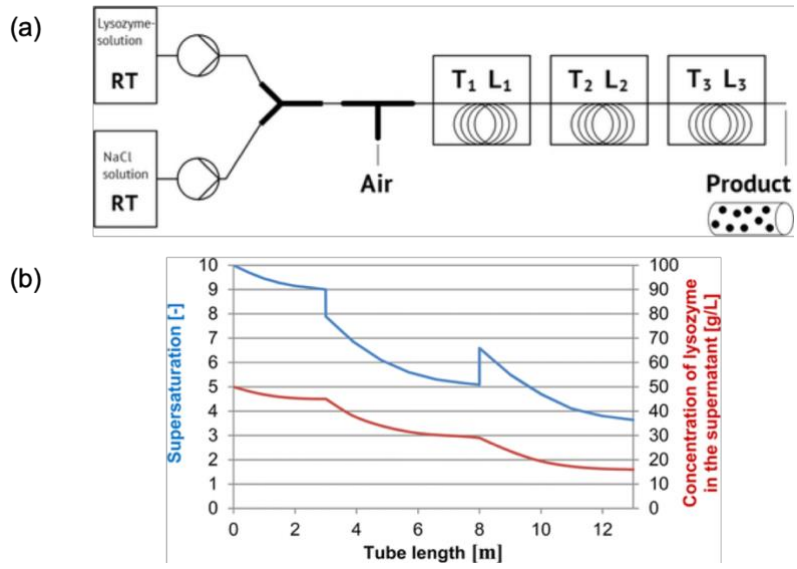

Figure 2.11 (a) Schematic diagram of the SFC; (b) supersaturation and concentration profiles along the SFC. Reprinted with permission from [46]. Copyright (2015) American Chemical Society

2.5.2.3 Oscillatory flow baffled crystallizer (OFBC)

OFBC is made up of a tubular reactor containing periodically spaced baffles with oscillatory motion superimposed on the flow of the crystallization solution. Repeating cycles of vortices are created along the tube length when the fluid passes through the baffles, resulting in powerful radial motion ensuring uniform radial mixing in every inter-baffle zone [238]. The uniform mixing leads to spatially homogeneous supersaturation level, hence uniform nucleation rate, resulting in superior crystallization performance compared to the PFC. Not unlike the SFC, the OFBC platform has been widely used for continuous crystallization of small-molecule pharmaceuticals [239]. The application of OFBC for continuous crystallization of proteins, however, was not pursued until recently in 2018.

The first few studies on the application of oscillatory flow in protein crystallization were performed in the batch mode. To address the aforementioned issue of protein denaturation in the FSF system, Parambil *et al.* [221] carried out batch crystallization of insulin in sealed capillaries. Oscillatory flow was applied to achieve good mixing of the crystallization solution. The new setup did not cause

denaturation of insulin and as a result the yield was doubled compared to without the oscillatory flow [221]. Castro *et al.* [240] developed the phase diagram for lysozyme crystallization in a meso-oscillatory flow reactor (meso-OFR) operated in a batch mode. In a subsequent study, Castro *et al.* [241] investigated the influence of oscillation amplitude and frequency on lysozyme crystallization in the meso-OFR operated in the batch mode.

The first application of oscillatory flow crystallizer for protein crystallization that was operated in the continuous mode was presented in Yang *et al.* [242] Using lysozyme as the model protein, the study started by determining the crystallization kinetics using a batch oscillatory flow crystallizer (BOFC) under oscillatory conditions of 10-25 mm amplitude (x_0) and 0.05-0.25 Hz frequency (f). In the BOFC, polyvinylchloride (PVC) tube (I.D. = 3 mm, 27 cm-long) was connected with a syringe pump operating under infuse and withdraw mode alternatively (**Figure 2.12a)**. The crystallization solution was a mixture of equal volume of lysozyme solution (30-100 mg/mL) in pH 4.9 Na(OAc) buffer and 1.1 M NaCl solution in the same buffer maintained at 20 ± 1°C.

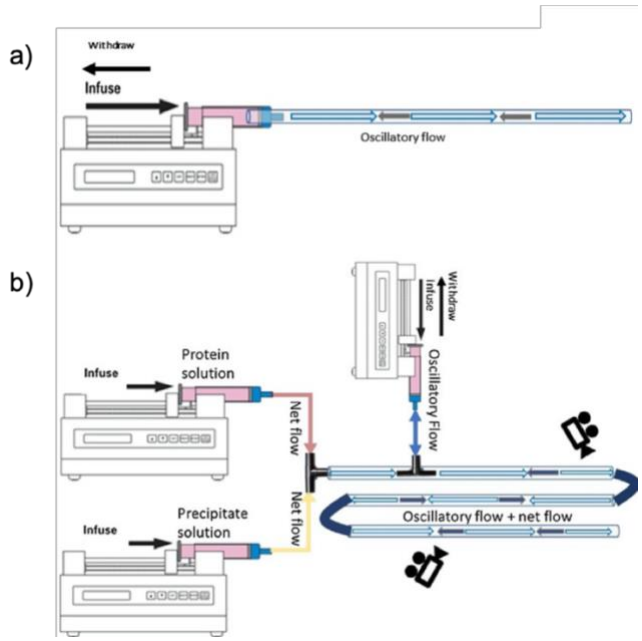

Figure 2.12 Schematics of (a) BOFC and (b) OFBC. Reprinted with permission from [242] Copyright (2018) Elsevier

After determining the crystallization kinetics, Yang *et al.* [242] proceeded to carry out the lysozyme crystallization in the OFBC. Two syringe pumps were used to mix the lysozyme and NaCl solutions in the tubular crystallizer (1.6 m-long PVC tube with I.D. = 3 mm) at flow rate of 0.06 mL/min. The oscillatory flow was generated by using a third syringe pump (**Figure 2.12b**). Higher amplitude and frequency of the oscillation was found to enhance the nucleation rate, resulting in a higher yield (i.e. 50% after 180 min residence time) and narrower CSD. While the crystal size data were not reported, the mean crystal size estimated from the microscope images provided was found to be around 15 μm. As a proof-of-concept study, Yang *et al.* [242] did not attempt to optimize the OFBC operating condition, resulting in less than ideal yield, despite the long residence time. Significantly, the work of Yang *et al.* [242] demonstrated for the first-time a successful transfer of the crystallization knowledge obtained in the batch platform to the continuous platform.

In a subsequent study, the same group of authors presented a systematic process workflow to develop a continuous crystallization process from scratch for a newly identified protein [243]. The proposed workflow consisted of four steps, i.e. (1) screening (μL), (2) scale-up in the batch mode (mL), (3) scale-up in the semi-continuous mode (mL), and lastly (4) scale-up in the continuous mode (mL-L). Adopting this process workflow for OFBC, Yang *et al.* [243] were able to improve the yield of the lysozyme crystallization slightly to 60% after 180 min residence time with mean crystal size of 11-12 μm. Moreover, the lysozyme crystals exhibited higher bioactivity than the raw lysozyme denoting the higher purity obtained by crystallization. In comparison to the SFC results of Neugebauer and Khinast [46], the OFBC produced comparable crystal size and a slightly lower yield (60% versus 68%) despite the OFBC's longer residence time (180 min versus 113.4 min). While the process workflow is certainly useful and applicable in the development of continuous protein crystallization, Yang *et al.* [243] acknowledged that, unlike lysozyme, most pharmaceutical proteins likely lacked solubility data and phase diagrams. Thus, it would remain a challenge to be able to transfer the crystallization process from the screening experiment to the scaled-up continuous platform.

2.5.3 Perspectives on current research needs

Crystallization holds promise to emulate or even surpass the prominent role of chromatography in the DSP of pharmaceutical proteins. Nearly all studies on crystallization of pharmaceutical proteins that were aimed at larger-scale production (not structural determination) were performed using the batch platform, which is notoriously prone to batch-to-batch inconsistency, poor scalability, and poor performance upon encountering process disturbance, leading to overall inefficiency [219]. These issues can be largely eliminated by shifting the crystallization process to the continuous platform, similar to what has been practiced for decades in other industries (e.g. electronics, petrochemicals), and more recently in the manufacturing of small-molecule pharmaceuticals [235].

The literature review showed that even though the benefits of the continuous platform in protein crystallization have been well-accepted by both the academics and industry players for almost a decade, a limited number of continuous protein crystallization studies are available in the literature (< 20) (**Table 2.5**). Thus, the progress lags behind the progress in continuous crystallization of small-molecule pharmaceuticals. In fact, the study, which reported parameters useful for evaluating the feasibility of continuous crystallization as the DSP step of pharmaceutical proteins (e.g. yield, purity, CSD, production capacity, and residence time), only came out not too long ago in 2015 using the SFC setup [46]. When it comes to the differences among the tubular configurations, SFC circumvents risks of channel blockage and sedimentation in PFC by incorporating a segmented gas stream. Further, compared with its OFBC counterpart, SFC does not require customized baffled tubes, additional tube baffles, and the extra oscillatory forces to ensure the mixing of the solution. Form both performance and cost point of views, SFC is advantages among the tubular crystallizers.

Admittedly, challenges in protein crystallization are many at both the molecular and macroscopic levels. Unlike small-molecule pharmaceuticals that can easily form bonds when there are collisions of molecules in a supersaturated medium, protein molecules not only need collisions, but also precise orientations upon collisions for the crystalline bonds to be formed. This translated macroscopically to the slow

nucleation and growth rates for proteins even at a high supersaturation level that is sufficient to produce fine small-molecule crystals [244, 245]. Another factor responsible for the slower pace of progress for continuous protein crystallization was the lack of well-understood proteins that could be used as the model protein.

Nevertheless, the limited number of studies on continuous protein crystallization showed that moderately high yield was achieved after reasonable residence time, where yields of around 90% and 50-70% were reported for the MSMPRC and tubular crystallizers, respectively. While the yield of continuous crystallizers was comparable to that obtained from the batch crystallizer, the continuous platform was capable of handling of a larger volume for the same residence time, resulting in higher production capacity. The production capacity of a single-channel continuous crystallizer was respectable in the range of 0.5 to 0.7 g/h, which could be increased further by optimizing the yield and by running parallel operation.

One aspect of the findings that needs to be more closely scrutinized is the reported CSD. The majority of the studies claimed that they produced crystals with good CSD using only microscopic images of uniformly sized crystals as the evidence. While size distribution charts of the crystals were presented in most studies, only the mean crystal size was quantified. There was a lack of information on the size distribution width, which is important in designing the downstream filtration and dosage formulation steps. Another aspect pertaining to the CSD that merits further investigation is how the CSD is affected by future efforts to increase the crystallization yield, as the yield for tubular crystallizers and residence time for MSPMRC clearly have much room for improvement. Attempts to increase the yield by increasing the residence time would likely lead to poorer CSD because crystal growth would become more predominant.

A number of strategies that have been proposed in batch protein crystallization to improve the yield, CSD, and purity can be also borrowed. One example of such strategy is by controlled crystallization in which the nucleation and growth phases are separated or decoupled, for example, by solvent freeze-out technique [246] and dilution technique [247]. In fact, the decoupling of nucleation and growth phases in the continuous mode has been attempted for protein crystallization by Gerdts et al.

[213] using microfluidics, though their objective was for crystal structure determination. In continuous small-molecule crystallization, such strategies includes the ultrasonication induced nucleation [54]. Other strategies are by (1) enhancing the crystal growth kinetics via the addition of additives, such as ionic liquids [43, 205, 248] and polymer additives [44], and by (2) promoting heterogeneous nucleation via membrane-assisted nucleation [249] and addition of seed materials [250].

Table 2.5 Summary of published studies on continuous crystallization of pharmaceutical proteins

Authors	Protein	Crystallizer type	Crystallizer dimension	RT*	Driving force	Operation condition	Yield	Average crystal size	Innovation	Ref
Kwon et al	Lysozyme	MSMPCR+ fine trap	1 L	2 h	Salting out + cooling	45 mg/mLLYZ, pH 4.5, 4% NaCl	-	-	Modelling	[220]
Hekmat et al	Lysozyme, mAb01	MSMPCR+ bypass	Tank: D=49 mm, 150 mL; tube: L=10 m, I.D =2 mm	30 h	Lysozyme: Salting out + cooling; mAb01: cooling + isoelectric	96 mg/mLLYZ, pH 4.6, 4% NaCl	93%	13 µm	Bypass cooling	[45]
Neugbauer et al	Lysozyme	SFC	L=13 m, I.D =2 mm	113.4 min	Salting out + cooling	30 mg/mLLYZ, pH 4.8, 1.1 M NaCl	68%	15-40 µm	Controlled supersaturation	[46]
Roberts et al	Lysozyme	FSF	50 mm × 1 mm I.D 100 mm × 1 mm I.D 160 mm × 2 mm I.D 30 cm × 6 mm O.D 30 cm × 4 mm O.D 30 cm × 2 mm O.D	40 h	Salting out + cooling	100 mg/mLLYZ, pH 4.6, 4% NaCl	80%	Up to 370 µm	Different capillaries used	[223]
Durbin et al	Lysozyme	FSF	Cell: 0.6 mm × 6 mm× 20 mm	10 days	Salting out + cooling	0.5-7.0% (w/v) LYZ, pH 4.6, 3.5% or 5.0 %NaCl	-	-	Study concentration dependence on salt concentration	[251]
Kwon et al	Lysozyme	PFC	-	-	Seeding Salting out	45 mg/mL, pH 4.5, 4% NaCl	-	-	Modelling	[57]
Yang et al	Lysozyme	OFBC	L= 160 cm, I.D =3 mm	180 min	Salting out	30-100 mg/mLLYZ, pH 4.9, 1.1 M NaCl	50%	~15 µm	First continuous OFC of protein	[242]
Yang et al	Lysozyme	OFBC	L= 160 cm, I.D =3 mm	180 min	Salting out	30-100 mg/mLLYZ, pH 4.8, 100 mg/mLNaCl	60%	11-12 µm		
Li et al	Lysozyme	Microfluidics	Channel 1.6 mm; gap 200 µm	24h 48h	Electric field Salting out	60 mg/mLLYZ, pH 4.8, 6% NaCl	13.3 ± 11.3% 34.4 ± 0.7%;	3 -7 µm	Electric-field-assisted nucleation	[212]
Zhang et al	Lysozyme	Membrane crystallization	Pore size 0.4 µm O.D 1.0 mm	25 h	Heterogeneous nucleation + Salting out + cooling	20, 30, 40 mg/mLLYZ, pH 8.3/6,5, 4%/ 6.5%/9% NaCl	-	-	Heterogenous nucleation	[210]
Wang et al	Lysozyme	MCr	-	6 days	Heterogeneous nucleation + Salting out + cooling	15 mg/m lLYZ, 25 mg/mLNaCl, 30 mg/mLglycerol in 60 mL of Na(OAc)-acetic acid buffer	-	10-30 µm; 100-150 µm	Heterogenous nucleation	[211]

CHAPTER 3 SALTING-OUT CRYSTALLIZATION OF GLYCOPEPTIDE ANTIBIOTICS: PHASE BEHAVIOR STUDY TO CONTROL THE CRYSTAL HABIT

This chapter has been submitted as **Pu, S.** and K. Hadinoto, Salting-out crystallization of glycopeptide antibiotics: Phase behavior study to control the crystal habit. Chemical Engineering Science, Volume 262, 2022, 118057 [252].

3.1 Introduction

Crystallization is a classical unit operation widely used in the purification of both small-molecule pharmaceuticals and large-molecule biologics (e.g., therapeutic proteins, monoclonal antibody, nucleic acids) [10]. In addition to crystal size, crystal habit (or external shape) has profound influences on the filterability [16], bulk density [253], adhesion tendency, which in turn affects flowability [254], and compactibility [255] of the crystals produced. These properties greatly influence the downstream processing efficiencies in steps such as filtration, centrifugation, drying, tableting, as well as storage and handling [17]. Moreover, crystal habit also influences the solubility, dissolution, and consequently the bioavailability and therapeutic activity of pharmaceuticals/biologics [18, 19, 256, 257].

Needle habit as one of the more commonly produced habits in pharmaceutical crystallization [258] is notorious for causing several downstream processing issues and difficult handling. For example, needle crystals tend to align with the flow of the mother liquor, thus blocking the filter pores and they are prone to fracture during filtration creating unwanted fines [259, 260]. Aqueous dispersions of needle crystals also exhibit a high viscosity requiring a higher energy requirement to transport them to filtration unit [193]. Needle crystals are brittle, prone to solvent inclusion [261], and typically associated with low bulk density, poor tablet quality, and difficulty in loading the required dose into capsules [262, 263]. For this reason, the design of

industrial crystallization processes has been geared towards avoiding needle crystal formation [263].

Crystal habit is governed by the relative growth rates of individual faces of the crystals. Understanding crystal growth mechanism of a compound is essential in order to control its crystal habit to avoid the needle habit formation. The crystal growth rates are governed by both internal crystal structure and crystallization conditions (e.g., supersaturation, temperature, pH). Crystal morphological modellings based on crystal growth theories (e.g., Bravais-Friedel-Donnay-Harker (BFDH), periodic bond chain (PBC), and slice attachment energy theories) have been carried out to predict the crystal habit [264, 265]. The crystal growth theories are typically coupled with kinetic models to incorporate the effect of crystallization conditions [204, 266]. From the crystal morphological modelling, organic small molecules can be categorized as either persistent (largely unavoidable), or controllable in their needle habit formation tendency [264]. Moreover, the crystal morphological modelling has enabled researchers to develop guidelines on solvent selection to avoid the needle habit formation, which have been validated with experimental data [267-269].

Besides crystal morphological modelling, various crystal habit modification techniques have been explored experimentally [270]. Solvent selection via its influence on the drug solubility has been the most widely investigated, particularly for small-molecule pharmaceuticals [271]. For example, the aspect ratio of anticholesterol drug lovastatin crystals could be lowered (less needle-like) by using less polar solvents (e.g., hexane, methylcyclohexane, ethyl acetate), in place of water-acetone mixture, or methanol used in industrial crystallization [272, 273]. An opposite trend was observed in the crystallization of anti-inflammatory drug ibuprofen, where the use of low-polarity solvents resulted in needle crystals [274].

The crystal habit can also be modified by adding a growth inhibiting agent that is adsorbed onto the fast-growing crystal face. For example, the addition of hydrophobic polymers resulted in the formation of plate-like lovastatin crystals, in place of needle crystals produced without additives [273]. The needle habit formation was suppressed by adding Polysorbate-80 surfactant and poly(sebacic anhydrite) in

the crystallization of antihypertensive drug nifedipine [275] and antifungal drug griseofulvin [276], respectively.

Another widely used experimental approach to modify the crystal habit is by precise manipulation of the supersaturation level via temperature cycling. For example, the aspect ratio of needle crystals of aspirin was successfully modified by multiple cycles of heating and cooling [237]. Successful crystal habit modifications by temperature cycling were also demonstrated in the crystallization of paracetamol [277] and a proprietary active pharmaceutical ingredient [278]. The needle habit formation can also be suppressed by simultaneous controls of multiple crystallization process variables (e.g., temperature, stirring rate, cooling rate, and seeding) as demonstrated in the crystallization of painkiller celecoxib [279].

Successful crystal habit modifications have also been demonstrated for biomacromolecules, particularly proteins, albeit they have not been as extensively studied as small-molecule pharmaceuticals. For example, needle habit formation of antimicrobial lysozyme could be avoided by (1) performing the crystallization under acidic condition and low temperature [171], (2) addition of ionic liquid as the habit modifier [205, 280], and (3) use of crosslinked polymers as seeds. Needle habit formation of ovalbumin and catalase, on the other hand, was promoted at lower pH [168]. In general, the aspect ratio of protein crystals was found to be most affected by pH and temperature [168, 281].

Besides proteins, another clinically important class of biological macromolecules is bioactive peptides, whose molecular weight (MW) typically falls between small-molecule pharmaceuticals and proteins (i.e., $1 \leq \text{MW} \leq 5$ kDa) [3]. Unlike proteins, crystallization of peptides for purification purposes has not been widely employed [11]. Ultrafiltration membrane and chromatography, which pose problems of low throughput and high operational costs, remain predominantly employed in industrial purification of bioactive peptides [12]. The few studies on peptide crystallization were mostly aimed at crystal structure determination [13-15]. To the best of our knowledge, modification of crystal habit in peptide crystallization had not been investigated before.

In the chapter, we investigated the feasibility of avoiding needle habit formation in peptide crystallization using vancomycin hydrochloride (Van) - a glycopeptide antibiotic - as the model peptide. Van (MW 1.45 kDa) is widely used to treat infections caused by MRSA (methicillin-resistant *Staphylococcus aureus*), penicillin-resistant *pneumococci*, and to treat infections in patients who are allergic to penicillin and cephalosporins [282]. Purification of Van, which is industrially produced from bacterial fermentation, requires multicycles of ion-exchange chromatography with pH adjustments, followed by antisolvent/salting-out crystallization as the final purification step [283].

While octahedral Van crystals were produced by hanging drop vapor diffusion crystallization [14], bulk crystallization of Van resulted in the undesirable needle crystals [284]. Not unlike protein crystallization, the significant influences of pH and temperature were demonstrated in bulk Van crystallization performed in stirred vessels, where a narrow workable range of pH and temperature existed with pH 2.5 and 10°C determined as the optimal condition [284]. Bulk Van crystallization was slow needing 24 h to reach 95% yield, despite combined cooling/salting-out/antisolvent (with acetone) crystallizations were employed. Even though the bulk crystallization rate could be enhanced by the addition of ionic liquid [285] and polymer seeds [286], needle crystals remained the predominant habit.

The first objective of the present work was to carry out a phase behavior study to determine crystallization conditions in which the needle habit could be avoided and to identify the predominant non-needle crystal habit produced. Recognizing the significant influences of solvent, pH, and temperature on the resultant crystal habit, we carried out the phase behavior study in conditions distinct from the ones employed in Lee *et al.* [284]. Specifically, we employed salting-out crystallization at room temperature using acetate buffer solution as the solvent, in contrast to simultaneous cooling/salting-out/antisolvent crystallization pursued in Lee *et al.* [284]. Phase behaviors of Van crystallization at different (i) pH, (ii) concentrations of Van and salt, and (iii) incubation time were examined in a high-throughput μL-scale crystallization setup.

The second objective of the present work was to carry out batch crystallization of the predominant non-needle crystal habit identified in the phase behavior study (i.e., octahedral crystals). The batch crystallization performances were characterized in terms of the (1) production yield and capacity, (2) purity, (3) crystal size distribution, (4) thermal stability, (5) interfacial water content, (6) dissolution characteristics, and lastly (7) antibiotic activity. The batch crystallization performances of the octahedral crystals were evaluated relative to the needle crystals, which represented the conventional crystal habit produced from bulk crystallization of Van.

3.2 Materials and Methods

3.2.1 Materials

Van (United States Pharmacopeia (USP) grade, ≥ 900 μg/mg) was purchased from Duly Biotech Co. Ltd. (Nanjing, China). Glycine (≥ 99%), glacial acetic acid, potassium dihydrogen phosphate (KH_2PO_4), sodium hydroxide (NaOH), sodium acetate (≥ 99%), ethanol (≥ 99.5%), and paraffin oil (puriss., Ph. Eur.) were purchased from Sigma Aldrich (Singapore). Hydrochloric acid (HCl, 37%) was purchased from VWR (Singapore). Mueller Hinton Broth (MHB) and phosphate buffered saline (PBS, pH 6.8) were purchased from BD Diagnostics (Singapore).

3.2.2 Methods

3.2.2.1 Phase behavior study

The phase behavior of room-temperature salting-out crystallization of Van was investigated in triplicates in 96-well plates (Greiner Bio-One, CELLSTAR®, Austria) using NaCl as the salting-out agent. The phase behavior study was carried out over a wide range of Van and NaCl concentration at four different pH values (i.e., pH 2.6, 3.6, 4.6, and 5.6). Stock solutions of Van and 2 M NaCl were prepared in 50 mM sodium acetate buffer adjusted to pH 3.6, 4.6, and 5.6 by adding HCl. Stock solutions of Van and NaCl at pH 2.6 were prepared in 50 mM glycine-HCl buffer. The buffer solutions were vacuum filtered prior to their use in 0.2-μm PES membrane filters (Nalgene, VWR, Singapore). A two-point calibrated pH meter (Mettler Toledo™ EL20 Benchtop pH Meter) was used for pH measurement.

For each pH investigated, the Van and NaCl stock solutions were diluted with the buffer solutions to yield eight Van solutions and twelve NaCl solutions with concentrations in the range of 30-100 mg/mL and 0-2 M, respectively. Next, as depicted in **Figure 3.1**, 50 µL of each of the twelve NaCl solutions were added to the wells of the 96-well plate, where NaCl concentrations increased from left to right columns. The wells in the leftmost column were used as the control wells where NaCl was not added. Afterwards, 50 µL of each of the eight Van solutions were added to the wells, where Van concentrations decreased from top to bottom rows, resulting in ninety-six Van-NaCl solutions of different compositions. The Van and NaCl solution were syringe filtered 0.22 µm Whatman® PTFE (Whatman, VWR, Singapore) prior to their mixing.

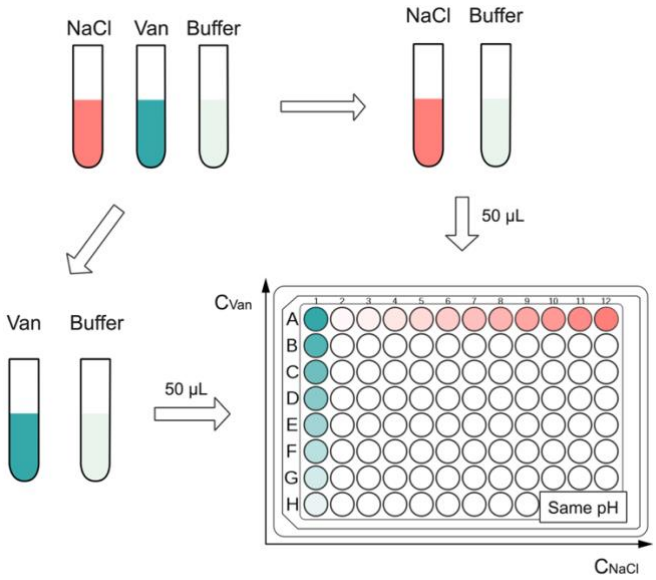

Figure 3.1 Schematic illustration of the experimental procedure of phase diagram preparation.

To prevent sample evaporation, each well was covered by 0.1 mL paraffin oil after which the plate was sealed with Corning® microplate sealing tape (Sigma Aldrich, Singapore). The 96-well plate was then placed in a chamber maintained at 22.5 ± 0.5 °C for 1, 7, and 14 days. On days 1, 7 and 14, the wells in the plate were examined under light microscope (CKX41, Olympus, Japan) at 400× magnification. The phase behavior in each well was characterized by whether clear solution,

precipitates, and crystals of different habits were present. The mean crystal size was determined by image analysis using ImageJ software (NIH, USA) with a minimum of 500 particle counts. The octahedral crystal size was reported in terms of the number-averaged Feret's diameter, whereas the needle crystal size was reported in terms of the number-averaged end-to-end length.

3.2.2.2 Van solubility in buffer solutions of different pH and ionic strength

For each pH investigated, Van was added at 50 mg/mL to 0.1 mL buffer solution containing different NaCl concentrations (i.e., 0 to 1 M) in 0.6-mL Corning® Eppendorf tubes (VWR, Singapore). The Van solution was then incubated in a shaking incubator at room temperature for 21 days to yield the respective crystalline solids. On days 7, 14, and 21, the Van solution was centrifuged at 14,500×g for 10 min (Sorvall 16R, Thermo Fisher Scientific, USA), after which the Van concentration in the supernatant, which characterized the Van solubility, was determined by UV-Vis spectrophotometer (UV Mini 1240, Shimadzu, Japan) at the absorbance wavelength of 280 nm. The Van solubility ($C_{Solubility}$) was determined from three replicates. Statistical analysis of the solubility results was performed by single-factor ANOVA in Microsoft Excel. Using the Van solubility values, the supersaturation levels of Van in the phase behavior study were calculated as $C/C_{Solubility}$, where C represented the Van concentration present in each well of the 96-well plate.

3.2.2.3 Batch crystallization of Van

Batch crystallization was carried out at two batch volumes, i.e., 1.5 and 15 mL using sealed cylindrical glass containers as the crystallization vessel. For the stand-alone needle (SAN) crystals, equal volumes of 100 mg/mL Van solution and 0.4 M NaCl solution (pH 5.6) were added to the vessel and incubated at room temperature for 24 h and 48 h under gentle shaking. The octahedral (O) crystals were prepared by the same procedures using 1.6 M NaCl solution instead. After incubation, the crystals produced were examined under light microscope and the crystallization solution was centrifuged at 14,500 rpm for 10 min to recover the Van crystals.

The yield (% w/w) of the batch crystallization was determined in triplicates according to **Eq. (3.1**), where C_i and C_o represented the initial and final Van concentrations present in the crystallization vessel, respectively. C_o was measured from the supernatant of the centrifuged crystallization solution by UV-Vis spectrophotometer. The crystals were then lyophilized at -52°C and 0.05 mbar for 24 h in Alpha 1-2 LD Plus freeze dryer (Martin Christ, Germany) for characterizations. The production capacity, which was defined as the mass of lyophilized Van crystals produced per unit volume of the crystallizer, was determined in triplicates.

$$\text{Yield } \left(\%\frac{w}{w}\right) = \frac{C_i - C_o}{C_o} \times 100\% \tag{3.1}$$

The purities of the O and SAN crystals were determined by dissolving 15 mg lyophilized crystals in 100 mL acetate buffer (pH 5.6). Van concentration in the buffer was subsequently determined by high performance liquid chromatography (HPLC) (1260 Infinity II (Agilent Technologies, Singapore) using ZORBAX Eclipse Plus C18 column (250 × 4.6 mm, 5-µm particle size) at detection wavelength of 280 nm [287]. 85:15 (v/v) mixture of 0.1% (w/v) aqueous acetic acid solution and ethanol was used as the mobile phase at flow rate of 0.5 mL/min, resulting in Van retention time of approximately 4.5 min.

3.2.2.4 Characterizations of Van crystals from batch crystallization

The crystal size distributions (CSD) of the O and SAN crystals were characterized by the Span defined in **Eq. (2.9**), where d_{10}, d_{50}, and d_{90} represented the crystal size at 10%, 50%, and 90% cumulative undersize of the CSD. The mean crystal size and d_{10}, d_{50}, and d_{90} were determined from a minimum of 1000 particle counts using ImageJ software (NIH, USA). The crystal morphology was examined by scanning electron microscope (SEM) (JSM 6390LA, JEOL, Japan) using lyophilized Van crystals as the sample. The crystals were coated with platinum at 20 mA for 120 s prior to SEM.

Fourier transform infrared spectroscopy (FTIR) analysis of the O and SAN crystals were carried out between 450 cm^{-1} and 4000 cm^{-1} at 1 cm^{-1} spectral resolution using Spectrum One FTIR (PerkinElmer, USA). Their crystalline forms were

examined by powder x-ray diffraction (PXRD) analysis performed between 5° and 70° with a step size of 0.02°/s using D2-Phaser X-ray Diffractometer (Bruker, Germany). Thermal stability of the O and SAN crystals were examined by thermogravimetric analysis (TGA) using TGA/DSC 1 (Mettler Toledo, USA) and differential scanning calorimetry (DSC) using 822e (Mettler Toledo, Switzerland) performed between 25°C and 650°C with a heating rate of 10 °C/min under nitrogen atmosphere.

The interfacial water contents (or trapped water) of the O and SAN crystals were determined by cryogenic DSC following the method of [288]. Briefly, the lyophilized crystals were dissolved in sodium acetate buffer (pH 5.6) at 20 mg/mL and a blank buffer solution was used as the reference sample. Cryo DSC analysis of the Van solution was performed under nitrogen atmosphere between -65°C to 25°C at a heating rate of 0.25°C/min. Because of amorphous structure of interfacial water, no endothermic peak was observed on the DSC melting thermograms. The interfacial water contents were determined from the difference in the melting enthalpy between the Van solution and buffer solution.

Specifically, the mass of water associated with 1 g of the protein in the solid phase (m_{water}) was calculated as follows:

$$m_{water} = \frac{(m_t - m_f)}{m_p} \tag{3.2}$$

where m_t is the total mass of water in liquid protein solution (mg); m_f is the mass of mobile water (not associated) in protein solution (mg); m_p is the mass of the protein in solution (mg). The mass of the mobile water in the protein solution (m_f) was calculated based on the value of phase transition enthalpy:

$$m_f = \frac{m_{sample}\Delta H_S}{\Delta H_{buff}} \tag{3.3}$$

where ΔH_S is the enthalpy of phase transition for the sample of the protein solution (J/g); ΔH_{buff} is the enthalpy of phase transition for the blank sample (J/g); m_{sample} is the mass of the sample (g).

The total mass of water in the protein solution was calculated as follows:

$$m_t = m_{sample}(1 - x_p - x_{salt}) \quad (3.4)$$

where x_p and x_{salt} are the mass fraction of the protein and salt in the sample solution, respectively.

3.2.2.5 Dissolution characteristics

Van is commonly administrated intravenously to treat various infections in hospitals, it is also commercially available in sterile powder form for dilution [282]. For patients with severe Clostridium difficile Infections (CDI), a gastrointestinal illness, Van has been recommended to be used orally as a first-line treatment in the form of capsules or solution [289]. Van acts locally in the lower gastrointestinal (GI) tract, after administration, a Van capsule releases the drug into the stomach and upper GI tract, where it dissolves in GI fluids and is transported along with the GI fluids to its site of action [290].

Van dissolution from the SAN and O crystals were examined under sink condition in triplicates at three pH values, i.e., pH 1.2, 4.5, and 6.8, representing the typical fasted stomach, fed stomach, and intestinal pHs, respectively [291]. The sink condition was defined by United States Pharmacopeia (USP) as a condition in which the maximum drug concentration dissolved in the medium was less than 1/3 of the thermodynamic saturation solubility of drug (C_{Sat}) in the said medium [292]. The dissolution medium was prepared from 0.1 N HCl (pH 1.2), acetate buffer (pH 4.5), and phosphate buffer (pH 6.8) solutions adjusted to the desired pH by adding HCl.

C_{Sat} values of Van at 37°C were experimentally determined to be approximately equal to 146, 100, and 90 mg/mL at pH 1.2, 4.5, and 6.8, respectively. Briefly, lyophilized Van crystals were added to 40 mL of the dissolution medium placed in a shaking incubator maintained at 37°C. At specific time points over 60 min, 1 mL aliquot was withdrawn, and the same volume of fresh medium was added as replenishment. The aliquot was centrifuged at 14,500 rpm for 10 min after which Van concentration in the supernatant was determined by UV-Vis spectrophotometer as

previously described. Statistical analysis was performed by single-factor ANOVA in Microsoft Excel.

3.2.2.6 Antibiotic activity

Antibiotic activities of the SAN and O crystals were examined from the minimum inhibitory concentration (MIC) against *Staphylococcus aureus* ATCC 29213 bacteria. The MIC was performed in triplicates by microbroth dilution method following the methods of Tran *et al.* [293]. Briefly, overnight inoculum of *S. aureus* was adjusted to 0.5 McFarland standards and diluted in MHB to produce 1.0×10^6 CFU/mL. Afterwards, 200 µL of the bacterial cell suspension was placed in the wells of a 96-well plate. Next, 200 µL Van solution with concentration in the range of 0 to 256 µg/mL were added to the wells. The plate was then incubated at 37°C for 24 h. Wells without Van and without bacteria were used as the positive and negative controls, respectively. The MIC was determined by the optical density of the bacterial cell suspension at 600 nm (OD_{600}) using a microplate reader (Synergy HT, Biotek, USA), where MIC was characterized by $OD_{600} < 0.1$ indicating no visible bacterial growth.

3.3 Results and discussion

3.3.1 Van solubility in buffer solutions of different pH and ionic strength

Prior to the phase behavior study, the solubility of Van in buffer solutions of different pH and NaCl concentrations (C_{NaCl}) was characterized to determine the supersaturation level in the phase behavior study. The low solubility of proteins/peptides near their isoelectric point (pI) might promote their crystallization because of the high supersaturation level. The possibilities of amorphous precipitation and aggregation, however, were high for crystallization condition near the pI [160]. For basic proteins, several studies had advocated crystallization at pH below the pI for enhanced crystallization propensity [169, 294, 295]. Van is a basic glycopeptide with pI of 8.1 [296]. Furthermore, Van exhibited maximum stability in buffer solution at pH between 3.0 and 5.7 [297]. For these reasons, Van solubility was investigated at pH < pI specifically at pH 2.6, 3.6, 4.6, and 5.6.

The results showed that Van solubility reached an equilibrium only after 14 days of incubation. Van solubility determined after 14 days of incubation was found to be

highly dependent on pH (**Figure 3.2**). As expected, the solubility was higher at the lower pH investigated (i.e., pH 2.6 and 3.6) as they were farther away from the pI. The higher Van solubility at pH 2.6 and 3.6 was most evident at low ionic strength at $C_{NaCl} \leq 0.3$ M. The pH-dependence of Van solubility was less evident at higher NaCl concentrations ($C_{NaCl} \geq 0.7$ M) as the ionic strength effect via salting out became more predominant.

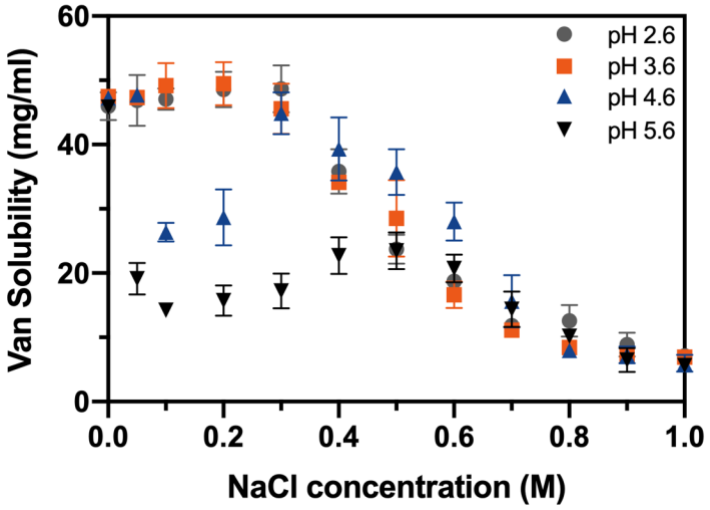

Figure 3.2 Van solubility in buffer solutions of different pH and NaCl concentrations

At pH 2.6 and 3.6, Van solubility remained relatively constant with increasing NaCl concentrations up to $C_{NaCl} = 0.3$ M above which the solubility started to decrease due to salting out of the peptide at high ionic strength. Specifically, Van solubility decreased from approximately 50 mg/mL in the absence of NaCl to below 10 mg/mL in the presence of 1.0 M NaCl. At pH 4.6 and 5.6, on the other hand, Van solubility exhibited a biphasic profile, where the solubility initially increased with increasing NaCl concentration up to $C_{NaCl} = 0.4$ M attributed to salting-in phenomenon. The increase in the Van solubility in the salting-in region was determined to be statistically significant with ANOVA p-values equal to 0.049 and 0.137 at pH 4.6 and 5.6, respectively.

At $C_{NaCl} > 0.4$ M, Van solubility at pH 4.6 and 5.6 gradually decreased with increasing NaCl concentration due to salting out. Specifically, Van solubility at pH

4.6 increased from ≈ 20 mg/mL in the absence of NaCl to ≈ 40 mg/mL at $C_{NaCl} =$ 0.4 M before it decreased to below 10 mg/mL at $C_{NaCl} = 0.4$ M. A similar trend was observed at pH 5.6, albeit the salting-in effect was not as pronounced. In this regard, the biphasic solubility profile attributed to the salting-in and salting-out events had been widely reported for a number of proteins [298-300].

3.3.2 Phase behavior of room-temperature salting-out crystallization of Van

In the phase behavior study, the observed phases in Van crystallization were classified into one of the following phases, (1) clear solution, (2) crystal formation, or (3) precipitate formation. This classification followed the phase behavior classification in protein crystallization . In the crystal formation phase, four different crystal habits were witnessed, namely octahedral (O), stand-alone needle (SAN), oblanceolate leave-like needle (OLN), and sea urchin-like needle (SUN) crystals (**Figure 3.3**). Certain crystallization conditions resulted in the formation of both O and OLN crystals as discussed in more details later.

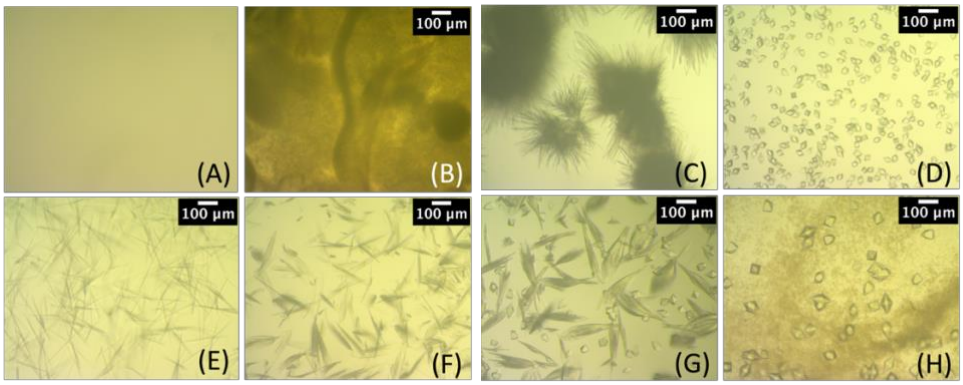

Figure 3.3 Microscopic images of different phase behaviors observed in salting-out room-temperature crystallization of Van: (A) clear solution; (B) precipitates; (C) sea urchin-like needle crystals (SUN); (D) octahedral crystals (O); (E) stand-alone needle crystals (SAN); (F) oblanceolate needle crystals (OLN); (G) OLN + O crystals; (H) O crystals + precipitates

In macromolecule crystallization, the precipitates were typically observed as aggregates or gel, which were identifiable under light microscope by their disordered opaque appearances [168]. The precipitates often served as the precursors for crystal

formation [301], hence they often co-existed with the crystals. In fact, this was observed in Van crystallization where the O crystals and precipitates co-existed under certain crystallization conditions as we elaborated later.

At pH 2.6, the phase diagram in **Figure 3.4A** showed that O crystals were produced after 1 day incubation at a minimum NaCl concentration of 0.4 M. At $C_{NaCl} < 0.4$ M, the supersaturation levels across all Van concentrations remained below or equal to unity (**Figure 3.4B**), hence no crystallization/precipitation took place. With increasing NaCl or Van concentrations, the incidence of O crystal formation increased due to the higher supersaturation levels. The numbers of wells producing the O crystals increased as the incubation time was increased from 1 day to 7 days and 14 days. The increased incidence of crystal production at longer incubation time was contributed by crystallization taking place at lower Van concentrations. The minimum $C_{NaCl} = 0.4$ M was, nevertheless, still required for crystallization. The lower Van concentrations translated to lower supersaturation levels and consequently slower crystallization rates; thereby longer incubation time was needed.

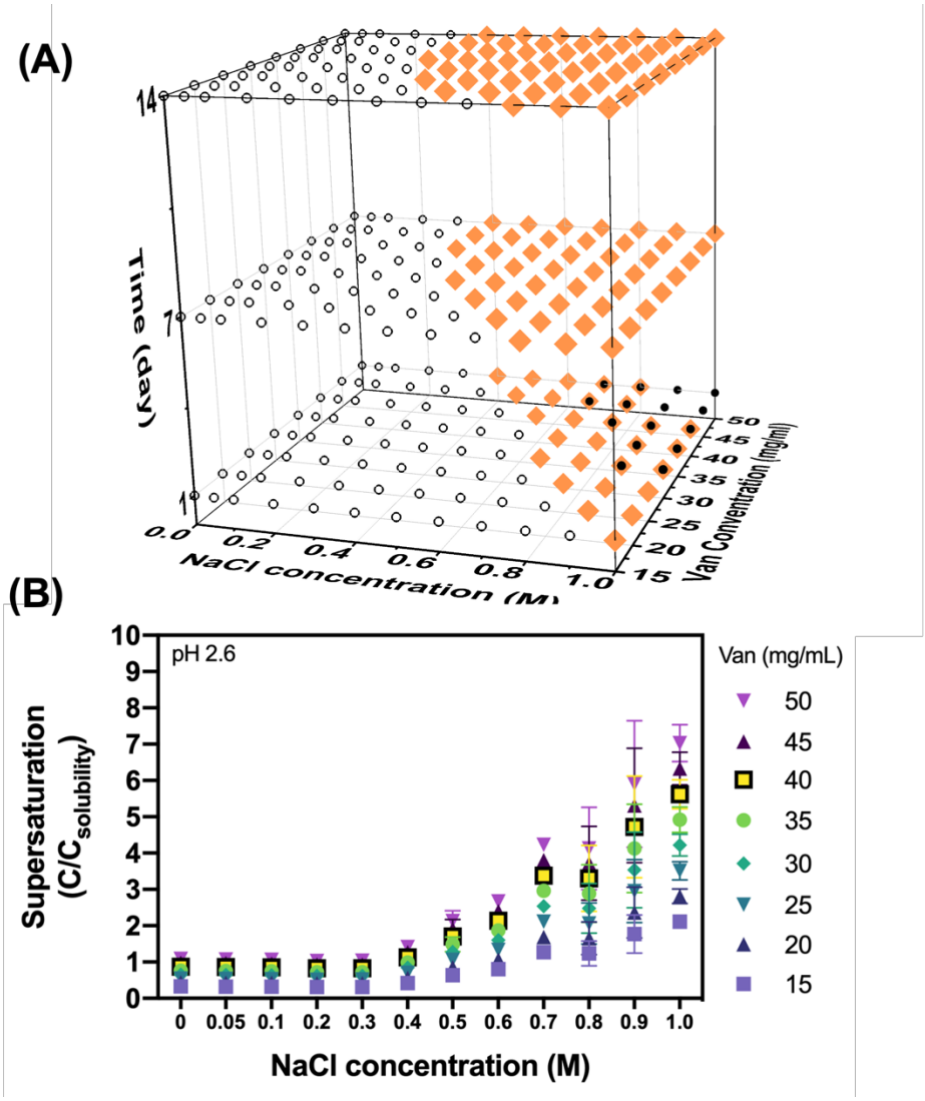

Figure 3.4 (A) Phase diagram of Van crystallization at pH 2.6 (unfilled circles: clear solution; orange diamond: O crystals; black circles: precipitates); (B) Van supersaturation levels at different conditions investigated in the phase diagram at pH 2.6

At the upper ends of both Van and NaCl concentrations, i.e., ≥ 30 mg/mL and ≥ 0.7 M, respectively, precipitates appeared together with the O crystals after 1 day. The precipitates, nevertheless, slowly transformed into the O crystals after 7 days. In this regard, transformation of precipitates to crystals had been reported in protein crystallization for a number of proteins, for example, lysozyme [302], ovalbumin [113], and monoclonal antibody [303]. The Ostwald's law of stages stated that in crystallization the least stable phase was typically isolated first after which it

transformed to the more thermodynamically stable phase over time [304]. The fact that the O crystals remained observed after 14 days signified O as a stable crystal habit of Van.

Regarding the crystal size, the size of the O crystals after 1-day incubation varied between roughly 10 to 70 μm depending on the supersaturation level (**Figure 3.5A**). Larger crystals were produced at higher supersaturation levels as rates of crystal growth typically increased with the supersaturation level [34]. At very high supersaturation levels (> 4), however, nucleation events were intensified which in turn suppressed crystal growth, resulting in the formation of small crystals [47]. A light microscope image of the representative O crystals produced at a high supersaturation level was presented in **Figure 3.5B**.

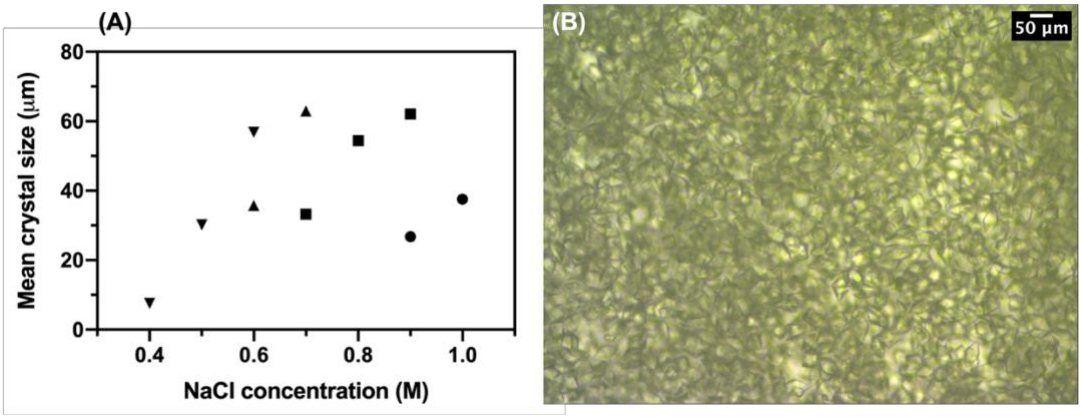

Figure 3.5 (A) Mean O crystal size at pH 2.6 under different Van concentration after 1 day (Circles: 20 mg/mL; squares: 30 mg/mL; triangles: 40 mg/mL; inverted triangles: 50 mg/mL); (B) Day 1-pH 2.6-50 mg/mL Van-0.8 M NaCl ($C/C_{Solubility} = 4.1 \pm 1.1$)

At pH 3.6 and 4.6, similar results were obtained as evidenced by the phase diagrams in **Figure 3.6A** and **Figure 3.7A**, respectively. The similar results at pH 2.6, 3.6, and 4.6 were not unexpected considering their comparable supersaturation profiles (**Figure 3.4B**, **Figure 3.6B**, **Figure 3.7B**). The O crystals produced at pH 3.6 and pH 4.6 also exhibited size in the range of 10 to 70 μm similar to the size obtained at pH 2.6 (**Figure 3.8**). The numbers of wells that produced crystals also increased with longer incubation time at pH 3.6 and 4.6.

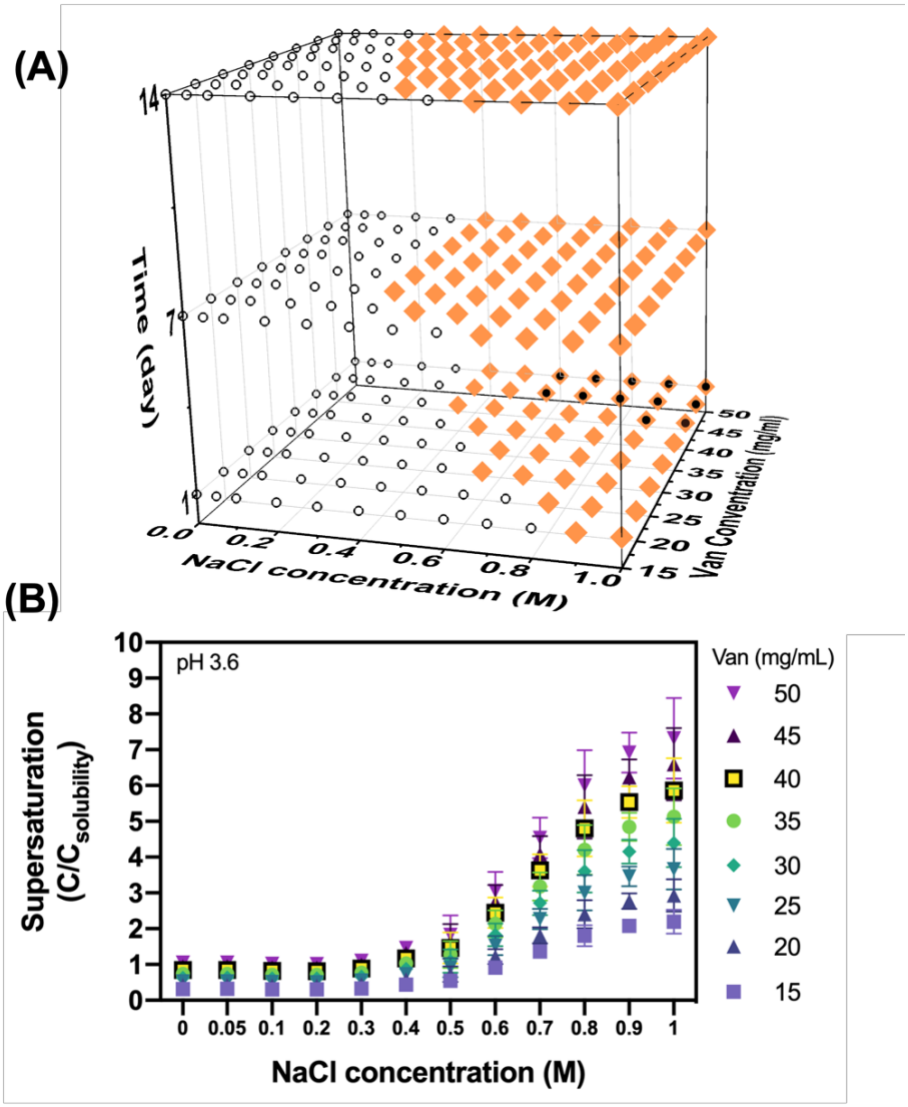

Figure 3.6 (A) Phase diagram of Van crystallization at pH 3.6 (unfilled circles: clear solution; orange diamond: O crystals; black circles: precipitates); (B) Van supersaturation levels at different conditions investigated in the phase diagram at pH 3.6

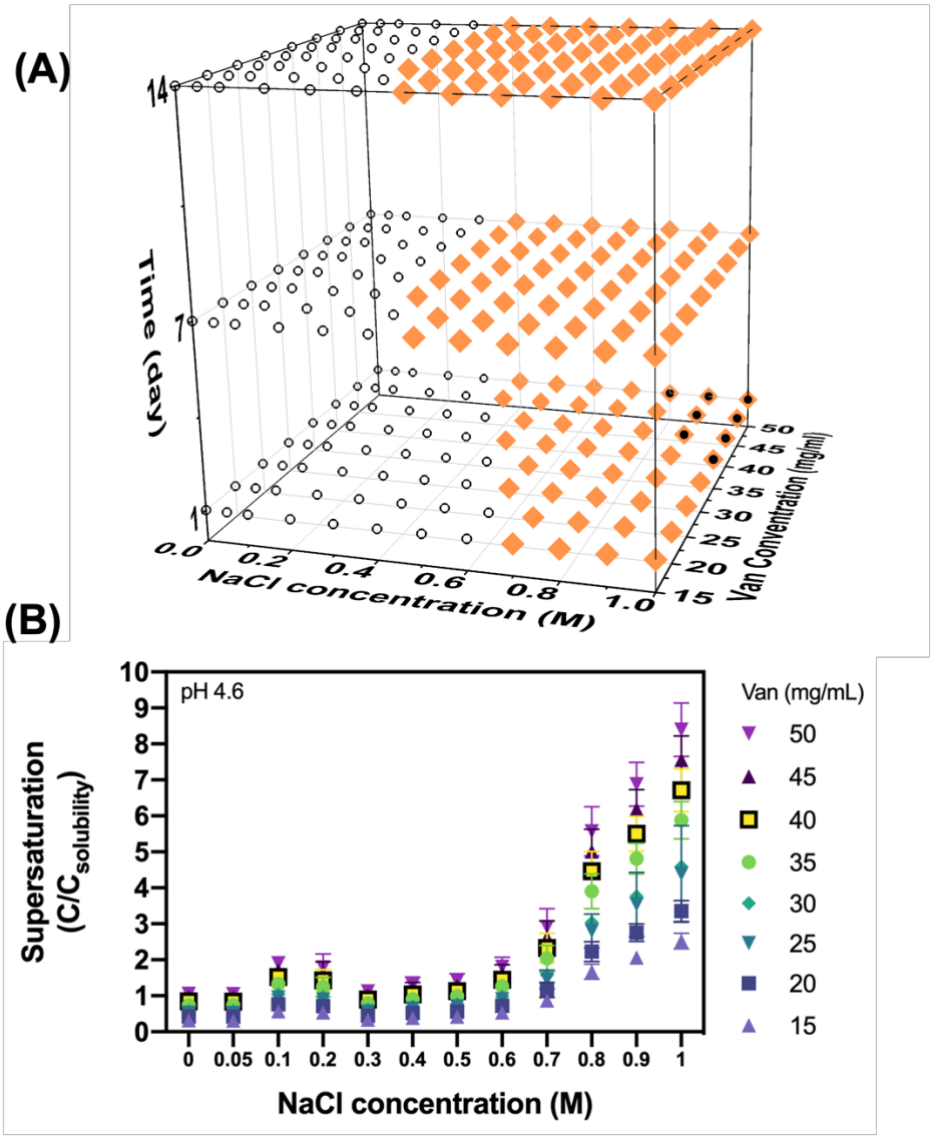

Figure 3.7 (A) Phase diagram of Van crystallization at pH 4.6 (unfilled circles: clear solution; orange diamond: O crystals; black circles: precipitates); (B) Van supersaturation levels at different conditions investigated in the phase diagram at pH 4.6

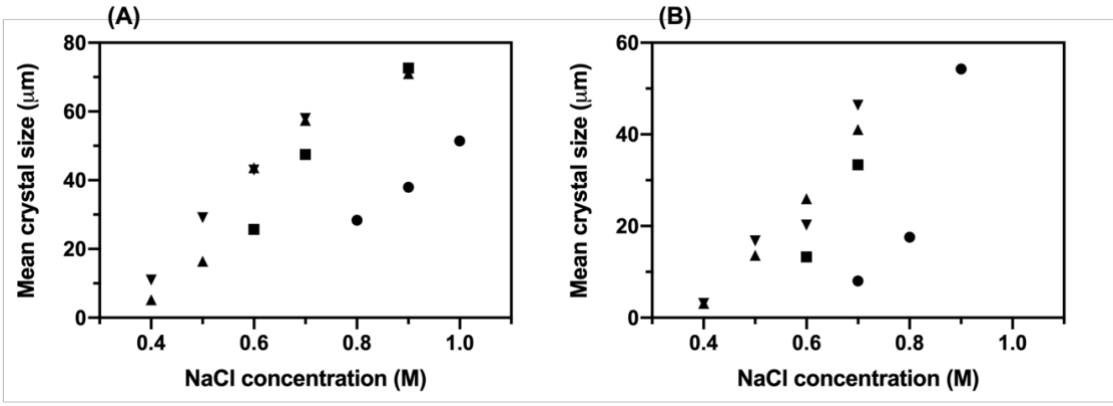

Figure 3.8 (A) Mean O crystal size at pH 3.6 under different Van concentration after 1 day (Circles: 20 mg/mL; squares: 30 mg/mL; triangles: 40 mg/mL; inverted triangles: 50 mg/mL); (B) Mean O crystal size at pH 4.6 under different Van concentration after 1 day (Circles: 20 mg/mL; squares: 30 mg/mL; triangles: 40 mg/mL; inverted triangles: 50 mg/mL)

Furthermore, at pH 3.6 and 4.6, 54 of the 96 wells (56.25%) produced the O crystals after 14 days, which was slightly higher than 48 of the 96 wells (50%) at pH 2.6. The increased incidence of crystal production at pH 3.6 and 4.6 was attributed to crystallization at the lower ends of Van and NaCl concentrations (i.e., lower supersaturation levels), which was not observed at pH 2.6. In this regard, the smaller net charge of the peptides at pH nearer to their pI translated to less repulsion between the peptide molecules, which in turn enhanced the peptide-peptide interactions. The stronger solutes-solutes interaction at pH nearer to the pI increased their crystallization propensity, whereby crystallization could take place at lower supersaturation levels.

In contrast, significantly different phase behaviors, where different crystal habits were produced, were observed from the phase diagram at pH 5.6 (Fig. 6A). Both O and SAN crystals were produced at pH 5.6 after 1 day incubation with O as the predominant habit. The O crystals were produced in the similar range of Van and NaCl concentrations as at pH 3.6 and 4.6. The SAN crystals, on the other hand, were produced in the lower NaCl concentration range, more specifically at 0.1 M $\leq C_{NaCl} \leq$ 0.4 M in which the salting-in event took place. Regarding the crystal size, the O crystals exhibited sizes in the range of 10 to 60 μm, while the SAN crystals were in

the size range of 100 to 800 μm (**Figure 3.10**). The sizes of both crystal habits increased with increasing supersaturation level similar to the trends observed at the lower pHs.

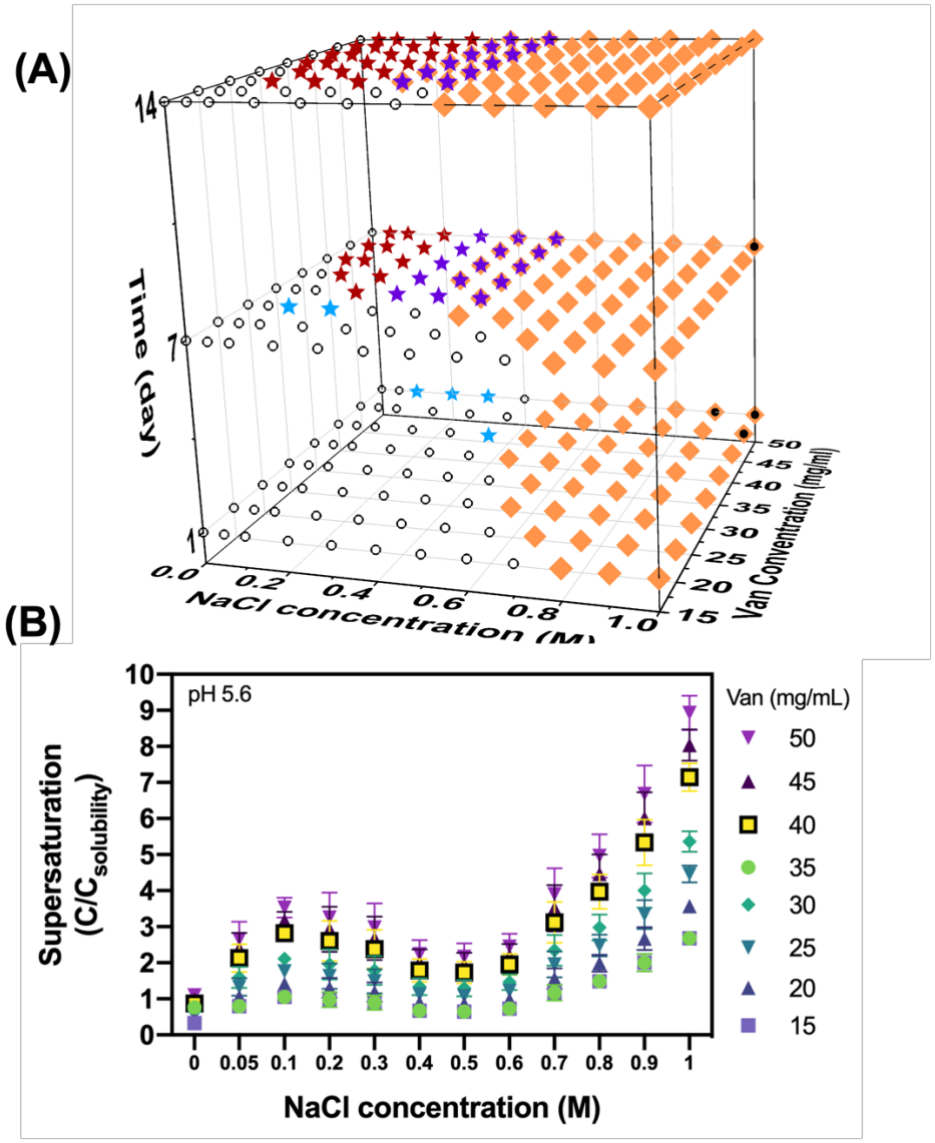

Figure 3.9 (A) Phase diagram of Van crystallization at pH 5.6 (unfilled circles: clear solution; orange diamond: O crystals; black circles: precipitates; blue stars: SAN crystals; purple stars: OLN crystals; red stars: SUN crystals); (B) Van supersaturation levels at different conditions investigated in the phase diagram at pH 5.6

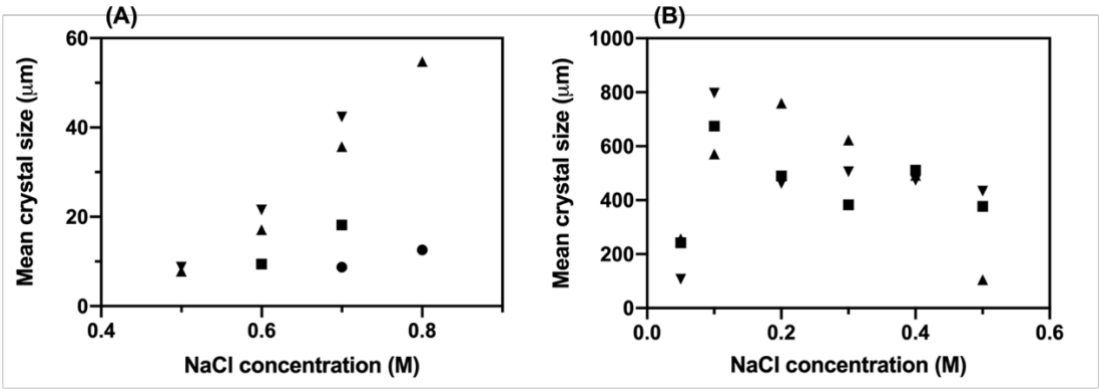

Figure 3.10 (A) Mean O crystal size at pH 5.6 under different Van concentration after 1 day (Circles: 20 mg/mL; squares: 30 mg/mL; triangles: 40 mg/mL; inverted triangles: 50 mg/mL); (B) Mean N crystal size at pH 5.6 under different Van concentration after 14 days (Squares: 40 mg/mL; triangles: 45 mg/mL; inverted triangles: 50 mg/mL)

Increasing the incubation time to 7 days resulted in the production of new needle habits, namely OLN and SUN crystals. The late appearance of the OLN and SUN crystals indicated their slower nucleation and growth rates than the O and SAN crystals. The OLN and SUN crystals were produced in the similar NaCl concentration range as the SAN crystals, i.e., 0.05 M $\leq C_{NaCl} \leq$ 0.5 M. Specifically, the SUN crystals were produced at C_{NaCl} = 0.1-0.3 M, while the OLN crystals were produced at C_{NaCl} = 0.4-0.5 M. The supersaturation levels were slightly higher at C_{NaCl} = 0.1-0.3 M than at C_{NaCl} = 0.4-0.5 M due to the salting-in effect (**Figure 3.9B**). Hence, the productions of the SUN and OLN crystals were sensitive to the supersaturation level. On this note, the OLN crystals could originate from either clear solution, or from the wells already containing the O crystals. The latter resulted in the co-existence of the O and OLN crystals as evident from the light microscope image shown earlier in **Figure 3.3G**.

A further increase in the incubation time to 14 days resulted in the disappearance of the SAN crystals and the SUN crystals became the most predominant needle habit, followed by the OLN crystals. Increasing the incubation time also increased the incidence of needle crystal production, where nearly all the wells with $C_{NaCl} \leq$ 0.5 M produced either the OLN or SUN crystals after 14 days, except at the two lowest

Van concentrations investigated (i.e., 15 and 20 mg/mL) due to insufficient supersaturation. While the needle crystals exhibited highly dynamic behaviors with increasing incubation time, the O crystals remained stable after 14 days. It is worth noting that for pH 2.6, 3.6 and 5.6, all supersaturated samples showed crystallization. At pH 4.6, when C_{NaCl}=0.1-0.2 M, wells that are slightly supersaturated did not consistently show needle crystals. This is probably caused by the higher nucleation barrier at pH 4.6.

The results of the phase behavior study revealed that (1) the O crystals could be produced at all acidic pHs investigated and the O crystal production was feasible across a wide range of Van (15-50 mg/mL) and NaCl (0.4-1.0 M) concentrations, particularly at higher pH and longer incubation time, (2) the needle crystals (i.e., SAN, SUN, and OLN) were only produced at pH 5.6 in the NaCl concentration range where salting-in event took place, i.e., C_{NaCl} = 0.1-0.5 M, (3) the production of the SUN and OLN crystals required longer incubation time (7 days) than the O and SAN crystals (1 day), hence their bulk crystallization might not be practical, and (4) the crystal sizes increased with increasing supersaturation level independent of the crystal habits. In short, the O crystals emerged as the predominant crystal habit in room-temperature salting-out crystallization of Van. Therefore, their bulk crystallization performances in a batch crystallizer were examined in the next section and compared with the performance of the SAN crystals.

3.3.3 Batch crystallization of O and SAN crystals

3.3.3.1 Production yield and capacity

Batch crystallizations of the O and SAN crystals were both carried out at pH 5.6 with incubation time of 24 h and 48 h. Following the phase diagram at pH 5.6 (**Figure 3.9A**), the O crystals were prepared at 0.8 M NaCl and 50 mg/mL Van, while the SAN crystals were prepared at 0.2 M NaCl and 50 mg/mL Van. High Van concentrations were used to maximize the supersaturation levels needed to achieve reasonably high yields in the batch crystallization. Under these conditions, the supersaturation levels of the O and SAN crystal preparations were approximately equal to 5.0 and 3.3, respectively, as shown earlier in **Figure 3.9B**. The batch crystallization was first carried out in a small 1.5-mL batch volume to assess the

transferability of the results of the phase behavior study, which was performed in the μL scale, to batch crystallization, which was performed in the mL scale.

The results showed that the O and SAN crystals from the phase behavior study were successfully reproduced in the 1.5-mL batch crystallization. SEM images of the lyophilized O and SAN crystals produced by batch crystallization were presented in **Figure 3.11A** and **Figure 3.11**B, respectively. The crystallization yields of the O and SAN crystals after 24 h were equal to 50.9 ± 5.7% (w/w) and 23.0 ± 2.5% (w/w), respectively, (**Figure 3.11C**) where the lower yield of the SAN crystals were attributed to the lower supersaturation level. Increasing the batch volume to 15 mL resulted in a similar 24-h yield for the O crystals at 47.0 ± 6.8% (w/w). In contrast, the 24-h yield of the SAN crystals in the 15 mL batch crystallization was reduced more than tenfold to 3.0 ± 0.1% (w/w), which indicated a much slower growth rate of the SAN crystals at larger batch volumes.

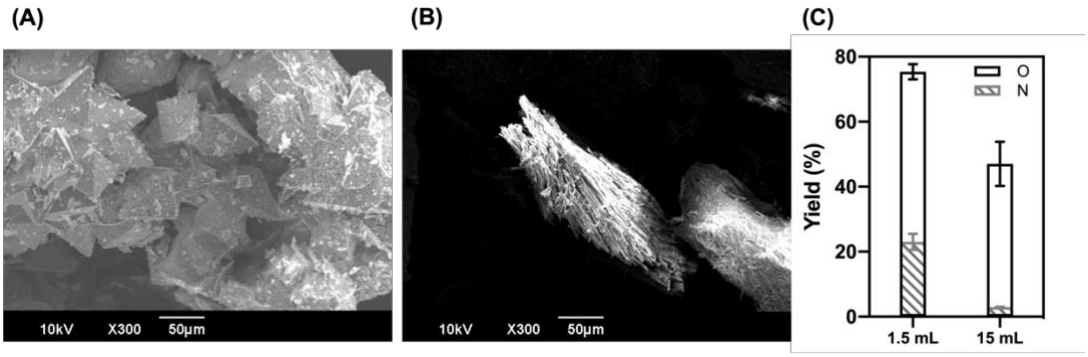

Figure 3.11 SEM images of (A) SAN crystals and (B) O crystals produced in batch crystallization; (C) comparison of production yields at 1.5 mL and 15 mL batch volumes

As the yield of the O crystal was minimally affected by the increase in the batch volume from 1.5 mL to 15 mL, poorer mixing in the 15 mL batch was unlikely to be the reason for the suppressed 24-h yield of the SAN crystals. In protein crystallization, high shear rates had been shown to suppress the crystal growth rates [305]. Following the methods described in [306], the shear rate was calculated based on **Eq. (3.5),** **((**3.6)**, (3.7),** and **(3.8**)

$$Re = \frac{\rho n d^2}{\eta_{app}} \tag{3.5}$$

$$Ne' = 70Re^{-1} + 25Re^{-0.6} + 1.5Re^{-0.2} \tag{3.6}$$

$$Ne' = \frac{P}{\rho n^3 d^4 V_L^{1/3}} \tag{3.7}$$

$$\dot{\gamma}_{eff} = L^{1/m+1}\left(\frac{P}{V_L}/K\right)^{1/m+1}\left(V_L^{\frac{1}{3}}/d\right)^{x/m+1}\left(V_L^{\frac{1}{3}}/d_0\right)^{y/m+1} \tag{3.8}$$

where Re is the Reynold's number, η_{app} is the dynamic apparent viscosity (Pa·s); ρ is the liquid density (kg/m^3); n is the shaking/stirring frequency (s^{-1}); d is the maximum shake flask and stirred tank diameter (m); Ne' is the modified Newton number (dimensionless); P is the power input (kW); $\dot{\gamma}_{eff}$ is the effective shear rate (s^{-1}); d_0 is the shaking diameter (m); K is the flow consistency index (Pa· s^m); $V_L$is the liquid volume (m^3); L is the proportionality factor (dimensionless); m is the flow behavior index (dimensionless), x and y is the exponent of the geometric number (dimensionless). The calculated value at the 15 mL batch is equal to roughly 39.0 s^{-1} compared to 18.6 s^{-1} for the 1.5 mL batch. We postulated that the increased shear rate in the 15 mL batch suppressed the growth rate of the SAN crystals, resulting in the low yield.

Due to the slow growth rate of the SAN crystals, the incubation time needed to be extended to 48 h for their production. The 48-h yield of the SAN crystals in the 15 mL batch was equal to 45.9 $\pm$ 0.5% (w/w), while the 48-h yield of the O crystals was equal to 76.8 $\pm$ 1.3% (w/w) (Table 1). The slow batch crystallization of the SAN crystals was also reported by Lee *et al.* [284] in a 13.5-mL batch, thereby necessitating the addition of an antisolvent on top of a salting-out agent. The production capacities (g/L) after 48 h incubation were determined to be equal to 43 $\pm$ 9 g/L and 27 $\pm$ 2 g/L for the O and SAN crystals, respectively.

3.3.3.2 Purity and crystal size distribution

The O crystals from the 15 mL batch exhibited a slightly higher purity than the SAN crystals at 95.4 ± 2.4% (w/w) versus 93.1 ± 1.2% (w/w), respectively (**Table 3.1**). The O crystals from the 15 mL batch exhibited Feret's diameter size of 4.3 ± 0.1 μm with Span equal to 1.72 ± 0.14 after 24 h incubation. The CSD of the O crystals showed that more than 50% of the O crystals produced were fine crystals having sizes around 2.5 μm and roughly 40% of the crystal population exhibited sizes between 5.0 and 7.5 μm (**Figure 3.12A**). After the same incubation time, the SAN crystals exhibited mean length of 9.5 ± 0.6 μm with Span equal to 1.07 ± 0.02 indicating their more uniform size distribution than the O crystals. The CSD of the SAN crystals showed evenly distributed sizes between 5 and 15 μm (**Figure 3.12B**).

Table 3.1 Summary of the O and SAN crystals' characteristics from the batch crystallization

15-mL batch crystallization	O crystals	SAN crystals
Yield (% w/w)	76.8 ± 1.3%	45.9 ± 0.5%
Production capacity (g/L)	43 ± 9	27 ± 2
Purity (% w/w)	95.4 ± 2.4	93.1 ± 1.2
Interfacial water content (w/w)	28 ± 3%	32 ± 4%

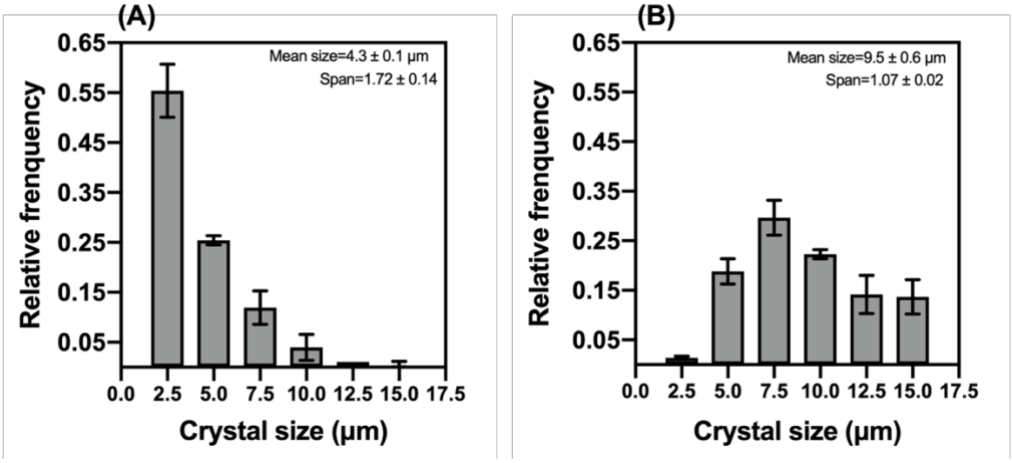

Figure 3.12 Crystal size distributions of the (A) O crystals and (B) SAN crystals from 15-mL batch crystallization

It was worth noting that after the same incubation time (i.e., 24 h), the crystals sizes from batch crystallization were smaller than the sizes observed earlier in the phase behavior study. The larger crystal sizes in the phase behavior study were not unexpected as the phase behavior study was performed under a static condition with minimal shear rates enabling the crystal growth to prosper over nucleation.

3.3.3.3 PXRD, FTIR

The PXRD analysis showed that the O and SAN crystals exhibited nearly identical PXRD patterns indicating their same internal crystal structures (**Figure 3.13A**). Strong intensity peaks, which were observed in PXRD patterns of crystalline small molecules, were absent in the PXRD patterns of Van. The PXRD patterns of the O and SAN crystals were similar to the PXRD patterns of the needle Van crystals reported previously by Lee *et al.* [284]. The FTIR analysis of the O and SAN crystal also yielded nearly identical spectra indicating their comparable peptide secondary structures (**Figure 3.13B**). The FTIR spectra showed characteristic peaks of Van at 3430, 1670, 1230, and 1070 cm^{-1}, which were attributed to N-H stretching vibration, C＝O stretching of the peptide bonds, C-O stretching of the phenols, and C-O stretching of the ether groups, respectively [307]. The peaks at 1510 and 1030 cm^{-1} were attributed to C-H bending of the aromatic group and C-O stretching of the alcohol groups, respectively.

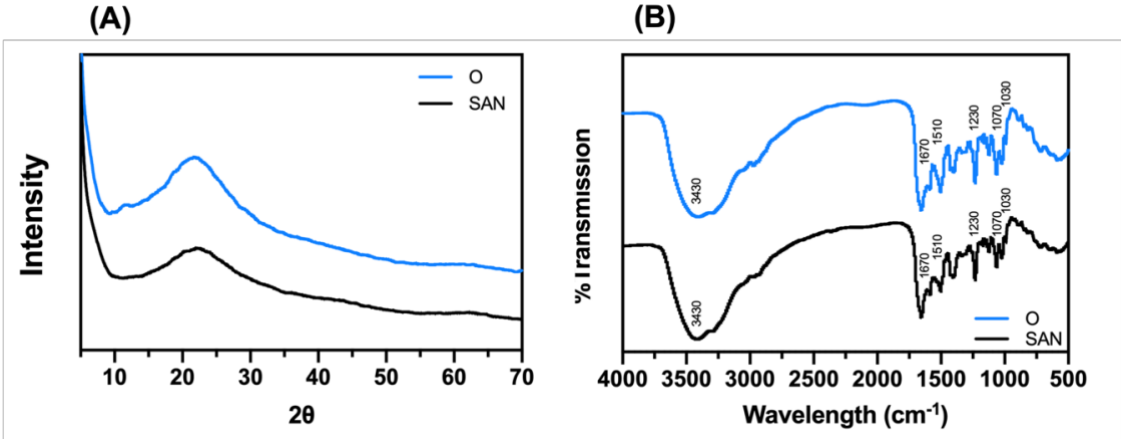

Figure 3.13 (A) PXRD patterns and (B) FTIR spectra of the O and SAN crystals from 15-mL batch crystallization

3.3.3.4 Thermal stability

The TGA analysis showed that the SAN crystal exhibited a larger mass loss (≈ 13%) upon heating below 100°C indicating their higher moisture content after lyophilization than the O crystals (≈ 10% mass loss) (**Figure 3.14A**). Both crystals remained thermally stable up to 230°C above which Van decomposition took place. The DSC thermographs of the lyophilization O and SAN crystals showed the appearance of broad endothermic peaks between 40°C and 110°C (**Figure 3.14B**). In DSC of proteins, the broad endothermic peak observed below 100°C was typically attributed to thermal denaturation events, where the protein molecules unfolded upon heating causing the loss of their stereochemical structures, thus their functions. Thermal denaturation was characterized by the thermal transition midpoint (T_m) where higher T_m indicated higher thermal stability of the proteins. T_m of the O and SAN crystals were determined to be equal to approximately 86.5°C and 69.3°C, respectively, indicating the former's higher thermal stability.

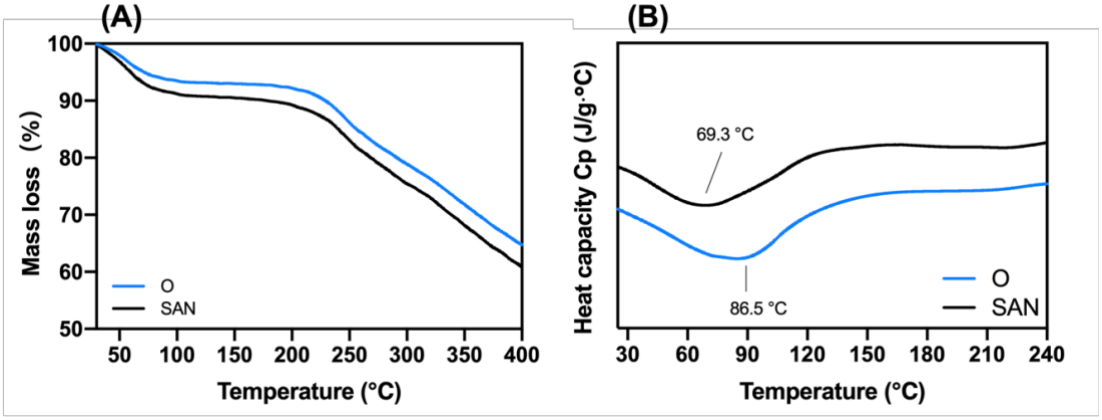

Figure 3.14 (A) TGA and (B) DSC thermographs of the O and SAN crystals from 15-mL batch crystallization

3.3.3.5 Interfacial water content

In crystallization of biomacromolecules, the large size disparity between the solute (e.g., proteins, peptides) and solvent (e.g., mostly water) molecules caused a significant number of solvent molecules to be trapped in the void spaces between the solute molecules in the crystals. In this regard, protein crystals typically contained 30-50% trapped water by mass, where the trapped water molecules could be either bound to the protein molecules or remain free [308]. Due to its large presence in the crystals, the interfacial water had significant influences on the solubility, stability, conformation, and bioactivity of protein molecules [307].

The interfacial water contents of the O and SAN crystals were determined to be equal to 28 ± 3% and 32 ± 4% (w/w), respectively (**Table 3.1**), which translated to 0.385 ± 0.048 g and 0.487 ± 0.077 g of trapped water per one gram of Van, respectively. The numerical variations between the interfacial water contents of the O and SAN crystals were determined to be not statistically significant. The interfacial water content of the glycopeptide crystals at roughly 30% (w/w) was found to be comparable to the interfacial water content of protein crystals.

3.3.3.6 Dissolution characteristics and antibiotic activity

The SAN crystals exhibited faster Van dissolution rates than the O crystals at the three pHs investigated (i.e., pH 1.2, 4.5, and 6.8) (**Figure 3.15**). The faster dissolution

rate of the SAN crystals could be attributed to their larger specific surface areas, which were calculated to be approximately equal to 1.15 m^2/g versus 0.50 m^2/g for the O crystals. The dissolution rates of both crystals were found to slow down with increasing pH due to the decrease in the Van solubility as the pH becomes nearer to the pI of Van. Specifically, approximately 90%, 80%, 65% of the SAN crystals were dissolved after 20 min at pH 1.2, 4.5, and 6.8, respectively. Whereas approximately 75%, 50%, and 45% of the O crystals were dissolved after the same period at pH 1.2, 4.5, and 6.8, respectively. The numerical variations between the dissolution rates of the O and SAN crystals were determined to be statistically significant as indicated in **Figure 3.15**.

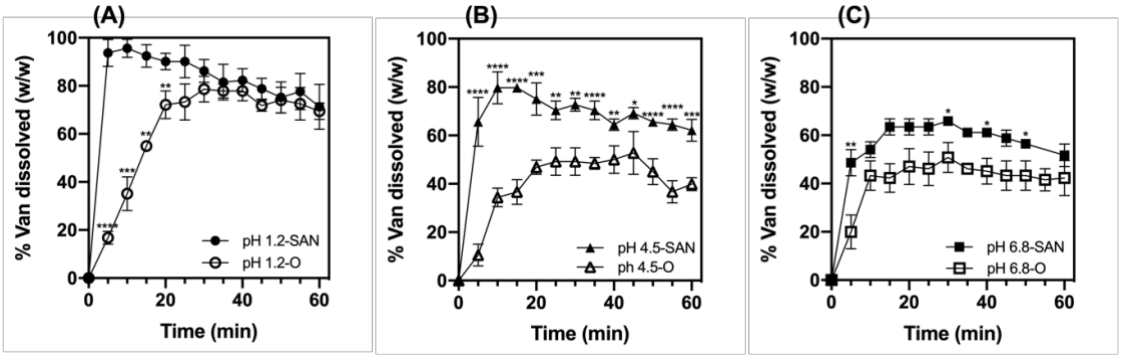

Figure 3.15 Van dissolution profiles of the O and SAN crystals at (A) pH 1.2; (B) pH 4.5; (C) pH 6.8 (ANOVA statistical significances for variations in the dissolution rates between the O and SAN crystals *p < 0.1, ** p< 0.01, *** p < 0.001, **** p < 0.0001)

The % dissolution of Van was found to plateau upon reaching the peak value, thereby complete dissolution of the Van crystals was not observed. In fact, for the SAN crystals, a statistically significant decrease in the % dissolution after reaching the peak value was observed over time at the three pHs investigated, i.e., pH 1.2 ($p < 0.001$), pH 4.5 ($p < 0.0001$), and pH 6.8 ($p < 0.01$). Whereas for the O crystals, the decrease in the % dissolution after reaching the peak value was only observed at pH 1.2 and 4.5 ($p < 0.01$). As the dissolution tests were carried out at below neutral pH, the decrease in the % dissolution over time was attributed to widely reported Van degradation in acidic conditions [297, 309, 310]. The use of phosphate buffer for the

dissolution tests at pH 6.8 also contributed to Van degradation as phosphate ions were found to hasten the Van degradation at pH between 3-7 [297].

Lastly, despite their distinct dissolution profiles, the O and SAN crystals exhibited the same MIC against *S. aureus* at 1 μg/mL with OD_{600} equal to 0.056 ± 0.008 for both crystals. The MIC values of the O and SAN crystals fell within the range of the typical MIC values of Van against *S. aureus* (i.e., 0.5-2 μg/mL) [311].

3.4 Conclusions

The phase behavior study revealed the O crystals as the predominant crystal habit in salting-out room-temperature crystallization of Van. The O crystals were produced across the range of pH (2.6 to 5.6), Van (15 to 50 mg/mL), and NaCl concentrations (0.4 to 1.0 M) investigated. The needle crystal formation was largely avoided except at pH 5.6 and at NaCl concentrations in which the salting-in event took place (0.1 to 0.5 M). Increasing the incubation time beyond 24 h resulted in a wider range of workable crystallization conditions for both the O and needle crystals. The outcomes of the phase behavior study were successfully transferred to batch crystallization in a shaking vessel. The batch crystallization's yield and production capacity of the O crystals were significantly higher than the SAN crystals due to the latter's slower growth rate under a high shear crystallization condition. The O crystals exhibited superior thermal stability as characterized by their higher denaturation temperature, while the SAN crystals exhibited a more uniform size distribution. Their distinct crystal habits led to their distinct dissolution profiles (i.e., slower dissolution rates for the O crystals) due to variations in their specific surface areas. The impacts of the distinct dissolution profiles of the two crystal habits on the pharmacokinetics of Van will need to be investigated in the future. The O and SAN crystals nevertheless were similar in terms of their purity, internal crystal structure (from PXRD), peptide secondary structure (from FTIR), interfacial water content, and antibiotic activity. The future research direction will be to explore different strategies (e.g., seeding, polymer additives) to speed up the crystallization of the O crystals aimed at improving the production yield and capacity.

CHAPTER 4 A COMPARATIVE STUDY OF ANTISOLVENT VERSUS SALTING-OUT PRECIPITATIONS OF GLYCOPEPTIDES: PRECIPITATION EFFICIENCY AND PRODUCT QUALITIES

This chapter has been submitted as **Siyu Pu,** Kunn Hadinoto, A Comparative Study of Antisolvent versus Salting-Out Precipitations of Glycopeptides: Precipitation Efficiency and Product Qualities, Powder Technology, Volume 415, 2023, 118181.

4.1 Introduction

Bioactive peptides represent an emerging class of pharmaceuticals showing distinct and often superior therapeutic traits from small-molecule drugs and protein biologics [3]. Bioactive peptides typically are a group of peptides containing less than 50 residues [312]. They are manufactured in the industrial scale by fermentation, enzyme proteolysis, or chemical synthesis, followed by downstream processing (DSP) steps to isolate and purify the peptides. Industrial DSP methods for bioactive peptides include chromatography, precipitation, ultrafiltration, or serial combinations of these methods [4]. Among these methods, affinity or ion-exchange chromatography has almost exclusively been the workhorse in DSP of bioactive peptides, similar to its prominent role in DSP of therapeutic proteins (e.g., monoclonal antibody) [5].

While chromatography has been well established to be a highly effective DSP method for both bioactive proteins and peptides, it bears shortcomings in its high operating costs due to costly adsorbents and limited production capacity, which fails to meet the augmented titers from the upstream production [6]. For this reason, the viability of non-chromatography purification methods to be the workhorse DSP method of bioactive proteins/peptides have been actively studied [7]. In this regard, besides precipitation and ultrafiltration, other non-chromatography purification methods for bioactive peptides include aqueous two-phase systems [86], magnetic solid phase extraction [11], and deep eutectic solvent extraction [313].

Among the non-chromatography methods, precipitation has been one of the most widely used DSP methods owed to its (1) simple and inexpensive operation, (2) good scalability with high throughput, and (3) versatility, where it can be employed at different purification stages from bulk recovery to selective isolation, where it is often used in conjunction with chromatography [4]. In precipitation, the solubility of the target proteins (or peptides) is reduced by manipulating their environmental conditions (e.g., pH, ionic strength, dielectric constant), resulting in the formation of a new solid phase. When the resulting solid phase exhibits a highly ordered molecular arrangement, the process is often referred as crystallization [252].

Common precipitation methods for proteins (also peptides) include isoelectric precipitation, salting out, and antisolvent precipitation using organic solvents [20]. In isoelectric precipitation, pH of the protein solution is adjusted to near the protein's isoelectric point (pI) at nearly zero ionic strength. As the protein's surface charges were reduced near the pI, the repulsive electrostatic forces among the protein molecules are diminished, resulting in increased hydrophobic protein-protein interaction, which ultimately leads to precipitation of the protein [24]. In salting out, the precipitation takes place at high ionic strength due to competitions between the salt ions and protein molecules in interacting with the solvent molecules (i.e., water), resulting in reduced solvent-solute interactions and consequently increased hydrophobic solute-solute interactions leading to precipitation [47].

In antisolvent precipitation, dielectric constant of the protein solution was lowered upon the addition of organic solvent, resulting in increased attractive electrostatic forces among the protein molecules, hence their lower solubility [152]. Moreover, polar groups of the organic solvent compete with water molecules to interact with polar groups of the protein, while simultaneously hydrophobic groups of the organic solvent disrupt intramolecular interaction of the protein. Both events resulted in lower protein solubility that leads to precipitation [6].

While antisolvent precipitation is ideal for large-scale protein purification as the solvent can be effectively recycled by distillation, the use of organic solvents for protein/peptide precipitation may lead to protein denaturation. For example, antisolvent precipitation using dimethyl sulfoxide (DMSO) at high concentrations

was shown to cause denaturation of lysozyme due to irreversible disruption of the protein's tertiary structures. Therefore, the operating condition (e.g., temperature, solvent to solute ratio) has to be carefully determined to avoid protein denaturation.

Different precipitation methods (i.e., isoelectric, salting-out, and antisolvent) have been shown to affect not only the precipitation efficiency (i.e., fraction of solute that precipitates), but also qualities of the precipitate proteins (e.g., solubility, bioactivity, stability, purity) [314]. For example, salting-out precipitation with zinc sulfate produced a superior efficiency in plasma protein precipitation compared to antisolvent and isoelectric precipitations [153]. In precipitation of peanut proteins, isoelectric precipitation produced precipitates with superior solubility and stability than those produced by antisolvent precipitation [150]. Moreover, the presence of salt ions used in salting-out precipitation was found to reduce the stability of precipitated human growth hormone, which was not observed in other precipitation methods [178].

Proteins were used as the principal model for studies on the precipitation of biological macromolecules [21]. Similar approaches as those used on protein precipitation have been used for peptide precipitation, despite the order-of-magnitude difference in their molecular weights, often resulting in high process uncertainties [22, 23]. To the best of our knowledge, very few studies have evaluated the effects of different precipitation methods on the efficiency and physical qualities of bioactive peptides. One such study by Leonil et al. [315] investigated the difference in the yields between salting-out and isoelectric precipitation methods in hydrophobic peptide precipitation from protein hydrolysate. Product qualities from the different precipitation methods, however, were not examined.

In the present work, we carried out a comparative study on the precipitation efficiency and the product qualities between antisolvent and salting-out methods in the precipitations of bioactive peptides. Vancomycin hydrochloride (Van) - a clinically important glycopeptide antibiotics widely used for the treatment of infections caused by MRSA (methicillin-resistant *Staphylococcus aureus*) and penicillin-resistant *pneumococci* [282] - was used as the model bioactive peptide. In our previous study [252], we had determined the optimal conditions (e.g., pH, salt concentration) for salting-out precipitation of Van, where stable crystalline Van

precipitates were found to be the predominant products. Stand-alone antisolvent precipitation of Van, on the other hand, had not been attempted before. Previous studies that used organic solvents to precipitate Van used the solvents to expedite the rate of salting-out and cooling precipitations [284, 316].

First, we carried out a high-throughput μL-scale phase behavior study of antisolvent Van precipitation using acetone as the antisolvent with the objective of determining the operating conditions in which stable precipitates were produced. The conditions investigated were (1) pH, (2) Van concentration, (3) acetone to Van concentration ratio, and (4) incubation time. Second, based on the operating condition identified in the phase behavior study, we performed mL-scale batch antisolvent precipitation of Van, and subsequently compared the precipitates produced with the crystalline Van precipitates from salting-out precipitation. The antisolvent Van precipitates were compared to the salting-out Van precipitates in terms of their (a) production yield, (b) morphology (i.e., size, shape), (c) purity, (d) internal molecular structure, (e) thermal stability, (f) dissolution characteristics, and (g) antimicrobial activity.

Third, in addition to examining the precipitate qualities right after preparation, we also examined the solid-state stability of the antisolvent Van precipitates after one and two months of accelerated storage. In this regard, peptides are generally more prone to denaturation than proteins because of peptides' inability to protect the reactive side chains in the interior of their globular structures, hence leaving the side chains exposed to the surrounding environment [107]. This is particularly true for precipitates with a lower degree of crystallinity because the dense molecular packing of crystalline structures can reduce the precipitates' interactions with their surrounding environment [165].

4.2 Materials and Methods

4.2.1 Materials

Van (United States Pharmacopeia (USP) grade, ≥ 900 μg/mg) was purchased from Duly Biotech Co. Ltd. (Nanjing, China). Acetone (≥ 99.8%) and hydrochloric acid (HCl, 37%) were purchased from Fisher Scientific (Singapore) and VWR

(Singapore), respectively. Ethanol (≥ 99.5%), glycine (≥ 99%), glacial acetic acid, paraffin oil (puriss., Ph. Eur.), potassium dihydrogen phosphate (KH_2PO_4), sodium hydroxide (NaOH), and sodium acetate (≥ 99%) were purchased from Sigma Aldrich (Singapore). Mueller Hinton Broth (MHB) and phosphate buffered saline (PBS, pH 6.8) were purchased from BD Diagnostics (Singapore). Bacterial species *Staphylococcus aureus* 29213 was procured from American Type Culture Collection (ATCC).

4.2.2 Methods

4.2.2.1 Phase behavior study of antisolvent Van precipitation

The phase behaviors of antisolvent Van precipitation were investigated in 96-well plates (Greiner Bio-One, CELLSTAR®, Austria) at room temperature (22.5 ± 0.5 °C) using acetone as the precipitant as Van was practically insoluble in acetone. The investigations were carried out in triplicates at four different pH values (i.e., 2.6, 3.6, 4.6, and 5.6) and at different Van and acetone concentrations. 50 mM acetate buffer solutions were prepared and adjusted to pH 3.6, 4.6, and 5.6 by addition of HCl. For investigation at pH 2.6, 50 mM glycine-HCl buffer was prepared. A two-point calibrated pH meter (Mettler Toledo™ EL20 Benchtop pH Meter) was used for pH measurement. Both buffer solutions were vacuum filtered prior to their use in 0.2-µm PES membrane filters (Nalgene, VWR, Singapore).

Stock solutions of 50 mg/mL Van were prepared in the buffer solutions of four different pH values. The stock solutions were syringe filtered through 0.22-µm Whatman® PTFE filters (Whatman, VWR, Singapore) prior to their use. The Van stock solutions were then diluted with their respective buffer solutions to produce eight Van solutions with concentrations in the range of 15 to 50 mg/mL. For each pH value investigated, 50 µL of the Van solution was added to the wells of the 96-well plate, where Van solution with the highest initial Van concentration (i.e., 50 mg/mL) was at the top row and Van solution with the lowest initial Van concentration (i.e., 15 mg/mL) was at the bottom row.

Afterwards, acetone was added to each well at eleven different acetone-to-Van volume ratios ($R_{Ace/Van}$) in the range of 0.25 to 5.0, with increasing $R_{Ace/Van}$ from

the left to the right columns. The leftmost wells which contained no acetone were used as the controls. Hence, 96 wells of different concentrated Van solutions and different acetone contents were produced at each pH. The Van concentration in each well after the addition of acetone was provided in **Table 4.1**.

Each well was then covered by 0.1 mL paraffin oil and the plate was subsequently sealed with Corning® microplate sealing tape (Sigma Aldrich, Singapore) to prevent evaporation. The 96-well plate was then incubated for 7 days in a chamber maintained at 22.5 ± 0.5°C. On days 1, 2, and 7, the wells in the plate were examined under light microscope (CKX41, Olympus, Japan) at 400 × magnification. The phase behavior in each well was characterized by whether clear solution or precipitates of different characteristics (e.g., light, heavy, gelation, crystals) were formed.

Table 4.1 Van concentration in each well after mixing with acetone at different $R_{Ace/Van}$ (The calculated acetone fraction is shown under the respective acetone ratio.)

$R_{Ace/Van}$ / Initial Van concentration (mg/mL)	0 (0)	0.25 (0.20)	0.5 (0.33)	1.0 (0.50)	1.5 (0.60)	2.0 (0.67)	2.5 (0.71)	3.0 (0.75)	3.5 (0.78)	4.0 (0.80)	4.5 (0.82)	5.0 (0.83)
50	50.0	40.0	33.3	25.0	20.0	16.7	14.3	12.5	11.1	10.0	9.1	8.3
45	45.0	36.0	30.0	22.5	18.0	15.0	12.9	11.3	10.0	9.0	8.2	7.5
40	40.0	32.0	26.7	20.0	16.0	13.3	11.4	10.0	8.9	8.0	7.3	6.7
35	35.0	28.0	23.3	17.5	14.0	11.7	10.0	8.8	7.8	7.0	6.4	5.8
30	30.0	24.0	20.0	15.0	12.0	10.0	8.6	7.5	6.7	6.0	5.5	5.0
25	25.0	20.0	16.7	12.5	10.0	8.3	7.1	6.3	5.6	5.0	4.5	4.2
20	20.0	16.0	13.3	10.0	8.0	6.7	5.7	5.0	4.4	4.0	3.6	3.3
15	15.0	12.0	10.0	7.5	6.0	5.0	4.3	3.8	3.3	3.0	2.7	2.5

4.2.2.2 Van solubility in buffer solution at different R_(Ace/Van) and pH

At each pH investigated (i.e., pH 2.6, 3.6, 4.6, and 5.6), the solubility of Van in buffer solutions of different acetone concentrations was determined in triplicates. Briefly, 50 µL of 50 mg/mL Van buffer solution was mixed with acetone at different $R_{Ace/Van}$ (i.e., 0.25 to 5.0) in 0.6-mL Corning® Eppendorf tubes (VWR, Singapore). The Van solution in the tubes was covered with paraffin oil to prevent evaporation and then incubated in a shaking incubator at 22.5 ± 0.5°C for 7 days. On days 2 and 7, the Van solution was centrifuged at 14,500×g for 10 min (Sorvall 16R, Thermo Fisher Scientific, USA) to remove undissolved Van. The Van concentration in the supernatant was subsequently determined to characterize the Van solubility ($C_{Solubility}$).

The Van concentration in the supernatant was determined by high performance liquid chromatography (HPLC) (1260 Infinity II, Agilent Technologies, Singapore) using ZORBAX Eclipse Plus C18 column (250 × 4.6 mm, 5-µm particle size) at detection wavelength of 280 nm. The mobile phase was 15% (v/v) aqueous ethanol solution with 0.1% (w/v) acetic acid at flow rate of 0.5 mL/min, resulting in Van retention time of approximately 4.5 min.

4.2.2.3 Batch precipitation of Van

Batch antisolvent precipitation of Van was carried out in triplicates at pH 5.6 and at $R_{Ace/Van}$= 1.5, 2.0, 2.5, 3.0, 3.5, 4.0, 4.5, and 5.0. Briefly, 0.5 mL of 50 mg/mL Van solution in acetate buffer (pH 5.6) was mixed with acetone at different $R_{Ace/Van}$ in a sealed glass tube placed in a shaking incubator maintained at 22.5 ± 0.5°C for 48 h. After 24 h and 48 h, the precipitates were recovered by centrifugation (14,500×g for 10 min) and lyophilized at -52°C and 0.05 mbar for 24 h in Alpha 1-2 LD Plus freeze dryer (Martin Christ, Germany) for characterizations. The concentration of Van in the supernatant was determined by HPLC as previously described.

The yield was calculated according to **Eq. (3.1**) where C_i and C_o represented the initial and final concentration of Van, respectively. Batch salting-out precipitation was carried out in a sealed glass tube at 22.5 ± 0.5°C using NaCl as the precipitant.

The optimal salting-out condition determined in [252] was used (i.e., pH 5.6, 50 mg/mL Van, 0.8 M NaCl, and 48 h incubation time). The salting-out precipitates were recovered by centrifugation and lyophilized following the same procedures described above.

4.2.2.4 Physical characterizations of Van precipitates

The morphology of the Van precipitates (both antisolvent and salting-out precipitates) after lyophilization was examined by scanning electron microscope (SEM) (JSM 6390LA, JEOL, Japan). The precipitates were coated with platinum at 20 mA for 120 s prior to SEM. The particle size was characterized by ImageJ software (NIH, USA) with a minimum of 200 particle counts. The purity (% w/w), which was defined as the mass of Van per unit mass of the precipitates, was determined by dissolving a known amount of Van (i.e., 1 mg) in acetate buffer (pH 5.6) after which the soluble Van concentration was determined by HPLC as described above.

The crystallinity of the Van precipitates was examined by powder x-ray diffraction (PXRD) analysis performed between 5° and 70° with a step size of 0.02°/s using D2-Phaser X-ray Diffractometer (Bruker, Germany). The PXRD data were compared with the reference PXRD spectrum of Van available in worldwide Protein Data Bank (https://www.wwpdb.org) [317]. The reference PXRD spectrum was extracted using Mercury (2022.1.0) software of Cambridge Crystallographic Data Centre.

Fourier transform infrared spectroscopy (FTIR) analysis was carried out on the Van precipitates between 450 cm^{-1} and 4000 cm^{-1} at 1 cm^{-1} spectral resolution (Spectrum One FTIR, PerkinElmer, USA). Thermal stability of the Van precipitates was determined by thermogravimetric analysis (TGA) (TGA/DSC 1, Mettler Toledo, USA) performed at heating rate of 10°C/min under nitrogen atmosphere between 25°C and 400°C. Denaturation temperature of the Van precipitates was characterized by cryogenic differential scanning calorimetry (DSC) (822e, Mettler Toledo, USA) performed at heating rate of 5°C/min under nitrogen atmosphere between -65°C to 400°C.

4.2.2.5 Dissolution rates

Dissolution rates of the lyophilized Van precipitates under a sink condition were examined in triplicates at three pH values, i.e., pH 1.2, 4.5, and 6.8, representing the typical pHs of fasted stomach, fed stomach, and intestines, respectively [291]. The dissolution mediums at pH 1.2, 4.5, and 6.8 were prepared from 0.1 N HCl, acetate buffer, and PBS, respectively, adjusted to the target pHs by adding HCl. The sink condition was defined by USP as a dissolution condition in which the maximum drug concentration in the medium was less than 1/3 of the thermodynamic saturation solubility of drug (C_{Sat}) in the said medium [318]. C_{Sat} values of Van in the dissolution mediums with pH 1.2, 4.5, and 6.8 were determined to be equal to approximately 146, 100, and 90 mg/mL, respectively, at 37°C.

Briefly, lyophilized Van precipitates were added to 40 mL of the dissolution medium placed in a shaking incubator maintained at 37°C. At specific time points over 60 min, 1 ml aliquot was withdrawn, and the same volume of fresh medium was added as replenishment. Next, the aliquot was centrifuged at 14,500×g for 10 min and Van concentration in the supernatant was determined by HPLC as previously described. The statistical significance of the dissolution profiles was analyzed within groups by one-way analysis of variance (ANOVA) in Microsoft Excel. The statistical significance of the difference between the dissolution profiles of the antisolvent and salting-out Van precipitates were analyzed by the least significant difference (LSD) test at p-value equal to 0.05.

4.2.2.6 Antimicrobial activity

Antimicrobial activity of the Van precipitates was characterized in terms of the minimum inhibitory concentration (MIC) against *S. aureus* ATCC 29213 bacteria. The MIC was determined in triplicates by the microbroth dilution method described in [319]. Briefly, overnight inoculum of *S. aureus* adjusted to 0.5 McFarland standards was diluted in MHB to produce 1.0×10^6 CFU/mL. Next, 200 µL of the bacterial cell suspension was placed in the wells of a 96-well plate. Afterwards, 200 µL solution of Van precipitates in deionized water were added to the wells at Van concentrations in the range of 0 to 256 µg/mL. The plate was incubated at 37°C for 24 h. Wells without Van and without bacteria were used as the positive and negative

controls, respectively. The MIC was characterized by the optical density of the cell suspension at 600 nm (OD_{600}) less than 0.1, which signified zero visible bacterial growth. The OD_{600} was determined using microplate reader (Synergy HT, Biotek, USA).

4.2.2.7 Accelerated storage stability

Storage stability of the antisolvent Van precipitates was examined by storing the lyophilized precipitates in an open container inside a desiccator under an accelerated storage condition (i.e., 40°C and 75% relative humidity) for two months. The 75% relative humidity (RH) was generated inside the desiccator by placing an open container of saturated NaCl solution at 40°C. The two-month accelerated storage was roughly equivalent to six-month ambient storage (i.e. 25°C and 55% relative humidity) [320]. The storage stability after one month and two months of accelerated storage was examined by PXRD, FTIR, TGA, and DSC analysis of the stored samples.

4.3 Results and discussion

4.3.1 Van solubility in buffer solution at different R_(Ace/Van) and pH

The solubility of Van in acetone at different $R_{Ace/Van}$ and pH was characterized to determine the supersaturation level in the phase behavior study. Recognizing that (1) the solubility of Van was at its lowest at pH equal or near to its pI (≈ 8.1) [296] and (2) Van in buffer solution was known to be most stable at pH between 3.0 and 5.7 [297], the present work investigated Van solubility at pH 2.6, 3.6, 4.6, and 5.6. The results showed that Van solubility equilibrated only after 7 days. A monotonically decrease in the Van solubility from around 45 mg/mL in the absence of acetone to as low as 0.5 mg/mL at $R_{Ace/Van}$ = 5 was observed at all pH with increasing $R_{Ace/Van}$ (**Figure 4.1**). The antisolvent effect of acetone was most evident at pH 5.6 at which the Van solubility decreased sharply from around 45 mg/mL without acetone to around 25 mg/mL at the lowest $R_{Ace/Van}$ investigated (i.e., 0.5).

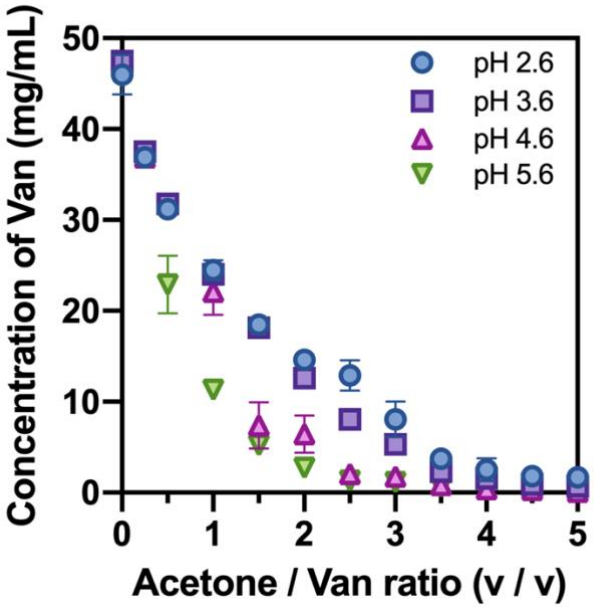

Figure 4.1 Van solubility in buffer solutions at different pH and R_(Ace⁄Van)

The Van solubility was found to be pH-dependent, where the solubility was lower at pHs 4.6 and 5.6 than at pHs 2.6 and 3.6, particularly at lower $R_{Ace/Van}$ (< 3.0). The lower Van solubility at higher pHs was not unexpected as the solubility decreased as the pH approached the pI. From these solubility data, the supersaturation levels of Van in the phase behavior study were calculated. Herein the supersaturation level was expressed as $C/C_{Solubility}$, where C was the Van concentration in the 96-well plate after mixing with acetone. Owed to the abovementioned lower Van solubility at higher pH, the supersaturation levels increased with increasing pH as presented later in **Figure 4.3B** to **Figure 4.6B**.

4.3.2 Phase behavior of antisolvent Van precipitation

The phase behaviors of antisolvent Van precipitation were characterized using the classification method for protein precipitation developed by Bergfors [321]. Using this method, the phase behaviors were classified by light microscopy as either clear solution (**Figure 4.2A**), or precipitates, where the precipitates could be in the form of (1) light precipitates (**Figure 4.2B**), (2) heavy precipitates (**Figure 4.2C**), (3) gelatinous precipitates (**Figure 4.2D**), (4) precipitates with well-defined edges

(**Figure 4.2E**, **Figure 4.2G**), and (5) crystalline precipitates (**Figure 4.2F**, **Figure 4.2H**).

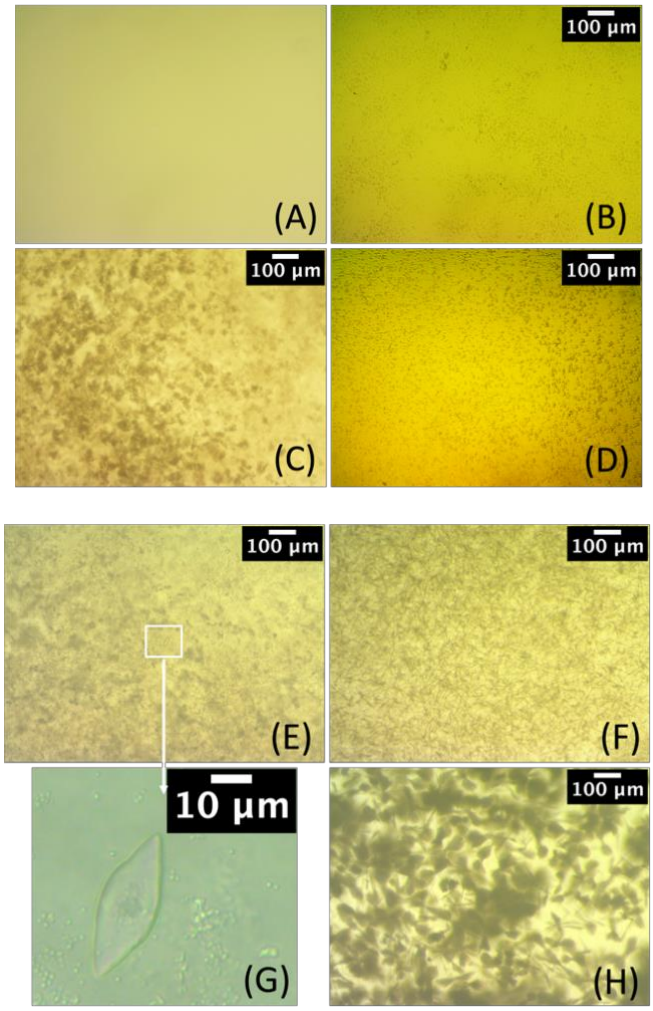

Figure 4.2 Light microscope images of (A) clear solution; (B) light precipitates; (C) heavy precipitates; (D) gelatinous precipitates; (E) precipitates with edges; (F) stand-alone needle crystals; (G) enlarged image of precipitates with edges; (H) sea urchin-like shaped crystals

In this regard, light precipitates were defined as sporadically sighted light-colored precipitates typically observed at low nucleation rates, whereas heavy precipitates referred to a large presence of dark-colored precipitates, which partially or fully blocked the lights. Gelatinous precipitates were characterized by a textural

change in the solution, which was often discernible in light microscopy by the appearance of many small droplets attributed to phase separation [321]. Precipitates with edges and crystalline precipitates were characterized by their more well-defined individual shapes and larger individual particle size compared to particles in the heavy precipitates. Crystalline precipitates produced by antisolvent precipitation exhibited needle habits, and they existed as either stand-alone needle crystals (**Figure 4.2F**), or sea urchin-like shaped crystals (**Figure 4.2G**). For comparison, the predominant crystalline precipitates in salting-out precipitation exhibited octahedral habit [252].

At pH 2.6, the phase diagram in **Figure 4.3A** indicated that light precipitates appeared after 1 day incubation in the wells with $R_{Ace/Van}$ > 3.0, where the supersaturation levels were at least equal to ≈ 1.5 or higher (**Figure 4.3B**). At high supersaturation levels (≈ > 4), which was observed at high initial Van concentrations (> 30 mg/mL) and high $R_{Ace/Van}$ (> 3.0), heavy precipitates were formed. Gelation was observed in one well at $R_{Ace/Van}$ = 3.5 and initial Van concentration of 20 mg/mL. The formation of light precipitates became more prevalent at longer incubation time, where light precipitates were formed after 7 days in the wells with $R_{Ace/Van}$ < 3.0. The lower supersaturation levels in these wells resulted in slower nucleation rates, causing the precipitates to form only after longer incubation time.

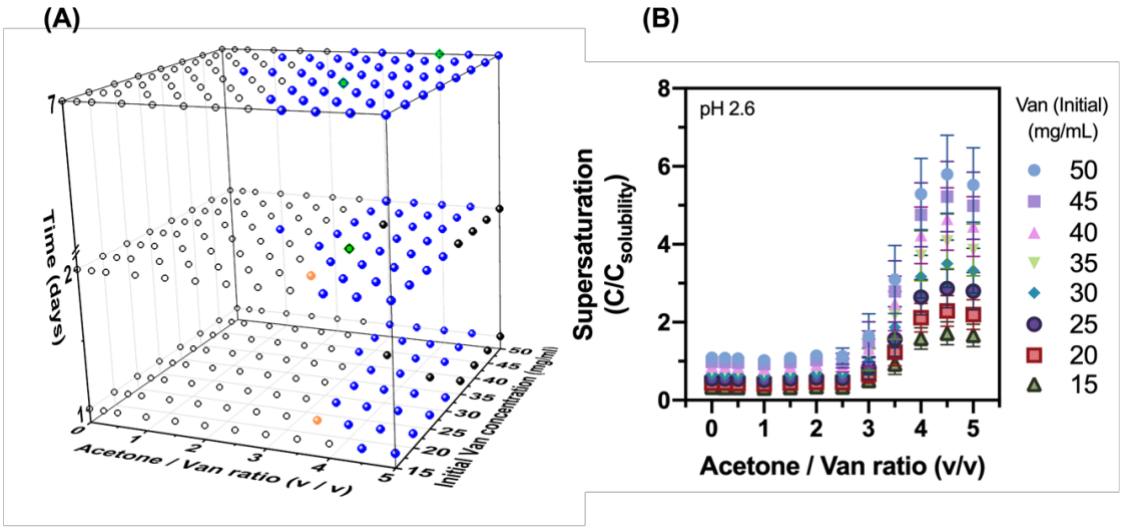

Figure 4.3 (A) Phase diagram of antisolvent Van precipitation at pH 2.6 (unfilled circles: clear solution; orange circles: gelatinous precipitates; blue circles: light precipitates; black circles: heavy precipitates; green diamond: crystal-like structure with edges); (B) Van supersaturation levels at pH 2.6

Besides increased formation of light precipitates, precipitates with edges began to appear in one to two wells at longer incubation time. Interestingly, the heavy precipitates disappeared after 7 days incubation where they were transformed to light precipitates. The heavy-to-light transformation of the precipitates could only be caused by re-dissolution of the heavy precipitates into the solution due to their instability [198]. In this regard, the Ostwald's law of stages stated that the least stable phase was typically isolated first in precipitation, after which the unstable phase was transformed to the more thermodynamically stable phase over time [304]. It was worth noting that even with a high supersaturation driving force, light precipitates were still the predominant products at pH 2.6, which indicated that most of Van remained in the solution. Hence, the precipitation propensity at pH 2.6 was low despite the relatively high supersaturation levels above unity.

At pH 3.6, similar phase behaviors were observed after 1 day incubation, where light and heavy precipitates were formed in the wells with high supersaturation levels (**Figure 4.4A**). The number of wells with heavy precipitates was slightly increased compared to at pH 2.6, which was not unexpected given the higher overall supersaturation levels at pH 3.6 due to the lower Van solubility at pH 3.6, particularly at $R_{Ace/Van} > 3.0$ (**Figure 4.4B**). Also similar to the observation at pH 2.6, the numbers of wells with precipitate formation were increased at longer incubation time.

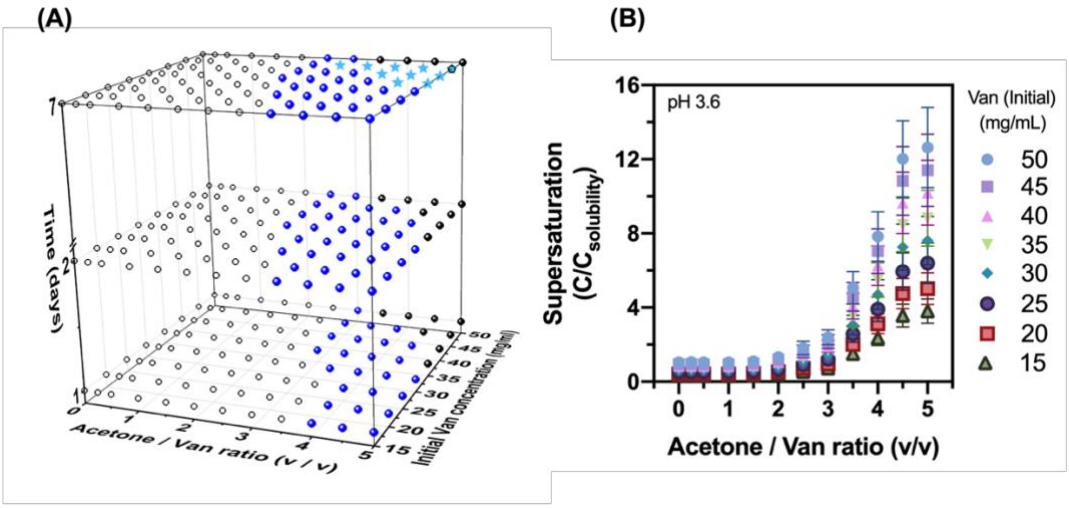

Figure 4.4 (A) Phase diagram of antisolvent Van precipitation at pH 3.6 (unfilled circles: clear solution; blue circles: light precipitates; black circles: heavy precipitates; blue stars: stand-alone needle crystals; (B) Van supersaturation levels at pH 3.6

The light and heavy precipitates in some of the wells were transformed to stand-alone needle crystals after 7 days incubation. This transformation was observed in the wells with high initial Van concentrations ($\geq$ 35 mg/mL), where the supersaturation levels were among the highest. The slow appearance of the crystalline precipitates indicated that a secondary precipitation process took place after nucleation, which was the primary precipitation process. The light and heavy precipitates either acted as seeds for crystals formation, or re-dissolved due to Ostwald ripening to precipitate again in the form of a more stable phase [134]. Compared to pH 2.6, the phase behaviors at pH 3.6 showed an improvement in the precipitation propensity as light precipitates were no longer the predominant products at high supersaturation levels.

At pH 4.6, a significant increase in the number of wells with heavy precipitates was observed after 1 day incubation (**Figure 4.5A**) attributed to the lower Van solubility, hence higher supersaturation level, with increasing pH (**Figure 4.5B**). Not unexpectedly, the same observation was made at pH 5.6 (**Figure 4.6A**, **Figure 4.6B**). At both pHs, the heavy precipitates in some of the wells slowly transformed to crystalline precipitates (both needle and sea-urchin like habits) after 7 days of incubation. The same trend was observed previously at pH 3.6. For the most part, the

heavy-to-crystalline transformation of the precipitates at pHs 4.6 and 5.6 occurred in the wells with $2.0 \leq R_{Ace/Van} \leq 3.0$. The supersaturation levels in these wells lay in the midrange of the supersaturation levels investigated (i.e., ≈ 4 to 6 for pH 4.6 and ≈ 8 to 11 for pH 5.6). Notably, at pH 5.6, the crystalline precipitates could be observed as early as on day 2 in a few wells signifying the faster secondary precipitation process at pH 5.6.

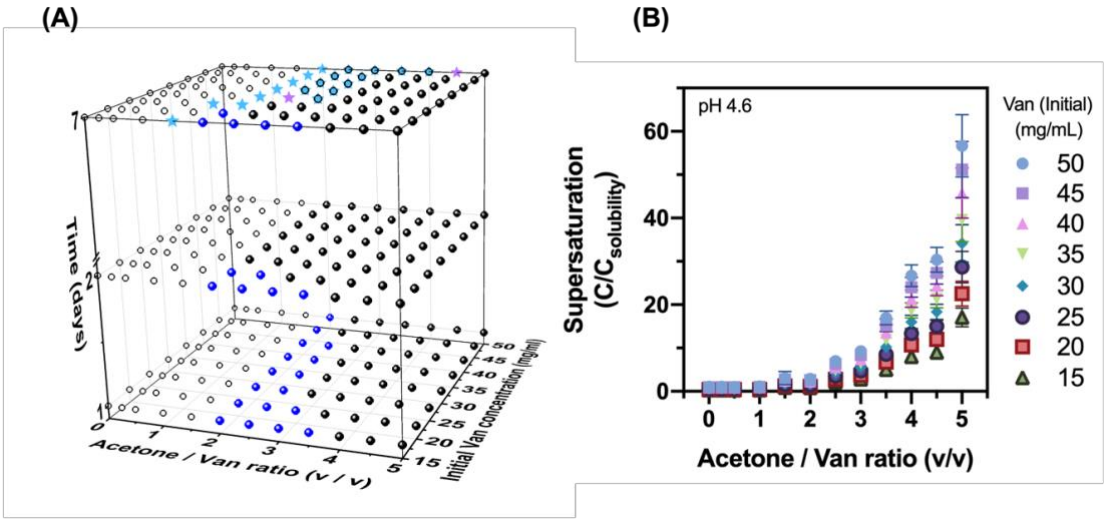

Figure 4.5 (A) Phase diagram of antisolvent Van precipitation at pH 4.6 (unfilled circles: clear solution; blue circles: light precipitates; black circles: heavy precipitates; blue stars: stand-alone needle crystals; purple stars: sea urchin-like shaped crystals; (B) Van supersaturation levels at pH 4.6

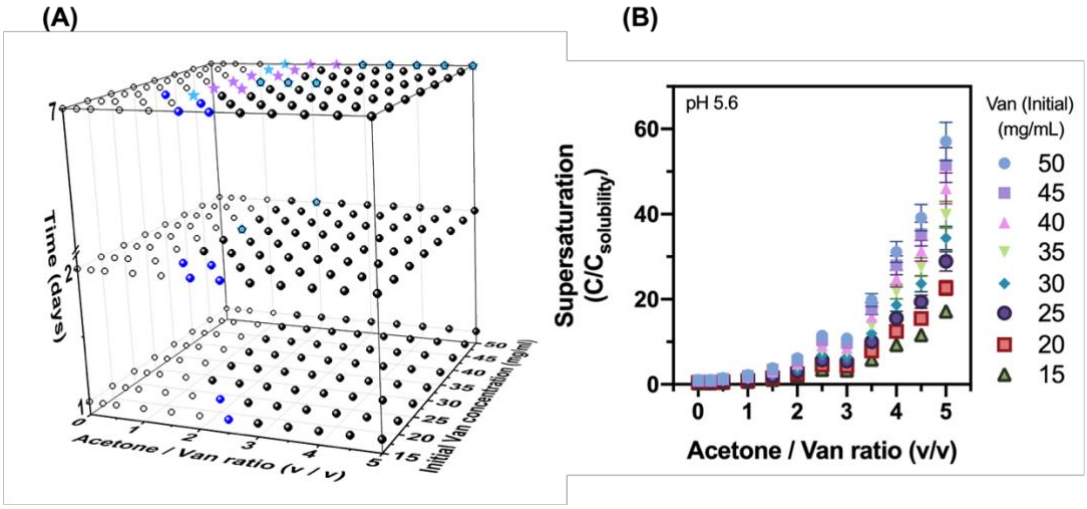

Figure 4.6 (A) Phase diagram of antisolvent Van precipitation at pH 5.6 (unfilled circles: clear solution; grey circles: light precipitates; black circles: heavy precipitates; blue stars: stand-alone needle crystals; purple stars: sea-urchin-like shaped crystals; (B) Van supersaturation levels at pH 5.6

Overall, the phase behavior results showed that higher pHs promoted higher precipitation propensity in the wells, which were attributed to the higher supersaturation levels at higher pH as we discussed earlier. Specifically, at pH 2.6, roughly 33% of the wells produced precipitates after 1 day incubation. This number increased to roughly 34%, 58%, and 64% at pH 3.6, 4.6, and 5.6, respectively (**Figure 4.3A**, **Figure 4.4A**, **Figure 4.5A**, **Figure 4.6A**). High propensity for precipitation was important as the study moved on to carry out the batch antisolvent Van precipitation, where production yield is one of the key performance indicators. For this reason, batch antisolvent precipitation of Van presented in the next section was to be carried out at the highest pH investigated, i.e., pH 5.6.

Among the precipitation products at pH 5.6, the crystalline precipitates would have the highest thermodynamic stability. However, their formation required long incubation time (7 days) rendering them less attractive for commercial applications. Furthermore, their needle habits were notorious for difficult handling and causing downstream processing issues in steps such as filtration, drying, and tableting [255]. Extensive research efforts had been pursued to avoid the production of undesirable needle habits in industrial crystallization [267]. Therefore, the present work deliberately opted not to operate in the condition in which needle-like crystalline precipitates were produced. In that case, the small particles in heavy precipitates would be the preferred products.

On this note, the use of organic solvent in protein precipitation ran the risk of denaturation of the protein, particularly if the precipitation was not carried out at below ambient temperature [115]. The same concern applied to the heavy precipitates produced in the antisolvent Van precipitation with acetone. The phase behavior study, nevertheless, showed that crystalline precipitates could grow out of the heavy precipitates suggesting that the Van molecules in the heavy precipitates remained in

their native state, rather than unfolding. Furthermore, the heavy precipitates were found to readily redissolved in water, which would have not been possible if the Van precipitates had denatured [321]. As we discussed in Section 3.4, further characterizations by PXRD and FTIR confirmed the structural integrity of the heavy precipitates.

4.3.2 Batch antisolvent precipitation: Optimal R_(Ace/Van)

At sufficiently high $R_{Ace/Van}$, the phase diagram at pH 5.6 in **Figure 4.6A** previously showed that heavy precipitates could be produced at nearly all initial Van concentrations investigated, i.e., C_{Van} = 15-50 mg/mL. Based on these findings, the batch antisolvent precipitation was carried out at C_{Van} = 50 mg/mL to maximize the supersaturation level and in turn the yield. At C_{Van} = 50 mg/mL, the phase diagram showed that heavy precipitates could be produced at $R_{Ace/Van} \geq 1.5$. The optimal $R_{Ace/Van}$ was subsequently determined by quantifying its impacts on the yield. The results in **Figure 4.7A** showed that the 48-h yield increased from roughly 61% (w/w) at $R_{Ace/Van}$ = 1.5 to around 85% and 95% at $R_{Ace/Van}$= 2.0 and 3.0, respectively, owed to the increase in the supersaturation level at higher $R_{Ace/Van}$ as shown earlier in **Figure 4.6B**.

Despite the nearly 100% yield, extensive use of acetone at very high $R_{Ace/Van}$ should be avoided as it might lead to Van denaturation, higher production costs, and environmental concerns [322]. For this reason, the optimal $R_{Ace/Van}$ was determined to be equal to 2.0 at which a reasonable 48-h yield was obtained. Notably, the batch antisolvent precipitation at $R_{Ace/Van}$ = 2.0 exhibited similar yields after 24 h and 48 h at 85 ± 0.6% and 84 ± 0.3%, respectively (**Figure 4.7B**). Hence, the batch antisolvent precipitation had practically been completed after 24 h.

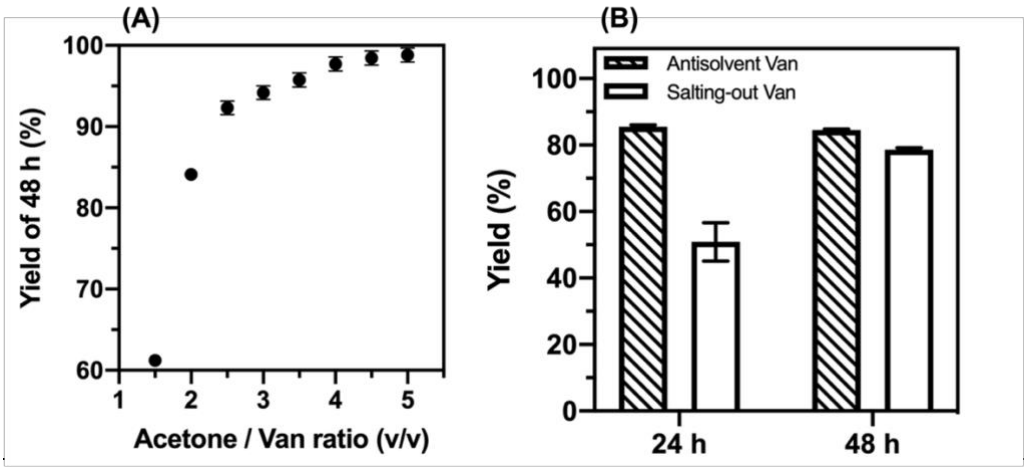

Figure 4.7 (A) 48-h yields of batch antisolvent Van precipitation as a function of R_(Ace⁄Van); (B) Comparisons of 24-h and 48-h yields of batch antisolvent and salting-out Van precipitations at their respective optimal conditions

For comparison, the yields of the batch salting-out precipitation, which produced octahedral Van crystals, were considerably lower at 51 ± 6% and 77 ± 1% after 24 h and 48 h, respectively (**Figure 4.7B**). At their optimal conditions, the supersaturation levels of the salting-out and antisolvent precipitations were found to be comparable at 5.0 ± 0.6 and 6.2 ± 0.5, respectively. Therefore, the higher yield of the antisolvent precipitation was less attributed to the difference in their supersaturation levels. Unlike heavy precipitates, which comprised submicron particles as discussed in the next section, the crystals from salting-out precipitation were much larger. We postulated that the slow integration rate of solute molecules onto crystalline surfaces during the crystal growth phase was the more likely cause for the slower precipitation rate of salting-out precipitation, resulting in its much lower yield, particularly after 24 h.

4.4 Antisolvent Van precipitates versus salting-out Van precipitates

4.4.1 Morphology and purity

The SEM image of the lyophilized heavy precipitates from antisolvent precipitation showed that they were made up of agglomerates of submicron particles, whose individual sizes were around 0.1-0.2 μm (**Figure 4.8A**). The size of the agglomerates was orders-of-magnitude larger at 144 ± 4 μm (**Figure 4.8B**). In

contrast, the salting-out precipitation produced octahedral crystals with individual sizes between 0.5 and 1.5 μm (**Figure 4.8C**). The purity of the antisolvent Van precipitates was high at 99 ± 0.5% (w/w) indicating only a trace of acetone and buffer ions present in the final product (Table 4.2). Likewise, the purity of the salting-out precipitates was equally high at 98 ± 2% (w/w).

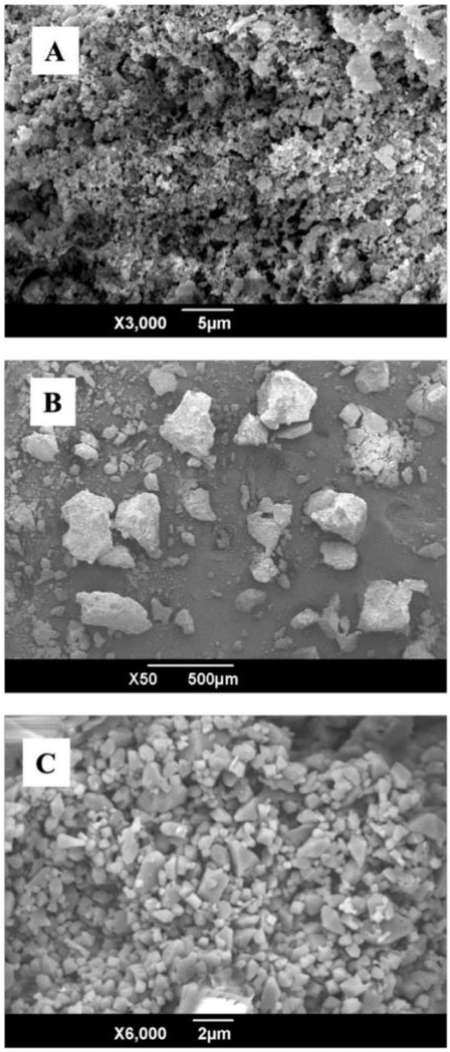

Figure 4.8 SEM images of (A) submicron particles making up the heavy precipitates produced in batch antisolvent precipitation; (B) antisolvent Van precipitates at lower magnification; (C) octahedral crystalline microparticles produced in batch salting-out precipitation

Table 4.2 Purity and MIC values of the antisolvent and salting-out Van precipitates

Precipitation Method	Purity (% w/w)	MIC (μg/mL)
Antisolvent Van precipitates	99 ± 0.5	0.5
Salting-out Van precipitates	98 ± 2	1

4.4.2 PXRD and FTIR

The PXRD analysis showed that the antisolvent Van precipitates exhibited PXRD spectrum that was similar to the reference PXRD spectrum of crystalline Van (**Figure 4.9A**), which signified crystalline structures of the antisolvent Van precipitates, despite their lack of obvious crystalline morphology. The submicron particles making up the heavy precipitates thus could be viewed as nanocrystals. Compared to the reference crystalline Van's spectrum, the main peak at $2\theta \approx$ 22-23 was narrower in the antisolvent Van precipitates' spectrum indicating larger crystallite sizes [323]. The salting-out Van precipitates also exhibited similar PXRD spectrum as the reference crystalline Van's, which was not unexpected because their octahedral morphology clearly indicated that they were crystalline particles.

The FTIR spectra of the antisolvent and salting-out Van precipitates were nearly identical to each other indicating their similar peptide secondary structures (**Figure 4.9B**). Both spectra showed peaks at 3430, 1670, 1230, and 1070 cm^{-1} that were unique to Van, attributed to N-H stretching vibration, C=O stretching of the peptide bonds, C-O stretching of the phenols, and C-O stretching of the ether groups, respectively [307]. Both spectra also showed peaks at 1510 and 1030 cm^{-1} attributed to C-H bending of Van's aromatic group and C-O stretching of Van's alcohol groups, respectively.

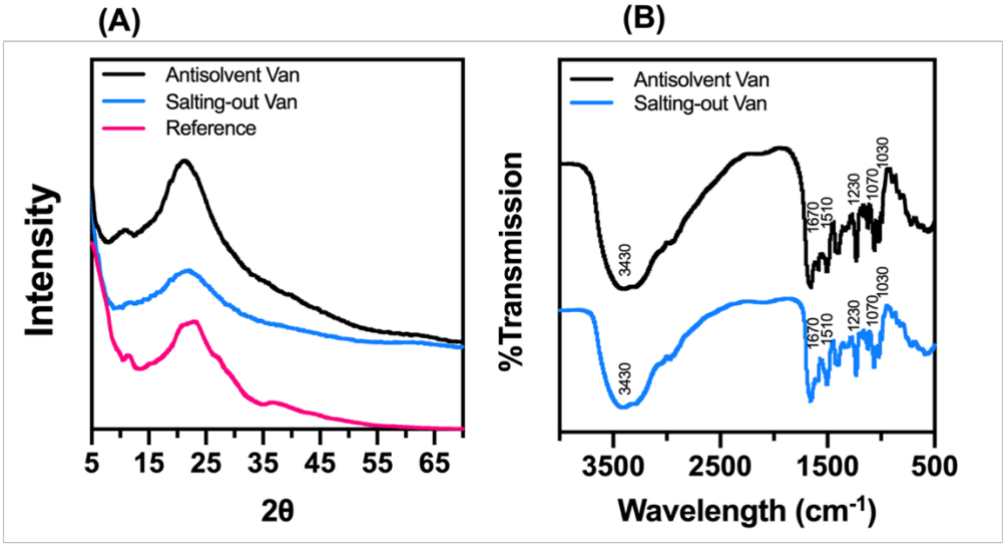

Figure 4.9 (A) PXRD and (B) FTIR spectra of the antisolvent and salting-out Van precipitates

4.4.3 Thermal stability

The TGA results showed that upon heating up to 100°C the antisolvent Van precipitates experienced a smaller mass loss (≈ 6.5%) compared to the salting-out Van precipitates (≈ 10%). The smaller mass loss signified the lower moisture content of the antisolvent Van precipitates after lyophilization (**Figure 4.10A**). Upon further heating above 100°C, both precipitates remained thermally stable up to 230°C above which Van decomposition began to take place, eventually resulting in nearly 35% and 20% mass losses at 400°C for the salting-out and antisolvent Van precipitates, respectively. The faster decomposition rate of the salting-out Van precipitates could be attributed to their aforementioned higher moisture content, which was known to expedite the decomposition of proteins by increasing their conformational flexibility [324].

DSC thermographs of proteins typically showed broad endothermic peaks attributed to thermal denaturation events of the proteins from which the denaturation temperature (T_m) could be determined. The DSC thermographs of the antisolvent and salting-out Van precipitates showed broad endothermic peaks between 40°C and 120°C (**Figure 4.10B**). The antisolvent and salting-out Van precipitates exhibited similar T_m at 82.4°C and 86.5°C, respectively.

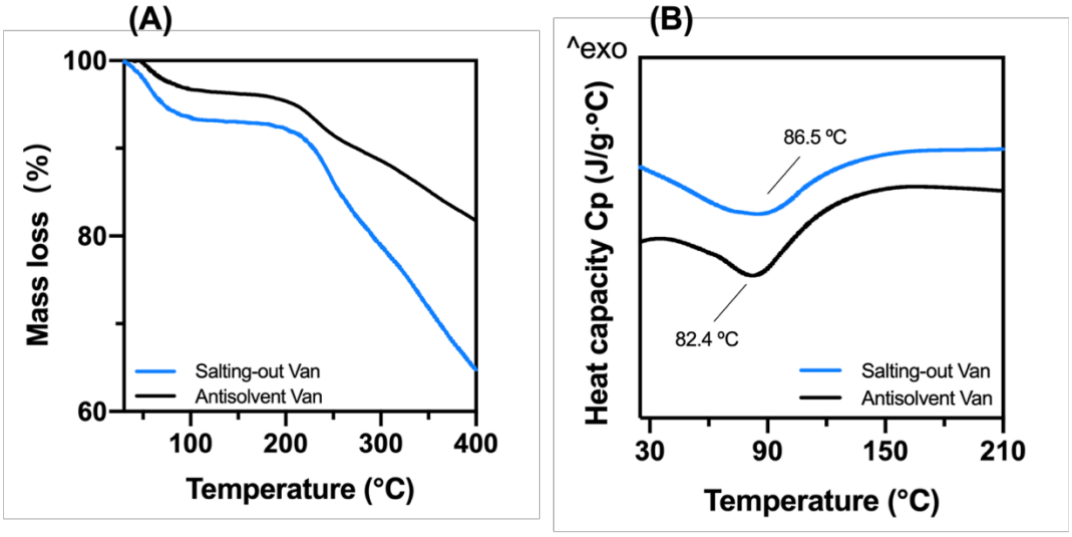

Figure 4.10 (A) TGA and (B) DSC thermographs of the antisolvent and salting-out Van precipitates

4.4.4 Dissolution rate and antimicrobial activity

The antisolvent Van precipitates exhibited faster dissolution rates than the salting-out Van precipitates at the three pHs investigated (i.e., pH 1.2, 4.5, and 6.8) (**Figure 4.11**). Specifically, the antisolvent Van precipitates exhibited ≈ 90%, 65%, and 65% (w/w) dissolutions after 30 min at pH 1.2, 4.5, and 6.8, respectively. For comparison, after the same period, the salting-out Van precipitates exhibited 75%, 50%, and 45% (w/w) dissolutions at pH 1.2, 4.5, and 6.8, respectively. The faster dissolution rates of the antisolvent Van precipitates were not unexpected as their size was smaller, hence larger specific surface areas for dissolution. For both precipitates, compared to the dissolution at pH 1.2, the Van dissolution rates at pH 4.5 and 6.8 were slower due to the lower Van solubility at higher pH, resulting in a smaller driving force for dissolution.

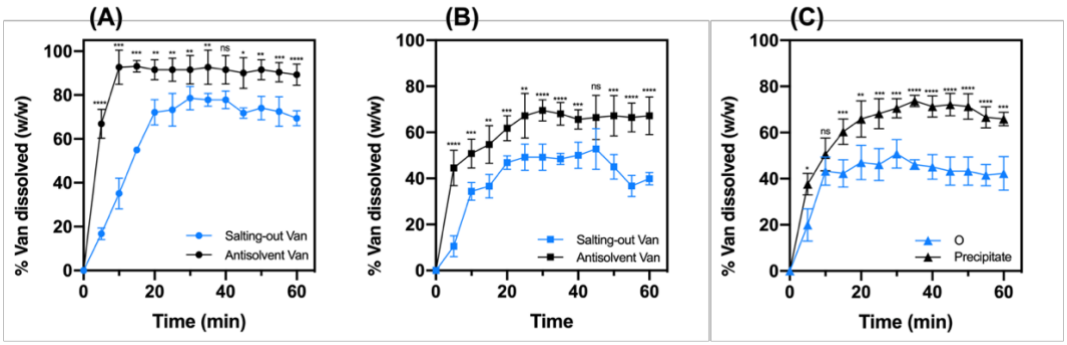

Figure 4.11 Dissolution profiles of the antisolvent and salting-out Van precipitates at pH (A) 1.2, (B) 4.5, and (C) 6.5 (ANOVA statistical significances for variations in the dissolution rates between the antisolvent and salting-out precipitates, *P < 0.1, ** P < 0.01, *** P < 0.001, **** P < 0.0001)

The antisolvent Van precipitates exhibited a slightly lower MIC against *S. aureus* at 0.5 µg/mL with OD_{600} equal to 0.046 ± 0.001. For comparison, the MIC of the salting-out Van precipitates against *S. aureus* was equal to 1 µg/mL with OD_{600} equal to 0.045 ± 0.002. Both MIC values were within the range of MIC values reported (i.e., 0.5-2 µg/mL) [311]. Importantly, the results demonstrated that both precipitation methods, including the use of organic solvent, did not adversely affect the bioactivity of Van.

4.4.5 Storage stability of the antisolvent Van precipitates

The SEM analysis revealed the antisolvent Van precipitates as nanoparticulate structures and the PXRD analysis indicated they were likely crystalline, despite their not exhibiting a typical crystal habit. Nanostructures of a compound were generally known to be less stable than their bulk forms upon exposures to heat and humidity due to their large surface areas [325]. Therefore, the storage stability of the antisolvent Van precipitates was investigated next by re-examining the PXRD, FTIR, TGA, and DSC analysis after storage.

First, both PXRD and FTIR analysis of the stored antisolvent Van precipitates showed negligible variations between the as-prepared precipitates and the precipitates stored for 1 month and 2 months at 40°C and 75% RH (**Figure 4.12A** and

Figure 4.12B). These results suggested minimal change in the crystallinity and peptide secondary structure of the antisolvent Van precipitates after storage. Second, TGA analysis of the stored precipitates as expected showed an increase in the moisture content from roughly 6.5% before storage to 15% after storage, while the onset temperature for decomposition was unchanged at around 230°C (**Figure 4.12C**). The higher moisture content after storage, nevertheless, resulted in faster decomposition rates for the stored precipitates with roughly 50% mass loss at 400°C. Three, the DSC analysis showed that T_m of the antisolvent Van precipitates were minimally affected by the accelerated storage, where T_m increased slightly from 82.4°C before storage to 82.5°C and 83.6°C after 1 month and 2 months of accelerated storage, respectively (**Figure 4.12D**). In short, the antisolvent Van precipitates were shown to maintain their physicochemical characteristics after storage.

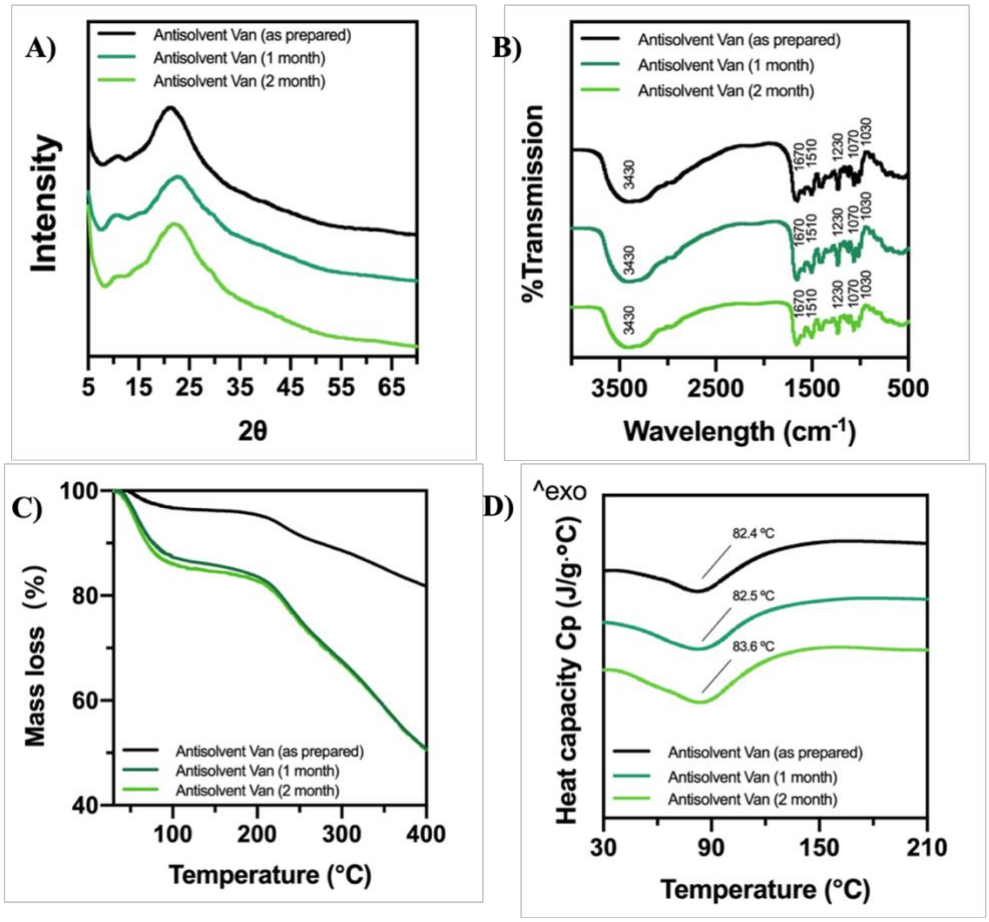

Figure 4.12 (A) PXRD, (B) FTIR, (C) TGA, (D) DSC results of antisolvent Van precipitates after 1 and 2 months of accelerated storage

4.4 Conclusion

The phase behavior study of antisolvent Van precipitation showed that operating at higher pHs (i.e., pH 4.6 and 5.6), which resulted in higher supersaturation levels, was needed to generate a sufficiently high Van precipitation propensity. At these pHs, heavy precipitates made up of agglomerates of submicron particles were the predominant products, which were readily produced after 1 day incubation in a wide range of Van concentrations and $R_{Ace/Van}$. At their respective optimal conditions, the batch antisolvent Van precipitation exhibited a significantly higher 24-h yield than the batch salting-out precipitation at roughly 85% and 51% (w/w), respectively. The antisolvent and salting-out Van precipitates exhibited similar PXRD and FTIR spectra indicating their similar internal molecular structures, despite their vastly different morphology. They also exhibited comparable purity, thermal stability, and antimicrobial activity. The antisolvent Van precipitates, nevertheless, exhibited faster dissolution rates attributed to their nanoscale size. Despite being nanostructures, the antisolvent Van precipitates exhibited good stability during accelerated storage at elevated heat and humidity. In short, the antisolvent route was determined to be the superior precipitation method of Van owed to its higher precipitation efficiency while exhibiting comparable product qualities as the salting-out precipitates.

CHAPTER 5 COMPARATIVE EVALUATIONS OF BULK SEEDED PROTEIN CRYSTALLIZATION IN BATCH VERSUS CONTINUOUS SLUG FLOW CRYSTALLIZERS

This chapter has been published as **Siyu Pu**, Kunn Hadinoto, Comparative evaluations of bulk seeded protein crystallization in batch versus continuous slug flow crystallizers, Chemical Engineering Research and Design, Volume 171, 2021, Pages 139-149. Permission has been granted by the licensed publisher "Elsevier" for utilization of the published content as a chapter in this thesis [326].

5.1 Introduction

Crystallization has been established as a viable alternative to chromatography for the downstream purification of pharmaceutical proteins, particularly at high upstream production titers at which the prohibitive costs and the lower efficiency of chromatography become evident [6, 327]. Moreover, from the drug product formulation's perspectives, protein crystals are known to exhibit higher purity, better physicochemical stability, and dissolution characteristics than their non-crystalline counterparts [9].

Bulk crystallization of pharmaceutical proteins, however, faces a challenge in controlling the resultant crystal size distribution (CSD) and its reproducibility [35, 36]. The CSD is important because it influences not only the efficiency of the down-stream processing steps (e.g., filtration, drying), but also the dissolution and consequently bioactivity of the protein crystals [37]. In pharmaceutical formulations, a good CSD is generally characterized by a unimodal crystal size with a narrow distribution width.

A number of strategies have been pursued to improve the CSD in bulk protein crystallization, for example, (1) seeded crystallization using either foreign materials (e.g., silica particles), or the protein crystals themselves as the seeds [39, 40]. (2)

sonocrystallization [41, 42], and (3) additive crystallization (e.g., ionic liquid, DNA) [44, 328]. These strategies rely on having controlled nucleation by operating in the crystallization's metastable zone, where spontaneous nucleation that is often responsible for poor CSD is highly improbable [172]. In these strategies, the nucleation is some- times bypassed altogether by operating at reduced supersaturation levels, or at high seed loading for seeded crystallization, to make crystal growth as the predominant mechanism of crystal formation [329].

A principally different approach to improve the CSD is by carrying out the protein crystallization in a continuous platform, in place of the conventional batch crystallizer [10]. The continuous platform enables the segmentation of the nucleation and growth events with precisely controlled supersaturation levels in each segment, resulting in improved CSD [45-48]. Compared to the batch platform, the continuous crystallizers also bring additional benefits, such as (i) shorter downtime, (ii) fewer upscaling issues, (iii) smaller equipment, which leads to lower capital and operating costs, and (iv) better process control, which leads to improved process safety and importantly enables the crystallization to take place at the most optimal condition [242].

Two basic types of continuous crystallizers are available, i.e. (1) mixed-suspension mixed-product removal crystallizer (MSMPRC) and (2) continuous plug flow crystallizer (CPFC). The MSMPRC operates similarly in principle to a perfectly mixed continuous stirred-tank reactor in which the concentrations of the crystals and solutes within the crystallizer's volume are spatially uniform, where the values were identical to the concentrations at the crystallizer's outlet. The crystals and solutes' concentrations in CPFC, on the other hand, are only uniform radially, but not along the axial tube length. In terms of the residence time of the crystals and solutes, the CPFC is identical to the batch crystallizer, where every single crystal and solute molecule spend the same amount of time inside the crystallizer, which is not evident in the MSMPRC. Theoretically, infinite number of small-volume MSMPRCs arranged in series would have similar crystallization performance as CPFC having the same total crystallizer volume.

In place of the mechanical agitation used in the MSMPRC, mixing in the CPFC is facilitated by oscillatory baffled designs, or hydrodynamically induced by self-

circulating liquid slugs [209]. The milder operating condition of CPFC makes it ideal for crystallization processes in which large unbroken crystals are desired, and also for crystallization of labile proteins with a strong denaturation tendency under shear (e.g. insulin) [200]. CPFC also offers supe- rior heat transfer owed to their larger surface-to-volume ratio, resulting in better crystal quality and higher crystallization efficiency in cooling crystallization.

The CPFC, nevertheless, has its own limitations, such as (1) limited production throughput, (2) risks of channel blockage, and (3) the fact that the residence time is dictated by the tube length and flowrate, which both have their operating limits. For example, operating at low flowrates to prolong the residence time in order to maximize crystal growth would increase the risk of channel blockage. Conversely, operating at high flow rates would require excessive tube length to achieve sufficient residence time, resulting in increased costs and energy requirement to maintain the flow [235]. With these limitations of the CPFC in mind, the present work aimed to examine the process improvements (e.g. higher throughput, superior crystal quality) that potentially could be gained by incorporating seeded crystallization into the CPFC.

In seeded crystallization, seed crystals of the solutes (or foreign seeds) are used to promote secondary nucleation by attrition, contacts, or shear nucleation at a reduced supersaturation level, while simultaneously inhibit the spontaneous nucleation. As a result, the onset of crystallization is well-defined, resulting in better control over the CSD and its reproducibility [330]. While seeded crystallization has been widely employed to grow a large single protein crystal for X-ray diffraction studies, to the best of our knowledge, seeded protein crystallization for bulk purification purposes so far has only been performed in the batch platform [39, 40, 44, 50, 51].

To reduce the risk of channel blockage, CPFC featuring gas-liquid slugs was used in the present work. In continuous slug flow crystallizer (CSFC), a segmented gas-liquid phase, which comprises a string of gas bubbles separated by liquid slugs of the crystallization solution, flows concurrently in the tubular crystallizer. The gas bubbles facilitate constant net flows of the crystals formed within the liquid slug, thus reducing the risk of channel blockage. It is worth pointing out that to facilitate the

introduction of the crystal seeds into the flow of solutes, we placed a continuous stirred-tank reactor upstream of the CSFC. Our preliminary investigation revealed that direct introduction of the seeds into the CSFC resulted in unsteady gas-liquid slug flow for the range of liquid flowrate investigated. This unstable flow issue was caused by inconsistent mixed flow of the seeds and the solutes in the Y-junction connector due to the low liquid flowrate used. The low liquid flowrate, nevertheless, was required to maintain adequate residence time for the notoriously slow protein crystallization.

Lysozyme (LYZ) was used as the model therapeutic protein with LYZ seeds pre-prepared in a batch crystallizer as the seed materials. The only other investigation on bulk seeded LYZ crystallization, which used pre-prepared LYZ crystals as the seed materials, employed low-pressure evaporative batch crystallization as the crystallization's driving force [39]. In the present work, we carried out simultaneous cooling and salting-out seeded crystallization of LYZ in the CSFC. The crystallization performance of the seeded CSFC was compared with that of the batch crystallizer in terms of the resultant (1) CSD and its reproducibility, (2) crystallization efficiency as charac- terized by the yield and production throughput, (3) crystal morphology, and (4) LYZ activity. The effects of (i) residence time and (ii) seed load-ing, on the CSD and crystallization efficiency were investigated. The performance of a hybrid batch-CSFC crystallizer was also examined for comparison.

5.2 Materials and methods

5.2.1 Materials

Lysozyme (LYZ) from chicken egg white (purity ≥ 90%, activity ≥ 20,000 units/mg) was purchased from Bio Basic (Singapore). Sodium acetate (≥ 99%), glacial acetic acid, sodium chloride (NaCl), and were sodium hydroxide (NaOH) were purchased from Sigma Aldrich (Singapore). A magnetic round-edge stirrer with the dimensions of 8-mm diameter and 50-mm long was used in all the mixing operations in the batch and continuous stirred- tank crystallizers.

5.2.2 Methods

5.2.2.1 Preparation and characterization of LYZ seeds

The seed crystals were prepared by dissolving 100 mg/mL LYZ in 100 mM NaOAc buffer containing 16 mg/mL NaCl adjusted to pH 4.6 by the addition of HCl and NaOH. The LYZ solution was then mixed at equal volume with 64 mg/mL NaCl solution used as the salting-out agent. The mixed solution containing 50 mg/mL LYZ and 40 mg/mL NaCl was then placed under stirring (250 RPM) at 22.5°C for 48 h to ensure equilibrium between the bulk liquid and the crystalline solid phase. Prior to mixing, the LYZ and NaCl solutions were syringe filtered using Uni-flo syringe filter (13 mm, 0.22 μm) (Whatman, UK). Deionized (DI) water was used in the preparation of both solutions. Prior to use, the seed suspension was diluted with saturated LYZ solution containing 12.8 mg/mL LYZ and 40 mg/mL NaCl.

The CSD of the LYZ seeds was determined by ImageJ analysis (NIH, USA) of the light microscope image of the seed suspension. The light microscope image was taken under the phase contrast mode at 400× magnification (CKX41, Olympus, Japan). The crystals' size was characterized by their Feret's diameter from a minimum of 1000 crystal counts. The CSD was expressed in terms of the number-mean Feret's diameter (d_{ave}) with d_{10}, d_{50}, and d_{90} representing the 10%, 50%, and 90% cumulative undersize of the CSD, respectively. The CSD width was determined by the Span value defined as Span = $(d_{90} - d_{10})/d_{50}$. The morphology of the seed crystals was characterized by scanning electron microscope (SEM) (JSM 6701F, JEOL, Japan) using 24-h lyophilized seeds as the sample.

5.2.2.2 Seeded LYZ crystallization in batch crystallizer

The batch crystallization of LYZ was performed in a 100-mL jacketed glass vessel maintained at an isothermal condition of 15°C by circulating cooling water (Polyscience 9501 refrigerated circulator, USA) (**Figure 5.1A**). LYZ was first dissolved at room temperature at 58 mg/mL in 100 mM NaOAc buffer (pH 4.6, 16 mg/mL NaCl). Afterwards, the LYZ solution was mixed in the cooled jacketed vessel with equal volume of 64 mg/mL NaCl solution under constant stirring (250 RPM), resulting in 50-mL solution containing 29 mg/mL LYZ and 40 mg/mL NaCl.

Subsequently, the LYZ seed suspension were added to the LYZ-NaCl solution at seed loading of 5% (w/w). Herein the seed loading was defined as the ratio of the mass of LYZ seeds added to the mass of LYZ solutes in the LYZ-NaCl solution (i.e., 29 mg/mL). The effects of the batch residence time (τ_{batch}) on the crystallization performance were investigated at τ_{batch} = 2, 3, 4, and 6 h. Control experiments in which LYZ seeds were not added were performed for comparison. The CSD of the LYZ crystals produced was characterized by ImageJ analysis as previously described. The reproducibility of the CSD was assessed from the coefficient of variation (CV) of d_{ave} and Span from the three independent replicates (n = 3), where CV was defined as the ratio of the standard deviation to the mean value.

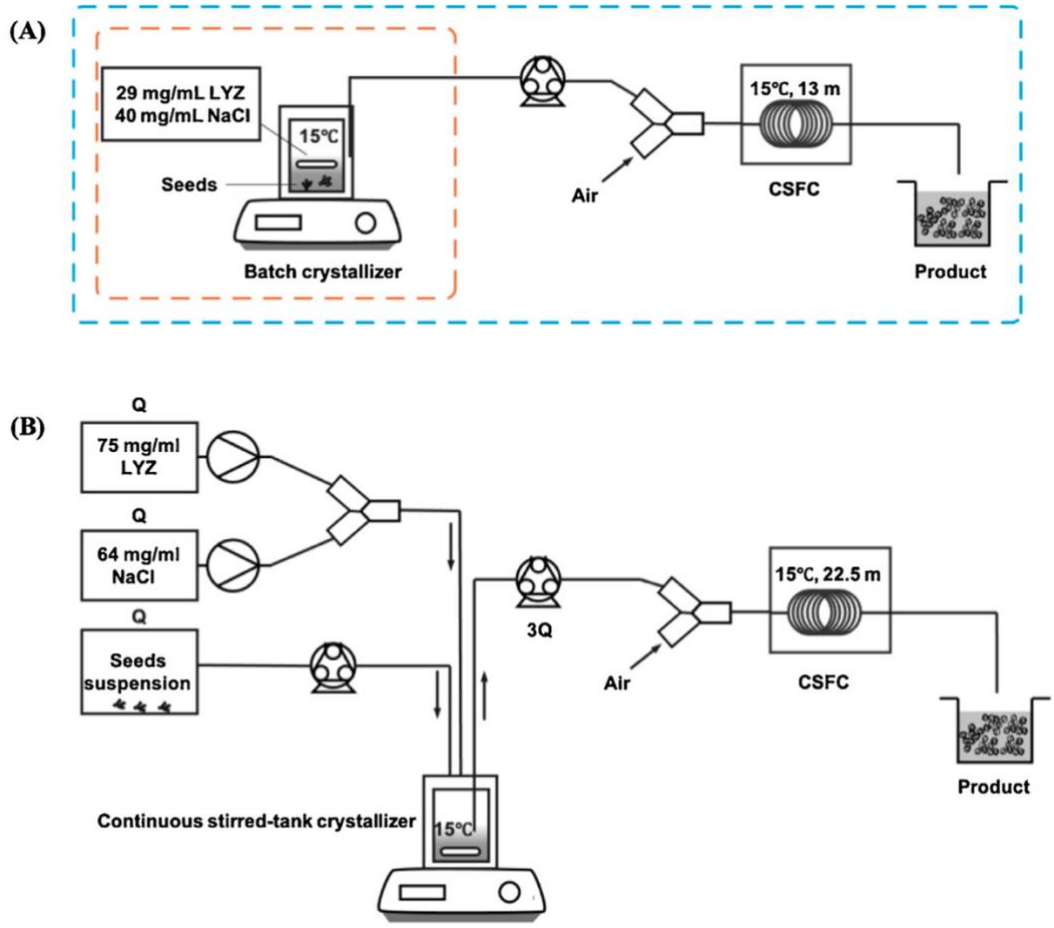

Figure 5.1 Schematics of the (A) batch crystallizer and hybrid batch-CSFC; (B) CSFC equipped with upstream continuous stirred-tank reactor for seeds introduction.

5.2.2.3 Seeded LYZ crystallization in the hybrid batch-CSFC

The hybrid batch-CSFC was constructed by connecting the abovementioned batch crystallizer to a downstream CSFC in a serial arrangement (**Figure 5.1A**). Briefly, 20-mL of the crystal suspension containing the 5% (w/w) seeds was pumped out from the batch crystallizer using a peristaltic pump (520 U/R2, Watson-Marlow, USA) at a flowrate of 0.265 mL/min. The crystal suspension was then mixed with gas bubbles in a polyethylene Y-junction connector (Cole Palmer, USA) placed 0.1 m upstream of the CSFC's inlet. A single syringe pump (NE-1010, New Era Pump Systems Inc., USA) was used to inject bubbles of filtered air into the crystal suspension at a fixed time interval using a 1-mL syringe (B. Braun, USA). Air bubbles having volume of ≈ 11.9 mm^3 was injected every 16 s to produce gas-liquid slug flow with air bubbles and liquid slugs' dimensions of 3 mm and 16 mm in length, respectively.

The slugs then flowed into a 6.5-m and 13-m-long isothermal CSFC immersed in 15°C water bath (Polyscience 9501 refrigerated circulator, USA). The tubes of the CSFC were made of Tygon® silicone microbore tubing having inner diameter (ID) of 2.38 mm and outer diameter (OD) of 3.97 mm. The crystal suspension was collected at the CSFC's outlet and the CSD was characterized as previously described. The experiment was repeated three times on three different days (n = 3) from which the CSD's reproducibility was characterized. A control experiment in which LYZ seeds were not added was performed.

5.2.2.4 Seeded LYZ crystallization in CSFC

The schematics of the CSFC equipped with an upstream continuous stirred-tank crystallizer for the purpose of introducing the LYZ seeds was presented in **Figure 5.1B**. Briefly, a dual-syringe pump (Legato 200, KD Scientific, USA) equipped with Luer-LokTM 30-mL syringes (BD, Canada) was used to transport the 75 mg/mL LYZ and 64 mg/mL NaCl solutions into the continuous stirred-tank crystallizer. Mixing of the LYZ and NaCl solutions was achieved by passing the solutions through a Y-junction connector. The flow rates of the LYZ and NaCl solutions were set to be equal at Q (mL/min) each. Separately, the LYZ seed suspension was pumped into the

stirred tank at the same flowrate (equal to Q) using a peristaltic pump (BT100, LongerPump®, China). The effects of seed loading were investigated at seed loading values of 5% and 10% (w/w).

The effluent of the stirred-tank crystallizer containing 29 mg/mL LYZ solutes and 40 mg/mL NaCl was then conveyed to the CSFC (ID 2.38 mm) at flowrate equal to 3Q using a peristaltic pump (520 U/R2, Watson-Marlow, USA). The temperatures of both the stirred-tank crystallizer and CSFC were maintained at 15◦C by circulating cooling water (Polyscience 9501 refrigerated circulator, USA). The effects of the residence time in the CSFC were investigated by varying the flowrate (Q = 0.150, 0.275, and 0.375 mL/min) and the tube length (17.2 m and 22.5 m). The crystal suspension was collected at the CSFC's outlet and the CSD was characterized as previously described. The experiment was repeated three times on three different days (n = 3) from which the CSD's reproducibility was characterized. Control experiments in which LYZ seeds were not added were performed.

Since the experimental condition in this chapter are close to the phase diagram below in the literature [331], the two points representing two streams of LYZ can be illustrated on the figure below. S1 represents the mixed solution from 75 mg/mL LYZ, 40 mg/mL (4%) and S2 represents the seeds suspension of 12.8 mg/mL LYZ, 40 mg/mL (4%). Therefore, all the possible concentrations in the tank are on the connected line of S1S2. It can be seen that the zone is well within the metastable zone.

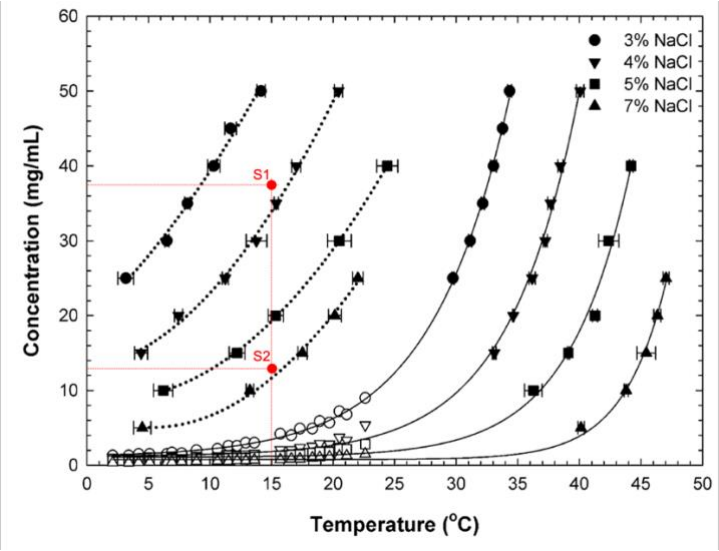

Figure 5.2 Phase diagram of CSFC

5.2.2.5 Crystallization efficiency

The crystallization efficiency of the different crystallization platforms was characterized by (i) the experimental yield, (ii) production capacity (PC), (iii) $M_{Product/Seed}$, and (iv) space-time yield (STY). The experimental yield (% w/w) was determined in triplicates following **Eq. (3.1**). For the batch crystallizer, C_i and C_o in **Eq. (3.1**) represented the initial and final concentrations of the LYZ solutes, whereas for the CSFC and hybrid batch-CSFC, C_i and C_o in **Eq. (3.1**) represented the concentrations of the LYZ solutes recovered at the crystallizers' inlet and outlet, respecively. Serving as a reference, the theoretical yield (% w/w) was calculated according to **Eq. (5.1**) in which C^* represented the thermodynamic saturation solubility of LYZ at the crystallization condition.

$$Theoreticial\ Yield\ (\%\,{}^{w}/_{w}) = \frac{C_i - C^*}{C_i} \times 100\% \qquad (5.1)$$

For a fair comparison among the different crystallization platforms, C_i was fixed at 29 mg/mL in the three crystallizers. Briefly, C_o was determined by centrifugation of 1.5-mL sus- pension of the product crystals (15,000 rpm, 5 min) after which the LYZ concentration in the supernatant was determined by UV–vis spectrophotometry (UV Mini 1240, Shimadzu, Japan) at the optimal absorbance wavelength of LYZ (i.e., 280 nm) [250].

The production capacity (PC) defined as the mass of crystals produced per unit time (mg/h) was determined in triplicates by collecting 5-mL aliquot of the product crystal suspension. For the hybrid batch-CSFC and CSFC, the time required to collect the 5-mL aliquot was recorded. The mass of crystals contained in the 5-mL aliquot was determined by centrifugation of the crystal suspension (15,000 rpm, 5 min), followed by lyophilization of the crystal sediments at −52 ◦C and 0.05 mbar for 24 h in Alpha 1–2 LD Plus freeze dryer (Martin Christ, Germany). Next, the lyophilized crystals were suspended in 1.5 mL 100 mM acetate buffer to dissolve the LYZ. The amount of LYZ in the buffer solution was subsequently determined by UV–vis spectrophotometry as previously described.

The space-time yield (STY), which was defined as PC per unit volume of the crystallizer (mg/h·L), was calculated to take into account the different volumes of crystallizers used. The total volumes of the crystallizers were equal to 50 mL (batch), 78 mL (hybrid batch-CSFC), and 127 mL and 150 mL for CSFC with tube lengths of 17.2 and 22.5 m, respectively. Lastly, $M_{Product/Seed}$ defined in **Eq. ((**5.2) was determined to account for the presence of the LYZ seeds in the product crystals. For the hybrid batch-CSFC and CSFC, $M_{Product/Seed}$ had to be larger than 100% to suggest successful transport of the product crystals.

$$M_{Product/Seed}(\%\ w/w) = \frac{PC}{Mass\ flow\ of\ LYZ\ seeds\ supplied} \times 100\% \quad ((5.2)$$

5.2.2.6 LYZ activity

The LYZ activity of the product crystals was examined in triplicates by the LYZ activity assay performed at 25 ◦C and pH 7.0. The assay measured the reduction in the turbidity level of *Micrococcus lysodeikticus* bacterial cell suspension caused by the lysis of the bacterial cell walls upon treatment with LYZ. Step-by-step procedures to measure the turbidity level described in Thomas et al. [332] were followed and not repeated here for brevity. The LYZ activity of the product crystals was reported in terms of its relative value (%) calculated with respect to the activity of the raw LYZ (before crystallization). Lyophilized LYZ crystals were used as the samples.

5.3 Results and discussion

5.3.1 LYZ seeds characteristics

LYZ seeds produced in the batch crystallizer exhibited d_{ave} = 2.8 ± 0.9 μm and d_{50} =2.5 ± 0.1 μm after 48h.Their Span value was equal to 1.02 ± 0.18 denoting relatively narrow CSD with d_{10} and d_{90} of 1.6 ± 0.1 μm and 4.2 ± 0.1 μm, respectively (**Figure 5.3A**). A closer look at the lyophilized LYZ seeds by SEM revealed the tetragonal shape of the seed crystals (**Figure 5.3B**), which was not unexpected as the tetragonal shape represented the most typical crystal habit of LYZ prepared by batch

crystallization [333]. The CSD of the seeds in the tank were tested for up to 2 h. There was no apparent change on the size as shown in Table 5.1.

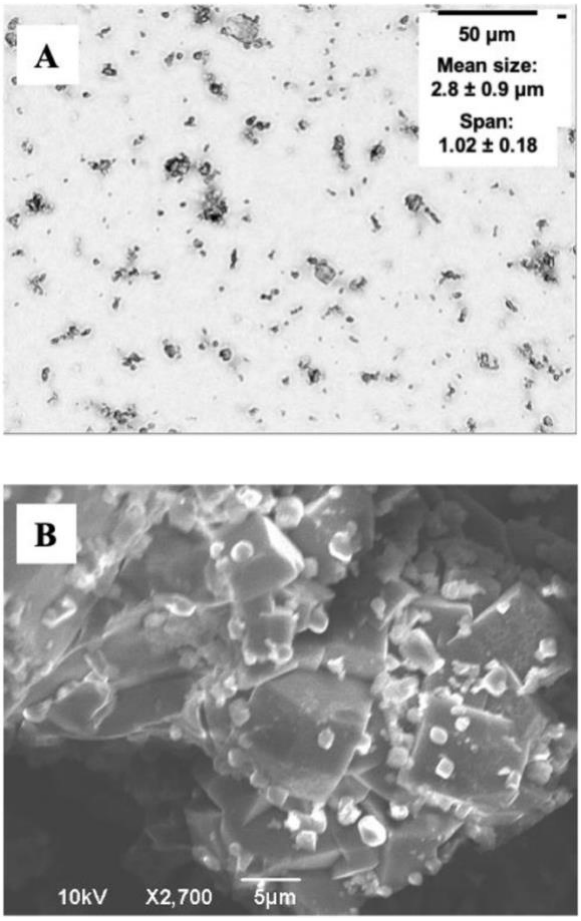

Figure 5.3 (A) Light microscope image; (B) SEM image of the LYZ seeds.

Table 5.1 CSD of crystals in the tank in continuous crystallization

τ_{Tank} (min)	d_{ave} (µm)	d_{10} (µm)	d_{50} (µm)	d_{90} (µm)	Span (µm)
20	3.49 ± 0.05	1.74 ± 0.28	3.09 ± 0.85	5.77 ± 1.19	1.07 ± 0.02
40	2.71 ± 0.09	1.43 ± 0.23	2.26 ± 0.66	3.90 ± 0.80	0.87 ± 0.02
60	2.53 ± 0.03	1.51 ± 0.24	2.31 ± 0.92	3.77 ± 0.78	0.58 ± 0.01
80	3.35 ± 0.07	1.87 ± 0.30	3.01 ± 0.82	5.14 ± 1.06	0.93 ± 0.02
100	3.87 ± 0.07	2.08 ± 0.33	3.50 ± 1.49	6.09 ± 1.25	0.62 ± 0.01

120	3.43 ± 0.06	2.10 ± 0.33	3.17 ± 1.24	5.06 ± 1.04	0.57 ± 0.01

5.3.2 Seeded LYZ crystallization in the batch crystallizer

At the crystallization condition of the batch crystallizer (15°C, 50 mM NaOAc buffer, 40 mg/mL NaCl, C^* of LYZ was determined to be equal to approximately 2.74 mg/mL using the empirical correlation of [334]. At this condition, the supersaturation level, which was defined as the ratio of the concentration of the LYZ solutes to C^* was calculated to be equal to approximately 8.8. Based on the LYZ crystallization's phase diagram of [331], this crystallization condition lay below the metastable zone limit, signifying improbable spontaneous nucleation.

Not unexpectedly, the results showed that in the absence of the LYZ seeds ("Control"), the experimental yield of the batch crystallization remained negligible even after τ_{batch}= 6 h (**Figure 5.4A**). For comparison, the theoretical yield at this crystallization condition was calculated to be equal to roughly 88% (w/w). The addition of the LYZ seeds at 5% (w/w) seed loading resulted in experimental yield equal to 10.0 ± 6.2% (w/w) after 2 h, which then increased to 53.0 ± 1.4% after 3 h (**Figure 5.4A**). The increase in the experimental yield, nevertheless, slowed down significantly after 3 h, where the yields after 4 h and 6 h were only slightly higher at 57.6 ± 4.2% and 63.3 ± 0.9%, respectively. It should be pointed out that for the crystallization conditions used, the system will need 24 h to reach the theoretical yield (data not showed).

The slow increase in the yield at longer τ_{batch} was not unexpected due to the decrease in the supersaturation level as crystallization took place. The supersaturation levels calculated from the remaining LYZ solutes were found to decrease to roughly 4.1 and 3.2 after 3 h and 6 h, respectively, resulting in an insufficient driving force for secondary nucleation and growth. The diminished crystallization rate at τ_{batch}> 3 h was also evident from the CSD plots of the LYZ crystals presented in **Figure 5.4B**. The growth of the seed32 crystals was reflected by the reduction in the relative frequency of the small crystals (≈1−3 μm) and correspondingly an increase in the relative frequency of the larger crystals (>5 μm). The diminished crystallization rate

at τ_{batch} > 3 h was evident from the minimal change in the CSD plots of the LYZ crystals between τ_{batch}= 3 h and τ_{batch}= 4 h.

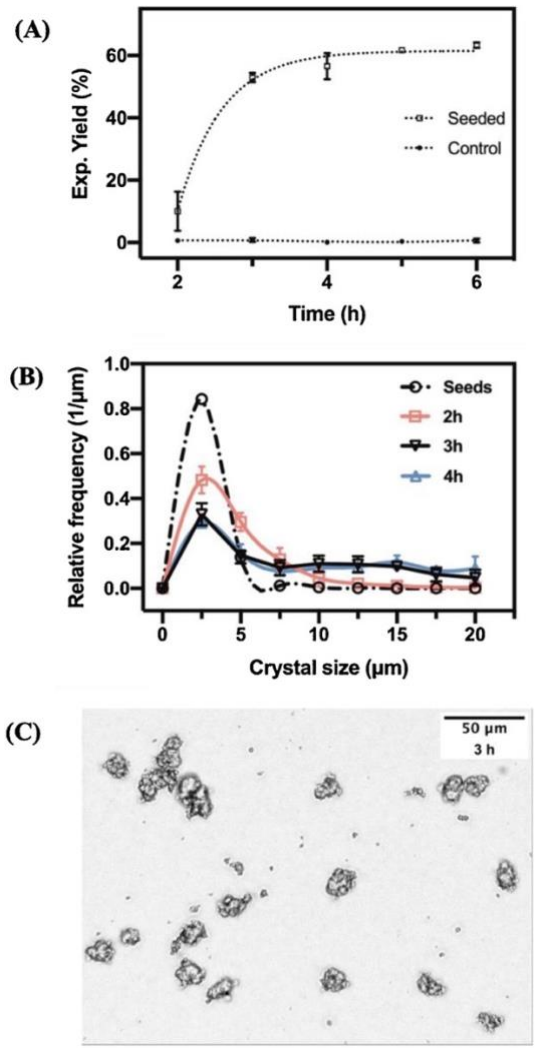

Figure 5.4 Seeded LYZ crystallization in the batch crystallizer at 5% (w/w) seed loading - (A) Experimental yield; (B) CSD as a function of $\boldsymbol{\tau_{batch}}$; (C) light microscope image of the LYZ crystals produced at $\boldsymbol{\tau_{batch}}$ = 3 h.

As a result of the slower crystallization rate at τ_{batch} > 3 h, the optimal PC and STY of the seeded batch crystallization were determined to be at τ_{batch} = 3 h at which PC and STY were equal to 231.7 ± 6.8 mg/h and 4633 ± 136 mg/h·L, respectively (**Table 5.2**). The $M_{Product/Seed}$ at τ_{batch}= 3 h was equal to 938 ± 27% (w/w) denoting efficient seeded crystallization. It was worth pointing out that even in the presence of

seeds, LYZ, like other macromolecules, crystallized at a much slower rate when compared to small-molecule compounds.

Table 5.2 Seeded LYZ crystallization in the batch crystallizer – CSD and crystallization efficiency as a function of $\boldsymbol{\tau_{batch}}$.

$\boldsymbol{\tau_{batch}}$ (h)	d_{ave} (μm)	d_{10} (μm)	d_{50} (μm)	d_{90} (μm)
2	4.7 ± 0.9	2.1 ± 0.3	4.0 ± 1.0	7.8 ± 1.6
3	8.3 ± 2.5	2.4 ± 0.7	7.1 ± 3.6	15.8 ± 2.4
4	9.3 ± 2.5	2.6 ± 0.4	8.5 ± 4.1	17.5 ± 2.8
6	5.9 ± 1.1	1.8 ± 0.1	3.4 ± 0.3	14.1 ± 3.0

$\boldsymbol{\tau_{batch}}$ (h)	Span	PC (mg/h)	$M_{Product/Seed}$ (% w/w)	STY (mg/L · h)
2	1.44 ± 0.03	54.3 ± 5.6	146 ± 15	1086 ± 111
3	2.38 ± 0.96	231.7 ± 6.8	938 ± 27	4633 ± 136
4	2.10 ± 0.72	174.6 ± 6.8	943 ± 36	3491 ± 135
6	2.97 ± 0.52	140.9 ± 2.6	1142 ± 21	3310 ± 241

At τ_{batch} = 3 h, the LYZ crystals produced exhibited d_{ave} = 8.3 ± 2.5 μm with a Span value of 2.38 ± 0.96 denoting a rather wide CSD (d_{10} =2.4 ± 0.7 μm, d_{50} =7.1 ± 3.6 μm, d_{90} =15.8 ± 2.4 μm) (**Table 5.2**). Significantly, despite the increase in the average crystal size, the CSD's mode did not shift significantly from the CSD's mode of the LYZ seeds at around 2.5 μm. This result suggested that there was still a significant number of small crystals at τ_{batch} = 3 h, which could be attributed to (i) the lack of growth of the LYZ seeds, or (ii) small crystals were freshly produced by secondary nucleation due to attrition/contacts in the batch crystallizers, or (iii) both.

A look at the light microscope image of the LYZ crystals produced at τ_{batch} = 3 h revealed that the large crystals in the population were made up of the agglomerates of smaller crystals, instead of large individual crystals (**Figure 5.4C**). The same observation was made from the light microscope images of the LYZ crystals produced at τ_{batch} = 4 h and 6 h (**Figure 5.5**). In fact, the formation of the agglomerates intensified at τ_{batch} = 4 h and 6 h as the production of small crystals increased at longer time, which was also reflected by the decrease in the d_{ave} to 5.9 ± 1.1 μm at τ_{batch} = 6 h. In this regard, the high shear rate generated by the mechanical stirring in a batch crystallizer was known in protein crystallization to promote

secondary nucleation [243], which concurrently limited the crystal growth, resulting in the production of predominantly small crystals.

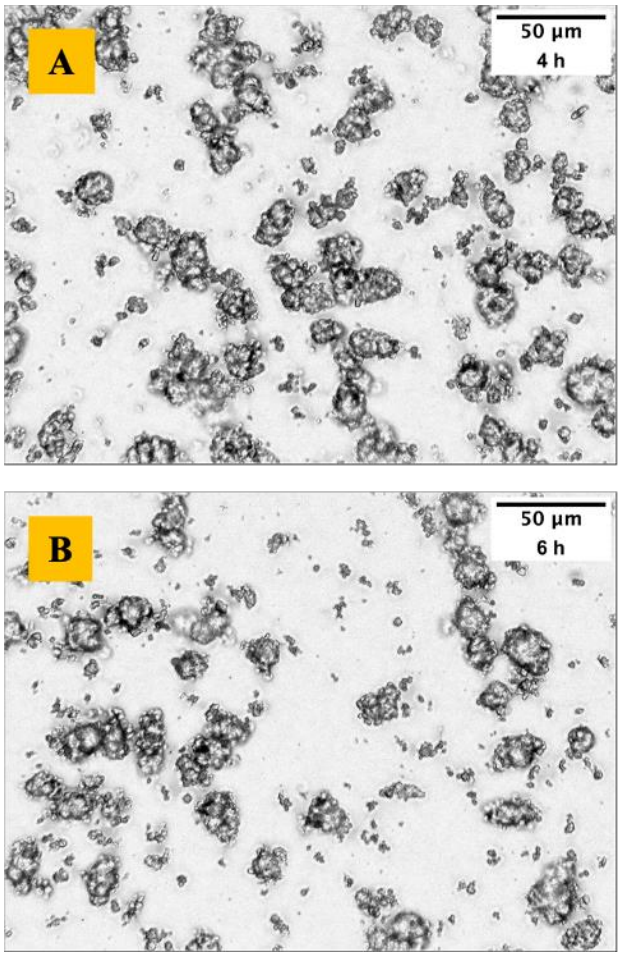

Figure 5.5 Light microscope images of the LYZ crystals produced in the batch crystallizer at $\boldsymbol{\tau_{batch}}$ = 4 and 6 h

With regard to the CSD's reproducibility, the LYZ crystals produced at τ_{batch} = 3 h exhibited CVs of d_{ave} and Span equal to 30.75% and 40.34%, respectively, indicating considerable fluctuations in the CSD among the independent replicates. Comparable CV values were observed at τ_{batch} = 4 h with CVs of d_{ave} and Span equal to 27.45% and 34.28%, respectively. These results were not unexpected as the batch platform had been notorious for its batch-to-batch variability in LYZ crystallization [335].

We postulated that the fluctuations in the CSD among the replicates were caused by the random nature of the agglomeration of the small crystals in the batch crystallizer. Therefore, in order to improve the CSD's reproducibility, we believed that the agglomeration should be limited by reducing the small crystals formation, while at the same time the crystal growth should be promoted. The formation of small crystals could be reduced by suppressing the secondary nucleation by operating the crystallization in an environment of reduced shear rates, such as in CSFC. By suppressing the secondary nucleation, crystal growth would become the predominant mechanism for crystal formation. This idea was manifested in our hybrid batch-CSFC design discussed in the next section.

5.3.3 Seeded LYZ crystallization in the hybrid batch-CSFC

To reduce the small crystals formation by secondary nucleation, we opted to reduce the residence time of the LYZ seeds and LYZ solutes spent in the batch crystallizer by transfer- ring out the batch solution at a constant flowrate (i.e., 0.265 mL/min) to a downstream CSFC. As a result, the τ_{batch} was reduced from 3 h in the fully batch crystallizer to 75 min in the hybrid batch-CSFC. In the hybrid platform, the nucleation and growth events were segmented to occur separately in the batch crystallizer and CSFC, respectively. The effects of the residence time of the CSFC (τ_{CSFC}) were investigated at τ_{CSFC} equal to 110 min and 220 min, which were achieved by varying the tube length (6.5 m and 13 m, respectively) at a fixed flowrate of 0.265 mL/min.

It was worth noting that the same crystallization condition (hence the supersaturation level) as the one studied in the batch crystallizer was used in the hybrid batch-CSFC. Not unexpectedly, the control experiment without seeds produced a negligible yield indicating the absence of crystallization. In the presence of the LYZ seeds at 5% (w/w) seed loading, the experimental yield at τ_{CSFC} = 110 min was determined to be equal to 10.2 ± 1.0% (w/w) (**Table 5.3**). The yield increased to 24.3 ± 2.5% (w/w) upon doubling τ_{CSFC} to 220 min. These results suggested that the LYZ crystallization in the hybrid batch-CSFC occurred at a much slower rate compared to that in the batch platform, where yield > 50% was achieved after a

similar residence time. The slower crystallization rate was caused by the suppression of the secondary nucleation, which was widely known to be the predominant mechanism of crystal formation in seeded crystallization [336].

Table 5.3 Seeded LYZ crystallization in the hybrid batch-CSFC – CSD and crystallization efficiency.

τ_{batch}, $\tau_{tubular}$ (min)	d_{ave} (μm)	d_{10} (μm)	d_{50} (μm)	d_{90} (μm)
75, 110-220	7.5 ± 1.4	1.8 ± 0.1	4.7 ± 1.1	17.7 ± 1.3
Span	Yield (% w/w)	PC (mg/h)	$M_{Product/Seed}$ (% w/w)	STY (mg/L · h)
3.47 ± 0.53	24.3 ± 2.5	3.3 ± 1.5	17 ± 7	57 ± 26

At τ_{CSFC} = 220 min, the LYZ crystals produced exhibited d_{ave} = 7.5 ± 1.3 μm with a Span value of 3.47 ± 0.53 indicating a very wide CSD (**Figure 5.6A**) with d_{10} =1.8 ± 0.1 μm, d_{50} =4.7 ± 1.1 μm, and d_{90} =17.7 ± 1.3 μm (**Table 5.3**). Indeed, the light microscope image of the LYZ crystals produced showed the appearance of two types of crystals, namely large tetragonal- shaped individual crystals (≈ 10−20 μm) and agglomerates of the smaller crystals (<5 μm) (**Figure 5.6B**). On one hand, the formation of the large individual crystals signified the success of the segmented nucleation and growth design in the hybrid batch-CSFC in enhancing the growth of the seed crystals. The extended growth of the seed crystals was not observed when the batch crystallizer was used. On the other hand, the still significant presence of the small crystals and their agglomerates indicated that the secondary nucleation was not completely suppressed in the hybrid batch-CSFC.

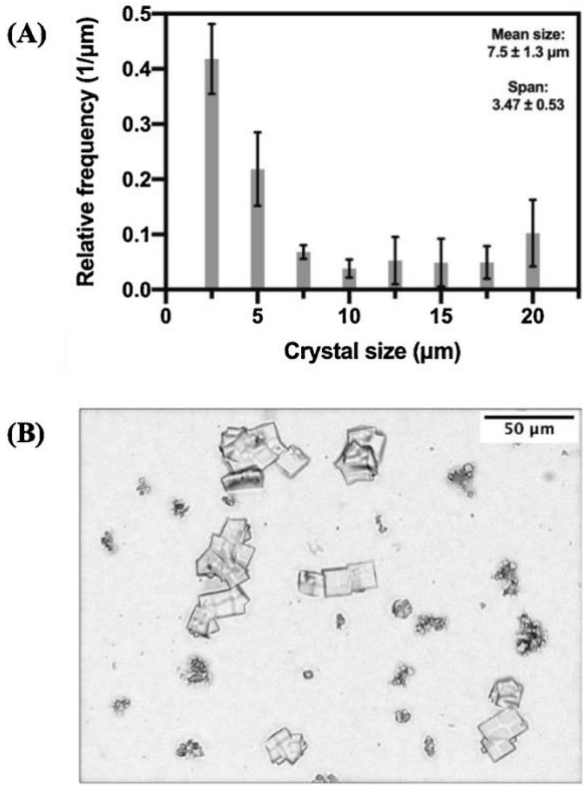

Figure 5.6 Seeded LYZ crystallization in the hybrid batch-CSFC at 5% (w/w) seed loading - (A) CSD; (B) light microscope image of the LYZ crystals produced.

For the CSD's reproducibility, the CVs of d_{ave} and Span were calculated to be equal to 17.29% and 15.27%, respectively. Compared to the CVs of the batch crystallizer, the lower CVs of the hybrid batch-CSFC signified an improvement in the variability of the crystallization process, which was as expected upon adoption of a continuous crystallizer. Nevertheless, the enhanced growth of the seed crystals and the improved variability exhibited by the hybrid batch-CSFC were obtained at the expense of the crystallization rate, which had slowed down considerably.

The slow crystallization rate in the hybrid batch-CSFC mandated an operation of the CSFC at a slow flowrate to avoid having to use unreasonable long tubes. As a result of the slow flowrate, the hybrid batch-CSFC was prone to poor production throughput. The $M_{Product/Seed}$ of the hybrid batch-CSFC was significantly less than 100% at 17 ± 7% (w/w), indicating that a large majority of the product crystals, as well as the original LYZ seeds, did not successfully exit the CSFC. The product crystals were likely sedimented inside the tube due to the low flowrate, despite the inertial force

afforded by the gas bubbles. This impediment to the flow led to practically negligible PC and STY for the hybrid batch-CSFC (**Table 5.3**).

In this regard, even though the $M_{Product/Seed}$ in the hybrid batch-CSFC could certainly be improved by increasing the flowrate, the higher flowrate would reduce both $\boldsymbol{\tau_{batch}}$ and τ_{CSFC}. In turn, the tube length of the CSFC ought to be extended to maintain a sufficient τ_{CSFC} for crystal growth and to achieve a reasonable yield. Consequently, the crystallization would predominantly take place in the longer CSFC as the LYZ seeds and solutes would only spend a short time in the batch crystallizer. Hence, operating the hybrid batch-CSFC at a higher flowrate would make it closer in mimicking a full CSFC. Therefore, we shifted our attention to a full CSFC as discussed in the next section.

5.3.4 Seeded LYZ crystallization in the CSFC

5.3.4.1 Effects of τ_{CSFC} and flow rate

At seed loading of 5% (w/w), the effects of τ_{CSFC} were examined by varying the flowrate (Q = 0.150−0.375 mL/min) at a fixed tube length of 22.5 m. Specific for Q = 0.150 mL/min, the CSFC's length was also investigated at 17.2 m to examine the impact of varying τ_{CSFC} at a fixed flowrate. The residence time in the continuous stirred-tank crystallizer ($\tau_{stirred-tank}$) and in the CSFC (τ_{CSFC}) at the different Q values were presented in **Table 5.4**, together with their resultant crystallization performances. The same crystallization condition as the one studied in the batch crystallizer was used in the CSFC, resulting in the similar supersaturation level. Not unexpectedly, the control experiments without the LYZ seeds produced negligible yield as the supersaturation level lay below the metastable zone limit.

At Q = 0.150 mL/min, the experimental yield was deter- mined to be equal to 18.9 ± 1.3% (w/w) at tube length of 17.2 m (τ_{CSFC} = 170 min). The yield increased to 27.9 ± 4.9% (w/w) upon extending the tube length to 22.5 m (τ_{CSFC} = 220 min). For comparison, the batch crystallizer resulted in yield > 55% under a similar residence time ($\boldsymbol{\tau_{batch}}$=240 min), hence denoting the much slower crystallization rate of LYZ in the CSFC at this Q. Similar to the hybrid batch-CSFC, the slow

crystallization rate in the CSFC at Q = 0.150 mL/min was attributed to the suppression of secondary nucleation in the low-shear rate environment of the millifluidic CSFC. In this regard, the shear rate in the CSFC at Q = 0.150 mL/min was calculated from the linear velocity to be equal to 0.71 s^{-1}, which was more than one order of magnitude lower than the shear rate experienced in the batch crystallizer (i.e., 60.2 s^{-1}). Sample calculations for the shear rate were provided in the Supplementary Materials.

Table 5.4 Seeded LYZ crystallization in the CSFC – crystallization efficiency.

Q (mL/min)	Seeds (% w/w)	$\tau_{stirred\ tank}$ (min)	τ_{CSFC} (min)	Exp. Yield (% w/w)	PC (mg/h)	$M_{Product/Seed}$ (% w/w)	STY (mg/L · h)
0.150	5	110	170	18.9 ± 1.3	9.0 ± 0.3	28 ± 7	71 ± 2
			220	27.9 ± 4.9	8.7 ± 0.1	27 ± 1	58 ± 2
0.250	5	67	133	37.0 ± 3.6	63.5 ± 9.7	92 ± 24	423 ± 64
0.375	5	45	90	27.7 ± 1.9	387.8 ± 107.6	418 ± 138	2585 ± 740
0.375	10	45	90	35.2 ± 5.5	495.9 ± 174.0	219 ± 82	3305 ± 820

The LYZ crystals produced at Q = 0.150 mL/min bore resemblance to the crystals produced in the hybrid batch-CSFC, where well-defined large tetragonal LYZ crystals were visible indicating extended growth of the seed crystals (**Figure 5.6A**). The LYZ crystals exhibited d_{ave} of 8.1 ± 0.3 μm with a Span value of 2.12 ± 0.65 μm (**Table 5.5**). Similar to the hybrid batch-CSFC, the CSFC at Q = 0.150 mL/min exhibited poor production throughput with $M_{Product/Seed}$ equal to 28 ± 7% (w/w), as a result of the flow impediment caused by the low flowrate. Consequently, the PC and STY were practically negligible at roughly 9 mg/h and 60 mg/h·L, respectively.

The results at Q = 0.150 mL/min suggested that the flowrate in the CSFC ought to be increased, which led to shorter τ_{CSFC} as the tube length was maintained constant. Increasing the flowrate to Q = 0.250 mL/min, which reduced τ_{CSFC} to 133 min, was able to increase $M_{Product/Seed}$, PC, and STY to 92 ± 24%, 63.5 ± 9.7 mg/h, and 423 ± 64 mg/h·L, respectively. The yield was also increased to 37.0 ± 3.6% (w/w) denoting more LYZ solutes were transformed into LYZ crystals. The higher yield was

achieved despite the shorter τ_{CSFC}, hence signifying a faster crystallization rate. The shorter τ_{CSFC} resulted in the formation of tetragonal LYZ crystals with smaller d_{ave} of 5.8 ± 0.3 m and a Span value of 1.24 ± 0.01 (**Table 5.5**). Compared to the LYZ crystals produced at Q = 0.150 mL/min, the light microscope image showed an increased frequency of small non-tetragonal crystals (<5 μm) similar to those produced in the batch crystallizer at Q =0.250 mL/min (**Figure 5.6B**).

The increased formation of the small crystals at Q = 0.250 mL/min was also evident from the increased relative frequency of < 5 μm crystals in the CSD plot (**Figure 5.6B**). This was reflected further by the smaller d_{50} at Q =0.250 mL/min compared to the d_{50} at Q =0.150 mL/min. The increased formation of the small crystals at a higher flowrate was not unexpected as the increased shear rate to 1.18 s^{-1} at Q =0.250 mL/min increased the propensity of secondary nucleation, and simultaneously led to diminished crystal growth. The increased occurrence of secondary nucleation at Q =0.250 mL/min provided an explanation for the higher yield, despite the shorter τ_{CSFC}. However, as $M_{Product/Seed}$ was still below 100%, the flow impediment remained in existence at Q =0.250 mL/min, therefore a further increase in the flowrate was needed.

Our investigation revealed that the flowrate ought to be increased to a minimum Q of 0.375 mL/min to achieve $M_{Product/Seed}$ higher than 100%. At Q =0.375 mL/min, $M_{Product/Seed}$ was determined to be equal to 418 ± 138% w/w, which signified that the flow impediment in the CSFC had been overcome. Thereby, the product crystals could be effectively recovered at the CSFC's outlet. At Q =0.375 mL/min, PC and STY were determined to be equal to 387.8 ± 107.6 mg/h and 2585 ± 740 mg/h·L, respectively. Significantly, these PC and STY values were in the same order of magnitude as the values exhibited by the batch crystallizer presented earlier in **Table 5.2** (i.e., PC = 231.7 ± 6.8 mg/h and STY=4633 ± 136 mg/h·L). Compared to Q =0.250 mL/min, the yield, however, decreased to 27.7 ± 1.9% (w/w) at Q =0.375 mL/min as a result of the shorter τ_{CSFC}, which was further reduced to 90 min.

The light microscope image in **Figure 5.6C** showed that the higher shear rate (1.77 s^{-1}) at Q =0.375 mL/min led to an even more formation of the small non-tetragonal crystals due to secondary nucleation. The shorter τ_{CSFC} also led to a

minimal amount of well-defined tetragonal LYZ crystals being produced as there was insufficient time for crystal growth. Nevertheless, as the small crystals readily formed agglomerates, the CSD plot in **Figure 5.6C** did not show an increase in the relative frequency of <5 μm crystals. In fact, the <5 μm frequency was reduced when compared to that at Q = 0.250 mL/min. The agglomerate formation led to d_{ave} of 6.5 ± 0.3 μm and a Span value of 1.22 ± 0.13 (**Table 5.5**).

In essence, the LYZ crystals produced at Q =0.375 mL/min share similar characteristics as the crystals produced in the batch crystallizer at τ_{CSFC}= 3 h, where agglomerates of small non-tetragonal LYZ crystals were also observed. The CSD analysis revealed that the agglomerates in the batch crystallizer were larger, resulting in the slightly larger d_{ave} and d_{50} at 8.3 ± 2.5 μm and 7.0 ± 3.6 μm, respectively. Two main differences in the LYZ crystals produced between the batch crystallizer and the CSFC at Q =0.375 mL/min lay in the resultant Span value and the CSD's reproducibility.

First, the Span value of the CSFC was lower at 1.22 ± 0.13 versus 2.38 ± 0.96 for the batch crystallizer, hence indicating a narrower CSD for the former. The narrower CSD was postulated to be caused by less formation of large agglomerates in the CSFC attributed to its first-in-first-out flow characteristics for the crystals produced. Second, the CSD's reproducibility in the CSFC was found to be greatly superior with CVs of d_{ave} and Span among the replicates calculated to be equal to approximately 5.1% and 10.6%, respectively. For comparison, as reported earlier, the CVs in the batch crystallizer were higher than 30%.

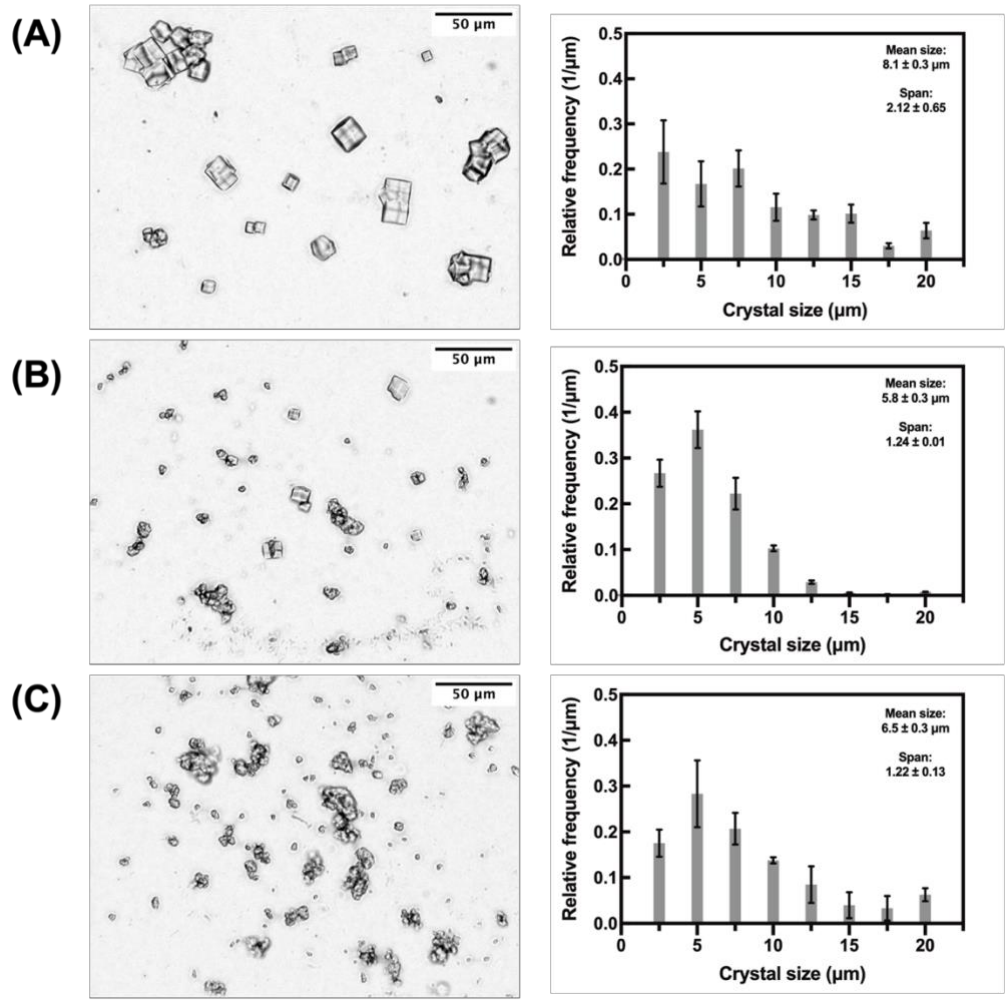

Figure 5.7 Seeded LYZ crystallization in the CSFC at 5% (w/w) seed loading - light microscope images and CSDs of the LYZ crystals produced investigated at different flowrates - (A) Q = 0.150; (B) Q = 0.250; (C) Q = 0.375 mL/min.

Table 5.5 CSD parameters of LYZ crystals produced in the continuous crystallizer

Q (mL/min)	Seeds (% w/w)	d_{Ave} (µm)	d_{10} (µm)	d_{50} (µm)	d_{90} (µm)	Span
0.375	5	6.50 ± 0.33	2.56 ± 0.21	5.33 ± 0.08	11.58 ± 0.45	1.22 ± 0.13
0.375	10	6.96 ± 0.29	3.13 ± 0.30	6.44 ± 0.22	11.00 ± 0.81	1.69 ± 0.02
0.250	5	5.77 ± 0.29	2.86 ± 0.23	5.25 ± 0.09	9.35 ± 0.36	1.24 ± 0.01
0.150	5	8.53 ± 3.17	3.48 ± 0.97	6.97 ± 2.12	14.81 ± 5.96	1.62 ± 0.24
		8.11 ± 0.33	2.41 ± 0.14	6.63 ± 1.30	15.63 ± 1.39	2.12 ± 0.65

5.3.4.2 Effects of seed loading

In this section, we explored the feasibility of improving the crystallization performance of the CSFC at Q =0.375 mL/min by increasing the seed loading to 10% (w/w). Compared to the results at 5% (w/w) seed loading, the results in Table 3 showed that the higher seed loading led to a higher yield of 35.2 ± 5.5% (w/w) and a higher PC of 495.9 ± 174.0 mg/h. The higher PC, however, did not suggest an increase in the crystal production because $M_{Product/Seed}$ was found to be lower at 219 ± 82% (w/w). The fact that $M_{Product/Seed}$ was roughly halved when the seed loading was doubled indicated that the number of crystals recovered as products was relatively unchanged, despite the higher yield.

The higher seed loading was found to have a relatively small impact on the CSD with d_{ave} = 7.0 ± 0.3 µm and Span =1.69 ± 0.02 (**Table 5.5**) (**Figure 5.7**). Similar to the crystals produced at 5% (w/w) seed loading, the light microscope image showed that the LYZ crystals produced at 10% (w/w) seed loading predominantly existed as agglomerates of small non-tetragonal crystals (**Figure 6.7**). For comparison, a previous study by Gross and Kind [39] on batch seeded evaporative crystallization of LYZ reported a decrease in d_{ave} upon increase in the seed loading, which was attributed to increased secondary nucleation. This trend was not observed in the present study likely due to the different crystallization's driving force and platform used.

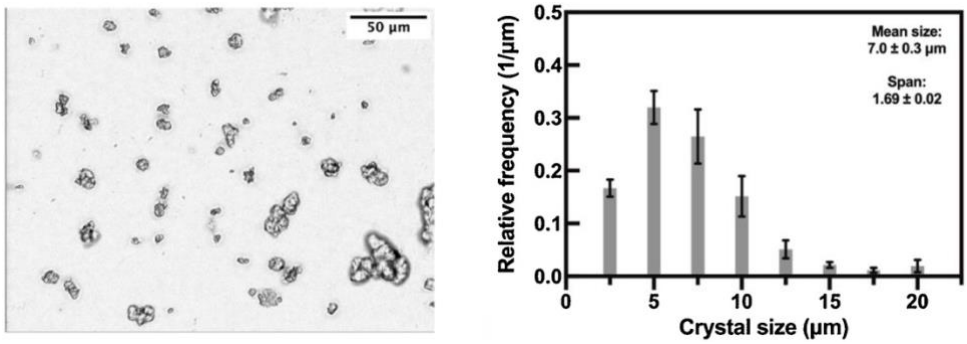

Figure 5.8 Seeded LYZ crystallization in the CSFC at 10% (w/w) seed loading and Q =0.375 mL/min - light microscope image and CSD.

5.3.5 LYZ activity

One of the most important criteria of any protein crystallization process is its ability to preserve the protein's activity during and after crystallization. During crystallization, impurities from within the process, as well as solvent inclusion, could be incorporated into the product crystals by adsorption onto the crystal surface and/or absorption into the crystal lattice [337]. Their inclusion would adversely affect the protein's activity. Furthermore, shear forces generated in the crystallizers could also cause protein unfolding and aggregation, resulting in reduced activity [338]. After taking into account the experimental uncertainties, the results in **Table 5.6** showed that nearly all the LYZ crystals exhibited comparable bioactivities as the highly pure LYZ crystals used as the raw materials. One exception was the LYZ crystals produced in the hybrid batch-CSFC, which exhibited a higher activity at 117.0 ± 3.3%, which was likely attributed to the increased presence of well-defined tetragonal LYZ crystals in its products. These results indicated that all the three crystallization platforms did not have an adverse effect on the LYZ activity.

Table 5.6 LYZ activities of the LYZ crystals produced from the different crystallization platforms.

Type of LYZ crystals	LYZ activity
Raw LYZ	100%
LYZ Seeds	103.5 ± 5.3%
Prepared by batch (3 h)	99.0 ± 5.5%
Prepared by hybrid batch-CSFC	117.0 ± 3.3%
Prepared by CSFC (Q = 0.150 mL/min, 5% seeds)	102.8 ± 5.2%
Prepared by CSFC (Q = 0.250 mL/min, 5% seeds)	105.8 ± 9.7%
Prepared by CSFC (Q = 0.375 mL/min, 5% seeds)	106.5 ± 5.4%

5.4 Conclusion

The present work established that performing bulk seeded crystallization of LYZ in the CSFC resulted in superior CSD's width and reproducibility compared to the batch crystallizer, which we attributed to the less random agglomeration of the smaller crystals produced. The CSFC produced LYZ crystals of similar d_{ave} and

morphology as the batch crystallizer, but at lower yield and STY due to the slower crystallization rate in the CSFC caused by its considerably lower shear rate compared to the batch crystallizer. The flowrate, which affected the residence time, was established as the governing process variable in the CSFC, where a minimum threshold existed for the flowrate below which the recovery of the seeds and product crystals were poor due to flow impediment. A trade-off existed upon increasing the flowrate between crystallization efficiency and crystal quality. At low flowrates below the minimum, large well-defined tetragonal LYZ crystals were produced owed to suppressed secondary nucleation, while concurrently crystal growth flourished owed to the prolonged residence time. Increasing the flowrate led to increased production of small non-tetragonal LYZ crystals with strong tendency to agglomerate, but with significantly improved recovery of the products. At the highest flowrate investigated, the CSFC produced LYZ crystals with $d_{ave} \approx 6.5$ μm, yield ≈ 28% (w/w), and STY ≈ 2585 mg/h·L. While the yield could be improved by extending the CSFC's length, this might lead to lower STY. The seed loading was found to have a minimal impact on the CSFC's performance. Lastly, the activity of the LYZ crystals were not adversely affected by the CSFC.

CHAPTER 6 IMPROVING THE REPRODUCIBILITY OF SIZE DISTRIBUTION OF PROTEIN CRYSTALS PRODUCED IN CONTINUOUS SLUG FLOW CRYSTALLIZER OPERATED AT SHORT RESIDENCE TIME

This chapter has been published as **Siyu Pu,** Kunn Hadinoto, Improving the reproducibility of size distribution of protein crystals produced in continuous slug flow crystallizer operated at short residence time, *Chemical Engineering Science*, Volume 230, 2021, 116181. Permission has been granted by the licensed publisher "Elsevier" for utilization of the published content as a chapter in this thesis [47].

6.1 Introduction

The market demands for protein-based biopharmaceuticals (e.g., monoclonal antibody, therapeutic enzymes, and protein vaccines) have steadily increased over the past decades, with expected global sales revenue of $125 billions for monoclonal antibody alone in 2020 [339]. Concurrently, significant advancements have been made in cell culture technologies to meet the increased demands, resulting in order-of-magnitude increase in the upstream production titers of pharmaceutical proteins [327]. To keep up with the increased production, crystallization has emerged as a promising downstream processing (DSP) strategy for the purification of pharmaceutical proteins that can potentially serve as a viable alternative to chromatography. Chromatography - the standard DSP workhorse - becomes much less efficient at high upstream production titers due to the high resin and buffer costs, small volume capacity, and the requirement for multicycles operation [6]. In addition to the cost benefits, crystalline proteins exhibit superior physicochemical stability, purity, and dissolution characteristics compared to amorphous proteins typically obtained from the conventional process [9]. While a large majority of studies on pharmaceutical protein crystallization have been performed in the batch platform, continuous protein crystallization has been pursued in recent years to address the

limitations of the batch process (e.g., batch-to-batch inconsistency, poor scalability, and significant process downtime) [209]. A similar shift towards the continuous platform has been pursued years earlier in the crystallization of small-molecule pharmaceuticals [216, 235, 340]. A number of studies have successfully demonstrated continuous crystallization of proteins using mixed-suspension mixed-product removal crystallizers (MSMPRC) [45] and two types of tubular crystallizers, i.e. slug flow crystallizer [46] and oscillatory flow baffled crystallizer [242, 243]. The state of the art of continuous crystallization of pharmaceutical proteins has been reviewed recently in [10].

Compared to MSMPRC, the mild operating condition in tubular crystallizers makes them ideal for crystallization processes in which particle attrition needs to be minimized as large crystals are desired, and also for crystallization of labile proteins with strong denaturation tendency under shear (e.g., insulin) [226]. Specific to cooling crystallization, tubular crystallizers offer better control of the heat transfer owed to their larger surface-to-volume ratio, resulting in better crystallization performance [200]. In protein crystallization, tubular crystallizers are typically operated at slow to moderate fluid velocity (<10 mm/s) as a number of flow crystallization studies showed that high shear rates inhibit the protein crystal's growth rate [251, 341], resulting in the production of fines that are less desirable for solid handling and drug dosage formulation purposes.

In slug flow crystallizers (SFC), a segmented gas-liquid flow, consisting of a string of gas bubbles separated by liquid slugs of the crystallization solution, flows concurrently in a tube [52]. The presence of the gas bubbles prevents tube clogging from occurring as the flowing bubbles facilitate constant net flows of the crystals produced in the liquid slugs [53]. The constant net flow of crystals also leads to narrow residence time distribution of the crystals, which in turn improves crystal qualities in small-molecule pharmaceutical crystallization [54]. Moreover, the internal fluid circulation in the liquid slugs renders each slug operate as a well-mixed crystallizer with homogeneous supersaturation, resulting in monodispersed crystals [55].

Using lysozyme as the model protein, Neugebauer and Khinast [46] reported for the first time the application of SFC to produce protein crystals by combined salting out and cooling crystallization principles. Lysozyme crystals with an estimated average size of ≈26 mm were successfully produced at ≈68% yield after 113 min residence time. The SFC was segmented into three sections in series (i.e., one for nucleation and two for crystal growth), where each section was set at different temperatures between 20°C and 22.5°C to achieve different supersaturation levels. As highlighted by the authors themselves, the crystallization could have been performed at lower temperatures to increase the supersaturation levels, thereby a higher crystallization yield could be obtained at the same residence time, or a comparable yield could be obtained at shorter residence time.

In this regard, short residence time operation of a crystallizer at a high supersaturation level is often desired to increase the production capacity (g/h) and consequently the space-time yield (g/ L·h). Crystallization at short residence time, however, is known to have adverse effects on the crystal quality, where small crystals with inconsistent size distributions are often produced due to (i) the higher nucleation rate as a result of the high supersaturation level and (ii) uncontrolled agglomeration of the small crystals produced [56, 57].

In the preliminary study of the present work, we carried out continuous crystallization of lysozyme in SFC operated at short residence time (<40 min) with a yield of ≈70%, which was comparable to the yield reported in [46]. The shorter residence time was achieved by increasing the supersaturation level via cooling crystallization at a lower temperature (i.e., 10°C). Not surprisingly, as discussed in more detail later, the results showed a bimodal crystal size distribution (CSD) with a significant production of crystalline fines. Furthermore, large fluctuations in the average crystal size and the CSD width also occurred between replicates (n = 4). Prolonging the residence time by extending the tube length aimed at stabilizing the process did not lead to an improvement in the reproducibility of the CSD either.

The objective of the present work was therefore to develop a crystallization strategy to improve the CSD and the reproducibility of the CSD of lysozyme crystals produced in SFC operated at short residence time and a high supersaturation level. In

most situations, a good CSD is characterized by a narrow size distribution of large crystals. Therefore, crystal growth is favored over nucleation, particularly secondary nucleation, which has a large influence on the resultant CSD [342]. Suppression of the nucleation at high supersaturation levels, however, is very challenging, even for macromolecules such as proteins, which are known to nucleate at a much slower rate than small molecules [39].

Our proposed strategy thus relied on limiting the space time of the nucleation by means of a segmented SFC design consisting of a short rapid nucleation segment and a longer segment for crystal growth, where the growth segment is operated at a higher temperature to quickly reduce the supersaturation level. The crystalline nuclei produced in the rapid nucleation segment of the SFC (achieved by crash cooling crystallization of lysozyme at 4°C) were intended to function essentially as seed crystals that would facilitate crystal growth in the growth segment. The proposed strategy was similar in principle to in-situ seeded crystallization performed at a high seed loading ratio aimed at suppressing nucleation and promoting crystal growth.

In the present work, two designs of segmented SFC that varied in (1) the temperature and length of the growth segment, and (2) the fluid velocity and lysozyme concentration of the crystallization solution entering the growth segment, were proposed and examined. The improved SFC designs were examined in terms of their resultant (i) CSD, (ii) reproducibility of the CSD, (iii) space-time yield, (iv) production efficiency, and (v) activity of the crystallized lysozyme. Their performance was compared with the base case design (i.e., non-segmented SFC operated at 10°C).

6.2 Materials and methods

6.2.1 Materials

Lysozyme (LYZ) from chicken egg white (purity $\geq$ 90%, activity $\geq$ 20,000 units/mg) was purchased from Bio Basic (Singapore). Sodium acetate ($\geq$99%), glacial acetic acid, sodium chloride (NaCl), and LYZ activity kit were purchased from Sigma-Aldrich (Singapore). The crystallization solution was prepared by

dissolving LYZ (50–200 mg/mL) in 100 mM sodium acetate buffer containing 16 mg/mL NaCl adjusted to pH 4.6 by the addition of acetic acid. Aqueous NaCl solution (64 mg/mL) was used as the salting-out agent. Deionized (DI) water was used in the preparation of all solutions. Prior to use, all solutions were filtered in 0.2-lm PES membrane filters (NALG565-0020, VWR, Singapore) under vacuum.

6.2.2 Methods

6.2.2.1 Base case SFC design

Tygon® silicone microbore tubing having inner diameter (ID) of 1.59 mm and outer diameter (OD) of 3.18 mm was used to construct the SFC with total length of 6.5 m. The tubing was coiled on a plastic spool and immersed in a circulating water bath (Model 9105, Polyscience, USA) set at 10°C to facilitate the cooling crystallization. Herein the 10°C cooling temperature was selected following the work of , which carried out LYZ crystallization in MSMPRC equipped with a cooled tubular bypass operated at 10°C, resulting in a significantly higher yield compared to that achieved at room-temperature.

The crystallization solutions comprising 90 mg/mL LYZ and 64 mg/mL NaCl solutions were prepared at room temperature (i.e., 22.5°C). A dual-syringe pump (Legato 200, KD Scientific, USA) equipped with 30-mL Luer-Lok syringes (BD, Canada) was used to continuously transport the crystallization solutions into the SFC. Mixing of the LYZ and NaCl solutions was achieved by passing the solutions through a polyethylene Y-junction connector (Cole-Parmer, USA) situated at the inlet of the SFC as illustrated in **Figure 6.1A**. The flowrates of the LYZ and NaCl solutions were both set at 0.15 mL/min, resulting in a 1:1 (v/v) mixture containing 45 mg/mL LYZ and 40 mg/mL NaCl in 50 mM acetate buffer at the SFC inlet.

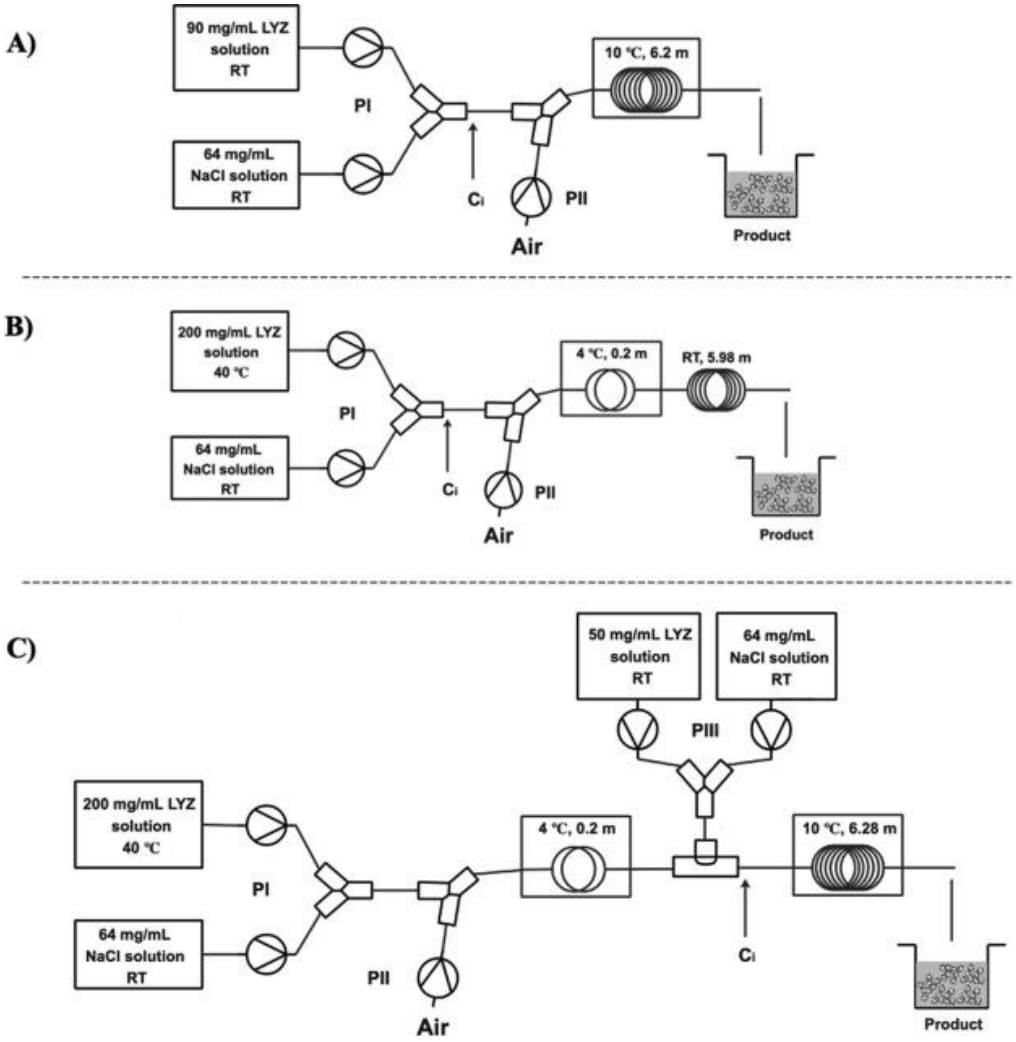

Figure 6.1 Schematic representations of the (A) base case; (B) "(N + G) 22.5°C"; (C) "(N + G) 10°C" SFC designs (RT = room temperature and P1, PII, PIII refer to the location of the syringe pumps).

A single syringe pump (NE-1010, New Era Pump Systems Inc., USA) was placed 0.1 m downstream of the Y-junction to inject air bubbles into the liquid flow at a fixed time interval using a 1- ml syringe (B. Braun, USA) filled with filtered air. Air bubbles having volume of ≈11.9 mm^3 was injected every 16 s to produce gas-liquid slug flow with air bubbles and liquid slugs' dimensions of 6 mm and 38 mm in length, respectively. The photograph of the gas-liquid slug flow was presented in **Figure 6.2**. The slugs then flowed into a 6.2-m long cooling crystallization section immersed in the 10°C water bath. The volumetric flow rate of the slug flow (liquid + gas) was

determined to be equal to ≈0.34 mL/min, which translated to fluid velocity of ≈2.83 mm/s.

Figure 6.2 Photograph of the gas bubble trains and the liquid slugs containing the crystallization solution from the base case SFC design

At 5-min interval, seven 1.5-mL aliquots of the LYZ crystal slurry were collected at the SFC outlet for characterizations. Afterwards, the flow to the SFC was stopped and the remnants inside the whole tube, which contained all the formed crystals and LYZ solutes that had not crystallized, were collected and analyzed. The study was repeated in SFC with total length (L) of 4.4, 8.6, 10.0, and 12.8 m to investigate the effects of residence time (s). Each crystallization experiment was repeated four times on four different days to investigate the reproducibility of the resultant CSD.

6.2.2.2 Improved SFC designs

The first segmented SFC design was schematically presented in **Figure 6.1B**. Briefly, the crystallization solutions comprising 200 mg/mL LYZ and 64 mg/mL NaCl solutions were prepared at 40°C and room temperature, respectively. The elevated temperature of 40°C was used to fully dissolve the high concentration of LYZ. The flowrates of the LYZ and NaCl solutions were set at 0.15 mL/min and the solutions were mixed after passing through a Y-junction, resulting in a 1:1 (v/v) mixture having temperature of ≈30°C and containing 100 mg/mL LYZ and 40

mg/mL NaCl in 50 mM acetate buffer. Air bubbles were injected at 0.02 m downstream of the Y-junction to produce gas–liquid slug flow with volumetric flow rate of ≈0.33 mL/min and fluid velocity of ≈2.77 mm/s.

The gas-liquid slugs then flowed into a 0.2-m long crash-cooling section of the SFC immersed in 4°C water bath. The crash-cooling section, which represented the rapid nucleation segment of the SFC, was positioned at 0.3 m downstream of the Y-junction for the air bubbles to ensure the existence of stable slug flow prior to the crash-cooling section. Upon exiting the crash-cooling section, the slurry flowed into the 5.98-m long growth segment of the SFC maintained at the room temperature (i.e., 22.5°C). Seven 1.5-ml aliquots of the LYZ crystal slurry were collected at the SFC outlet for characterizations. Overall, the SFC in the first design had a total length of 6.5 m of which 0.2 m and 5.98 m were designated for the rapid nucleation and growth segments, respectively. Henceforth, this SFC design was referred to as "(N + G) 22.5°C" design in the texts, where N and G stood for nucleation and growth, respectively, and 22.5°C referred to the temperature of the growth segment.

The second segmented SFC design was schematically shown in **Figure 6.1C**. The second design was identical to the "(N + G) 22.5°C" design in the rapid nucleation segment, but differed in the growth segment. In the second design, a fresh stream of LYZ was added and a lower temperature of the growth segment (i.e., 10°C) was used. Specifically, fresh streams of 50 mg/mL LYZ and 64 mg/mL NaCl solutions (both at 0.15 mL/min) prepared at room temperature were mixed after passing through a Y-junction to produce a 1:1 (v/v) mixture containing 25 mg/mL LYZ and 40 mg/mL NaCl. This fresh LYZ stream was then mixed with the stream exiting the crash-cooling section to produce a mixture containing approximately 54.4 mg/mL LYZ. Sample calculations for the LYZ concentration after mixing was provided in the Supplementary Materials. At 0.1 m downstream of the mixing point, the mixed LYZ streams flowed into the 6.28-m long growth segment of the SFC maintained at 10°C. Seven 1.5-ml aliquots of the LYZ crystal slurry were collected at the SFC outlet for characterizations. The volumetric flow rate of the mixed streams was equal to ≈0.61 mL/min, which translated to fluid velocity of ≈5.12 mm/s. Overall, the SFC in the second design had a total length of 7.0 m of which 0.2 m and 6.28 m were designated

for the rapid nucleation and growth segments, respectively. Henceforth, the second design was referred to as "(N + G) 10°C" design, where 10°C referred to the temperature of the growth segment. Herein the reported results of the "(N + G) 22.5°C" and "(N + G) 10°C" designs were based on four independent replicates performed on four different days.

6.2.2.3 Physical characterizations of LYZ crystals

The LYZ crystals produced were examined immediately upon collection using light microscope equipped with a camera (CKX41, Olympus, Japan) under the phase contrast mode at 400× magnification. The crystal size (d) was determined from the micro- scope images using the Feret's diameter macro in ImageJ software (NIH, USA). The CSD was determined from the number-averaged size (d_{Ave}) calculated from a minimum of 1000 crystal counts. The CSD's width (or Span) was calculated following **Eq. (2.9)**, where d_{10}, d_{50}, and d_{90} were the crystal size (mm) corresponding to the 10%, 50%, and 90% cumulative undersize of the CSD. The reproducibility of the CSD was determined from the coefficient of variation (CV) of the CSDs obtained from the four independent replicates, where CV was defined as the ratio of the standard deviation to the mean value.

The LYZ activity of the crystallized LYZ was examined in triplicates by the LYZ activity assay performed at 25°C and pH 7.0. The assay measured the reduction in the turbidity level of *Micrococcus lysodeikticus* bacterial cell suspension caused by the lysis of the cell walls upon exposure to LYZ. Step-by-step procedures to measure the turbidity level described in [332] were followed and not repeated here for brevity. LYZ crystals after 24-h lyophilization were used as the samples. Herein the activity of the crystallized LYZ was reported as its relative value (%) calculated with respect to the activity of the raw LYZ used in the feed.

6.2.2.4 Crystallization efficiency

The supersaturation level (S) in the different segments of the SFC was calculated by the ratio of the LYZ concentration entering that segment (C_S) to the

thermodynamic solubility of LYZ at the segment's temperature (C^*). The LYZ solubility in 50 mM acetate buffer containing 40 mg/mL NaCl (4% w/v) (pH 4.6) as a function of temperature was estimated using the empirical correlation provided in [343]. C_S of the crystallization slurry entering the growth segment was determined by centrifugation of the slurry (15,000 rpm, 5 min), followed by UV–Vis spectrophotometric analysis of the supernatant (UV Mini 1240, Shimadzu, Japan) at the optimal absorbance wavelength of LYZ, i.e. 280 nm [250].

The crystallization yield (% w/w) of the different SFC designs was determined in triplicates according to **Eq. (**3.1**)**, where C_i and C_o represented the concentration of LYZ solutes recovered in the SFC's inlet and outlet streams, respectively. The exact locations where C_i was sampled were indicated in **Figure 6.1** for each of the SFC design. The collected slurry sample (1.5 mL) was centrifuged after which the LYZ concentration in the supernatant was deter- mined by UV–Vis spectrophotometry as previously described. To complement the yield measurement, the LYZ concentration in the supernatant of the remnants after centrifugation was also measured by UV–Vis spectrophotometry, where R represented the ratio of the LYZ concentration in the supernatant of the remnant to C_i.

The production capacity (PC) in g/h was determined in triplicates by collecting 1.5-mL sample of the crystal slurry at the SFC outlet and the time duration for the sample collection was recorded. The mass of crystals contained in the slurry was deter- mined as follows: the slurry sample was centrifuged (15,000 rpm, 5 min) after which the sediments were lyophilized at -52°C and 0.05 mbar for 24 h in Alpha 1–2 LD Plus freeze dryer (Martin Christ, Germany). Afterwards, the lyophilized crystals were suspended in 1.5 mL 100 mM acetate buffer to dissolve the LYZ and the amount of LYZ was subsequently determined by UV–Vis spectrophotometry as previously described. The production efficiency (PE) was then calculated as the ratio of PC to the total mass flowrate of LYZ at the inlet.

The space-time yield, which was defined as the production capacity per unit volume of the crystallizer (g/L·h), was calculated from the PC value according to **Eq. (6.1)**. The volume of the 6.5-m long SFC used in the base case and ''(N + G) 22.5°C"

design was equal to 0.0129 L, whereas the volume of the 7.02-m long SFC used in the ‘‘(N + G) 10°C” was equal to 0.0139 L.

$$Space - time\ yield = \frac{PC}{Volume\ of\ SFC} \quad (6.1)$$

6.3 Results and discussion

6.3.1 Base case SFC design

6.3.1.1 Yield and stability

In the first part of the study, we carried out continuous crystallization of LYZ in the base case SFC design, which exemplified a short-residence-time operation of an SFC made possible by its operation at a high supersaturation level. In this regard, the S value in the base case design was approximately equal to 24.3 calculated based on the LYZ solubility (C^*) at 10°C (**Table 6.1**). From the phase diagram of LYZ crystallization at 10°C and 4% (w/v) NaCl presented in [331], this S value lay in the nucleation zone high above the metastable zone, hence primary nucleation should readily take place. For comparison, Neugebauer and Khinast [46] used a lower S value equal to 10 calculated based on the LYZ solubility at 22.5°C.

Table 6.1 Operating conditions and supersaturation levels of the base case and improved SFC designs.

SFC design	Temperature (°C)	Segment length (m)	C* (mg/mL)	C_S (mg/mL)	S	Inlet LYZ (g/h)
Base case	10	6.20	1.86 ± 0.10	45	24.3	0.81
(N+G) 22.5°C	4	0.20 (N)	1.14 ± 0.07	100	87.7	1.80
	22.5	5.98 (G)	5.80 ± 0.13	79.5	13.8	
(N+G) 10°C	4	0.20 (N)	1.14 ± 0.07	100	87.7	2.38
	10	6.28 (G)	1.86 ± 0.10	54.6	29.3	

As part of this study, we investigated the effects of residence time (τ) on the crystallization yield and CSD from which the optimal τ was determined. To the best of the authors’ knowledge, the effect of τ on protein crystallization in SFC had not

been investigated experimentally before. Herein τ was varied by varying L between 4.4 m and 12.8 m, resulting in s between 25.9 ± 0.2 min and 77.3 ± 0.4 min, respectively (**Table** 6.2). In addition, for each L investigated, the stability of the process, as characterized by the fluctuations in the LYZ concentration at the SFC outlet (C) among the seven aliquots taken at 5-min interval, was examined.

Table 6.2 Effects of the residence time on the yield and CSD for the base case SFC design.

Tube length (m)	Residence time (min)	Yield (% w/w)	d_{Ave} (μm)	d_{10} (μm)	d_{50} (μm)	d_{90} (μm)	Span
4.4	25.9 ± 0.2	57.07 ± 1.31	4.51 ± 1.40	1.65 ± 0.53	3.45 ± 1.13	8.62 ± 3.37	2.02 ± 0.45
6.5	38.8 ± 0.2	70.64 ± 1.19	8.90 ± 2.77	3.98 ± 2.49	7.63 ± 1.28	14.32 ± 5.60	1.34 ± 0.30
8.6	51.5 ± 0.3	74.56 ± 1.07	8.97 ± 2.79	3.55 ± 1.14	7.60 ± 2.48	16.62 ± 6.50	1.72 ± 0.39
10.0	59.7 ± 0.3	76.97 ± 0.85	9.04 ± 2.81	2.94 ± 0.94	7.25 ± 2.37	16.71 ± 6.53	1.90 ± 0.43
12.8	77.3 ± 0.4	79.17 ± 0.77	9.11 ± 2.83	3.63 ± 1.16	8.11 ± 2.65	14.95 ± 5.84	1.40 ± 0.31

The results of the stability test in Figure **6.3**A showed that the fluctuations in C/C_i among the seven aliquots decreased with increasing L (longer τ). This suggested that the operation at short τ below a certain threshold should be avoided as exemplified by the large fluctuations in C/C_i for L = 4.4 m. The stability test was performed using 28 data points (i.e., seven aliquots for each of the four independent replicates). The fluctuations were gradually reduced with increasing L as the complex multiphase gas-liquid-solid flow in the SFC became more fully developed.

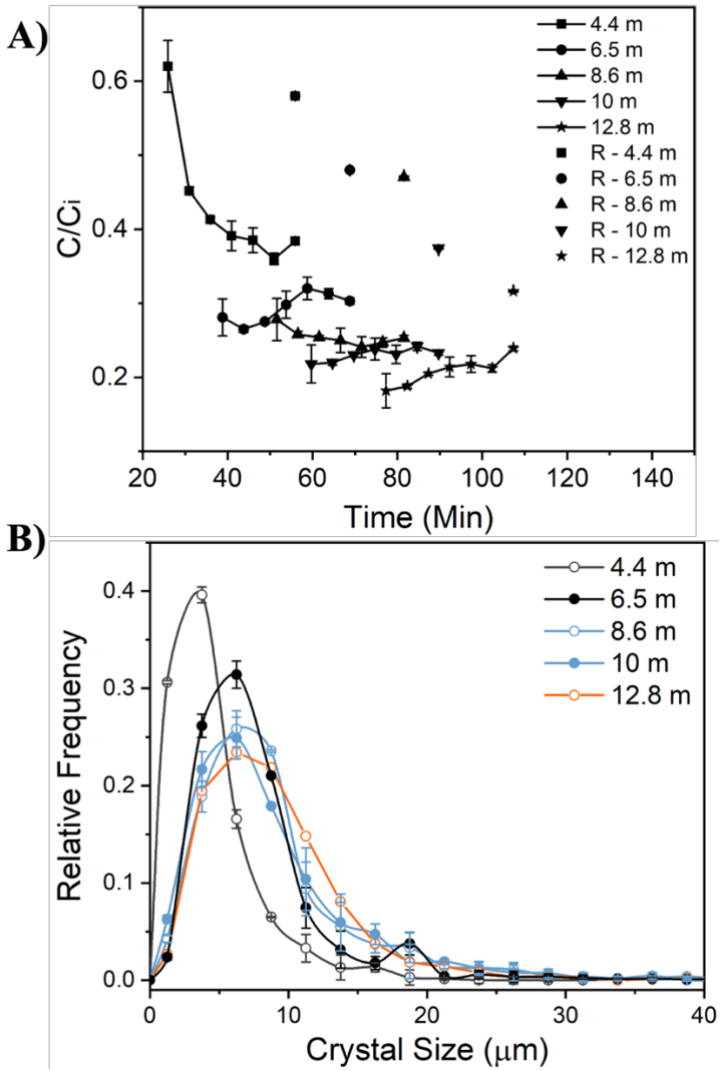

Figure 6.3 Effects of residence time (τ) on (A) the stability of the process and (B) CSD of the base case SFC design.

As expected, the yield calculated from the stable aliquots increased with increasing s from 57.07 ± 1.31% (w/w) at L = 4.4 m to 79.17 ± 0.77% (w/w) at L = 12.8 m (**Table** 6.2). Noticeably, the yield increased by only approximately less than 10% when L was almost doubled from 6.5 m to 12.8 m, which signified greatly diminished crystal growth rates at longer s due to the lower super- saturation level. In the present work, yield of ≈ 70% was achieved after τ = 38.8 ± 0.2 min (L = 6.5 m). For comparison, a significantly longer s of 113 min (L = 13 m) was needed in to achieve a comparable yield (≈ 68%) due to the lower S value used in their work. The higher yield at longer τ was also evident from the decrease in the LYZ solutes'

concentration in the remnants with increasing L. Specifically, R decreased from ≈ 0.580 at L = 4.4 m to ≈0.316 at L = 12.8 m indicating that as expected more LYZ solutes were crystallized at longer L (**Figure 6.3A**).

With regard to the CSD, the effects of increasing τ on d_{Ave} were found to be insignificant beyond L = 4.4 m. Specifically, d_{Ave} was equal to ≈ 4.5 mm at L = 4.4 m and it increased to ≈ 9 mm upon increasing L to 6.5 m (**Table** 6.2). d_{Ave} then remained constant at ≈ 9 mm for L between 6.5 m and 12.8 m. Based on the trends in the yield and d_{Ave}, there was little benefit in operating at L > 6.5 m as both yield and d_{Ave} increased very little with any further increase in L due to the diminished crystal growth rates.

On this note, the present d_{Ave} was significantly smaller than d_{Ave} ≈ 26 mm estimated from the CSD provided in [46]. The result was not unexpected as the higher S used in the present work led to an increased in the nucleation rate that promoted the formation of small crystals. The small crystals produced in the base case design, nevertheless, were less desirable as it would lead to difficult particle handling. Moreover, as discussed in the next section, the small crystals would lead to random agglomeration that adversely affected the CSD's reproducibility. Hence, improvements to the base case design that could increase the crystal size, while maintaining the short τ, were pursued in the present work.

6.3.1.2 CSD and its reproducibility

Next, the effects of τ on the CSD and its reproducibility between replicates (n = 4) were examined. The CSD at L = 6.5 m showed a bimodal CSD with frequency peaks at around 6.25 mm and 19 mm with Span value of 1.34 ± 0.30 denoting its large distribution width (**Figure 6.3B**). The same peak at 6.25 mm was observed in the CSD produced at L = 8.6, 10.0, and 12.8 m, albeit at a lower frequency, as the frequency was shifted towards larger crystal sizes as reflected by the increase in the frequency between 10 and 25 mm (**Figure 6.3B**). The shift towards the larger size resulted in larger Span values. Nevertheless, it did not lead to any significant increase in d_{Ave} as mentioned earlier.

The microscope image of the crystals produced at L = 6.5 m showed the appearance of individual LYZ crystals with sizes smaller than 10 mm and their agglomerates (**Figure 6.4A**). The second peak in the CSD at around 19 mm was thus attributed to the agglomerates of the individual crystals. In this regard, the microscope images of the crystals produced at L = 8.6, 10.0, and 12.8 m showed increased presence of agglomerates, while in contrast, the presence of agglomerates was not as evident at L = 4.4 m (**Figure 6.5**). The increased presence of agglomerates at longer τ observed in the microscope images was reflected in the CSD by the aforementioned shift in the frequency towards the larger crystal sizes.

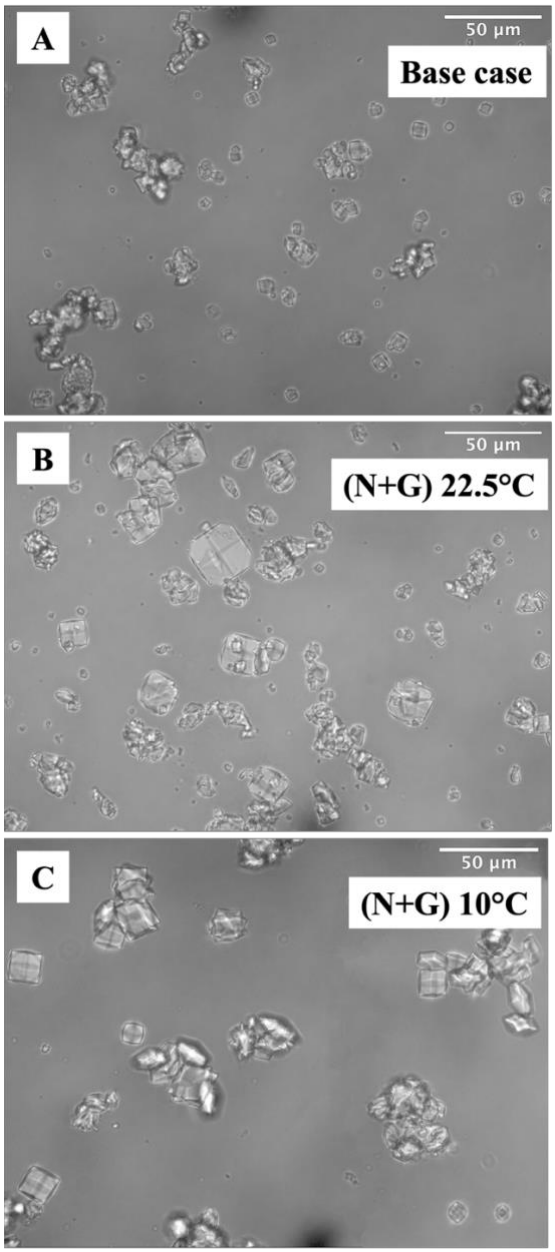

Figure 6.4 Light microscope images of the LYZ crystals produced by the (A) base case; (B) "(N + G) 22.5 °C"; (C) "(N + G) 10 °C" SFC designs.

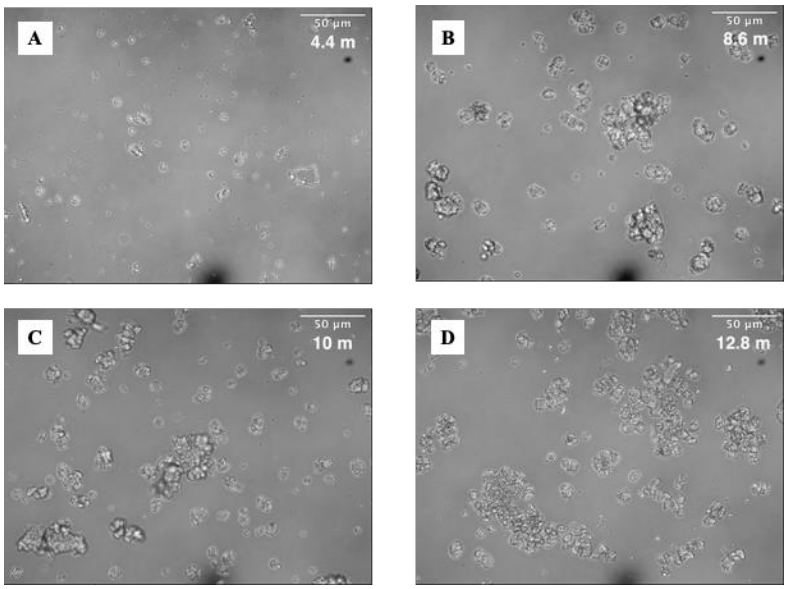

Figure 6.5 Light microscope images of the LYZ crystals produced at different residence time as expressed in terms of the tube length (A) 4.4 m; (B) 8.6 m; (C) 10 m; (D) 12.8 m

The increased agglomeration at longer τ was not unexpected as the longer τ led to more production of crystals, which were prone to agglomeration due to their small size as a result of the high nucleation rate. Furthermore, as the crystals recirculated within liquid slugs confined to a narrow tube, the more crystals produced, the higher tendency of the crystals to form agglomerates. The increased presence of agglomerates at longer τ, however, did not lead to statistically significant variations in d_{Ave}, as well as in d_{10}, d_{50}, d_{90}, and Span values of the CSD (**Table** 6.2). In fact, there were large fluctuations among the four replicates in each of these values, as evidenced by the large standard deviations and consequently CV values higher than 30%. In short, the CSD of the base case design exhibited low reproducibility caused by a strong tendency of the small crystals to form random agglomerates.

Taking into account the yield, d_{Ave}, and the fact that longer s led to more agglomeration, the optimal s for the base case design was determined to be equal to

≈ 39 min at L = 6.5 m. At this τ, the yield and PC of the base case design were determined to be equal to 70. 64 ± 1.19% (w/w) and 0.27 ± 0.02 g/h, respectively, which corresponded to space–time yield of 20.68 ± 1.76 g/L·h (**Table 6.3**). The improved SFC designs presented in the next section would be operated at comparable s or shorter for fair comparison with the base case design. Importantly, the crystallized LYZ exhibited comparable cell lysis activity as the raw LYZ at 89.5 ± 8.4%, hence indicating the absence of significant protein denaturation upon exposure to the shear forces in the SFC.

Table 6.3 Crystallization efficiency of the base case and improved SFC designs.

SFC design	Base case	(N+G) 22.5°C	(N+G) 10°C
Yield (% w/w)	70.64 ± 1.19	73.53 ± 1.80	66.99 ± 4.54
Residence time (min)	38.8 ± 0.2	39.1 ± 0.7	25.1 ± 0.8
PC (g/h)	0.27 ± 0.02	0.99 ± 0.03	1.30 ± 0.08
PE (% w/w)	33 ± 2	55 ± 2	54 ± 3
Space-time yield (g/L·h)	20.68 ± 1.76	76.74 ± 2.17	92.98 ± 8.12
LYZ activity (%)	89.5 ± 8.4	95.6 ± 4.9	93.7 ± 5.9

In the base case design, the PE calculated with respect to the inlet LYZ flowrate (i.e., 0.81 g/h) was equal to 33 ± 2% (w/w), hence approximately only 1=3 of the LYZ in the feed solution was successfully recovered as LYZ crystals at the outlet. The rests either remained as solutes or crystallized but did not come out of the SFC. In this regard, the yield was reported earlier to be equal to ≈70%, thus more than 2=3 of the LYZ in the feed crystallized. Therefore, nearly half of the crystallized LYZ remained in the tube, despite the presence of the moving air bubbles. This signified poor residence time distribution of the crystals as net movement of crystals became irregular. We postulated that random agglomeration of the small crystals that in turn caused local obstruction to the flow might be responsible for the poor residence time distribution of the crystals, which explained for the observed low reproducibility of the CSD.

6.3.2 Improved SFC design

6.3.2.1 "(N + G) 22.5 °C" design

In this section, we presented two improved SFC designs based on the principle of segmented nucleation and growth aimed at producing larger crystals and with improved CSD's reproducibility. In both designs, the nucleation segment was limited to a short length of 0.2 m (<5% of the total tube length) corresponding to τ_N of ≈1.2 min to minimize the formation of small crystals. The nucleation was induced by crash cooling of a highly concentrated LYZ solution at 4 °C to ensure sufficient formation of nuclei despite the short space time. The S value of the crash cooling section was equal to ≈87.7 calculated based on the LYZ solubility at 4 °C (**Table 6.1**). Under this highly supersaturated condition, metastable liquid-liquid phase separation (LLPS), where protein-rich and protein-lean phases coexisted, would occur according to the phase diagram of [344].

In the LLPS regime, the nucleation took place in the protein-lean phase and the crystals grew isotropically due to the high supersaturation driving force, resulting in the formation of round, convex shaped crystals [172, 345]. Indeed, the microscope image of the LYZ crystals produced in the crash-cooling section showed the appearance of round, convex shaped crystals accompanied by their agglomerates (**Figure 6.6A**). The CSD of the crash-cooled crystals showed a broad peak between 3.75 and 8.75 mm (**Figure 6.6B**) with d_{Ave} of 7.96 ± 1.04 mm (**Table 6.4**). The CSD exhibited a high Span value of 2.00 ± 0.27 due to the presence of both fines and large agglomerates.

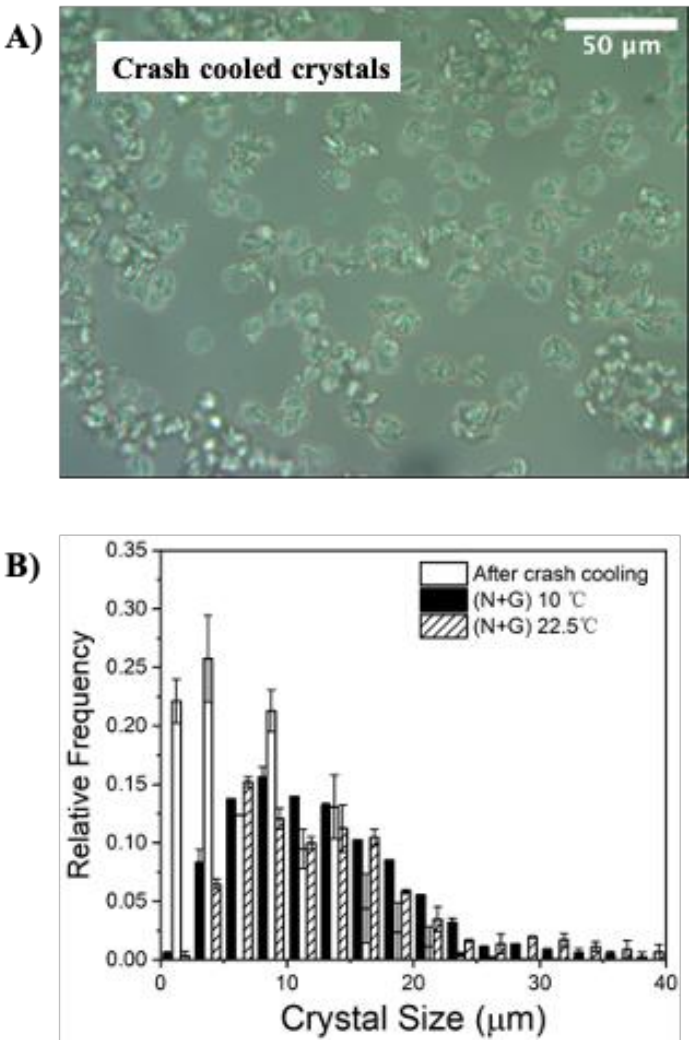

Figure 6.6 (A) light microscope image of the LYZ crystals produced in the crash-cooling section; (B) CSD of the crash-cooled crystals in comparison to the final crystal products of the "(N+G) 22.5 °C" and "(N+G) 10 °C" SFC designs

Table 6.4 CSDs of the base case and improved SFC designs and their reproducibility.

SFC design	Base case	Crash-cooled crystals	(N+G) 22.5°C	(N+G) 10°C
d_{Ave}	8.90 ± 2.77	7.96 ± 1.04	13.82 ± 2.0	13.15 ± 0.86
CV of d_{Ave}	0.311	0.131	0.145	0.065
d_{10}	3.98 ± 2.49	1.92 ± 0.10	5.31 ± 0.56	5.16 ± 0.17
CV of d_{10}	0.625	0.052	0.105	0.033

d_{50}	7.63 ± 1.28	7.10 ± 1.93	11.86 ± 1.74	11.50 ± 1.17
CV of d_{50}	0.168	0.272	0.147	0.102
d_{90}	14.32 ± 5.60	15.89 ± 1.83	25.33 ± 6.37	22.43 ± 2.19
CV of d_{90}	0.391	0.115	0.251	0.097
Span	1.34 ± 0.30	2.00 ± 0.277	1.70 ± 0.24	1.50 ± 0.02
CV of Span	0.224	0.135	0.142	0.013

The crash-cooled crystals then flowed into the 5.98-m long growth segment at 22.5 °C corresponding to τ_G of ≈36 min. The total τ of the "(N + G) 22.5 °C" design including the transit length between segments was determined to be equal to 39.1 ± 0.7 min (**Table 6.3**). As a result of the temperature rise and prior crystallization in the crash-cooling section, the S value of the LYZ solution entering the growth segment was lowered to ≈13.8 calculated based on the LYZ solubility at 22.5 °C. The LYZ concentration profile along the tube length in **Figure 6.7A** showed a quick drop in the LYZ concentration in the first 1.5 m of the growth segment to reach ≈ 31 mg/mL at L = 2.1 m corresponding to S value of ≈ 5.4. The quick drop in the LYZ concentration was attributed to rapid growth of the crash-cooled crystals at high S. Because of the high initial S in the growth segment, secondary nucleation also likely contributed to the decrease in the LYZ concentration.

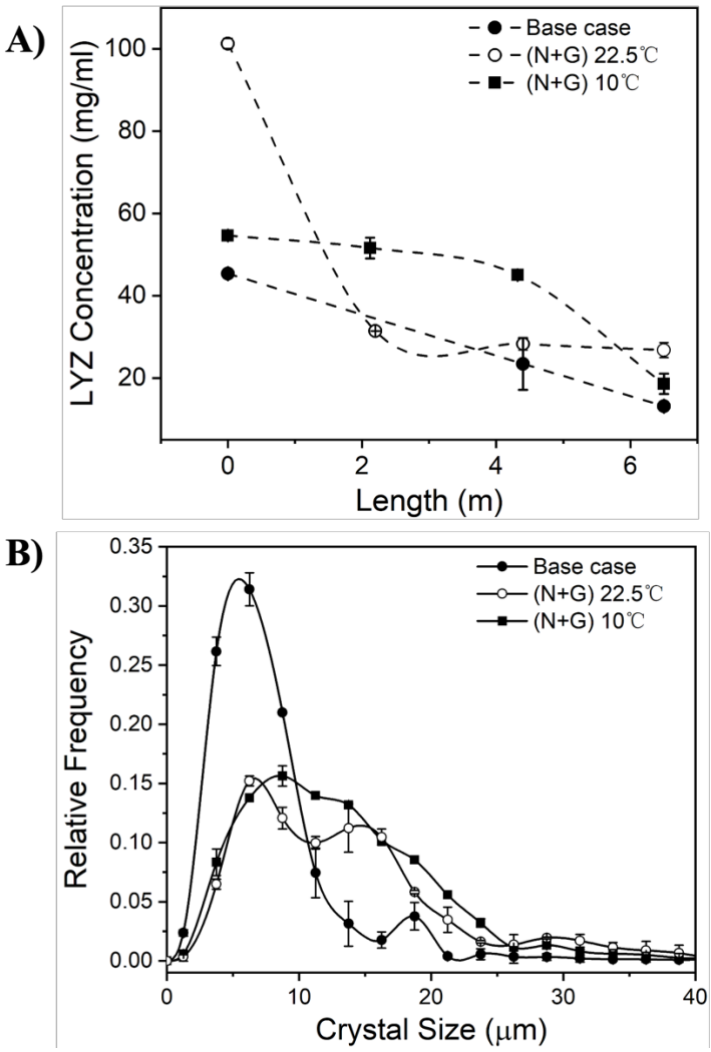

Figure 6.7 (A) The LYZ concentration profiles along the SFC tube length and (B) the resultant CSDs of the base case and improved SFC designs.

The LYZ concentration decreased at a much slower rate in the later part of the growth segment to reach ≈ 27 mg/mL at the outlet (L = 6.48 m), indicating that the crystal growth slowed down considerably at lower S. For comparison, the base case design produced a constant rate of decrease in the LYZ concentration as a function of L (**Figure 6.7A**). The base case's concentration profile was similar to that reported by [46] in each of their constant-temperature segments.

The LYZ crystal produced in the "(N + G) 22.5 °C" design exhibited a broad bimodal CSD with peaks at around 6.25 mm and 16.25 mm (**Figure 6.7B**) with d_{Ave} equal to 13.82 ± 2.0 mm (**Table 6.4**). Compared to the CSD of the base case, the

frequency of crystals with sizes in the range of 15–25 mm had been significantly increased and the small crystals' frequency (<10 mm) had been reduced by more than half. Nevertheless, the small crystals' population remained substantial as evidenced by the more dominant peak at 6.25 mm. In terms of the CSD's reproducibility, the "(N + G) 22.5 °C" design exhibited lower CV values for d_{Ave}, d_{10}, d_{50}, d_{90}, and Span compared to the base case (**Table 6.4**). Nevertheless, the CV values remained above 10%, which we postulated to be caused by random agglomeration of the smaller crystals similar to what was observed in the base case.

Indeed, the microscope image of the crystals showed the appearance of large LYZ crystals (>15 mm) accompanied by many smaller crystals that mostly existed as agglomerates (**Figure 6.4B**). The significant presence of small crystals served as evidence that secondary nucleation took place in the growth segment. Agglomerations of the smaller crystals were reflected in the CSD by the considerable frequency of crystals having sizes in the 25 to 40 mm range. The presence of these large-sized agglomerates led to a wide size distribution reflected by the high Span value of 1.70 ± 0.24 (**Table 6.4**). On this note, even though agglomeration also took place in the base case, the frequency of crystals in the size range of 25 to 40 mm was almost negligible in the CSD of the base case, hence indicating smaller agglomerate size in the base case caused by the different operating condition between the two designs.

Compared to the base case, the yield of the "(N + G) 22.5 °C" design was only slightly higher at 73.53 ± 1.80% (w/w), which was not unexpected considering their similar s (**Table 6.3**). The PC, on the other hand, was significantly higher at 0.99 ± 0.03 g/h attributed to its higher LYZ concentration in the feed (i.e., 100 versus 45 mg/mL). This translated to space–time yield of 76.74 ± 2.17 g/L·h, which was nearly four times higher than that of the base case. The PE calculated with respect to the inlet LYZ flowrate (i.e., 1.80 g/h) was equal to 55 ± 2% signifying more efficient recovery of the LYZ crystals compared to the base case, where fewer crystals remained in the tube. This indicated better residence time distribution of the crystals, resulting in the aforementioned smaller fluctuations in the CSD among the four replicates (i.e., lower CV).

Similar to the base case, the crystallized LYZ from the "(N + G) 22.5 °C" design also exhibited comparable cell lysis activity as the raw LYZ at 95.6 ± 4.9% (**Table 6.3**), hence indicating the minimal effect of the crash-cooling section on the LYZ's physical integrity. In short, while the ''(N + G) 22.5 °C" design was able to increase the crystal size, space–time yield, and PE compared to the base case, while maintaining similar s as the base case, the reproducibility of its CSD still left much room for improvement.

6.3.2.2 "(N + G) 10 °C" design

In the "(N + G) 10 °C" design, we increased the velocity of the slug flow entering the growth segment to reduce the agglomeration with the objective of improving the CSD's reproducibility. This approach was based on the work of [46] that reported agglomeration in the SFC was reduced at higher velocity as the contact time among the crystals in the liquid slugs was reduced. As increasing the fluid velocity, hence shear rates, might have undesired effects of suppressing the crystal growth, which led to smaller crystals and lower yield, we strategized to increase the fluid velocity while simultaneously increased the supersaturation level to maintain the yield. This was achieved by lowering the temperature of the growth segment from 22.5 °C to 10 °C, hence making it identical to that of the base case. The fluid velocity was increased via mixing the stream exiting the crash-cooling section with a stream of fresh LYZ solution upstream of the growth segment.

As discussed in more detail later, this strategy enabled us to operate the SFC at a higher fluid velocity, hence shorter τ, without jeopardizing the yield too much. The velocity of the crystallization solution entering the growth segment was nearly doubled from 2.83 mm/s to 5.12 mm/s upon the addition of the fresh LYZ solution, resulting in s of 25.1 ± 0.8 min (**Table 6.3**). The S value of the LYZ solution entering the growth segment was equal to ≈ 29.3 calculated based on the LYZ solubility at 10 °C. This S value in the growth segment was the highest among the three cases studied (**Table 6.1**).

Despite the highly supersaturated condition, the LYZ concentration profile along the tube length showed a slow decrease in the first 4 m of the growth segment, hence indicating the absence of rapid crystal growth (**Figure 6.7A**). The rate of decrease in the LYZ concentration, nevertheless, picked up considerably in the last 2 m of the segment, resulting in a comparable yield (66.99 ± 4.54% w/w) with the base case (**Table 6.3**). In this regard, the suppression of the growth rate of LYZ crystals at high supersaturation levels had been studied by [346], where they showed that under a highly supersaturated condition, protein molecules exhibited a tendency to crystallize too quickly, often in the wrong orientations, hence blocking the binding sites to the subsequent growth units.

The LYZ crystals produced in the "(N + G) 10 °C" design exhibited a broad unimodal CSD with a peak at around 8.75 mm (**Figure 6.7B**) and d_{Ave} of 13.15 ± 0.86 mm (**Table 6.4**). Similar to the "(N + G) 22.5 °C" design, the "(N + G) 10 °C" design was able to reduce the production of small crystals (<10 mm) by more than half owed to its short nucleation segment. At the same time, it increased the size of the individual crystals owed to its prolonged growth segment at high S. Compared to the "(N + G) 22.5 °C" design, the "(N + G) 10 °C" design produced higher frequencies of crystals having sizes in the range of 10 to 25 mm. Moreover, the "(N + G) 10 °C" design also produced lower frequencies of crystals having sizes in the range of 25 to 40 mm, which indicated fewer large-sized agglomerates were formed. This was reflected in its lower Span value (1.50 ± 0.02) and lower d_{90} (22.43 ± 2.19) mm compared to that observed in the "(N + G) 22.5 °C" design (**Table 6.4**).

Therefore, even though the "(N + G) 10 °C" and "(N + G) 22.5 °C" designs exhibited similar d_{Ave} at around 13–14 mm, a closer look at their CSDs revealed the distinct crystal populations between the two. Indeed, the microscope image of the crystals produced by the "(N + G) 10 °C" design showed the predominant presence of large individual tetragonal LYZ crystals (>15 mm), which was observed to a much lesser degree in both the base case and the "(N + G) 22.5 °C" designs (**Figure 6.4C**). Nevertheless, the presence of agglomerates of the smaller crystals remained evident. In fact, agglomerations of the larger crystals were also observed in the microscope image, which explained for the abovementioned high Span value of the CSD.

Despite the existence of agglomerates, the "(N + G) 10 °C" design exhibited a much-improved reproducibility of the CSD, where the CV values for d_{Ave}, d_{10}, d_{50}, d_{90}; and Span among the four replicates were equal to 6.5%, 3.3%, 10.2%, 9.7%, and 1.3%, respectively (**Table 6.4**). We attributed the much-improved CSD's reproducibility to the higher fluid velocity that in turn reduced the formation of large-sized agglomerates, which likely had an adverse effect on the crystals' residence time distribution. Furthermore, unlike the "(N + G) 22.5 °C" design, where rapid growth of the crash-cooled crystals were observed in the beginning of the growth segment (as indicated by the LYZ concentration profile in **Figure 6.7A**), the "(N + G) 10 °C" design resulted in a slower, more steady growth of the crash-cooled crystals throughout most of the growth segment's length. This might also contribute to the improved CSD's reproducibility by virtue of the less disruption to the flow caused by the crystals.

Despite the shorter s, the PC of the "(N + G) 10 °C" design at 1.30 ± 0.08 g/h was the highest among the three cases studied, resulting in the space–time yield of 92.98 ± 8.12 g/L·h (**Table 6.3**). For comparison, the space–time yield in [46] was considerably lower at approximately 17.7 g/L·h, thus the benefit of operating the SFC at short s was evident. The high space–time yield was attributed to the ability of the "(N + G) 10 °C" design to maintain the yield at ≈ 67% despite its shorter s, by virtue of its operation at high S throughout the growth segment. The PE calculated with respect to the inlet LYZ flowrate (i.e., 2.38 g/ h) at 54 ± 3% (w/w) was comparable to that of the "(N + G) 22.5 °C" design and was superior to that of the base case. Lastly, similar to the previous two cases, the crystallized LYZ from the "(N + G) 10 °C" design also exhibited comparable cell lysis activity as the raw LYZ at 93.7 ± 5.9% (**Table 6.3**).

6.4 Conclusion

The CSD of LYZ crystals produced in SFC operated at short residence time and a high supersaturation level was demonstrated to have low reproducibility between replicates (n = 4) and small average crystal size (<10 mm). The presence of random agglomerates of the small crystals, which were prevalent in the crystals' population

due to the high nucleation rate, was postulated to be the cause for the low CSD's reproducibility via the adverse effect that the agglomerates had on the crystals' residence time distribution. The CSD's reproducibility was improved to a certain degree by having a segmented SFC design comprising a short nucleation segment and a much longer growth segment operated at different temperatures. The improved reproducibility in the average crystal size and the distribution width was by virtue of the decreased production of the small crystals in the segmented SFC design.

The CSD's reproducibility was further improved to a more acceptable level with CV 10% by (i) operating the segmented SFC design at a higher fluid velocity, resulting in less formation of large-sized agglomerates attributed to the shorter contact time among the crystals, while simultaneously (ii) operate the growth segment at a higher supersaturation level to maintain the desired yield and crystal size, as the high fluid velocity inevitably led to shorter residence time. The optimal SFC design produced LYZ crystals with an average size of ≈ 13–14 mm at yield of ≈ 67% and space- time yield of ≈ 93 g/L·h with residence time under 30 min. Minimal effect of the crystallization process on the LYZ activity was observed. Nevertheless, while the CSD's reproducibility was successfully improved, the CSD of the optimal SFC design exhibited a significant distribution width (Span ≈ 1.50) as the agglomeration persisted, albeit to a lesser extent. Since agglomerations were caused by small size of crystals, other method such as temperature cycling might be good to dissolve fine crystals and promote the growth of individual crystal growth, which ultimately mitigate the agglomeration. Therefore, the future research direction should aim to improve the monodispersity of LYZ crystals produced in SFC operated at short residence time.

CHAPTER 7 CONCLUSIONS AND RECOMMENDATIONS

7.1 Conclusions

Precipitation and crystallization are two classic unit operations used in the downstream processing of biopharmaceutical industry. Due to the recent development of upstream processing in the increase of titers, precipitation and crystallization has been considered promising alternatives to the traditional chromatography-based purification strategies for much lower cost, comparable purification performance, and most importantly, the possibility to be integrated into a continuous setup. Herein the objectives of this dissertation were to evaluate the performance of precipitation and crystallization of bioactive glycopeptides vancomycin hydrochloride (Van) and protein lysozyme (LYZ) in terms of (1) the phase behavior study of Van in salting out crystallization, and the investigation of the physicochemical properties of crystals produced with different habits (**Chapter 3**); (2) the phase behavior study of Van in antisolvent precipitation, and the comparison of the physicochemical properties of precipitates produced with different precipitation methods (**Chapter 4**); (3) the comparative study of bulk seeded crystallization of lysozyme in batch- and continuous slug flow-crystallizer (CSFC) (**Chapter 5**), and (4) the investigation of method to improve CSD in continuous slug flow crystallization of lysozyme (**Chapter 6**).

First, using NaCl as precipitant, the phase behaviors of Van have been investigated, with two major crystal habits, i.e., octahedral (O) and stand-alone needle (SAN) crystals determined, and their physicochemical properties compared. It was found that O crystal was the predominant crystal habit in salting-out room-temperature crystallization of Van. The O crystals were produced across the range of pH (2.6 to 5.6), Van (15 to 50 mg/mL), and NaCl concentrations (0.4 to 1.0 M) investigated. The needle crystal formation was largely avoided except at pH 5.6 and at NaCl concentrations in which the salting-in event took place (0.1 to 0.5 M). Although O and SAN crystals showed similar purity, internal crystal structure, peptide secondary structure, interfacial water content, and antibiotic activity, the O crystals exhibited superior thermal stability while the SAN crystals exhibited a more uniform size distribution. Their distinct crystal habits led to their distinct dissolution

profiles (i.e., slower dissolution rates for the O crystals) due to variations in their specific surface areas.

Second, using acetone as antisolvent, the phase behaviors of vancomycin hydrochloride have been investigated. It was found that higher pHs (i.e., pH 4.6 and 5.6), which resulted in higher supersaturation levels, was needed to generate a sufficiently high Van precipitation propensity. At these pHs, heavy precipitates made up of agglomerates of submicron particles were the predominant products. At their respective optimal conditions, the batch antisolvent Van precipitation exhibited a significantly higher 24-h yield than the batch salting-out precipitation at roughly 85% and 51% (w/w), respectively. The antisolvent and salting-out Van precipitates exhibited similar PXRD and FTIR spectra indicating their similar internal molecular structures, despite their vastly different morphology. They also exhibited comparable purity, thermal stability, and antimicrobial activity. The antisolvent Van precipitates, nevertheless, exhibited faster dissolution rates attributed to their nanoscale size. Despite being nanostructures, the antisolvent Van precipitates exhibited good stability during accelerated storage at elevated heat and humidity. In short, the antisolvent route was determined to be the superior precipitation method of Van owed to its higher precipitation efficiency while exhibiting comparable product qualities as the salting-out precipitates.

Third, in the comparative study, it was found that performing bulk seeded crystallization of LYZ in the CSFC resulted in superior CSD's width and reproducibility compared to the batch crystallizer, which was attributed to the less random agglomeration of the smaller crystals produced. The CSFC produced LYZ crystals of similar d_{ave} and morphology as the batch crystallizer, but at lower yield and STY due to the slower crystallization rate in the CSFC caused by its considerably lower shear rate compared to the batch crystallizer. The flowrate, which affected the residence time, was established as the governing process variable in the CSFC, where a minimum threshold existed for the flowrate below which the recovery of the seeds and product crystals were poor due to flow impediment. A trade-off existed upon increasing the flowrate between crystallization efficiency and crystal quality. At the highest flowrate investigated, the CSFC produced LYZ crystals with dave $\approx$ 6.5 μm,

yield ≈ 28% (w/w), and STY ≈ 2585 mg/h·L. While the yield could be improved by extending the CSFC's length, this might lead to lower STY. The seed loading was found to have a minimal impact on the CSFC's performance. Lastly, the activity of the LYZ crystals were not adversely affected by the CSFC.

Fourth, The CSD of LYZ crystals produced in SFC operated at short residence time and a high supersaturation level was demonstrated to have low reproducibility between replicates (n = 4) and small average crystal size (<10 mm). The CSD's reproducibility was improved to a certain degree by having a segmented SFC design comprising a short nucleation segment (N) and a much longer growth segment (G) operated at different temperatures. Lastly, the CSD's reproducibility was further improved to a more acceptable level with CV 10% by (i) operating the segmented SFC design at a higher fluid velocity, resulting in less formation of large-sized agglomerates attributed to the shorter contact time among the crystals, while simultaneously (ii) operate the growth segment at a higher supersaturation level to maintain the desired yield and crystal size, as the high fluid velocity inevitably led to shorter residence time. The optimal SFC design produced LYZ crystals with an average size of ≈ 13–14 mm at yield of ≈ 67% and space-time yield of ≈ 93 g/L·h with residence time under 30 min.

7.2 Recommendations for future works

1) In the crystallization of Van (Chapter 3), the production efficiency of O crystals of Van could be enhanced via improvement of the process. For example, the nucleation of the crystallization could be enhanced by better (both micro- and macro-) mixing, adjusting shear of the environment, and introduction of external fields (ultrasound, laser, electromagnetic) [347, 348]. Besides, heterogeneous nucleation can be induced by nucleants such as 1) seeds, 2) natural nucleants such as mineral surfaces, dried seaweed, horse hair, cellulose, and hydroxyapatite, etc., 3) charged surfaces such as functionalized mica with negatively charged sulfonated polystyrene films and positively charged silanized sheets, 4) porous nucleants, 5) Langmuir–Blodgett thin film template, 6) Molecularly imprinted polymers (MIPs) [349].

2) The difference of specific area in O and SAN crystals of Van might affect their dissolution profiles of on the pharmacokinetics behaviors, which ultimately affect the bioavailability of the API [18, 19]. Therefore, it is worth to investigate pharmacokinetics behaviors of these two crystal habits.

3) Nearly all the success stories of continuous protein crystallization reported thus far were based on the use of lysozyme as the model protein. Lysozyme is a highly popular choice for the model protein because not only it is relatively easy to crystallize, but also its solubility limit, phase diagram, and even its optimal crystallization conditions have been extensively investigated [172]. Thus, it is useful to explore these fundamental knowledges of other proteins and peptides for crystallization research. Specifically, high-throughput screening with machine learning might be promising [350, 351].

4) The precise control of the crystallization process is of great significance to the improvement of the total efficiency of the production process and the quality, which was not pursued in this dissertation. Thus, adopting online Process Analytical Technology (PAT) [352] and Quality by Design to the process is essential. Also, the comprehensive effects of critical process parameters (CPPs) make the process complex to understand and volatile to control [352]. Modeling of the continues crystallization process is useful to pursue as well in understanding the process [231].

5) The existing studies of continuous crystallization of proteins use highly pure lysozyme/antibody as the raw material for the continuous crystallization, which is ironic considering they were evaluating the feasibility of continuous crystallization as the DSP step for the purification of proteins. In the actual process, the crystallization solution might contain impurities such as other proteins/peptides, the hydrolysate of proteins/peptides, and other small

molecule impurities. First, the precipitants used in salting-out and antisolvent might crystallize/precipitate these protein/peptide impurities. Therefore, it would be desired to collect the solubility data and phase behaviors of these impurities during salting-out with NaCl and antisolvent crystallization with acetone. A series of crystallization conditions (pH, NaCl concentration, acetone concentration etc.) could then be determined to achieve selective crystallization of Van. Second, the impurities might affect the crystallization of Van. Specifically, the nucleation and crystal growth of Van might be affected, which will ultimately result in change of the yield, crystal size, and crystal shape. In fact, several studies have investigated the effect of impurities on the batch crystallization of proteins [97, 148, 353-356], and this is a promising future research direction for us to explore.

6) In order to transfer the manufacturing of biopharmaceuticals to an ultimately end-to-end continuous process, the DSP can be firstly investigated to be integrated in a fully continuous train of processes. Specifically, the processes of precipitation, crystallization, and formulation can be integrated continuously as has been reported for small-molecule pharmaceuticals [357, 358].

7) Obtaining Van precipitates with high quality from a productive process was not pursued in the bulk crystallization and precipitation in Chapter 3 and 4. Therefore, continuous crystallization of Van should be explored given the vast potential of the continuous crystallization platform in improving CSD and CSD reproducibility and at the same time improving the process efficiency.

CHAPTER 8 LIST OF PUBLICATIONS

Siyu Pu, Kunn Hadinoto, Continuous crystallization as a downstream processing step of pharmaceutical proteins: A review, *Chemical Engineering Research and Design*, Volume 160, 2020, Pages 89-104.

Siyu Pu, Kunn Hadinoto, Comparative evaluations of bulk seeded protein crystallization in batch versus continuous slug flow crystallizers, *Chemical Engineering Research and Design*, Volume 171, 2021, Pages 139-149.

Siyu Pu, Kunn Hadinoto, Improving the reproducibility of size distribution of protein crystals produced in continuous slug flow crystallizer operated at short residence time, *Chemical Engineering Science*, Volume 230, 2021, 116181.

Pu, S. and K. Hadinoto, Salting-out crystallization of glycopeptide antibiotics: Phase behavior study to control the crystal habit. *Chemical Engineering Science*, Volume 262, 2022, 118057.

Siyu Pu, Kunn Hadinoto, A Comparative Study of Antisolvent versus Salting-Out Precipitations of Glycopeptides: Precipitation Efficiency and Product Qualities, *Powder Technology*, Volume 415, 2023, 118181.

REFERENCES

1. IQVIA. *Revenue of the worldwide pharmaceutical market from 2001 to 2021 (in billion U.S. dollars) [Graph]. In Statista. Retrieved June 21, 2022, from https://www.statista.com/statistics/263102/pharmaceutical-market-worldwide-revenue-since-2001/*. 2021.

2. Evaluate. *(July 16, 2020). Global pharmaceutical revenue distributed by technology from 2012 to 2026* (in billion U.S. dollars) [Graph]. In Statista. Retrieved June 21, 2022, from https://www.statista.com/statistics/309457/world-pharmaceutical-revenue-distribution-by-technology/*. 2020.

3. Lau, J.L. and M.K. Dunn, *Therapeutic peptides: Historical perspectives, current development trends, and future directions.* Bioorganic & medicinal chemistry, 2018. **26**(10): p. 2700-2707.

4. Agyei, D., et al., *Bioprocess challenges to the isolation and purification of bioactive peptides.* Food and Bioproducts Processing, 2016. **98**: p. 244-256.

5. De Luca, C., et al., *Downstream Processing of Therapeutic Peptides by Means of Preparative Liquid Chromatography.* Molecules, 2021. **26**(15): p. 4688.

6. dos Santos, R., A.L. Carvalho, and A.C.A. Roque, *Renaissance of protein crystallization and precipitation in biopharmaceuticals purification.* Biotechnology advances, 2017. **35**(1): p. 41-50.

7. Roque, A.C.A., et al., *Anything but conventional chromatography approaches in bioseparation.* Biotechnology Journal, 2020. **15**(8): p. 1900274.

8. Harrison, R.G., et al., *8. Precipitation*, in *Bioseparations Science and Engineering (2nd Edition)*. Oxford University Press.

9. Puhl, S., L. Meinel, and O. Germershaus, *Recent advances in crystalline and amorphous particulate protein formulations for controlled delivery.* asian journal of pharmaceutical sciences, 2016. **11**(4): p. 469-477.

10. Pu, S. and K. Hadinoto, *Continuous Crystallization as a Downstream Processing Step of Pharmaceutical Proteins: A Review.* Chemical Engineering Research and Design, 2020.

11. Yu, X., et al., *Development of magnetic solid phase extraction platform for the purification of bioactive γ-glutamyl peptides from garlic (Allium sativum).* Lwt, 2020. **127**: p. 109410.

12. de Castro, R.J.S. and H.H. Sato, *Biologically active peptides: Processes for their generation, purification and identification and applications as natural additives in the food and pharmaceutical industries.* Food Res Int, 2015. **74**: p. 185-198.

13. Guo, M., et al., *Triglycine (GGG) Adopts a Polyproline II (pPII) Conformation in Its Hydrated Crystal Form: Revealing the Role of Water in Peptide Crystallization.* J Phys Chem Lett, 2021. **12**(34): p. 8416-8422.

14. Schäfer, M., T.R. Schneider, and G.M. Sheldrick, *Crystal structure of vancomycin.* Structure, 1996. **4**(12): p. 1509-1515.

15. Karle, I.L., H.N. Gopi, and P. Balaram, *Crystal structure of a hydrophobic 19-residue peptide helix containing three centrally located D amino acids.* Proceedings of the National Academy of Sciences, 2003. **100**(24): p. 13946-13951.

16. Bourcier, D., et al., *Influence of particle size and shape properties on cake resistance and compressibility during pressure filtration.* Chemical Engineering Science, 2016. **144**: p. 176-187.

17. Azad, M.A., et al., *Impact of critical material attributes (CMAs)-particle shape on miniature pharmaceutical unit operations.* AAPS PharmSciTech, 2021. **22**(3): p. 1-11.

18. Phan, C.U., et al., *Impact of Crystal Habit on the Dissolution Rate and In Vivo Pharmacokinetics of Sorafenib Tosylate.* Molecules, 2021. **26**(11): p. 3469.

19. Modi, S.R., et al., *Impact of crystal habit on biopharmaceutical performance of celecoxib.* Crystal growth & design, 2013. **13**(7): p. 2824-2832.

20. Matulis, D., *Selective precipitation of proteins.* Current protocols in protein science, 2016. **83**(1): p. 4.5. 1-4.5. 37.

21. Martinez, M., et al., *Precipitation as an Enabling Technology for the Intensification of Biopharmaceutical Manufacture.* Trends Biotechnol, 2019. **37**(3): p. 237-241.

22. Dallas, D.C., et al., *Current peptidomics: applications, purification, identification, quantification, and functional analysis.* Proteomics, 2015. **15**(5-6): p. 1026-1038.

23. Baghalabadi, V., H. Razmi, and A. Doucette, *Salt-Mediated Organic Solvent Precipitation for Enhanced Recovery of Peptides Generated by Pepsin Digestion.* Proteomes, 2021. **9**(4): p. 44.

24. McPherson, A. and J.A. Gavira, *Introduction to protein crystallization.* Acta Crystallographica Section F: Structural Biology Communications, 2014. **70**(1): p. 2-20.

25. Jackson, R., *Process for the crystallization of the ammonium and alkali metal salts in insulin*. 1973, Google Patents.

26. Smejkal, B., et al., *Fast and scalable purification of a therapeutic full - length antibody based on process crystallization.* Biotechnology and bioengineering, 2013. **110**(9): p. 2452-2461.

27. Zang, Y., et al., *Towards protein crystallization as a process step in downstream processing of therapeutic antibodies: screening and optimization at microbatch scale.* PLoS One, 2011. **6**(9): p. e25282.

28. Hebel, D., et al., *Stirred batch crystallization of a therapeutic antibody fragment.* Journal of biotechnology, 2013. **166**(4): p. 206-211.

29. Smejkal, B., et al., *Protein crystallization in stirred systems—scale - up via the maximum local energy dissipation.* Biotechnology and bioengineering, 2013. **110**(7): p. 1956-1963.

30. Flores, H., et al., *Apo-2 ligand/trail formulations*. 2005, Google Patents.

31. Peters, J., T. Minuth, and W. Schröder, *Implementation of a crystallization step into the purification process of a recombinant protein.* Protein expression and purification, 2005. **39**(1): p. 43-53.

32. Hekmat, D., et al., *Non-chromatographic preparative purification of enhanced green fluorescent protein.* Journal of biotechnology, 2015. **194**: p. 84-90.

33. Takakura, T., et al., *High-level expression and bulk crystallization of recombinant L-methionine γ-lyase, an anticancer agent.* Applied microbiology and biotechnology, 2006. **70**(2): p. 183-192.

34. Lee, A.Y., D. Erdemir, and A.S. Myerson, *Crystals and crystal growth.* Handbook of Industrial Crystallization, 2019. **3**: p. 32-75.

35. Chen, R.Q., et al., *An ignored variable: solution preparation temperature in protein crystallization.* Sci Rep, 2015. **5**: p. 7797.

36. Hekmat, D., et al., *Crystallization of lysozyme: from vapor diffusion experiments to batch crystallization in agitated ml-scale vessels.* Process Biochemistry, 2007. **42**(12): p. 1649-1654.

37. Hekmat, D., *Large-scale crystallization of proteins for purification and formulation.* Bioprocess and biosystems engineering, 2015. **38**(7): p. 1209-1231.

38. Randolph, A.D. and M.A. Larson, *Chapter 2 - PARTICLE DISTRIBUTIONS*, in *Theory of Particulate Processes (Second Edition)*, A.D. Randolph and M.A. Larson, Editors. 1988, Academic Press. p. 19-49.

39. Barros Groß, M. and M. Kind, *Comparative study on seeded and unseeded bulk evaporative batch crystallization of tetragonal lysozyme.* Crystal Growth & Design, 2017. **17**(6): p. 3491-3501.

40. Weichsel, U., et al., *Enhanced Crystallization of Lysozyme Mediated by the Aggregation of Inorganic Seed Particles.* Crystal Growth & Design, 2017. **17**(3): p. 967-981.

41. Ferreira, J., et al., *Ultrasonic protein crystallization: Promoting nucleation in microdroplets through pulsed sonication.* Chemical Engineering Research and Design, 2020. **162**: p. 249-257.

42. Mao, Y., et al., *Enhancement of lysozyme crystallization under ultrasound field.* Ultrasonics Sonochemistry, 2020. **63**: p. 104975.

43. Hebel, D., et al., *Development and scale up of high-yield crystallization processes of lysozyme and lipase using additives*. Crystal Growth & Design, 2013. **13**(6): p. 2499-2506.

44. Zhang, B., et al., *Enhancement of Lysozyme Crystallization Using DNA as a Polymeric Additive.* Crystals, 2019. **9**(4): p. 186.

45. Hekmat, D., et al., *Continuous crystallization of proteins in a stirred classified product removal tank with a tubular reactor in bypass.* Crystal Growth & Design, 2017. **17**(8): p. 4162-4169.

46. Neugebauer, P. and J.G. Khinast, *Continuous Crystallization of Proteins in a Tubular Plug-Flow Crystallizer.* Cryst Growth Des, 2015. **15**(3): p. 1089-1095.

47. Pu, S. and K. Hadinoto, *Improving the reproducibility of size distribution of protein crystals produced in continuous slug flow crystallizer operated at short residence time.* Chemical Engineering Science, 2021. **230**.

48. Thomas, K.M., S. Kwon, and R. Lakerveld, *Continuous Protein Crystallization in Mixed-Suspension Mixed-Product-Removal Crystallizers.* Crystal Growth & Design, 2021. **21**(2): p. 757-769.

49. Cheraghian Radi, H., B. Hajipour-Verdom, and F. Molaabasi, *Macromolecular crystallization: basics and advanced methodologies.* Journal of the Iranian Chemical Society, 2021. **18**(3): p. 543-565.

50. Chen, W., et al., *High Protein-Loading Silica Template for Heterogeneous Protein Crystallization.* Crystal Growth & Design, 2020. **20**(2): p. 866-873.

51. Yan, E.-K., et al., *Seeding Protein Crystallization with Cross-Linked Protein Crystals.* Crystal Growth & Design, 2018. **18**(2): p. 1090-1100.

52. Liu, H., C.O. Vandu, and R. Krishna, *Hydrodynamics of Taylor Flow in Vertical Capillaries: Flow Regimes, Bubble Rise Velocity, Liquid Slug Length, and Pressure Drop.* Industrial & Engineering Chemistry Research, 2005. **44**(14): p. 4884-4897.

53. Jiang, M., et al., *Continuous-flow tubular crystallization in slugs spontaneously induced by hydrodynamics.* Crystal Growth & Design, 2014. **14**(2): p. 851-860.

54. Jiang, M., et al., *Indirect ultrasonication in continuous slug-flow crystallization.* Crystal Growth & Design, 2015. **15**(5): p. 2486-2492.

55. Mou, M., et al., *Continuous Generation of Millimeter-Sized Glycine Crystals in Non-Seeded Millifluidic Slug Flow.* Crystals, 2019. **9**(8): p. 412.

56. Fakatselis, T.E., *Residence time optimization in continuous crystallizers.* Crystal growth & design, 2002. **2**(5): p. 375-379.

57. Kwon, J.S.-I., et al., *Crystal shape and size control using a plug flow crystallization configuration.* Chemical Engineering Science, 2014. **119**: p. 30-39.

58. Rader, R.A., *(Re) defining biopharmaceutical.* Nature biotechnology, 2008. **26**(7): p. 743-751.

59. Mullard, A., *FDA approves 100th monoclonal antibody product.* Nature reviews. Drug discovery, 2021.

60. Lu, R.-M., et al., *Development of therapeutic antibodies for the treatment of diseases.* Journal of biomedical science, 2020. **27**(1): p. 1-30.

61. Corti, D., et al., *Tackling COVID-19 with neutralizing monoclonal antibodies.* Cell, 2021. **184**(12): p. 3086-3108.

62. Jahanshahlu, L. and N. Rezaei, *Monoclonal antibody as a potential anti-COVID-19.* Biomedicine & Pharmacotherapy, 2020. **129**: p. 110337.

63. Mitragotri, S., P.A. Burke, and R. Langer, *Overcoming the challenges in administering biopharmaceuticals: formulation and delivery strategies.* Nature reviews Drug discovery, 2014. **13**(9): p. 655-672.

64. Jozala, A.F., et al., *Biopharmaceuticals from microorganisms: from production to purification.* brazilian journal of microbiology, 2016. **47**: p. 51-63.

65. Kshirsagar, R. and T. Ryll, *Innovation in Cell Banking, Expansion, and Production Culture*, in *New Bioprocessing Strategies: Development and Manufacturing of Recombinant Antibodies and Proteins*, B. Kiss, U. Gottschalk, and M. Pohlscheidt, Editors. 2018, Springer International Publishing: Cham. p. 51-74.

66. Tripathi, N.K. and A. Shrivastava, *Recent Developments in Bioprocessing of Recombinant Proteins: Expression Hosts and Process Development.* Frontiers in Bioengineering and Biotechnology, 2019. **7**.

67. Singh, N. and S. Herzer, *Downstream Processing Technologies/Capturing and Final Purification*, in *New Bioprocessing Strategies: Development and Manufacturing of Recombinant Antibodies and Proteins*, B. Kiss, U. Gottschalk, and M. Pohlscheidt, Editors. 2018, Springer International Publishing: Cham. p. 115-178.

68. Turner, R., et al., *Manufacturing of Proteins and Antibodies: Chapter Downstream Processing Technologies*, in *New Bioprocessing Strategies: Development and Manufacturing of Recombinant Antibodies and Proteins*, B. Kiss, U. Gottschalk, and M. Pohlscheidt, Editors. 2018, Springer International Publishing: Cham. p. 95-114.

69. Azevedo, A.M., et al., *Chromatography-free recovery of biopharmaceuticals through aqueous two-phase processing.* Trends in biotechnology, 2009. **27**(4): p. 240-247.

70. Zydney, A.L., *Continuous downstream processing for high value biological products: a review.* Biotechnology and bioengineering, 2016. **113**(3): p. 465-475.

71. Shukla, A.A. and J. Thömmes, *Recent advances in large-scale production of monoclonal antibodies and related proteins.* Trends in biotechnology, 2010. **28**(5): p. 253-261.

72. Szkodny, A.C. and K.H. Lee, *Biopharmaceutical Manufacturing: Historical Perspectives and Future Directions.* Annual Review of Chemical and Biomolecular Engineering, 2022. **13**.

73. Labrou, N.E., *Protein Purification Technologies*, in *Protein Downstream Processing: Design, Development, and Application of High and Low-Resolution Methods*, N.E. Labrou, Editor. 2021, Springer US: New York, NY. p. 3-10.

74. Labrou, N.E. and Labrou, *Protein downstream processing*. 2021: Springer.

75. Danielsson, Å., *Chapter 17 - Affinity Chromatography*, in *Biopharmaceutical Processing*, G. Jagschies, et al., Editors. 2018, Elsevier. p. 367-378.

76. Gronemeyer, P., R. Ditz, and J. Strube, *Trends in upstream and downstream process development for antibody manufacturing.* Bioengineering, 2014. **1**(4): p. 188-212.

77. Kelley, B., R. Kiss, and M. Laird, *A Different Perspective: How Much Innovation Is Really Needed for Monoclonal Antibody Production Using Mammalian Cell Technology?*, in *New Bioprocessing Strategies: Development and Manufacturing of Recombinant Antibodies and Proteins*, B. Kiss, U. Gottschalk, and M. Pohlscheidt, Editors. 2018, Springer International Publishing: Cham. p. 443-462.

78. Nadar, S., et al., *Intensified downstream processing of monoclonal antibodies using membrane technology.* Biotechnology Journal, 2021. **16**(3): p. 2000309.

79. Strube, J., F. Grote, and R. Ditz, *Bioprocess design and production technology for the future.* Biopharmaceutical production technology, 2012. **1**: p. 657-705.

80. Yang, X., et al., *Towards next generation high throughput ion exchange membranes for downstream bioprocessing: A review.* Journal of Membrane Science, 2022: p. 120325.

81. Tsuru, T., et al., *Peptide and amino acid separation with nanofiltration membranes.* Separation science and technology, 1994. **29**(8): p. 971-984.

82. Bazinet, L. and L. Firdaous, *Separation of bioactive peptides by membrane processes: technologies and devices.* Recent patents on biotechnology, 2013. **7**(1): p. 9-27.

83. Khoo, K.S., et al., *Liquid biphasic system: A recent bioseparation technology.* Processes, 2020. **8**(2): p. 149.

84. Kruse, T., M. Kampmann, and G. Greller, *Aqueous Two‐Phase Extraction of Monoclonal Antibodies from High Cell Density Cell Culture.* Chemie Ingenieur Technik, 2021. **93**(3): p. 497-502.

85. Van Alstine, J.M., G. Jagschies, and K.M. Łącki, *Chapter 12 - Alternative Separation Methods: Crystallization and Aqueous Polymer Two-Phase Extraction*, in *Biopharmaceutical Processing*, G. Jagschies, et al., Editors. 2018, Elsevier. p. 241-267.

86. Jiang, B., et al., *Separation and enrichment of antioxidant peptides from whey protein isolate hydrolysate by aqueous two-phase extraction and aqueous two-phase flotation.* Foods, 2019. **8**(1): p. 34.

87. Lappe, R., V. Sant'Anna, and A. Brandelli, *Extraction of the antimicrobial peptide cerein 8A by aqueous two-phase systems and aqueous two-phase micellar systems.* Natural Product Research, 2012. **26**(23): p. 2259-2265.

88. Santos, R.d., et al., *Magnetic precipitation: A new platform for protein purification.* Biotechnology Journal, 2020. **15**(9): p. 2000151.

89. Brechmann, N.A., et al., *Antibody capture process based on magnetic beads from very high cell density suspension.* Biotechnology and Bioengineering, 2021. **118**(9): p. 3499-3510.

90. Brechmann, N.A., et al., *Pilot-scale process for magnetic bead purification of antibodies directly from non-clarified CHO cell culture.* Biotechnology progress, 2019. **35**(3): p. e2775.

91. Safarik, I. and M. Safarikova, *Magnetic techniques for the isolation and purification of proteins and peptides.* Biomagnetic research and technology, 2004. **2**(1): p. 1-17.

92. Hammerschmidt, N., et al., *Continuous precipitation of IgG from CHO cell culture supernatant in a tubular reactor.* Biotechnology Journal, 2015. **10**(8): p. 1196-1205.

93. Sim, S.L., et al., *Branched polyethylene glycol for protein precipitation.* Biotechnology and bioengineering, 2012. **109**(3): p. 736-746.

94. Sommer, R., et al., *Combined polyethylene glycol and CaCl2 precipitation for the capture and purification of recombinant antibodies.* Process Biochemistry, 2014. **49**(11): p. 2001-2009.

95. Sommer, R., et al., *Capture and intermediate purification of recombinant antibodies with combined precipitation methods.* Biochemical Engineering Journal, 2015. **93**: p. 200-211.

96. Hubbuch, J., M. Kind, and H. Nirschl, *Preparative protein crystallization.* Chemical Engineering & Technology, 2019. **42**(11): p. 2275-2281.

97. Maosoongnern, S., et al., *Crystallization of lysozyme from lysozyme–ovalbumin mixtures: Separation potential and crystal growth kinetics.* Journal of Crystal Growth, 2017. **469**: p. 2-7.

98. Li, X., et al., *Protein crystal occurrence domains in selective protein crystallisation for bio-separation.* CrystEngComm, 2020. **22**(27): p. 4566-4572.

99. Chen, W., et al., *Biopurification of monoclonal antibody (mAb) through crystallisation.* Separation and Purification Technology, 2021. **263**: p. 118358.

100. Patil, R. and J. Walther, *Continuous manufacturing of recombinant therapeutic proteins: upstream and downstream technologies*, in *New Bioprocessing Strategies: Development and Manufacturing of Recombinant Antibodies and Proteins*. 2017, Springer. p. 277-322.

101. Khanal, O. and A.M. Lenhoff. *Developments and opportunities in continuous biopharmaceutical manufacturing*. in *MAbs*. 2021. Taylor & Francis.

102. Jungbauer, A., *Continuous downstream processing of biopharmaceuticals.* Trends in biotechnology, 2013. **31**(8): p. 479-492.

103. Strube, J., et al., *Process intensification in biologics manufacturing.* Chemical Engineering and Processing-Process Intensification, 2018. **133**: p. 278-293.

104. Samaras, J.J., M. Micheletti, and W. Ding, *Transformation of Biopharmaceutical Manufacturing Through Single-Use Technologies: Current State, Remaining Challenges, and Future Development.* Annual Review of Chemical and Biomolecular Engineering, 2022. **13**: p. 73-97.

105. *Fundamental Chemical and Structural Principles*, in *Peptides: Chemistry and Biology*. 2002. p. 5-59.

106. Hruby, V.J. and D. Patel, *6 - Structure–Function Studies of Peptide Hormones: An Overview*, in *Peptides*, B. Gutte, Editor. 1995, Academic Press: San Diego. p. 247-286.

107. Korang-Yeboah, M., et al., *Effect of formulation and peptide folding on the fibrillar aggregation, gelation, and oxidation of a therapeutic peptide.* International Journal of Pharmaceutics, 2021. **604**: p. 120677.

108. Spencer, R.K. and J.S. Nowick, *A newcomer´s guide to peptide crystallography.* Israel journal of chemistry, 2015. **55**(6-7): p. 698-710.

109. Przybycien, T.M., *Protein-protein interactions as a means of purification.* Current opinion in biotechnology, 1998. **9**(2): p. 164-170.

110. Erickson, H.P., *Size and shape of protein molecules at the nanometer level determined by sedimentation, gel filtration, and electron microscopy.* Biol Proced Online, 2009. **11**: p. 32-51.

111. Mewis, J. and N.J. Wagner, *1. Introduction to Colloid Science and Rheology*, in *Colloidal Suspension Rheology*. 2012, Cambridge University Press.

112. Stradner, A. and P. Schurtenberger, *Potential and limits of a colloid approach to protein solutions.* Soft Matter, 2020. **16**(2): p. 307-323.

113. Greene, D.G., *The formation and structure of precipitated protein phases*. 2016: University of Delaware.

114. Curtis, R. and L. Lue, *A molecular approach to bioseparations: protein–protein and protein–salt interactions.* Chemical Engineering Science, 2006. **61**(3): p. 907-923.

115. Rothstein, F., *Differential precipitation of proteins: science and technology.* Protein purification process engineering, 2019: p. 115-208.

116. Xu, Q. and X. Zhao, *Electrostatic interactions versus van der Waals interactions in the self-assembly of dispersed nanodiamonds.* Journal of Materials Chemistry, 2012. **22**(32): p. 16416-16421.

117. Leite, F.L., et al., *Theoretical models for surface forces and adhesion and their measurement using atomic force microscopy.* Int J Mol Sci, 2012. **13**(10): p. 12773-856.

118. Adair, J.H., E. Suvaci, and J. Sindel, *Surface and Colloid Chemistry*, in *Encyclopedia of Materials: Science and Technology*, K.H.J. Buschow, et al., Editors. 2001, Elsevier: Oxford. p. 1-10.

119. Zhou, H.-X. and X. Pang, *Electrostatic interactions in protein structure, folding, binding, and condensation.* Chemical reviews, 2018. **118**(4): p. 1691-1741.

120. Dumetz, A.C., *Protein interactions and phase behavior in aqueous solutions: Effects of salt, polymer, and organic additives*. 2007: University of Delaware.

121. Okur, H.I., et al., *Beyond the Hofmeister Series: Ion-Specific Effects on Proteins and Their Biological Functions.* The Journal of Physical Chemistry B, 2017. **121**(9): p. 1997-2014.

122. Kramer, R.M., et al., *Toward a molecular understanding of protein solubility: increased negative surface charge correlates with increased solubility.* Biophys J, 2012. **102**(8): p. 1907-15.

123. Dumetz, A.C., et al., *Protein phase behavior in aqueous solutions: crystallization, liquid-liquid phase separation, gels, and aggregates.* Biophysical journal, 2008. **94**(2): p. 570-583.

124. Ataka, M. and M. Asai, *Systematic studies on the crystallization of lysozyme: Determination and use of phase diagrams.* Journal of Crystal Growth, 1988. **90**(1-3): p. 86-93.

125. Retailleau, P., M. Ries-Kautt, and A. Ducruix, *No salting-in of lysozyme chloride observed at low ionic strength over a large range of pH.* Biophysical journal, 1997. **73**(4): p. 2156-2163.

126. Howard, S.B., et al., *The solubility of hen egg-white lysozyme.* Journal of Crystal Growth, 1988. **90**(1-3): p. 94-104.

127. Novák, P. and V. Havlíček, *Protein extraction and precipitation*, in *Proteomic profiling and analytical chemistry*. 2016, Elsevier. p. 51-62.

128. Yu, Z.-Q., F.-K. Zhang, and R.B.H. Tan, *Liquid–liquid phase separation in pharmaceutical crystallization.* Chemical Engineering Research and Design, 2021. **174**: p. 19-29.

129. Asherie, N., *Protein crystallization and phase diagrams.* Methods, 2004. **34**(3): p. 266-272.

130. Wang, Y., et al., *Liquid–Liquid Phase Separation in Oligomeric Peptide Solutions.* Langmuir, 2017. **33**(31): p. 7715-7721.

131. Rousseau, F., J. Schymkowitz, and L. Serrano, *Protein aggregation and amyloidosis: confusion of the kinds?* Current Opinion in Structural Biology, 2006. **16**(1): p. 118-126.

132. Vekilov, P.G., *Nucleation and growth mechanisms of protein crystals*, in *Handbook of Crystal Growth*. 2015, Elsevier. p. 795-871.

133. Govada, L. and N.E. Chayen, *Choosing the method of crystallization to obtain optimal results.* Crystals, 2019. **9**(2): p. 106.

134. Karpiński, P. and J. Bałdyga, *Precipitation processes.* Handbook of Industrial Crystallization, 2019: p. 216-265.

135. Tan, S.C. and B.C. Yiap, *DNA, RNA, and protein extraction: the past and the present.* Journal of Biomedicine and Biotechnology, 2009. **2009**.

136. Zoller, H.F., *Precipitation of Grain-Curd Casein from Pasteurized Milk, Including Sweet Cream Buttermilk.* Industrial & Engineering Chemistry, 1921. **13**(6): p. 510-514.

137. Aschaffenburg, R., *Preparation of β-casein by a modified urea fractionation method.* Journal of Dairy Research, 1963. **30**(2): p. 259-260.

138. Agarwal, A., et al., *Downstream Processing; Applications and Recent Updates*, in *Bioprocessing for Biofuel Production: Strategies to Improve Process Parameters*, N. Srivastava, et al., Editors. 2021, Springer Singapore: Singapore. p. 29-55.

139. Cohn, E.J., *The properties and functions of the plasma proteins, with a consideration of the methods for their separation and purification.* Chemical Reviews, 1941. **28**(2): p. 395-417.

140. Sasaki, A., et al., *Isolation and characterization of a corticotropin-releasing hormone-like peptide from human placenta.* The Journal of Clinical Endocrinology & Metabolism, 1988. **67**(4): p. 768-773.

141. Krishnan, L., *Vancomycin precipitation process*. 1993, Google Patents.

142. Raphael, M. and S. Rohani, *Sunflower protein precipitation in a tubular precipitator.* The Canadian Journal of Chemical Engineering, 1999. **77**(3): p. 540-554.

143. Raphael, M., S. Rohani, and F. Sosulski, *Isoelectric precipitation of sunflower protein in a tubular precipitator.* The Canadian Journal of Chemical Engineering, 1995. **73**(4): p. 470-483.

144. Ting, B.C.P., et al., *Fractionation of egg proteins and peptides for nutraceutical applications*, in *Separation, extraction and concentration processes in the food, beverage and nutraceutical industries*. 2013, Elsevier. p. 595-618.

145. Soto-Sierra, L., P. Stoykova, and Z.L. Nikolov, *Extraction and fractionation of microalgae-based protein products.* Algal research, 2018. **36**: p. 175-192.

146. Baghalabadi, V. and A.A. Doucette, *Mass spectrometry profiling of low molecular weight proteins and peptides isolated by acetone precipitation.* Analytica Chimica Acta, 2020. **1138**: p. 38-48.

147. Periasamy, P., et al., *A simple organic solvent precipitation method to improve detection of low molecular weight proteins.* Proteomics, 2021. **21**(19): p. 2100152.

148. Cheng, Y.-C., et al., *Salting-out of lysozyme and ovalbumin from mixtures: predicting precipitation performance from protein− protein interactions.* Industrial & Engineering Chemistry Research, 2008. **47**(15): p. 5203-5213.

149. Salcedo-Chávez, B., et al., *Optimization of the isoelectric precipitation method to obtain protein isolates from amaranth (Amaranthus cruentus) seeds.* Journal of Agricultural and Food Chemistry, 2002. **50**(22): p. 6515-6520.

150. Wu, H., et al., *Comparative studies on the functional properties of various protein concentrate preparations of peanut protein.* Food Research International, 2009. **42**(3): p. 343-348.

151. Schubert, P.F. and R.K. Finn, *Alcohol precipitation of proteins: the relationship of denaturation and precipitation for catalase.* Biotechnology and Bioengineering, 1981. **23**(11): p. 2569-2590.

152. Yoshikawa, H., et al., *Mechanistic insights into protein precipitation by alcohol.* International journal of biological macromolecules, 2012. **50**(3): p. 865-871.

153. Polson, C., et al., *Optimization of protein precipitation based upon effectiveness of protein removal and ionization effect in liquid chromatography–tandem mass spectrometry.* Journal of Chromatography B, 2003. **785**(2): p. 263-275.

154. Hammerschmidt, N., S. Hobiger, and A. Jungbauer, *Continuous polyethylene glycol precipitation of recombinant antibodies: sequential precipitation and resolubilization.* Process Biochemistry, 2016. **51**(2): p. 325-332.

155. McDonald, P., et al., *Selective antibody precipitation using polyelectrolytes: a novel approach to the purification of monoclonal antibodies.* Biotechnology and bioengineering, 2009. **102**(4): p. 1141-1151.

156. Mullerpatan, A., et al., *Purification of proteins using peptide-ELP based affinity precipitation.* Journal of Biotechnology, 2020. **309**: p. 59-67.

157. Roe, S., *Protein purification techniques: a practical approach*. Vol. 244. 2001: OUP Oxford.

158. Burgess, R.R., *Protein precipitation techniques.* Methods in enzymology, 2009. **463**: p. 331-342.

159. Duong-Ly, K.C. and S.B. Gabelli, *Chapter Seven - Salting out of Proteins Using Ammonium Sulfate Precipitation*, in *Methods in Enzymology*, J. Lorsch, Editor. 2014, Academic Press. p. 85-94.

160. Rupp, B., *Biomolecular crystallography: principles, practice, and application to structural biology*. 2009: Garland Science.

161. Morris, C.W., *Protein Precipitation for the Purification of Therapeutic Protein*. 2019, UCL (University College London).

162. Hilbrig, F. and R. Freitag, *Protein purification by affinity precipitation.* Journal of chromatography B, 2003. **790**(1-2): p. 79-90.

163. Van Alstine, J.M., G. Jagschies, and K.M. Łącki, *Chapter 11 - Alternative Separation Methods: Flocculation and Precipitation*, in *Biopharmaceutical Processing*, G. Jagschies, et al., Editors. 2018, Elsevier. p. 221-239.

164. Harrison, R.G., et al., *9. Crystallization*, in *Bioseparations Science and Engineering (2nd Edition)*. Oxford University Press.

165. Shenoy, B., et al., *Stability of crystalline proteins.* Biotechnology and bioengineering, 2001. **73**(5): p. 358-369.

166. Jen, A. and H.P. Merkle, *Diamonds in the rough: protein crystals from a formulation perspective.* Pharmaceutical research, 2001. **18**(11): p. 1483-1488.

167. McPherson, A., *Protein Crystallization*, in *Protein Crystallography: Methods and Protocols*, A. Wlodawer, Z. Dauter, and M. Jaskolski, Editors. 2017, Springer New York: New York, NY. p. 17-50.

168. Dumetz, A.C., et al., *Effects of pH on protein–protein interactions and implications for protein phase behavior.* Biochimica et Biophysica Acta (BBA)-Proteins and Proteomics, 2008. **1784**(4): p. 600-610.

169. Zhang, C.-Y., et al., *A strategy for selecting the pH of protein solutions to enhance crystallization.* Acta Crystallographica Section F: Structural Biology and Crystallization Communications, 2013. **69**(7): p. 821-826.

170. Somero, G.N., *Proteins and temperature.* Annual review of physiology, 1995. **57**: p. 43-68.

171. Yu, X., J. Ulrich, and J. Wang, *Crystallization and stability of different protein crystal modifications: A case study of lysozyme.* Crystal Research and Technology, 2015. **50**(2): p. 179-187.

172. Liu, Y., X. Wang, and C.B. Ching, *Toward Further Understanding of Lysozyme Crystallization: Phase Diagram, Protein−Protein Interaction, Nucleation Kinetics, and Growth Kinetics.* Crystal Growth & Design, 2010. **10**(2): p. 548-558.

173. Weber, M., M.J. Jones, and J. Ulrich, *Crystallization as a purification method for Jack Bean Urease: on the suitability of Poly (Ethylene Glycol), Li2SO4, and NaCl as precipitants.* Crystal Growth and Design, 2008. **8**(2): p. 711-716.

174. Chayen, N.E., *Turning protein crystallisation from an art into a science.* Current opinion in structural biology, 2004. **14**(5): p. 577-583.

175. Yu, L.X., et al., *Understanding pharmaceutical quality by design.* Aaps j, 2014. **16**(4): p. 771-83.

176. Guideline, I.H.T., *Pharmaceutical development.* Q8 (2R). As revised in August, 2009.

177. Alt, N., et al., *Determination of critical quality attributes for monoclonal antibodies using quality by design principles.* Biologicals, 2016. **44**(5): p. 291-305.

178. Lai, M. and E. Topp, *Solid-state chemical stability of proteins and peptides.* Journal of pharmaceutical sciences, 1999. **88**(5): p. 489-500.

179. Chang, L.L. and M.J. Pikal, *Mechanisms of protein stabilization in the solid state.* Journal of pharmaceutical sciences, 2009. **98**(9): p. 2886-2908.

180. Elkordy, A.A., R.T. Forbes, and B.W. Barry, *Stability of crystallised and spray-dried lysozyme.* International Journal of Pharmaceutics, 2004. **278**(2): p. 209-219.

181. Shi, K., H. Bi, and Y. Jiang, *Characterization of physiochemical and biological properties of spherical protein crystals for sustained release.* Asian Journal of Pharmaceutical Sciences, 2013. **8**(1): p. 58-63.

182. Hekmat, D., D. Hebel, and D. Weuster-Botz, *Crystalline proteins as an alternative to standard formulations.* Chemical Engineering & Technology: Industrial Chemistry-Plant Equipment-Process Engineering-Biotechnology, 2008. **31**(6): p. 911-916.

183. Yu, L., *Amorphous pharmaceutical solids: preparation, characterization and stabilization.* Advanced drug delivery reviews, 2001. **48**(1): p. 27-42.

184. Pikal, M.J. and D.R. Rigsbee, *The stability of insulin in crystalline and amorphous solids: observation of greater stability for the amorphous form.* Pharmaceutical research, 1997. **14**(10): p. 1379-1387.

185. Randolph, A.D. and M.A. Larson, *Chapter 1 - PARTICULATE PROCESSES*, in *Theory of Particulate Processes (Second Edition)*, A.D. Randolph and M.A. Larson, Editors. 1988, Academic Press. p. 1-18.

186. Seville, J. and C.-Y. Wu, *3.2.3.2 Attributes of a Particle Size Distribution*, in *Particle Technology and Engineering - An Engineer's Guide to Particles and Powders - Fundamentals and Computational Approaches*. Elsevier.

187. Hilfiker, R. and M. Von Raumer, *Polymorphism in the Pharmaceutical Industry: Solid Form and Drug Development*. 2019: John Wiley & Sons.

188. Prasad, M.R., et al., *Basics of Crystallization Process Applied in Drug Exploration*, in *Dosage Form Design Parameters*. 2018, Elsevier. p. 67-103.

189. Myerson, A.S. and R. Ginde, *2 - Crystals, crystal growth, and nucleation*. 2001, Butterworth-Heinemann. p. 33-65.

190. Chernov, A.A., *Growth Mechanisms*, in *Modern crystallography III*. 1984, Springer. p. 104-158.

191. Myerson, A.S. and R. Ginde, *Crystals, crystal growth, and nucleation*, in *Handbook of industrial crystallization*. 2002, Elsevier. p. 33-65.

192. Lovette, M.A., et al., *Crystal shape engineering.* Industrial & engineering chemistry research, 2008. **47**(24): p. 9812-9833.

193. Wood, W., *A bad (crystal) habit—and how it was overcome.* Powder technology, 2001. **121**(1): p. 53-59.

194. Shen, P., et al., *Physicochemical and structural properties of proteins extracted from dehulled industrial hempseeds: Role of defatting process and precipitation pH.* Food Hydrocolloids, 2020. **108**: p. 106065.

195. Green, A.A. and W.L. Hughes, *Protein fractionation on the basis of solubility in aqueous solutions of salts and organic solvents.* 1955.

196. Griebenow, K. and A.M. Klibanov, *On protein denaturation in aqueous− organic mixtures but not in pure organic solvents.* Journal of the American Chemical Society, 1996. **118**(47): p. 11695-11700.

197. Magsumov, T., et al., *The effect of dimethyl sulfoxide on the lysozyme unfolding kinetics, thermodynamics, and mechanism.* Biomolecules, 2019. **9**(10): p. 547.

198. Lim, D.G., et al., *Effects of precipitation process on the biophysical properties of highly concentrated proteins.* Journal of Pharmaceutical Investigation, 2020. **50**(5): p. 493-503.

199. McPherson, A., *Introduction to protein crystallization.* Methods, 2004. **34**(3): p. 254-265.

200. Besenhard, M.O., et al., *Crystal Engineering in Continuous Plug-Flow Crystallizers.* Crystal growth & design, 2017. **17**(12): p. 6432-6444.

201. Laramy, C.R., M.N. O'Brien, and C.A. Mirkin, *Crystal engineering with DNA.* Nature reviews. Materials, 2019. **4**(3): p. 201-224.

202. Civati, F., *Control of polymorphism, crystal size and habit in pharmaceuticals*, in *School of Chemistry*. 2019, National University of Ireland Galway.

203. Kwon, J.S.I., et al., *Modeling and control of protein crystal shape and size in batch crystallization.* AIChE Journal, 2013. **59**(7): p. 2317-2327.

204. Nayhouse, M., et al., *Crystal shape modeling and control in protein crystal growth.* Chemical engineering science, 2013. **87**: p. 216-223.

205. Yu, X., et al., *Evaluating the role of ionic liquids (ILs) in the crystallization of lysozyme.* Journal of Molecular Liquids, 2019: p. 112018.

206. Somasundaram, B., et al., *Progression of continuous downstream processing of monoclonal antibodies: Current trends and challenges.* Biotechnology and Bioengineering, 2018. **115**(12): p. 2893-2907.

207. Yang, O., S. Prabhu, and M. Ierapetritou, *Comparison between Batch and Continuous Monoclonal Antibody Production and Economic Analysis.* Industrial & Engineering Chemistry Research, 2019. **58**(15): p. 5851-5863.

208. Hammerschmidt, N., et al., *Economics of recombinant antibody production processes at various scales: Industry - standard compared to continuous precipitation.* Biotechnology journal, 2014. **9**(6): p. 766-775.

209. Chen, W., H. Yang, and J.Y. Yew Heng, *CHAPTER 10 Continuous Protein Crystallization*, in *The Handbook of Continuous Crystallization*. 2020, The Royal Society of Chemistry. p. 372-392.

210. Zhang, X., et al., *The study of continuous membrane crystallization on lysozyme.* Desalination, 2008. **219**(1-3): p. 101-117.

211. Wang, L., et al., *Tailored robust hydrogel composite membranes for continuous protein crystallization with ultrahigh morphology selectivity.* ACS applied materials & interfaces, 2018. **10**(31): p. 26653-26661.

212. Li, F. and R. Lakerveld, *Electric-field-assisted protein crystallization in continuous flow.* Crystal Growth & Design, 2018. **18**(5): p. 2964-2971.

213. Gerdts, C.J., et al., *Time-controlled microfluidic seeding in nL-volume droplets to separate nucleation and growth stages of protein crystallization.* Angewandte Chemie International Edition, 2006. **45**(48): p. 8156-8160.

214. Li, L. and R.F. Ismagilov, *Protein crystallization using microfluidic technologies based on valves, droplets, and SlipChip.* Annual review of biophysics, 2010. **39**: p. 139-158.

215. Zheng, B., L.S. Roach, and R.F. Ismagilov, *Screening of protein crystallization conditions on a microfluidic chip using nanoliter-size droplets.* Journal of the American chemical society, 2003. **125**(37): p. 11170-11171.

216. Zhang, D., et al., *Progress of pharmaceutical continuous crystallization.* Engineering, 2017. **3**(3): p. 354-364.

217. Parambil, J.V., et al., *Influence of solvent polarity and supersaturation on template-induced nucleation of carbamazepine crystal polymorphs.* Journal of Crystal Growth, 2017. **469**: p. 84-90.

218. Kwon, J.S.-I., et al., *Enhancing the crystal production rate and reducing polydispersity in continuous protein crystallization.* Industrial & Engineering Chemistry Research, 2014. **53**(40): p. 15538-15548.

219. Chen, J., et al., *Pharmaceutical crystallization.* Crystal growth & design, 2011. **11**(4): p. 887-895.

220. Kwon, J.S.-I., et al., *Modeling and control of crystal shape in continuous protein crystallization.* Chemical Engineering Science, 2014. **107**: p. 47-57.

221. Parambil, J.V., et al., *Effects of oscillatory flow on the nucleation and crystallization of insulin.* Crystal Growth & Design, 2011. **11**(10): p. 4353-4359.

222. Huettmann, H., et al., *Preparative crystallization of a single chain antibody using an aqueous two-phase system.* Biotechnology and bioengineering, 2014. **111**(11): p. 2192-2199.

223. Roberts, M.M., J.Y. Heng, and D.R. Williams, *Protein crystallization by forced flow through glass capillaries: enhanced lysozyme crystal growth.* Crystal Growth & Design, 2010. **10**(3): p. 1074-1083.

224. Alvarez, A.J. and A.S. Myerson, *Continuous plug flow crystallization of pharmaceutical compounds.* Crystal Growth & Design, 2010. **10**(5): p. 2219-2228.

225. Besenhard, M.O., et al., *Modeling a seeded continuous crystallizer for the production of active pharmaceutical ingredients.* Crystal Research and Technology, 2014. **49**(2-3): p. 92-108.

226. Besenhard, M.O., et al., *Crystal size control in a continuous tubular crystallizer.* Crystal growth & design, 2015. **15**(4): p. 1683-1691.

227. Eder, R.J., et al., *Continuously seeded, continuously operated tubular crystallizer for the production of active pharmaceutical ingredients.* Crystal growth & design, 2010. **10**(5): p. 2247-2257.

228. Jiang, M., et al., *Towards achieving a flattop crystal size distribution by continuous seeding and controlled growth.* Chemical engineering science, 2012. **77**: p. 2-9.

229. Zhao, Y., et al., *Kinetic identification and experimental validation of continuous plug flow crystallisation.* Chemical Engineering Science, 2015. **133**: p. 106-115.

230. Benitez-Chapa, A.G., K.D. Nigam, and A.J. Alvarez, *Process Intensification of Continuous Antisolvent Crystallization Using a Coiled Flow Inverter.* Industrial & Engineering Chemistry Research, 2019.

231. Hohmann, L., et al., *Analysis of crystal size dispersion effects in a continuous coiled tubular crystallizer: experiments and modeling.* Crystal Growth & Design, 2018. **18**(3): p. 1459-1473.

232. Raphael, M., S. Rohani, and F. Sosulski, *Recent Studies on Recovery of Oilseed Protein by Precipitation*. 1997, ACS Publications.

233. Yu, F., et al., *Enhancement of Continuous Crystallization of Lysozyme through Ultrasound.* Organic Process Research & Development, 2021. **25**(11): p. 2508-2515.

234. Liu, H., C.O. Vandu, and R. Krishna, *Hydrodynamics of Taylor flow in vertical capillaries: flow regimes, bubble rise velocity, liquid slug length, and pressure drop.* Industrial & engineering chemistry research, 2005. **44**(14): p. 4884-4897.

235. Jiang, M. and R.D. Braatz, *Designs of continuous-flow pharmaceutical crystallizers: developments and practice.* CrystEngComm, 2019.

236. Su, M. and Y. Gao, *Air–Liquid Segmented Continuous Crystallization Process Optimization of the Flow Field, Growth Rate, and Size Distribution of Crystals.* Industrial & Engineering Chemistry Research, 2018. **57**(10): p. 3781-3791.

237. Neugebauer, P., et al., *Crystal shape modification via cycles of growth and dissolution in a tubular crystallizer.* Crystal growth & design, 2018. **18**(8): p. 4403-4415.

238. McGlone, T., et al., *Oscillatory flow reactors (OFRs) for continuous manufacturing and crystallization.* Organic Process Research & Development, 2015. **19**(9): p. 1186-1202.

239. Lawton, S., et al., *Continuous crystallization of pharmaceuticals using a continuous oscillatory baffled crystallizer.* Organic Process Research & Development, 2009. **13**(6): p. 1357-1363.

240. Castro, F., et al., *Protein crystallization as a process step in a novel meso oscillatory flow reactor: study of lysozyme phase behavior.* Crystal Growth & Design, 2016. **16**(7): p. 3748-3755.

241. Castro, F., et al., *Influence of mixing intensity on lysozyme crystallization in a meso oscillatory flow reactor.* Crystal Growth & Design, 2018. **18**(10): p. 5940-5946.

242. Yang, H., et al., *Continuous protein crystallisation platform and process: Case of lysozyme.* Chemical Engineering Research and Design, 2018. **136**: p. 529-535.

243. Yang, H., et al., *Development and Workflow of a Continuous Protein Crystallization Process: A Case of Lysozyme.* Crystal Growth & Design, 2019. **19**(2): p. 983-991.

244. Hong, M.S., et al., *Challenges and opportunities in biopharmaceutical manufacturing control.* Computers & Chemical Engineering, 2018. **110**: p. 106-114.

245. Nanev, C.N., *Peculiarities of protein crystal nucleation and growth.* Crystals, 2018. **8**(11): p. 422.

246. Ryu, B.H. and J. Ulrich, *Controlled nucleation and growth of protein crystals by solvent freeze-out.* Crystal Growth & Design, 2012. **12**(12): p. 6126-6133.

247. Chayen, N.E., *Methods for separating nucleation and growth in protein crystallisation.* Progress in biophysics and molecular biology, 2005. **88**(3): p. 329-337.

248. Wang, Z., et al., *Manipulating crystallization in lysozyme and supramolecular self-arrangement in solution using ionic liquids.* CrystEngComm, 2018. **20**(16): p. 2284-2291.

249. Polino, M., et al., *Protein Crystallization by Membrane-Assisted Technology.* Crystal Growth & Design, 2019. **19**(8): p. 4871-4883.

250. Zhang, B., et al., *DNA Origami as Seeds for Promoting Protein Crystallization.* ACS applied materials & interfaces, 2018. **10**(51): p. 44240-44246.

251. Durbin, S. and G. Feher, *Crystal growth studies of lysozyme as a model for protein crystallization.* Journal of Crystal Growth, 1986. **76**(3): p. 583-592.

252. Pu, S. and K. Hadinoto, *Salting-Out crystallization of glycopeptide Vancomycin: Phase behavior study to control the crystal habit.* Chemical Engineering Science, 2022. **262**: p. 118057.

253. Kim, W.-S. and K.-K. Koo, *Enhancement in Bulk Density of l-Methionine Agglomerates by Cooling Crystallization with pH Control Using Additives.* Crystal Growth & Design, 2019. **19**(6): p. 3469-3476.

254. Shah, U.V., et al., *Effect of crystal habits on the surface energy and cohesion of crystalline powders.* International journal of pharmaceutics, 2014. **472**(1-2): p. 140-147.

255. Pudasaini, N., et al., *Downstream processability of crystal habit-modified active pharmaceutical ingredient.* Organic process research & development, 2017. **21**(4): p. 571-577.

256. Yin, J.C., et al., *Study of the crystal shape and its influence on the anti-tumor activity of tumor necrosis factor-related apoptosis-inducing ligand (Apo2L/TRAIL)*. Crystal Research and Technology: Journal of Experimental and Industrial Crystallography, 2008. **43**(8): p. 888-893.

257. Ren, Y., et al., *Impact of Crystal Habit on Solubility of Ticagrelor.* Crystals, 2019. **9**(11): p. 556.

258. Cote, A., et al., *Perspectives on the Current State, Challenges, and Opportunities in Pharmaceutical Crystallization Process Development.* Crystal Growth & Design, 2020. **20**(12): p. 7568-7581.

259. Steenweg, C., J. Habicht, and K. Wohlgemuth, *Continuous Isolation of Particles with Varying Aspect Ratios up to Thin Needles Achieving Free-Flowing Products.* Crystals, 2022. **12**(2): p. 137.

260. MacLeod, C.S. and F.L. Muller, *On the Fracture of Pharmaceutical Needle-Shaped Crystals during Pressure Filtration: Case Studies and Mechanistic Understanding.* Organic Process Research & Development, 2012. **16**(3): p. 425-434.

261. Meekes, H., et al., *Needle crystal morphology explained.* Chemical Engineering & Technology: Industrial Chemistry - Plant Equipment - Process Engineering - Biotechnology, 2003. **26**(3): p. 256-261.

262. Black, S.N., *Crystallization in the Pharmaceutical Industry.* Handbook of Industrial Crystallization, 2019: p. 380-413.

263. Ghazi, N., et al., *Investigating the Effect of APAP Crystals on Tablet Behavior Manufactured by Direct Compression.* AAPS PharmSciTech, 2019. **20**(5): p. 168.

264. Civati, F., et al., *Factors Controlling Persistent Needle Crystal Growth: The Importance of Dominant One-Dimensional Secondary Bonding, Stacked Structures, and van der Waals Contact.* Crystal Growth & Design, 2021.

265. Li, R.F., et al., *Integration of crystal morphology modeling and on-line shape measurement.* AIChE Journal, 2006. **52**(6): p. 2297-2305.

266. Winn, D. and M.F. Doherty, *Predicting the shape of organic crystals grown from polar solvents.* Chemical engineering science, 2002. **57**(10): p. 1805-1813.

267. Lovette, M.A. and M.F. Doherty, *Needle-shaped crystals: causality and solvent selection guidance based on periodic bond chains.* Crystal growth & design, 2013. **13**(8): p. 3341-3352.

268. Taulelle, P., et al., *Pharmaceutical compound crystallization: Growth mechanism of needle-like crystals.* Chemical Engineering & Technology: Industrial Chemistry-Plant Equipment-Process Engineering-Biotechnology, 2006. **29**(2): p. 239-246.

269. Tilbury, C.J., et al., *Predicting the Effect of Solvent on the Crystal Habit of Small Organic Molecules.* Crystal Growth & Design, 2016. **16**(5): p. 2590-2604.

270. Hadjittofis, E., et al., *Influences of crystal anisotropy in pharmaceutical process development.* Pharmaceutical Research, 2018. **35**(5): p. 1-22.

271. Li, J., et al., *A design aid for crystal growth engineering.* Progress in Materials Science, 2016. **82**: p. 1-38.

272. Turner, T.D., et al., *Habit modification of the active pharmaceutical ingredient lovastatin through a predictive solvent selection approach.* Journal of Pharmaceutical Sciences, 2019. **108**(5): p. 1779-1787.

273. Hatcher, L.E., et al., *Tuning morphology in active pharmaceutical ingredients: Controlling the crystal habit of lovastatin through solvent choice and non-size-matched polymer additives.* Crystal Growth & Design, 2020. **20**(9): p. 5854-5862.

274. Rasenack, N. and B. Müller, *Properties of ibuprofen crystallized under various conditions: a comparative study.* Drug development and industrial pharmacy, 2002. **28**(9): p. 1077-1089.

275. Kumar, D., et al., *Effect of surfactant concentration on nifedipine crystal habit and its related pharmaceutical properties.* Journal of Crystal Growth, 2015. **422**: p. 44-51.

276. Jarmer, D.J., et al., *Supercritical fluid crystallization of griseofulvin: Crystal habit modification with a selective growth inhibitor.* Journal of pharmaceutical sciences, 2005. **94**(12): p. 2688-2702.

277. Lovette, M.A. and M.F. Doherty, *Predictive Modeling of Supersaturation-Dependent Crystal Shapes.* Crystal Growth & Design, 2012. **12**(2): p. 656-669.

278. Eren, A., et al., *Experimental investigation of an integrated crystallization and wet-milling system with temperature cycling to control the size and aspect ratio of needle-shaped pharmaceutical crystals.* Crystal Growth & Design, 2021. **21**(7): p. 3981-3993.

279. Banga, S., et al., *Modification of the crystal habit of celecoxib for improved processability.* Journal of pharmacy and pharmacology, 2007. **59**(1): p. 29-39.

280. Judge, R.A., et al., *The effect of ionic liquids on protein crystallization and X-ray diffraction resolution.* Crystal Growth and Design, 2009. **9**(8): p. 3463-3469.

281. Liang, M., et al., *Shape evolution and thermal stability of lysozyme crystals: effect of pH and temperature.* Bioprocess and Biosystems Engineering, 2013. **36**(1): p. 91-99.

282. Bruniera, F., et al., *The use of vancomycin with its therapeutic and adverse effects: a review.* Eur Rev Med Pharmacol Sci, 2015. **19**(4): p. 694-700.

283. Lee, J.W., et al., *Process of purifying vancomycin hydrochloride*. 2006, Google Patents.

284. Lee, J.-Y., et al., *Systematic evaluation and optimization of crystallization conditions for vancomycin purification.* Korean Journal of Chemical Engineering, 2010. **27**(5): p. 1538-1546.

285. Ha, G.S. and J.-H. Kim, *Effect of an ionic liquid on vancomycin crystallization.* Korean Journal of Chemical Engineering, 2015. **32**(4): p. 576-582.

286. Kim, Y.-N., J.-Y. Lee, and J.-H. Kim, *Improvement of a crystallization process for the purification of vancomycin.* Process Biochemistry, 2011. **46**(10): p. 2068-2073.

287. Aleixa do Nascimento, P., A.C. Kogawa, and H. Salgado, *A New Ecological HPLC Method for Determination of Vancomycin Dosage form.* Current Chromatography, 2020. **7**(2): p. 82-90.

288. Kołodziej, M., et al., *Design of Bulk Protein Crystallization Based on Phase Diagrams Accounting for the Presence of Interfacial Water.* Crystal Growth & Design, 2017. **18**(1): p. 393-401.

289. Surawicz, C.M., et al., *Guidelines for Diagnosis, Treatment, and Prevention ofClostridium difficileInfections.* Official journal of the American College of Gastroenterology | ACG, 2013. **108**(4).

290. FDA, U.S., *FDA Draft Guidance on Vancomycin Hydrochloride*, U.S. FDA, Editor. 2008.

291. Hens, B., et al., *Low buffer capacity and alternating motility along the human gastrointestinal tract: implications for in vivo dissolution and absorption of ionizable drugs.* Molecular pharmaceutics, 2017. **14**(12): p. 4281-4294.

292. Phillips, D.J., et al., *Overcoming sink limitations in dissolution testing: a review of traditional methods and the potential utility of biphasic systems.* Journal of Pharmacy and Pharmacology, 2012. **64**(11): p. 1549-1559.

293. Tran, T.-T., et al., *An evaluation of inhaled antibiotic liposome versus antibiotic nanoplex in controlling infection in bronchiectasis.* International journal of pharmaceutics, 2019. **559**: p. 382-392.

294. Charles, M., S. Veesler, and F. Bonneté, *MPCD: a new interactive on-line crystallization data bank for screening strategies.* Acta Crystallographica Section D: Biological Crystallography, 2006. **62**(11): p. 1311-1318.

295. Kirkwood, J., et al., *Using isoelectric point to determine the pH for initial protein crystallization trials.* Bioinformatics, 2015. **31**(9): p. 1444-1451.

296. Horká, M., et al., *CIEF separation, UV detection, and quantification of ampholytic antibiotics and bacteria from different matrices.* Analytical and Bioanalytical Chemistry, 2014. **406**(25): p. 6285-6296.

297. Mathew, M. and V.D. Gupta, *Stability of vancomycin hydrochloride solutions at various pH values as determined by high-performance liquid chromatography*. Drug development and industrial pharmacy, 1995. **21**(2): p. 257-264.

298. Giffard, M., et al., *Salting-in effects on urate oxidase crystal design.* Crystal Growth and Design, 2008. **8**(12): p. 4220-4226.

299. Maurer, R.W., S.I. Sandler, and A.M. Lenhoff, *Salting-in characteristics of globular proteins.* Biophysical Chemistry, 2011. **156**(1): p. 72-78.

300. Myrvold, B.O., *Salting-out and salting-in experiments with lignosulfonates (LSs)*. Holzforschung, 2013. **67**(5): p. 549-557.

301. Baumgartner, K., et al., *Determination of protein phase diagrams by microbatch experiments: Exploring the influence of precipitants and pH.* International Journal of Pharmaceutics, 2015. **479**(1): p. 28-40.

302. Wöll, A.K., et al., *Analysis of phase behavior and morphology during freeze-thaw applications of lysozyme.* International journal of pharmaceutics, 2019. **555**: p. 153-164.

303. Pantuso, E., et al., *On the Aggregation and Nucleation Mechanism of the Monoclonal Antibody Anti-CD20 Near Liquid-Liquid Phase Separation (LLPS)*. Scientific Reports, 2020. **10**(1): p. 8902.

304. Luft, J.R., J.R. Wolfley, and E.H. Snell, *What's in a Drop? Correlating Observations and Outcomes to Guide Macromolecular Crystallization Experiments.* Crystal Growth & Design, 2011. **11**(3): p. 651-663.

305. Stroobants, S., et al., *Influence of Shear on Protein Crystallization under Constant Shear Conditions.* Crystal Growth & Design, 2020. **20**(3): p. 1876-1883.

306. Giese, H., et al., *Effective shear rates in shake flasks.* Chemical Engineering Science, 2014. **118**: p. 102-113.

307. Cerchiara, T., et al., *Chitosan based micro-and nanoparticles for colon-targeted delivery of vancomycin prepared by alternative processing methods.* European Journal of Pharmaceutics and Biopharmaceutics, 2015. **92**: p. 112-119.

308. Ostwald, W., *Studien über die Bildung und Umwandlung fester Körper.* 1. Abhandlung: Übersättigung und Überkaltung, 1897. **22U**(1): p. 289-330.

309. Rochani, A., et al., *Stability-indicating HPLC method to determine the stability of extemporaneously prepared vancomycin oral solution cups.* American Journal of Health-System Pharmacy, 2022. **79**(1): p. e34-e40.

310. Claudius, J.S. and S.H. Neau, *The solution stability of vancomycin in the presence and absence of sodium carboxymethyl starch.* International journal of pharmaceutics, 1998. **168**(1): p. 41-48.

311. Van Hal, S., T.P. Lodise, and D.L. Paterson, *The clinical significance of vancomycin minimum inhibitory concentration in Staphylococcus aureus infections: a systematic review and meta-analysis.* Clinical Infectious Diseases, 2012. **54**(6): p. 755-771.

312. Akbarian, M., et al., *Bioactive Peptides: Synthesis, Sources, Applications, and Proposed Mechanisms of Action.* International Journal of Molecular Sciences, 2022. **23**(3): p. 1445.

313. Bai, C., Q. Wei, and X. Ren, *Selective extraction of collagen peptides with high purity from cod skins by deep eutectic solvents.* ACS Sustainable Chemistry & Engineering, 2017. **5**(8): p. 7220-7227.

314. McPherson, A. and J.A. Gavira, *Introduction to protein crystallization.* Acta crystallographica. Section F, Structural biology communications, 2014. **70**(Pt 1): p. 2-20.

315. Leonil, J., et al., *Precipitation of hydrophobic peptides from tryptic casein hydrolysate by salt and pH.* Enzyme and microbial technology, 1994. **16**(7): p. 591-595.

316. Ha, G.-S. and J.-H. Kim, *Kinetic and thermodynamic characteristics of crystallization of vancomycin.* Korean Journal of Chemical Engineering, 2017. **34**(9): p. 2451-2458.

317. Berman, H., K. Henrick, and H. Nakamura, *Announcing the worldwide protein data bank.* Nature Structural & Molecular Biology, 2003. **10**(12): p. 980-980.

318. Cheow, W.S., T.Y. Kiew, and K. Hadinoto, *Amorphous nanodrugs prepared by complexation with polysaccharides: Carrageenan versus dextran sulfate.* Carbohydrate polymers, 2015. **117**: p. 549-558.

319. Yu, H., et al., *Dry powder inhaler formulation of high-payload antibiotic nanoparticle complex intended for bronchiectasis therapy: spray drying versus spray freeze drying preparation.* International journal of pharmaceutics, 2016. **499**(1-2): p. 38-46.

320. Arathoon, W., *Large-scale cell culture in biotechnology.* Science, 1986. **232**(4756): p. 1390-1395.

321. Bergfors, T.M., *Protein crystallization*. 2009: Internat'l University Line.

322. Clarke, C.J., et al., *Green and sustainable solvents in chemical processes.* Chemical Reviews, 2018. **118**(2): p. 747-800.

323. Waseda, Y., E. Matsubara, and K. Shinoda, *Diffraction from polycrystalline samples and determination of crystal structure*, in *X-ray diffraction crystallography*. 2011, Springer. p. 107-167.

324. Breen, E., et al., *Effect of moisture on the stability of a lyophilized humanized monoclonal antibody formulation.* Pharmaceutical research, 2001. **18**(9): p. 1345-1353.

325. Phan, H.T. and A.J. Haes, *What does nanoparticle stability mean?* The Journal of Physical Chemistry C, 2019. **123**(27): p. 16495-16507.

326. Pu, S. and K. Hadinoto, *Comparative evaluations of bulk seeded protein crystallization in batch versus continuous slug flow crystallizers.* Chemical Engineering Research and Design, 2021. **171**: p. 139-149.

327. Zhu, M.M., et al., *Industrial Production of Therapeutic Proteins: Cell Lines, Cell Culture, and Purification*, in *Handbook of Industrial Chemistry and Biotechnology*, J.A. Kent, T.V. Bommaraju, and S.D. Barnicki, Editors. 2017, Springer International Publishing: Cham. p. 1639-1669.

328. Hebel, D., et al., *Development and Scale up of High-Yield Crystallization Processes of Lysozyme and Lipase Using Additives.* Crystal Growth & Design, 2013. **13**(6): p. 2499-2506.

329. Kang, Y.-S. and J.D. Ward, *Analysis of Seed Loading and Supersaturation Trajectories for Two-Dimensional Crystallization Systems.* Industrial & Engineering Chemistry Research, 2017. **56**(38): p. 10798-10812.

330. Yousuf, M. and P.J. Frawley, *Secondary Nucleation from Nuclei Breeding and Its Quantitative Link with Fluid Shear Stress in Mixing: A Potential Approach for Precise Scale-up in Industrial Crystallization.* Organic Process Research & Development, 2019. **23**(5): p. 926-934.

331. Maosoongnern, S., et al., *Introducing a Fast Method to Determine the Solubility and Metastable Zone Width for Proteins: Case Study Lysozyme.* Industrial & Engineering Chemistry Research, 2012. **51**(46): p. 15251-15257.

332. Mathew Thomas, K. and R. Lakerveld, *An Airlift Crystallizer for Protein Crystallization.* Industrial & Engineering Chemistry Research, 2019.

333. Pusey, M.L. and A. Nadarajah, *A model for tetragonal lysozyme crystal nucleation and growth.* Crystal growth & design, 2002. **2**(6): p. 475-483.

334. Cacioppo, E., S. Munson, and M.L. Pusey, *Protein solubilities determined by a rapid technique and modification of that technique to a micro-method.* Journal of crystal growth, 1991. **110**(1-2): p. 66-71.

335. Tait, S., E.T. White, and J.D. Litster, *A study on nucleation for protein crystallization in mixed vessels.* Crystal Growth and Design, 2009. **9**(5): p. 2198-2206.

336. Agrawal, S. and A. Paterson, *Secondary nucleation: mechanisms and models.* Chemical Engineering Communications, 2015. **202**(5): p. 698-706.

337. Darmali, C., et al., *Mechanisms and control of impurities in continuous crystallization: a review.* Industrial & Engineering Chemistry Research, 2018. **58**(4): p. 1463-1479.

338. Bekard, I.B., et al., *The effects of shear flow on protein structure and function.* Biopolymers, 2011. **95**(11): p. 733-45.

339. Ecker, D.M., S.D. Jones, and H.L. Levine, *The therapeutic monoclonal antibody market.* mAbs, 2015. **7**(1): p. 9-14.

340. Wang, T., et al., *Recent progress of continuous crystallization.* Journal of Industrial and Engineering Chemistry, 2017. **54**: p. 14-29.

341. Vekilov, P. and F. Rosenberger, *Protein crystal growth under forced solution flow: experimental setup and general response of lysozyme.* Journal of crystal growth, 1998. **186**(1-2): p. 251-261.

342. Long, B., H. Yang, and Y. Ding, *Impact of seed loading ratio on the growth kinetics of mono-ammonium phosphate under isothermal batch crystallization.* Korean Journal of Chemical Engineering, 2016. **33**(2): p. 623-628.

343. Cacioppo, E. and M.L. Pusey, *The solubility of the tetragonal form of hen egg white lysozyme from pH 4.0 to 5.4.* Journal of crystal growth, 1991. **114**(3): p. 286-292.

344. Muschol, M. and F. Rosenberger, *Liquid–liquid phase separation in supersaturated lysozyme solutions and associated precipitate formation/crystallization.* The Journal of chemical physics, 1997. **107**(6): p. 1953-1962.

345. Gorti, S., E.L. Forsythe, and M.L. Pusey, *Kinetic roughening and energetics of tetragonal lysozyme crystal growth.* Crystal growth & design, 2004. **4**(4): p. 691-699.

346. Schmit, J.D. and K. Dill, *Growth Rates of Protein Crystals.* Journal of the American Chemical Society, 2012. **134**(9): p. 3934-3937.

347. McGinty, J., et al., *Nucleation and Crystal Growth in Continuous Crystallization.* 2020.

348. Erdemir, D., A.Y. Lee, and A.S. Myerson, *Crystal Nucleation*, in *Handbook of Industrial Crystallization*, A.Y. Lee, A.S. Myerson, and D. Erdemir, Editors. 2019, Cambridge University Press: Cambridge. p. 76-114.

349. Zhou, R.-B., et al., *A review on recent advances for nucleants and nucleation in protein crystallization.* CrystEngComm, 2017. **19**(8): p. 1143-1155.

350. Ito, S., G. Ueno, and M. Yamamoto, *DeepCentering: fully automated crystal centering using deep learning for macromolecular crystallography.* Journal of synchrotron radiation, 2019. **26**(4): p. 1361-1366.

351. Elbasir, A., et al., *DeepCrystal: a deep learning framework for sequence-based protein crystallization prediction.* Bioinformatics, 2019. **35**(13): p. 2216-2225.

352. Gao, Y., et al., *Application of PAT-based feedback control approaches in pharmaceutical crystallization.* Crystals, 2021. **11**(3): p. 221.

353. Judge, R.A., E.L. Forsythe, and M.L. Pusey, *The effect of protein impurities on lysozyme crystal growth.* Biotechnology and bioengineering, 1998. **59**(6): p. 776-785.

354. Díaz Borbón, V. and J. Ulrich, *Solvent freeze out crystallization of lysozyme from a lysozyme - ovalbumin mixture.* Crystal Research and Technology, 2012. **47**(5): p. 541-547.

355. Baker, B.Y., et al., *Crystallization of proteins from crude bovine rod outer segments*, in *Methods in enzymology*. 2015, Elsevier. p. 439-458.

356. Lorber, B., et al., *The influence of impurities on protein crystallization; the case of lysozyme.* Journal of crystal growth, 1993. **128**(1-4): p. 1203-1211.

357. Adamo, A., et al., *On-demand continuous-flow production of pharmaceuticals in a compact, reconfigurable system.* Science, 2016. **352**(6281): p. 61-67.

358. Rogers, L., et al., *Continuous production of five active pharmaceutical ingredients in flexible plug-and-play modules: a demonstration campaign.* Organic Process Research & Development, 2020. **24**(10): p. 2183-2196.